Hydrodynamics and Chemistry of Silica scale formation in Hydrogeothermal systems

Pavlo Kokhanenko

A thesis presented for the degree of Doctor of Philosophy
in Mechanical Engineering
at the University of Canterbury,
Christchurch, New Zealand
2014

ACKNOWLEDGMENTS

Firstly, I would like to acknowledge the invaluable role of my supervisory team in this project. I'm grateful to my senior supervisor, Associate Professor Mark Jermy, for the opportunity to undertake this PhD study, for his expertise and brilliant ideas that enriched me as well as this thesis. The amount of time and effort he invested into guiding me through this project is unlikely quantifiable. I would like to acknowledge the practical expertise, guidance, encouragement and interest in this research provided by Associate Professor Kevin Brown. Without Kevin's contribution the thesis would definitely lack practical value. The support and encouragement provided by Dr. Mathieu Sellier have been highly appreciated. Dr. Sid Becker, although not being on the supervisory team, provided enormous support and was a major delight to work with.

Mighty River Power commitment to the research and development made this project possible. It has been most generous in allocating budget for the project. Special thanks go to Simon Addison and Farrell Siega.

The University of Canterbury provided stimulating and supportive setting for the project and safe, exciting environment for me and my family to live in. The financial support in a form of a UC Doctoral Scholarship and teaching load was much appreciated.

The project greatly benefited from the multi-disciplinary assistance of many wise and experienced people at the University of Canterbury: Mike Flaws, David Read, Eric Cox, Julian Phillips, Kevin Stobbs, Scott Amies, Garry Cotton, Ken Brown and Bruce Robertson.

Special thanks go to Luke Sinclair for doing a great job building the experimental rig which was a centerpiece of the experimental part of the project and also for introducing me to the project and helping to settle in New Zealand.

I would like to thank my parents for providing emotional and financial support to undertake this study. I'm also grateful to Luke's parents, Linda and Chris, for making me and my family feel at home in Christchurch and taking such a good care of Veronika while I was burning in the lab.

I would also like to express my gratitude to the academic staff of the Applied Physics Department of the National Aviation University in Kiev were I got my undergraduate degree.

I’m much obliged for their commitment to teaching excellence which provided the skills and knowledge that helped me throughout this study.

Last, but not least I thank Dr. Natalia Kabaliuk for her help in writing, editing and proofreading this dissertation. It was also great to have my daughter, Veronika, around to double check the results.

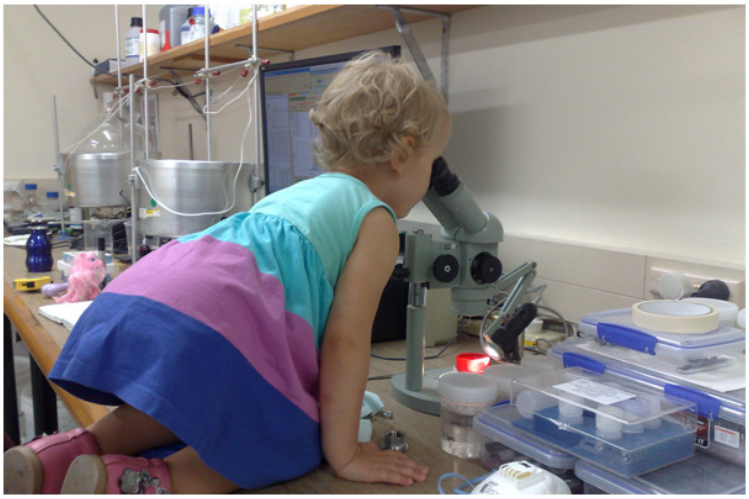

ABSTRACT

The extraction of geothermal heat can cause precipitation of the minerals dissolved in geothermal fluid. Their deposition on the walls of wells and above-ground plant and in pores near reinjection wells, also known as mineral scaling, is one of the main obstacles to increasing the effectiveness of utilization of the limited geothermal resources. If not controlled properly it can result in accumulation of a significant amount of scale which obstructs pipes and reinjection wells and reduces the efficacy of heat exchangers.

The most abundant mineral in geothermal fluid is silica and thus its precipitation can cause the highest scaling rate. While this dissertation is devoted to the study of silica scaling the results obtained may be applicable to other minerals with similar deposition mechanism.

Oversaturated silica is known to precipitate from aqueous solution either by the direct chemisorption of single silicic acid molecules (monomers) or by forming colloidal particles suspended in the solution. These particles can subsequently be transported to, and attach onto, a wall. This process of colloidal silica deposition was previously recognised to cause much faster scaling than the direct deposition of silica monomers under typical geothermal plant conditions.

While the chemical kinetics of silica polymerization and colloid formation are relatively well understood, transport of these colloids and their stability, which control their aggregation and attachment rates, on the other hand are not.

Previous studies of the silica scaling process have identified prominent effects of geothermal brine hydrodynamics on the scaling rate. It was found to increase with the flow rate and particle size, thus suggesting the dominance of the advective (inertial) deposition of colloidal silica. However, this conclusion contradicted the present theory of particle transport in turbulent flows which argues the dominance of the diffusive transport for the relevant range of particle sizes (<1 μm).

The development and continuing improvement of the anti-scaling measures required deeper understanding of the complex combination of the phenomena involved in the process of silica scaling. This was pursued in the present study using theoretical and experimental methods.

First, the rate of colloidal silica transport from a turbulent flow onto the internal surface of a circular pipe, a cylinder and a flat plate were calculated using available analytical and numerical methods. The obtained theoretical transport rate was found to be about four orders of magnitude higher than the corresponding experimental scaling rate. The latter was determined in the previous studies to be $4.2 \cdot 10^{-8}$ kg/s/m^2 for silica colloids of 125 nm in diameter which corresponded to the dimensionless deposition velocity (the dimensionless deposition velocity is the scaling rate normalised by the particle mass concentration and friction velocity) of $1.2 \cdot 10^{-6}$ for the dimensionless particle relaxation time of $2 \cdot 10^{-4}$.

Next, based on the standard DLVO theory of particle interactions and in the framework of the Smoluchowski approach the probability of colloidal silica particle attachment to a wall was found to be 10^{-6}.

Therefore, the theoretical scaling rate, calculated as a product of this probability and the above-mentioned transport rate was two orders of magnitude lower than the experimental scaling rate. This suggested that the implemented theoretical approach either underestimated particle transport rate or overestimated particle stability. Both possibilities are explored in this dissertation.

In addition, the silica scaling rate was measured for a range of conditions: particle size from 20 to 60 nm, particle concentration 1600-10000 ppm, friction velocity from 0.09 to 0.18 m/s ($Re = 9\text{-}50 \cdot 10^3$) and ionic strength from 30 to 80 mM, pH 8.1-9.5 and temperature from 25 to 44 °C. For this, laboratory experiments were designed and progressively modified in order to improve the repeatability of the results and to study the scaling process. In these experiments colloidal silica deposition onto the walls of mild steel pipe sections was studied with a recirculating flow rig with variable (but controllable) particle size, concentration, flow rate, pH and ionic strength of the solution. In addition, a parallel plate flow test section was designed and built which will provide better capabilities for the control over the hydrodynamic and test surface conditions in future experiments.

The control over the chemical conditions was achieved by the use of the synthetic colloidal solutions. Two methods of their production – hydrolysis of either sodium metasilicate or active silicic acid – were employed. The influence of the synthesis conditions, ion content and pH on the long term behaviour of these colloidal solutions was investigated. The particle size data, obtained using dynamic light scattering (DLS) and verified by electron microscopy, was analysed and compared against the predictions of the current models of nanoparticle

growth and stability. The kinetic aggregation was identified to be the dominant particle growth mechanism.

Experimental data collected during the long-term observations of the particle growth allowed relationships between the aggregative stability and such parameters as the particle size, ion concentration and pH of the solution to be elucidated. In particular, the aggregative stability of 10-20 nm particles was found to be 10^8-10^{10} which is 7-9 orders of magnitude higher than the corresponding DLVO stability. It was also found to decrease with the increase of the particle size. This agreed with the theory of the colloid stabilization by steric interactions. Moreover, the model of the "gel" layer was used to explain the observed "anomalies" of the colloidal silica behaviour. The deposition experiments conducted with these synthetic colloidal solutions showed that the scaling rate increased with the particle size, flow rate and ionic strength (IS) of the solution. Thus, it was measured to be $9.7 \cdot 10^{-9}$ kg/s/m^2 for the 45 nm particles in a solution with IS = 0.05 M, which corresponded to the dimensionless deposition velocity of $6.6 \cdot 10^{-8}$ for a dimensionless particle relaxation time of $2.2 \cdot 10^{-6}$.

The scaling rate was calculated for these conditions by multiplying the corresponding transport rate and the actual attachment probability determined as an inverse of the experimental stability. It was found to agree with the experimental value within an order of magnitude. In addition, the observed increase of the scaling rate with the increase of particle size was explained by the compensation of the decreased rate of the particle transport by faster decrease of actual particle stability (increase in attachment probability). Therefore the contradiction between the theory and the experiment was resolved for the particles of 20 to 60 nm in diameter.

Moreover, the observations of the dimensions and distribution of the scale elements formed in some of the present experiments strongly suggested the significance of the advective (inertial) mechanism of particle deposition. This and comparative analysis of other experimental and theoretical data suggested that the present theory may underestimate the convective transport of the particles onto a rough wall. Therefore, the hypothesis of the parallel-to-wall advective deposition of the nanoparticles onto the roughness/scale elements (not accounted in the current theory) was proposed. The corresponding mass transfer problem was solved analytically using experimentally found dimensions of the scale elements. The additional transport was found to decrease the above-stated discrepancy between the theoretical and experimental scaling rate for large (125 nm) particles by one order of magnitude. The remaining difference of one order of magnitude was speculated to be due to

the underestimation of these particles attachment probability derived with the standard DLVO theory. The actual aggregative stability of the silica colloids larger than 60 nm in diameter and for a wider range of IS values is of interest for future experimental studies.

An improved understanding of the interrelation between the chemical and hydrodynamic phenomena in the process of silica scaling and its dominant mechanisms was achieved in this dissertation. This allowed optimization of the present anti-scaling practices aimed to minimize the negative effects of mineral scaling on the operation of geothermal power stations. Besides the practical recommendations, which may ultimately help to increase the efficiency of geothermal power stations, the results of the present study may be of value in the fields of mass transfer and colloid science.

PUBLICATIONS ARISING FROM THIS RESEARCH

Journal Papers

1. **Kokhanenko P.**, Jermy M., Brown K., Silica aquasols of incipient instability: synthesis, growth and stability, Journal of Colloid and Interface Science, 2015 (**current**)
2. **Kokhanenko P**., Jermy M., Brown K., Experimental study of colloidal silica aggregation and deposition in a turbulent flow, Journal of Fluid Mechanics, 2015 (**current**)
3. **Kokhanenko P**., Jermy M., Development of the water tunnel and HFA traversing system for parallel flow examination, Flow Measurements and Instrumentation, 2015 (**current**)

Conference Proceedings

1. **Kokhanenko P**., Jermy M., Brown K., Hydro- and electrochemical aspects of silica colloid deposition from a turbulent flow onto a rough wall, 19th Australasian Fluid Mechanics Conference, Melbourne, Australia, 8-11 December, 2014.
2. **Kokhanenko P**., Jermy M., Brown K., Experimental and theoretical observations of scaling rate and implications for anti-scaling practises, 36th New Zealand Geothermal Workshop, Auckland, New Zealand, 2014.
3. **Kokhanenko P.**, Brown, K. and Jermy, M.: Hydrodynamic particle transport in silica scale deposition. 35th New Zealand Geothermal Workshop, Rotorua, New Zealand, 2013.
4. **Kokhanenko P**., Masuri S., Jermy M., Sellier M. and Brown K., Hydrodynamics and electrochemistry of silica scaling, 34th New Zealand Geothermal Workshop, Auckland, New Zealand, 2012.

TABLE OF CONTENTS

LIST OF FIGURES

LIST OF TABLES

LIST OF ABBREVIATIONS

AS – amorphous silica
SSI – silica supersaturation index
OR – Ostwald ripening
DLVO - theory of particle interactions named
after Derjaguin and Landau, Verwey and Overbeek
CFD – computational fluid dynamics
MS – mild steel
SMS – sodium metasilicate
IE – ion-exchange
PCS – photon correlation spectroscopy
DLS – dynamic light scattering
PSD – particle size distribution
SEM – scanning electron microscopy
EDS – energy-dispersive X-ray spectroscopy
CTA – constant temperature anemometry
HFA – hot-film anemometer

1 INTRODUCTION

1.1 Mineral scaling as an undesirable process accompanying geothermal resource utilisation

The thermal energy of Earth's interior is one of the attractive sustainable sources of energy. The Earth's total internal heat content of 10^{31} joules ($3 \cdot 10^{15}$ TW·hr) (1) originates partially from the radioactive decay of isotopes in the mantle and crust and partially from the primordial heat. The 47 terawatts flow of heat (2) to Earth's surface by conduction, convection and advection through the core, mantle and crust correspondingly (3) is not eternal and, assuming its constancy, can be estimated to deplete not sooner than 7.3 billion years from now. This being on a par with the time the Sun will reach the tip of the red-giant branch and expand by 256 times of its current size (4) suggests that the lack of geothermal heat will be the least of humanity's, if any (5), (6), problems.

Currently, from 0.6 to 32 % (1) of the estimated electricity generating potential of geothermal energy and only 0.08 % of the total geothermal heat flux is utilised. The latter includes 12 GW of geothermal power generation (7) and 28 GW of direct geothermal heating (1) capacity installed worldwide. Therefore, even 100 fold increase of geothermal energy production, if performed properly, cannot significantly affect the ability of future generations to use this energy source.

The Earth's geothermal resources (see above: 10^{31} joules) can theoretically cover humanity's energy needs ($550 \cdot 10^{18}$ joules in 2013 (8)) entirely for many millennia, but only a small fraction may be profitably exploited. Resent estimates show that still over $(200 – 2000) \cdot 10^{21}$ joules of geothermal power would be extractable with foreseeable technology improvements (9). This would be sufficient to provide for all present energy needs for at least few millennia.

Moreover, unlike all other renewable energy sources (solar, hydro, wind) geothermal has relatively low temporal variability on a time scale much longer than annual and daily variations pertinent to other renewables, but shorter than the depletion time estimated above. The geothermal power station thus can provide baseload power (10).

On the other hand, geothermal sources have a disadvantage of highly uneven spatial distribution. Their development historically has been localized in areas close to tectonic plate boundaries where high temperature geothermal resources are available close to the surface. Recent technological advances have expanded the accessibility of geothermal resources and allowed potential widespread exploration. Even though the cost of generating geothermal power has decreased by 25% since 1980s (11), the drilling and exploration for deep resources remain very expensive (12).

Geothermal power generation is particularly important for the New Zealand economy. It contributed 20.5 % of total primary energy supply in 2013 (13).

The technology of geothermal power conversion varies depending on temperature, type and location of available geothermal resources. Vapour or liquid dominated hydrothermal systems, most often found in the vicinity of sources of heat within the Earth's crust (volcanic activity, magma intrusions) are exploited by retrieving steam/liquid mixtures from relatively shallow (1-3 km) hot reservoir (aquifer) through production wells. Its enthalpy is utilised for electricity generation and then it is usually pumped back underground.

Unlike hydrothermal systems, enhanced geothermal systems can provide geothermal energy anywhere in the world. In this case, 4-6 km wells are drilled into hot dry rock, with the permeability enhanced by high pressure water, and are used to circulate water or liquefied carbon dioxide and retrieve geothermal heat for power generation (9).

The power generation scheme depends on temperature and phase composition of the resource. In dry steam power plants, superheated steam from high enthalpy reservoir (240 - 300 °C, 1800-2800 kJ/kg) is used directly to spin the turbine generator, condensed and returned underground for reheating (9).

Flash power plants are built on the more common liquid dominated geothermal fields. In this case high-pressure water (at 200-350 °C, 800-2800 kJ/kg) brought to the surface and flashed (vaporised at lowered pressure) in cyclone separators (14). The steam obtained from the single or double flashed liquid powers a turbine. Separated liquid (brine) and steam condensate are pumped underground.

Lower temperature resources and brine separated in flash power plants can still be utilised in binary power plants (water temperature can be as low as 57°C (15)). An organic working fluid with much lower boiling temperature than water is evaporated in heat exchangers by further lowering thermal energy of the low temperature (water) resource. Vaporised organic

working fluid is used to power a turbine, condensed and returned to the heat exchanger for reheating. Cooled down geothermal water is also returned underground for reheating.

The thermal efficiency and profitability of geothermal power station is particularly sensitive to temperature (enthalpy) of retrieved fluid. Dry steam power plants have higher thermal efficiency, with 21% being the highest recorded value. Thermal efficiency of the flash power plants can be between 6 % and 20 %, whereas binary power plants have the lowest efficiency of 1-13% (14).

Low thermal efficiency of the geothermal power plants does not affect their operational costs as much as it would with fuel powered stations. In addition, regardless of their low efficiency binary power plants allow for more geothermal energy, which otherwise would be lost, to be harnessed thus increasing the overall efficiency of the power station.

Reinjection of the spent (cooled) geothermal fluid is a crucial element in all abovementioned techniques of geothermal energy extraction. Not only does it complete the cycle and replenish water content of the underground reservoir, but also avoids negative ecological effects of dumping it above ground. The geothermal waters usually contain undesirable dissolved minerals, including toxic heavy metals and arsenic, so dumping these discharges above ground contaminates soil, surface and ground water.

The geothermal waters before being extracted from a liquid dominated reservoir are in a prolonged contact with hot rock body and thus they are saturated with many minerals present in the reservoir. The mineral content of geothermal waters is determined by the rock types of the reservoir, its temperature and pressure (Table 1). It varies significantly from field to field and even from one well to another.

The equilibrium concentration of the minerals is generally higher at higher temperatures of the geothermal fluid. When this fluid is flashed and cooled down in the power generation process it can become oversaturated with respect to some minerals. Which, especially silica, may start to precipitate and deposit on the internal surfaces of the power plant equipment decreasing both its thermal and hydraulic performance, and requiring high cost maintenance.

Moreover, during the reinjection, precipitation of the minerals causes even bigger problems. It gradually clogs up the wells and fractures in rock and leads to the loss of the reinjectivity. Thus, about 10% per year decline of reinjectivity was observed at Kawerau power station (16). As a result the reinjection has to be performed at higher pressure and temperatures to keep the production at constant level. This reduces plant power thermal efficiency and the

effectiveness of geothermal resource utilisation. Ultimately, conveyance capacity of reinjection wells drops to the point when replacement wells are needed to be drilled. The estimated total drilling costs of 4 to 6 million USD (based on 2007 prices), which includes drilling rig mobilisation, for a single 1.5 and 2.5 km well correspondingly (17) surely makes this a significant capital expenditure.

Table 1: Geochemistry of fluid from different hydrothermal systems (mg/kg)

	1	2	3	4	5	6	7	8	9	10	11	12	13
T °C	275.1	125	292	224									
pH	9.06	8.7	7.1	8.6									
$NH_{4,3}$	0.3				333		0.1	3.2			4	439	
Na^{+}	273	960	12730	1750	53000	8300	212	1525	1730	1300	5000	1977	31500
K^{+}	54	144	1990	105	16700	300	27	176		225	990	558	9500
Li^{+}	1.42	9	6.59		194	27	0.3	10.2			17	21.9	81
Ca^{2+}	3	15	2249	4.8	27400	521	1.5	50	580	21	320	128	4380
Mg^{2+}	<0.24	0.005	9.81	1.2	33	0.5			149	0.03	0.1	<0.5	4
Rb	1.8		5.24		170	11	0.04						
Cs		2			20	39	<0.02				14		
Sr											400	1100	
$Fe^{2,3+}$	<0.3	<0.1			15	1.5	0.1		167		<0.4	1.6	19
Al^{3+}	<0.27	0.3			2	0.05					0.31		
Br	4		87.3		99	17.7					870		
Sb		0.1	0.0006										
As^{3+}	3.3	4.5	0.146										
Cl^{-}	244.9	1688	25054	1819	151000	16.03	197	2675	4630	2200	9100	4135	65400
SO^{4-}	249.7	34	2.44	133	64	2	61	120	33	28		26	20
HCO^{3-}	81.1												
CO_3^{2-}	6.3												
CO_2					1600	44	55	55	28		5000		280
B^{-}		22	11.3	68	257	9.4	0.6	102		58	312	7300	125
F^{-}	4.24	12	0.137	7.3	15	2.4	1.9	6.6			0.9		4
H_3BO_3	110.8												
SiO_2	772.3	490	943	286	>461	>864	>480	>430	92	>610	>510	>700	>950

(1) Verkhne-Mutnovskaya hydrothermal field (Drill hole 4Э), Russia (18)
(2) Wairakei, NZ (19)
(3) REYKJANES, ICELAND (Drill hole H9) (20)
(4) Germencik, Turkey (O B-9) (21)
(5) Salton Sea USA; (22)
(6) Cerro Prieto, Mexico;
(7) Hvergerdi, Iceland;
(8) Rotokawa, New Zealand;
(9) Onikobe, Japan;
(10) Mak-Ban, Philippines;
(11) Salak, Indonesia;
(12) Mote Amiata, Italy;
(13) Milos, Greece;

Besides the geothermal power production the precipitation of minerals also plays negative role in wider industry. Thus, the build-up of scale from dissolved and colloidal silica in cooling towers and evaporation systems is a major problem that costs industry millions of

dollars each year in facility down time, maintenance, discharge water treatments, and anti-scaling chemical additives.

1.2 Experimental studies of mineral scaling: scaling mechanism

The process of mineral precipitation from aqueous solutions, called mineral scaling, was extensively studied over the last 50 years. A large number of experimental studies of the scaling process, specifically silica scaling, have been made during the period of active geothermal power development.

This section presents an overview of such experiments performed with geothermal fluids and synthetic brines. Their results allowed the initial conception of the scaling mechanism and laid the foundation for the present study. The gaps, ambiguities and contradictions which were remaining in the understanding of silica scaling have determined the aim and scope of this dissertation.

First of all, a brief discussion of the chemistry of silica is needed as it controls the onset of precipitation (23). The concentration of silica in the hot geothermal fluid is controlled by the solubility of quartz, which increases with temperature. However at temperatures below 200 °C characteristic for the cooled geothermal brine in flash or binary power plants, the crystallisation of quartz is extremely slow and the concentration of silica in brine is controlled by the solubility of amorphous silica (23). Therefore, silica scaling normally occurs as a result of precipitation of amorphous silica and as was shown by Weres (23) and Fleming (24) can take two forms: direct deposition of the dissolved silica, in a form of $Si(OH)_4$ species (referred as monomers, monomeric silica or silicic acid) and deposition of polymerised silica (in a form of polymers and colloidal particles). More detailed review of silica solubility, kinetics of its polymerisation and colloidal chemistry is presented in Section 1.3.

A number of measurements of geothermal scaling rate were conducted in the past at different geothermal fields (25). Reported scaling rates, presented in Table 2, reflect variability in the corresponding chemical (see Table 1) and hydrodynamic conditions.

Mroczek and McDowell (26) attempted to determine experimentally the morphology and deposition rate of silica from the geothermal fluid at Wairakei power station in New Zealand under varied pressure and temperature conditions. Different silica scale morphologies on the

container and pipe walls were observed. The scaling rate was shown to increase with the time of contact of working surfaces with the geothermal fluid.

The study by Brown and McDowell (27) suggested that higher levels of aeration and turbulence lead to higher deposition rates.

Table 2: Field and laboratory scaling rates

Field/experiments name	Silica scaling rate*, $\times 10^{-7}$ kg/s/m^2
Wairakei, NZ	3.3
Ohaaki, NZ	0.42
Hveragerdi, Iceland	1.1
Verkhne-Mutnovskaya, Russia	25
Cylinder in a crossflow: 125nm particles	0.42

*scaling rates normalized to the geometric surface area

P. A. Taylor (25) studied silica scaling process in reinjection pipeline at variable flow rate and turbulence levels. Various scaling rates and scale morphologies were observed. The scaling was believed to be caused by the deposition of silica monomers (silicic acid) present in the experiment. Faster deposition was observed at lower Reynolds numbers and on the elements protruding into the flow.

The influence of temperature and flow rate of geothermal fluid on silica deposition in pipes and gravel beds was investigated by Mroczek and McDowell (26). Deposition on pipe surfaces was found to be relatively insensitive to the variation in the flow rate or temperature. Significant decrease of the deposition rates with the distance from the pipe inlet was observed at lower temperatures. This was explained by the deposition of polymeric silica (colloidal silica) near the inlet and consequent quick decrease of monomeric silica concentration downstream, that resulted in lower deposition rates.

Mroczek and Reeves (28) studied temperature and flow rate dependence of silica deposition from the aqueous solutions containing aged polymerised silica and fresh unpolymerised silica. Monomeric silica concentration was found to be responsible for scaling rate and scale morphology. The maximum deposition rate occurred with mixtures containing 80% monomeric and 20 % polymerised silica. The degree of polymerisation (or size of silica nanoparticles) was suggested to be not as important as monomeric silica concentration.

Geothermal brine from Broadlands and Wairakei fields in New Zealand was used to study the time dependence of silica scaling processes by Rothbaum et al (29) and Yanagase et al (30). The brine was acidified in these experiments. Obtained scale material was sampled and its

chemical composition and deposition rate were determined. The composition and morphology of scales varied widely and quartz was found in some tests.

Rothbaum et al (29) showed that silica polymerisation had small influence on the rate of silica deposition. Thus, it was suggested that ageing of geothermal fluid does not prevent silica scale formation. An increase in silica deposition rates was observed with aerated geothermal fluid. Less deposition was observed at lower pH of the carrier fluid.

Meanwhile Yanagase et al (30) concluded that aging water and allowing the silica to polymerize was beneficial for reducing scaling.

Brown and McDowell (27) also investigated the effect of aeration on silica scaling process. No influence of injection of gases on the deposition process was observed. This was explained by a lower degree of polymerisation than in Rothbaum's experiments. Deposition rate was found to be higher at lower temperatures. Thus the scaling process was assumed to start as colloidal silica attachment to the surface and proceed as monomeric silica deposition.

All these studies suggested that monomeric silica deposits readily, even before polymerisation occurs; deposition rate is either constant or increases with increasing solid surface-brine contact time and is strongly influenced by hydrodynamic conditions; tougher and more adhesive silica scale was formed at higher temperatures. Though, no quantitative description for colloidal deposition and hydrodynamic effects was gained.

The possibility of silica scale control by means of employing a special retaining container for a geothermal fluid was investigated by Mahon et al (31). The retaining tank that allowed fluid residence time of one hour was created. Silica deposition in the discharge pipe from a diluted (1:1 with cold water) and undiluted geothermal fluid after one hour of residence time were studied. Silica deposition rates were shown to be lower in aged and diluted brine.

Gunnarsson (32) studied ageing of the separated brine from geothermal station in Iceland. He used a long horizontal pipe as a retaining tank and showed a reduction by half in the level of saturation in a geothermal fluid after two hours of residence time.

Currently, silica scaling in geothermal applications is controlled by acidifying the geothermal brine (33). An acid is added to the brine with the aim to lower its pH to 4-5. This prolongs the nucleation stage of the colloidal silica formation (23). As a result effectively no colloidal particles form while the brine flows from the production to the re-injection well.

Under normal operation of the acid-dosing system no major scaling by deposition of the colloidal silica occurs in the aboveground equipment (34). Meanwhile, deposition of silica in reservoir formation is still likely to take place. This can lead to a decrease in injectivity. In addition, there is a high risk of silica deposition in re-injection wells and aboveground pathways (heat exchangers, injection pipe) during an abnormal operation of the acid-dosing system (e.g. start-up of the dosing plant) (34).

Moreover, deposition of another dissolved mineral – stibnite – can contribute to the mineral scaling problem through a similar colloidal mechanism of deposition. In this case, the formation of the colloidal stibnite is accelerated by brine acidification (whether this acidification occurs by addition of acidic concentrate or of sulphuric acid). Even though this mineral is present in a lower concentration than silica, over time, it can accumulate on the heat-exchanger surfaces and cause a sensible increase of their thermal resistance. Therefore, periodic cleaning of the heat-exchangers is required to maintain their efficiency. This naturally affects the productivity and operational expenditures of the binary power plant.

Several experimental studies of the silica scaling in the formation rocks were performed.

The deposition from Otake geothermal brine in a cylindrical column packed with 2 mm in diameter aluminium beads was investigated by Itoi et al (35). Formed scale was sampled, dried and weighed to determine the rate of silica deposition. Scaling occurred mainly near the entrance to the packed column.

The influence of a brine pH on scaling in packed beds was studied by Kiyota et al (36). A high deposition rate was observed at the inlet section of the column which decreased downstream. Decrease of the pH of the brine from about 6.7 to 5.5 caused a significant reduction of the deposition rate.

Experiments with ceramic zirconia beads were conducted at the Wairakei geothermal fields in New Zealand (37). Relative uniformity of silica deposition along the column was observed and associated with only monomeric silica deposition taking place over the relatively short fluid residence time.

In addition to the experiments with geothermal fluids there are a number of works devoted to the silica scaling from artificially manufactured brines. In this case, colloidal silica sols with known silica concentration and colloidal particles size were used in deposition experiments. Thus, Weres and Tsao (38) studied deposition of polymerised amorphous silica in quartz tubing. They used synthetic brine, which contained certain amount of hydrochloric acid and

various salts to mimic geothermal brine from the Cerro Prieto geothermal field. Scaling rates dropped downstream in the quartz tubing. This was associated with the colloidal silica attachment to the wall and subsequent monomeric silica deposition.

Silica deposition on polyphenylenesulfide (PPS) and polytetrafluoroethylene (PTFE)-blended PPS coatings were examined by Sugama and Gawlik (39). Silica scale was observed on non-coated steel samples, whereas the coated ones remained clean.

Chan et al (40) investigated silica scaling in closed loop with circulated synthetic brine at high pressure and temperature. Silica deposition on inner surfaces of titanium tubes and an initial drop in thermal resistance followed by its progressive increase were observed.

Experimental studies were performed by Garibaldi and Freeston (41) to test the effect of hydrodynamic conditions on silica scaling processes in geothermal applications. They investigated silica deposition on stainless steel plates and cylinders placed in an open waste water channel at Wairakei station. A significant increase in scaling rates was observed after a week of comparatively slow deposition. The scale was found along the stagnation line and on the back of the cylinder with fibrous deposits on the frontal surface and cellular on the back. The flat plate sample showed different scale morphologies: the region within 10 mm from the leading edge was free of scale, within the next 150 mm a fibrous deposit was observed and on the rest of the plate scale had arranged into periodic ripples. For the locations with low stream velocities, higher rate of silica scale formation was observed. Thus diffusion was assumed to be the dominant mechanism of silica transport to the surface. Fibrous deposits were believed to form where the boundary layer is laminar, while its turbulisation was assumed to cause the rippled patterns of the scale.

Dunstall and Brown (42) performed experiments on a pilot geothermal plant at Wairakei. In contrast to the previous experiments, better control over hydrodynamic flow conditions and colloidal silica size were achieved in these experiments. The pilot plant allowed observation of scaling process from uniform flow, with velocity varying from 0.5 m/s to 3 m/s, of aged geothermal brine with known particle size that was between 10 and 125 nm. The deposition on long mild steel plates with sharpened leading edges and with a trip wire to provide a turbulent boundary layer was studied. It was shown that the protective zinc coating present on the plates greatly increased the rate of silica deposition. No observable influence of hydrodynamic conditions on silica deposition was found. Larger particles caused higher scaling rates.

Deposition experiments with the carbon steel cylinders without zinc coating in a cross-flow with variable velocity and particle size were also performed by (43). The deposition rate was found to increase with particle size and flow rate (Fig. 1). No deposition was found on the stagnation line. The width of the clean zone was wider for lower velocities (with constant particle size) and for smaller particles (with constant velocity). There was no deposition on the back of the samples. U-shaped scale formation was observed near the top and bottom of the samples. The scale location suggested no effect of governing gravitational forces.

In addition, the silica colloids formed ridges of scale parallel to the cylinder axis and perpendicular to the flow direction. The height of the silica ridges was found to vary significantly around the cylinder circumference. The maximum height of ~0.25 mm was measured at approximately 21° from the upstream stagnation point.

Additional experiments showed that the angle from the stagnation line to where the maximum thickness of deposit occurred increased with decreasing particle size. Higher deposition rates were associated with higher surface roughness.

From a series of experiments with a cylinder that had a tripping wire installed at 45° from the stagnation line it was concluded that the tripping had no effect on the silica deposition rate downstream of the reattachment region.

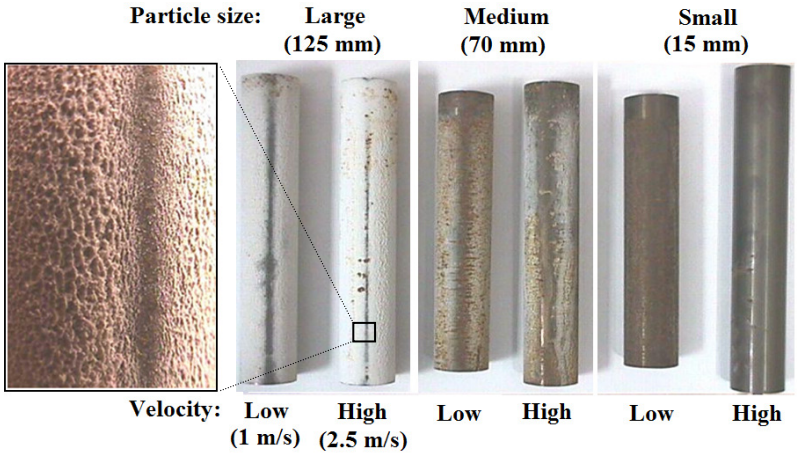

Figure 1: Geothermal silica scale on cylinders in a cross flow (43)

Ultimately, driven by the observation of higher rates of deposition for larger particles and with larger fluid velocity, Dunstall and Brown concluded that, first, the formation and deposition of amorphous colloidal silica is responsible for the majority of silica scaling in geothermal applications. Second, inertial impaction of the colloidal particles was argued to be the dominant mechanism of their transport to the surfaces.

Moreover, several numerical studies on silica particles transport and deposition at different hydrodynamic conditions were performed recently.

Jamieson (44) developed a numerical model of monomeric and colloidal silica deposition in a turbulent channel flow. The deposition of monomeric silica was treated in the same way as in the model by (45) and with ideal particle attachment (no repulsive forces) assumed. Transport from bulk flow through the viscous sublayer to walls was assumed to be performed by inertial impaction, Brownian diffusion, and convection due to turbulent bursts. This model complimented with a number of assumptions on the degree of silica polymerisation was successfully applied to some field tests in New Zealand and Iceland. Brownian diffusion was stated to be the main particles transport mechanism. The variation in scaling rates was believed to be associated with the changes in the viscous layer thickness. The prevalence of turbulent diffusion near rough surface was associated with the viscous sublayer distortion due to surface texture (roughness).

Deposition of colloidal silica onto a flat plate parallel to flow was simulated by Pott (46) using the same approach as (44). Silica scaling rates were found to increase for smaller particles and decrease with the distance from the plate leading edge. Therefore, the dominant particle transport mechanism that controls deposition was argued to be Brownian diffusion of colloidal silica through the viscous sublayer. Pott concluded that the variations in scaling rates due to hydrodynamic effects were likely caused by the changes in the viscous sublayer thickness. The significance of the surface roughness was indicated but never quantified.

From his numerical study of the hydrodynamic influence on silica scaling Zipfel (47) concluded that scaling proceeds faster at the location with higher wall shear stress and for larger particles presented in the brine. So, he concluded that the dominant particle transport mechanism must be the inertial impaction.

While these field and numerical experiments provided valuable insight into the effects of the flow rate and brine oversaturation with silica on the scaling rate, they failed to give a complete description of the mechanism of silica scaling in geothermal applications. Significant differences in conditions and methodology between these experiments lead to their incomparability and, therefore, contradictory conclusions. Thus, Brownian diffusion and inertial impaction were suggested to be dominant mechanisms of colloidal silica transport in different studies. The role of the Saffman lift forces, turbophoresis and surface physical and

chemical properties in silica scaling process haven't been fully explored (although they were studied within general theory of particle transport described below in section 1.4).

Current understanding of the silica scaling mechanism, established as a result of all previous studies, is illustrated in a stepwise manner in Fig.2.

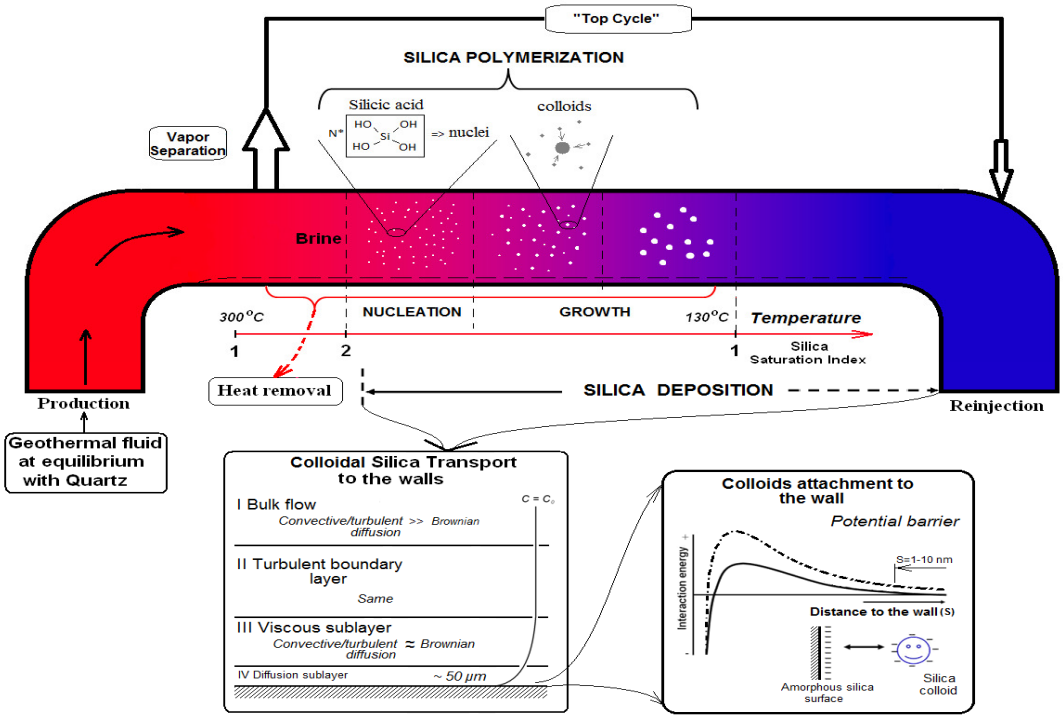

Figure 2: The mechanism of silica scaling in geothermal applications

Silica scaling occurs when geothermal water becomes supersaturated with respect to amorphous silica due to the loss of steam or heat. It starts as chemisorption of single silicic acid molecules directly from solution to a wall. The degree of oversaturation is characterised by the silica saturation index:

$$SSI = \frac{Actual\ Silica\ Concetration}{Saturation\ Silica\ Concetration} \quad (1)$$

Once the solution oversaturation with silica reaches certain critical level (SSI_{crit} = 2.5 at 75°C, (23)), formation of colloidal silica particles starts, which is followed by their transport and attachment to the walls. The latter mechanism of colloidal deposition results in a much greater scaling rate, than former, so called direct deposition of silica monomers. It is not sufficiently well understood because of the conjunction of chemical and hydrodynamic phenomena.

Formation of colloidal silica involves two stages: the homogeneous nucleation and subsequent growth of the nuclei. The growth of the particles can then proceed by precipitation of remaining "oversaturated" monomers from solution on to formed particles or, once all excess silica has precipitated, by the processes of Ostwald ripening and particle aggregation (Section 1.3.3). The new state of the brine loaded with colloidal particles of amorphous silica is called silica aquasol.

Transport of the nanoparticles to the walls is performed by different mechanisms depending on the local properties of the flow. In the bulk flow, far from the walls, and in the turbulent part of the boundary layer, where the convective or turbulent diffusion are significant, the distribution of silica colloids is virtually uniform.

Closer to a wall, in the viscous sublayer, where the flow is stagnated and turbulent pulsations are gradually damped the relative role of Brownian diffusion in particles transport increases.

Finally, in the innermost part of the viscous boundary layer the matter diffuses only by the molecular mechanism. This region, called the diffusion sublayer (DBL), causes most of the mass transfer resistance. However, in a particular case of the particles as transported entities another transport mechanism is feasible – the inertial penetration of the DBL. Depending on the flow configuration and their size the particles may obtain the moment from the average flow or turbulent eddies just enough to be projected to the wall all the way through the DBL.

Once at the wall the particle may form a bond with it. The theory that attempts to quantify the probability of such outcome is called the DLVO theory. It considers a combination of attractive and repulsive forces acting between charged nanoparticles suspended in water solution. It predicts the probability of two colliding particles (or a particle and a wall) to form a bond (see Section 1.3.3 for details).

A key point to note is that when there is already some silica deposit present on the surface the further interactions are effectively between silica and silica. In this case the particles (wall) carry same surface charge and are repelled as they get closer. At some separation distance the intermolecular attraction forces overcome long-range electrostatic repulsion and bond the particles to the surface. So, in order for a particle to stick to the surface it must first overcome the potential barrier.

The following sections of this chapter will demonstrate that the processes of silica colloid nucleation and their growth (by monomer precipitation) are reasonably well understood. While the theory of particle transport in turbulent flow over rough surfaces is fairly well

developed (Section 1.4), it is still believed to be missing some mechanisms relevant to the mineral scaling problem. Thus, an additional convective (inertial) mechanism of particle transport not accounted for in the current theory was estimated in this dissertation (Section 6.2).

The process of particle binding to solid surfaces is probably the least understood of all processes involved in silica scaling. A key question is whether the rate at which particles accumulate on the surface is limited by the rate of their transport through the fluid near the wall, or by the fraction of particles which form permanent bonds at the surface. This fraction is a function of, yet poorly understood, aggregative stability of the colloidal particles. Even though the DLVO theory of colloidal silica is well developed it still fails to describe stability of colloidal silica for conditions relevant to geothermal applications. It is author's hope that the experimental observations of colloid stability performed during this project and the ideas they stimulated (Section 6.1) will contribute both to a better understanding of mineral scaling problem and to the wider field of colloid science.

The practical problems associated with the silica scaling cannot be resolved without in-depth understanding of the mechanisms of silica deposition from the suspending flow. The present knowledge is incomplete and sometimes contradictory. Even though there is a common consent on the significance of the hydrodynamics effects in silica deposition process, individual studies emphasize different governing mechanisms. Available computer models are ill-supported by empirical data and haven't proved their reliability. Previous experimental results were obtained within a narrow range of controllable parameters (hydrodynamics and chemistry).

Therefore, new laboratory experiments were designed and progressively modified (Chapter 3) in order to improve the repeatability of the results and study the details of the scaling process. In these experiments colloidal silica deposition onto the walls of mild steel pipe sections was studied with a recirculating flow rig with the variable (but controllable) particle size and concentration, flow rate, pH and ionic strength of the solution (Chapters 4 and 5).

The new knowledge obtained as a result of this study has formed the basis for improvement of the present anti-scaling practices aimed to minimize negative effects of mineral scaling on the operation of the geothermal power stations (Chapter 8).

1.3 Colloid chemistry of silica

To properly predict silica scaling from both monomeric, or direct, and colloidal deposition, and ultimately mitigate their adverse effects, one needs to understand their occurrence and progression in the conditions representative of geothermal power systems (25).

As it was mentioned above, direct scaling starts as soon as solution becomes oversaturated with silica (SSI > 1). At the same time an equilibrium process of formation and break up of silica polymers proceeds in solution (Fig.3). Once a critical level of oversaturation is reached a rapid process of homogeneous nucleation yields amorphous silica phase in the form of colloidal particles suspended in the liquid phase. It also depletes the dissolved silica below the critical concentration. The growth of the formed particles continues by precipitation of remaining oversaturated silica monomers (2.5>SSI>1) on their surface. Even further coarsening of the colloidal system in processes of Ostwald ripening and aggregation can proceed after equilibrium saturation of solution with silica is established. The rates of these processes, and/or corresponding equilibrium sizes of the polymers, nuclei and particles depend on the silica saturation index, solution temperature, ionic strength and pH. This section presents the state of the art empirical and analytical relationships describing these processes.

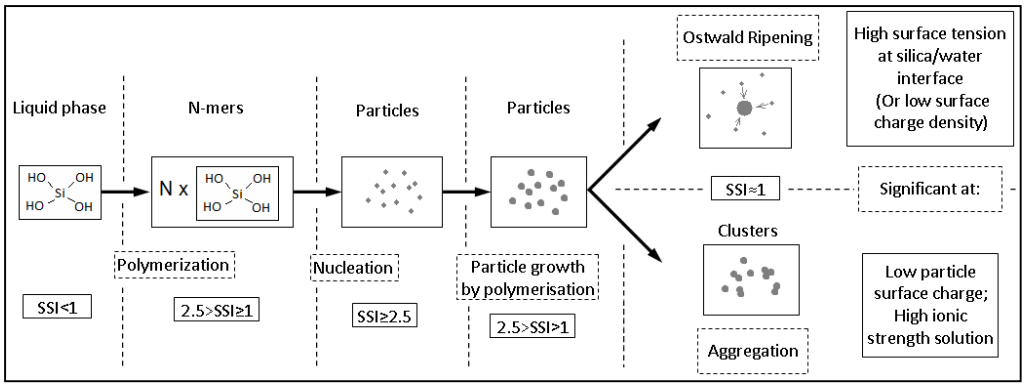

Figure 3: Formation and evolution of the colloidal silica

1.3.1 Solubility of silica in water

The degree of solution oversaturation with silica, SSI, and thus the rate of its precipitation depend on the actual and equilibrium concentration of silica in this solution per Eq.1. The former is determined by the chemistry and temperature of an individual geothermal resource (Table 1). The latter is equal to silica solubility in water. It increases with temperature and pH according to Eq.2 (48):

$$C_e(T, pH) = C(T)[1 + \{10^{pH} \times K_1/\beta_{(H_3SiO_4^-)}\}] \quad (2)$$

here C is silica concentration in mg/kg: $\log C(T) = -\frac{731}{T} + 4.52$; T is absolute temperature; K_1 is a dissociation constant for the reaction $H_4SiO_4 \leftrightarrow H^+ + H_3SiO_4^-$: $\log K_1 = -\frac{2549}{T} - 15.36 \cdot 10^{-6}T^2$; $\beta_{(H_3SiO_4^-)}$ is the activity coefficient of $H_3SiO_4^-$ ion determined by Eq.3:

$$\log \beta_{(H_3SiO_4^-)} = -\frac{A_D z^2_{(H_3SiO_4^-)}\sqrt{IS}}{1+b^0_{(H_3SiO_4^-)}B_D\sqrt{IS}}; \quad (3)$$

where $z_{(H_3SiO_4^-)}$ is the charge of the ion, $b^0_{(H_3SiO_4^-)} = 10^{-10}m$ its effective ionic radius, A_D = 0.51 and B_D= $0.32 \cdot 10^8$ are the Debye–Huckel parameters and

$$IS = \frac{1}{2}\sum_{i=1}^{n} c_i z_i^2 \quad (4)$$

is the ionic strength of the solution, where c_i is the molar concentration of ion i (mol·dm^{-3}), z_i is the charge number of that ion, and the sum is taken over all ions in the solution.

These semi-empirical relationships reflect that silicic acid solubility increases with solution ionic strength. However the presence of other dissolved salts in solution was shown to significantly decrease silica solubility - by factor of two for 1 M NaCl (49) and three for 5ppm Al (50). Salt ions exclude silicic acid molecules from their hydration spheres and also decrease the activity of water – both resulting in lower silica solubility.

The combined effect of several salts can be accounted with

$$\log\left(\frac{C_e}{C_{mix}}\right) = \sum_j (D_j m_j) \quad (5)$$

where C_{mix} is the molal solubility in mixed solution, D_j - Setchenow parameter which characterizes two abovementioned effects for the various salts and temperatures and m_j - molality of individual salt (49).

1.3.2 Kinetics of silica colloid nucleation and growth

Knowledge of the chemical kinetics of colloidal silica formation and growth is required for the quantification of timescales of the relevant processes of colloids occurrence under geothermal power plant conditions. It also helped to improve the process of silica colloids synthesis used in this study (Section 3.2).

The process of colloidal silica formation starts when the solution becomes sufficiently supersaturated with silica and proceeds through the following steps (23), (24):

1. Formation of silica polymers of less than critical nucleus size
2. Nucleation of an amorphous silica phase in the form of colloidal particles
3. Continued growth of these particles via silicic acid polymerisation at their surface
4. A surface rearrangement whereby chemisorbed silicic acid molecules condense into the solid silica

Nucleation is a stochastic process with which relatively fast separation of a phase of matter from another phase starts. There are two types of nucleation mechanisms: heterogeneous and homogeneous.

In heterogeneous nucleation an unstable phase, in our case of amorphous silica (AS), condenses onto seeded centres like dust motes and metal ions. This type of nucleation is more common as it is significant when there is high number of seed centres and low degree of phase instability in the system (or low oversaturation of the solution in our case).

However, due to the low interfacial energy of silica/water system (51), colloidal AS particles usually form by homogeneous nucleation (steps 1 and 2). Dissolved silicic acid molecules bond together by replacing their silanol (Si-OH) groups with siloxane (Si-O-Si) bonds. The progressive growth of these polymers yields low molecular weight nuclei suspended in solution (step 1). For them to become centres of subsequent continuous silica condensation they need to reach critical nucleus size (~10-100 SiO_2 units or 0.2-2 nm) (23),

$$r_c = \frac{2\gamma v_s}{k_B T \ln SSI} \tag{6}$$

here $v_s \approx 4.5 \times 10^{-29}$ m^3 is the volume of a molecule of silica in solid phase (52), γ is the surface tension on AS-water interface, and SSI is silica saturation index defined by Eq.1. The surface tension on AS-water interface was found to decrease significantly with increasing pH (23): from 0.049 to 0.0016 J/m^2 for pH change from 5 to 9 (at 25°C). Less prominent decrease of AS-water interfacial energy with increasing temperature was identified: from 0.0392 to 0.029 J/m^2 for temperature range from 25 °C to 150 °C (at pH 7.5).

If the initial oversaturation is lower than a certain value the nucleation produces particles smaller than r_c with solubility equal or higher than the actual monomer concentration and thus they cannot grow further.

The evolution of the silicic acid concentration in oversaturated solution is illustrated by the La Mer diagram in Fig. 4 (53). Nucleation starts only when the SSI exceeds some critical value: SSI_{cr}= 2.1 at 95 ^{o}C; 2.5 at 75 ^{o}C; 3.3 at 30 ^{o}C (23).

The steady nucleation rate derived from Lothe-Pound theory (23) is

$$I_N = ZA_C\, R_{md} v_s^{-1} Q_{LP} e^{\left(\frac{-\Delta F}{k_B T}\right)} \quad (7)$$

here $\Delta F = \frac{16\pi\gamma^3}{3(v_s^{-1}\, k_B\, T \ln SSI)^2}$ is a free energy of formation of critical size nucleus from dissolved silica; A_C is area of the critical nucleus; Z is the "Zeldovich" factor which is close to unity; Q_{LP} is "Lothe-Pound" factor, it accounts for the difference in degrees of freedom of critical nucleus when it's embedded in solid AS and when it's in aqueous solution and R_{md} is a molecular deposition rate.

The induction time, or nucleation period, elapsing from the moment of supersaturating the solution until the moment of detectable decrease of the silicic acid concentration was shown to depend significantly on solution pH (52). It was shown to decrease approximately by order of magnitude for each pH unit increase in range from pH 4.5 to 6.5.

The nucleation rate was found by fitting experimental data to the theoretical model of homogeneous nucleation (Eq.7) (52). At pH=4.5, T=75-100 ^{o}C and SSI=2.73 it is equal $5 \cdot 10^6$ nuclei cm^{-3} s^{-1}. The diameter of the critical nucleus at these conditions was calculated to be 0.8 nm, which means it consisted of 45 molecules of silica.

Strong effect of pH on the nucleation rate was attributed to the increasing ionisation of AS surface at higher OH^- concentration (23). Presence of the ionised sites on AS surface of nuclei is apparently more important for its growth than the decrease of the surface tension on AS-water interface, and thus lower critical nucleus size (Eq.6), also associated with higher pH.

As it follows from Eq.6 size of the critical nucleus is inversely proportional to the temperature (neglecting weak temperature dependence of the surface tension). Therefore, given the SSI and all else being constant, the homogeneous nucleation rate (Eq.7) increases with temperature. Although, in general the opposite thermal effect on the silica saturation ratio, thereby the nucleation rate, compensates this and change of temperature has little effect upon the induction time.

As silica monomers concentration starts to decrease after reaching its maximum the nuclei smaller than critical radius at given SSI start to dissolve (Fig.4). Their dissolution somewhat retards decrease of silica concentration due to rapid growth of the bigger particles. This effect, known as Ostwald ripening, is responsible for high monodispersity of the silica sols.

The presence in solution of other dissolved salts accelerates molecular deposition of silica monomers and reduces critical nucleus size. As was mentioned above, they decrease silica solubility (and thus increase SSI). They also lower the AS/water surface energy by increasing surface ionization. All these effects result in acceleration of homogeneous nucleation by an order of magnitude for 1M NaCl (49).

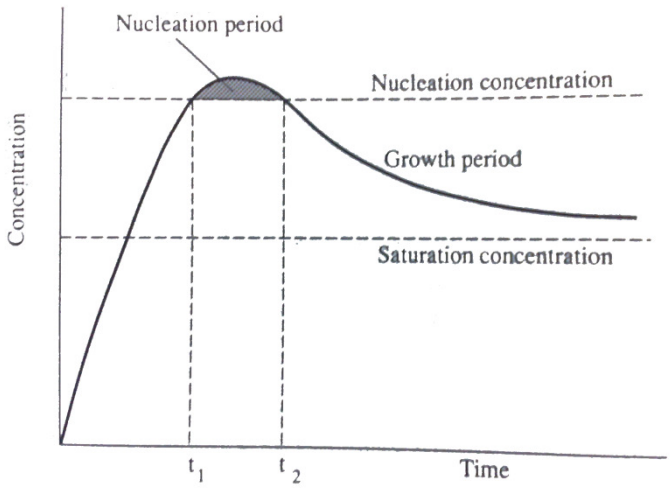

Figure 4: The La Mer diagram of the nucleation process (53)

The rate of deposition of silica monomers onto existing nuclei of AS (step 3 above) was measured to be proportional to AS surface area available for deposition and to increase monotonically with pH, salt concentration and temperature (23), (24), (45). Based on their experimental results Weres (at 50-100^{o}C, pH 6.2 – 7.8, 0.7M buffered) and Fleming (25-50 ^{o}C, pH 4 – 8, 0-1MNaCl) explained pH and ionic strength effects by a polymerization rate being directly proportional to the surface density of ionized hydroxyl groups, SiO^{-}.

In his kinetic experiments Fleming (24) studied growth of colloidal silica particles separately from nucleation (steps 1 and 2) by keeping SSI below 2 and seeding the solution with Ludox colloidal silica. Two different kinetic regimes of colloidal silica growth by monomer deposition were identified (Fig.5). At first, chemisorption of dissolved silica onto the particle surface (Region I) quickly reduces monomers concentration (C) in solution. Then, after

certain concentration C_x is reached, slow condensation of chemisorbed silica into solid silica follows (Region II).

In Region I, where $C > C_x$, dissolved silica undergoes condensation polymerization reaction between hydroxyl groups of the amorphous silica surface and silicic acid itself:

$$\equiv SiOH^{-}_{(S)} + Si(OH)_{4(aq)} \leftrightarrow \equiv Si - O - Si(OH)_{3(s)} + H_2O_{aq} \quad (8)$$

or in "ionized form"

$$\equiv SiO^{-}_{(S)} + Si(OH)_{4(aq)} \leftrightarrow \equiv SiOSi(OH)_{3(s)} + OH^{-}_{aq} \quad (9)$$

Chemisorbed silicic acid molecules and water are the products of this reaction.

The regeneration of surface charge occurs rapidly via the reaction

$$\equiv SiOH + OH^{-} = \equiv SiO^{-} + H_2O \quad (10)$$

Therefore surface charge density can be assumed to always be at its constant, equilibrium value determined by pH, ionic strength and temperature. Considering this Fleming determined a mass-action expression for silicic acid concentration in Region I as

$$\frac{-\mathrm{dC}}{\mathrm{dt}} = \mathrm{kA_s[SiO^{-}](C - C_x)} \quad (11)$$

here $C_x = C_e \frac{\Gamma_{sat}}{\Gamma_e}$ is a pseudoequilibrium concentration and A_s is surface area of AS per volume of solution, Γ_{sat} and Γ_e are correspondingly max and equilibrium surface concentration of chemisorbed silicic acid, $-Si(OH)_3$ and k is rate constant determined below.

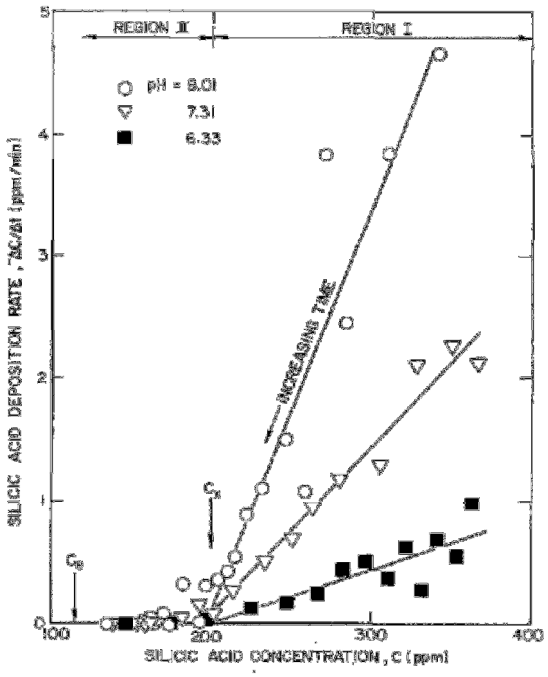

Figure 5: Kinetic regimes of silica polymerisation onto particles (24)

Fleming determined C_x as the "solubility" of silica surface saturated with chemisorbed silicic acid. He also stated that it does not change with pH and ionic strength of the solution (for pH = 4-8, 0-1M NaCl) and found its temperature dependence:

$$\ln C_x = A - \frac{H_S}{RT} \tag{12}$$

here $A = 9.74 \pm 0.29$, $H_S = 2.63 \pm 0.19\ kcal/mole$, so $\ln C_x = 9.74 - \frac{2630}{RT} \pm 0.40$.

Since solution pH controls AS surface charge, the dependence pH of the rate of reaction of chemisorption (Eq.8, 9) can be completely modelled by [SiO^-] term in Eq.11. Same as with the nucleation, decrease of pH from 8 to 4, lowers the [SiO^-] surface concentration and the effective rate constant for step 3 by two orders of magnitude.

Besides pH the surface charge is also affected by the presence of dissolved salts in solution. This additional effect can be expressed through the dependence of rate constants in Eq.11 from the solution ionic strength IS:

$$\mathrm{k} = \mathrm{k}_0 \exp \frac{\mathrm{A_{DH}}\sqrt{\mathrm{IS}}}{1+\sqrt{\mathrm{IS}}}, \tag{13}$$

here $A_{DH} = 1.17\ mol^{-1/2}kg^{1/2}$ is a Debye-Huckel constant for water at 25°C and $\mathrm{k}_0(25°\mathrm{C}) = 1.03 \pm 0.12\ \mathrm{M}^{-1}\mathrm{s}^{-1}$ is an intrinsic rate constant. Its temperature dependence is governed by the Arrhenius' law

$$k_0 = A_0 \exp\frac{-E}{RT} \tag{14}$$

with the pre-exponential factor A_0 and activation energy E were determined to be (24):

$$\ln A_0 = 22.1 \pm 1.5; E = 13.1 \pm 0.9 \frac{kcal}{mol} \tag{15}$$

so $\ln k_0 = 22.1 - \frac{13100}{RT} \pm 2.$

Therefore the rate of chemisorption of monomeric silica onto AS colloids depends on the solution parameters in the same way as the rate of nucleation and was determined to be equal $5.6 \cdot 10^{-8}$ cm s^{-1} and $1.2 \cdot 10^{-7}$ cm s^{-1} for pH 7.3 and 8.0 correspondingly (24).

As silicic acid concentration in solution approaches C_x its absorption and dissolution rates approach equality and the overall rate becomes limited by rate of incorporation of chemisorbed silicic acid into solid silica, or else called surface rearrangement:

$$-Si(OH)_3 \rightarrow \equiv SiOH \tag{16}$$

From this point onward the concentration of silicic acid in solution reduces together with the concentration of chemisorbed silica (Eq.16) per absorption equilibrium (Eq.8, 9).

A kinetic equation for the surface rearrangement rate was determined to have a power law form, which is commonly used in crystallization kinetics (24):

$$\frac{-dC}{dt} = K_{sr}(C - C_e)^3 \tag{17}$$

here $K_{sr} = k_{sr} A_s \Gamma_e^2 C_e^{-2}$ is the rate constant determined by Fleming through the following expressions: $k_{sr}\Gamma_e^2 = A_{sr}\exp\frac{-E_{sr}}{RT}$, $\ln A_{sr} = 13.7 \pm 2.7$, $E_{sr} = 13.5 \pm 1.8$ kcal/mol, so $\ln k_{sr}\Gamma_e^2 = 13.7 - \frac{13500}{RT} \pm 4.0.$

Therefore, for the wide range of parameters investigated by Fleming (pH 4 – 8, 0 - 1 M NaCl), the rate of the final phase of colloidal AS silica formation (step 4 above), surface rearrangement, was found to depend on the temperature per Arrhenius law and on pH and IS only through the silica solubility, i.e. it can be said to be directly proportional to *SSI*.

Until now the kinetics of the reactions of silica polymerisation which occur upon the surface of amorphous silica particles was reviewed. At the same time, particle growth can also be looked on from the point of view of transport of dissolved silica through the solution to the particle surface. The diffusion and adsorption controlled nanoparticle growth regimes were recognised in (54). Rapid decrease of particle mobility, due to Brownian diffusion, with its

size was shown to cause decrease of rate of monomer transport to the surface of growing particle. Therefore, narrowing of the particle size distribution due to particles growth rate decreasing with their size was related to diffusion-controlled growth. It was shown to produce monodisperse colloids. Whereas, adsorption controlled growth was suggested to always yield polydisperse colloids.

Although, a generalized diffusion model for particle growth was developed recently (55), within which the conditions of so called particle size "focusing" were clarified. Focusing of particle size distribution was shown to be possible reaction controlled regime, although at a much lower rate (over longer time interval). For this the monomer diffusion D and surface reaction rate *k* must be high while their ratio D/k should remain small: for D/k > 1000 nm the "focusing" starts and proceeds very slowly only after particles reach micron size range (55).

If the rate of silica monomers chemisorption at the particle surface (e.g. $k = 5.6 \cdot 10^{-8}$ cm s^{-1} at pH 7.3) is adopted as the surface reaction rate then for ∅10 nm colloidal silica in water at 25 °C the product $kR_p = 2.8 \cdot 10^{-12} cm^2 s^{-1}$ is much smaller than silica monomer diffusion for the same conditions (56): $D = 1.02 \cdot 10^{-5} cm^2 s^{-1}$. This suggests that particle growth by precipitation of oversaturated silica (i.e. for 2.5>SSI>1) is controlled by its adsorption at the surface of the particles.

The relatively high value of the diffusion to reaction ratio - *D/k* = 180 nm - characteristic for silica (at pH 7.3) suggests that production of monodisperse colloidal silica by monomer precipitation on existing particles is a time demanding, yet feasible, process. Moreover as discussed above, the rates of surface reactions of silica precipitation can be accelerated by increasing solution pH. While doing this may not be recommended for geothermal applications, this is what was done to produce more or less monodisperse silica aquasols for the purposes of current research (Section 3.2).

Finally, with established chemical kinetics of colloidal silica nucleation and growth the timescales for these processes can be estimated at the conditions representative of a geothermal power station. Figure 6 gives schematic illustration of such conditions and average fluid residence times for the Kawerau power station.

The downhole temperature, pH (57) and ionic strength (25) indicate that solubility of silica for State 1 (Fig.6), where it is in equilibrium with quartz, is about 1000 ppm. This corresponds to the silica solubility detected aboveground.

Brine oversaturation with silica after first steam separator (State 2, Fig.6) calculated (Eq. 1, 2 and 5) for the temperature, pH at this point and silica concentration measured prior to separator (1000ppm) is equal to SSI=1.7. A higher concentration of both silica and dissolved salts, which decreases silica solubility even more, cause an increase of oversaturation degree. Thus, if for example brine is concentrated by factor of 1.15, meaning that 1000 kg of extracted geothermal fluid is separated into 130 kg of steam and 870 kg of brine, then corresponding oversaturation degree for brine in State 2 would be equal SSI=2.3. This agrees well with a maximum measured operational value for the Kawerau power plant (57) of SSI_{max}=2.3.

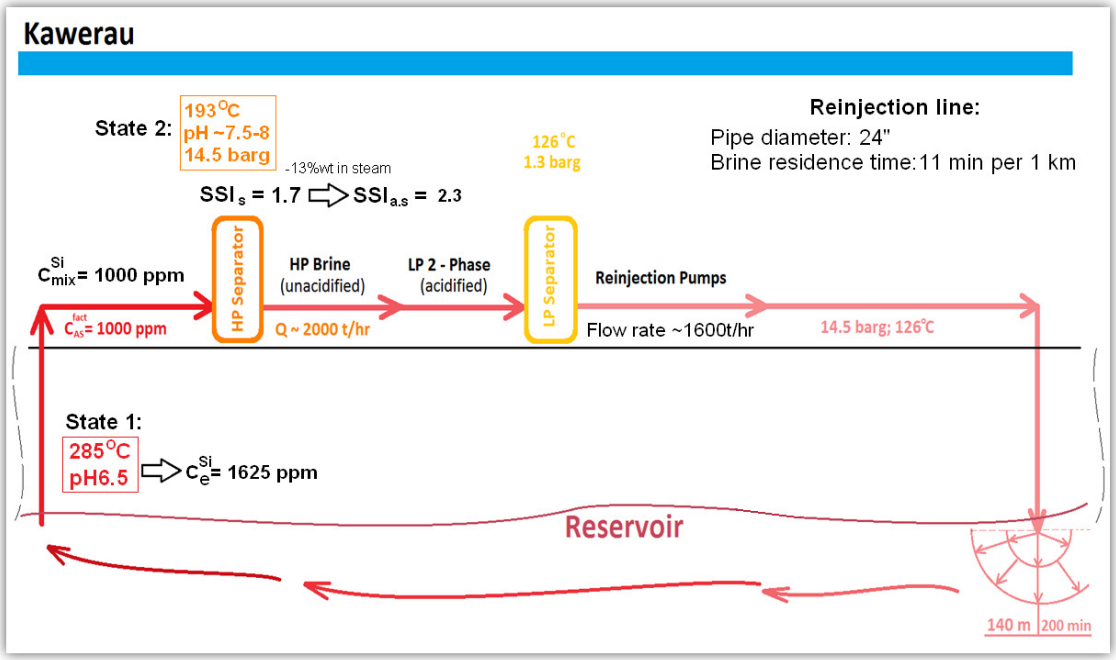

Figure 6: Operational parameters of the Kawerau power plant

Now with the known temperature, pH and SSI of the separated brine the duration of colloidal silica formation and growth steps discussed above can be estimated and compared with brine time of residence in above- and underground pathways.

The first step, formation of silica polymers of less than critical nucleus size, is fast and has little effect upon the final polymerization rate. Any of the remaining three can be rate-limiting.

Table 3 below provides characteristic times of particle nucleation and growth estimated based on the empirical results by Weres at al. and Fleming correspondingly. Two cases are compared: brine with no acid dosing after separation (pH 7.5) and acidified brine (pH 5.7).

Table 3: Summary of silica precipitation time scales

Characteristic time of	Without acid dosing pH=7.5, T=150°C, SSI_0=2.3	With acid dosing pH=5.7, T=150°C, SSI_0=2.3
Si particles nucleation (step 2, (23))	5-10 min	≥ 10000 min
Si particles growth (step 3, (24))	100-200 min	3000 min
Average brine residence in the reinjection pipeline	11 min/km	

Brine acidification effectively delays homogeneous nucleation of colloidal silica well beyond the time it gets reinjected. However, heterogeneous nucleation, which is generally faster than homogeneous because the nucleation barrier is much lower in presence of seed centres, can accelerate overall rate of silica precipitation. The rate of heterogeneous nucleation is much harder to predict because of usually unknown concentration of seed nuclei.

Moreover, once the brine is back underground its pH can gradually return to normal. This plus the contact with a vast number of seed centres (rock/quartz grains) can result in complete polymerisation of any oversaturated silica within some distance from the reinjection well outlet.

Brine aboveground residence time being much smaller than timescale of particles growth by monomer chemisorption (even in non acidified brine) suggests that colloidal AS surface rearrangement rarely takes place above the ground. However, synthetic colloidal silica solutions used in the present study are aged for at least 1 week (10080 min) before being used in the experiments allowing surface rearrangement to take place.

1.3.3 Ostwald ripening

The relationships describing behaviour of oversaturated silica solutions (*SSI*>1) summarised above were used for qualitative analysis of the production conditions in Section 3.3.

The colloidal system may undergo further coarsening through particle aggregation and Ostwald ripening (OR) after the saturation concentration of the dissolved silica is established. A summary of the relevant kinetic relationships for these two processes are presented in this (OR) and the following subsection (1.3.3). It describes behaviour of the colloidal silica at SSI ≈ 1 and, as such, is used later in section 7.1 for the quantitative analysis of the experimental observations of long-term evolution and stability of synthetic colloidal solutions.

The Ostwald ripening (OR) (58), which takes place at SSI ≈1, is the final stage of silica nanoparticle growth by monomer precipitation. It reflects tendency of the colloidal system to minimise the interface between the colloidal and liquid phase. Thus, smaller particles, with higher surface energy, dissolve. The released monomers diffuse and precipitate on the bigger particles further growing them and lowering the systems free surface energy. This process was studied extensively both analytically and numerically, using mean-field (59), (60) and (61) and molecular dynamics approaches (62) .

Two limiting kinetic regimes of OR were identified – the diffusion and reaction limited regimes. The former, described by Lifshitz-Slyozov theory (59), takes place when the diffusion of the monomers is much slower than their absorption at the surface. The latter case of slow absorption was described theoretically by Wagner (60). OR theories predict the existence of a limiting self-similar particle size distribution (PSD) with a tail toward smaller particles and no particles larger than 1.5 times the average size a_n (63). However, in many freshly prepared colloidal solutions the PSD is skewed to higher sizes from the average a_n with many particles larger than 1.5 a_n and the transition to the limiting PSD was shown take a long time (64).

During diffusion controlled OR $\left(D \ll kR_p\right)$ the rate of average particle size $\langle R_p \rangle$ growth follows a "1/3" power law relationship (59):

$$\langle R_p \rangle^3 = \langle R_p \rangle_0{}^3 + \frac{8\gamma C_\infty \vartheta^2 D}{9R_g T} t \tag{18}$$

Here *t* is time, $D = (1.02 \pm 0.02) \times 10^{-5} cm^2 s^{-1}$ is a diffusion coefficient of the silicic acid in water at 25°C (56), $\gamma = 0.039 \frac{N}{m}\ (at\ pH\ 7.5); 0.0016\ \frac{N}{m}\ (at\ pH\ 9.5)$ is the surface tension at amorphous silica – water interface (23), C_∞ is the solute concentration at a plane interface, which is assumed to be equivalent to C_e (Eq.2), $\vartheta = 3 \cdot 10^{-5} \frac{m^3}{mol}$ is molar volume of silicon dioxide, R_g gas constant and *T* temperature.

In the long-time limit Equation 18 reduces to (61)

$$\langle R_p \rangle = \left[\langle R_p \rangle_0{}^3 + K(\phi) t\right]^{1/3} \tag{19}$$

here $K(\phi) = 0.444$ for particle volume fraction $\phi \Longrightarrow 0$ and 1.3 for $\phi = 4.5 \cdot 10^{-2}$.

For the reaction controlled OR $(D \gg kR)$ the average particle size increases with time as

$$\langle R_p \rangle^2 = \frac{64\gamma C_\infty \vartheta^2 k}{81 R_g T} t \quad (20)$$

As was established above the product of surface reaction constant and particle radius $kR_p = 2.8 \cdot 10^{-12} cm^2 s^{-1}$ is much smaller than silica monomer diffusion coefficient $D = 1.02 \cdot 10^{-5} cm^2 s^{-1}$ for Ø10 nm colloidal silica in water at 25 °C. This suggests a reaction limited kinetics of the OR for colloidal silica. Therefore the average particle size growth due to OR must follow "1/2" power law (Eq.20): $d(nm) = 1.04 \left({}^{nm}/_{s^{0.5}} \right) \cdot [t(s)]^{0.5}$.

1.3.4 Aggregation and stability of colloidal silica

The process of cluster formation, or aggregation, as a result of the particle bonding in Brownian collisions was described within the classical mean-field Smoluchowski approach (65). This approach was later extended to take into account the probability of the particle bonding upon the collision (66) and the non-Brownian collisions, induced by velocity gradients and turbulence in the suspending fluid (67).

The probability of two colliding colloidal particles forming an aggregate is determined by the interparticle interactions. For the charged particles in a liquid these interactions can be modelled as a superposition of van der Waals attraction and electrostatic double layer repulsion forces. The corresponding potentials, as the functions of the particle and solution parameters, were derived within standard Derjaguin–Landau–Verwey–Overbeek (DLVO) theory (68), (69) and (70).

Interestingly, colloidal silica does not always behave according to the DLVO theory. It exhibits higher stability at low pH and lower stability at high pH than predicted by standard DLVO theory (71), (72). This anomalous stability was suggested to be due to existence of the gel layer of "hairy" hydrated (poly)silicic acid chains on the surface of the particles (72). If compared to the case of the solid particle surface considered in DLVO theory, this layer affects charge distribution in the vicinity of the particle surface and causes an additional strong, short-range repulsion of steric origin. The thickness of this gel layer, and thus its effect on the silica colloid stability, was shown to vary with the solution pH and IS (73). Thus, a 150 nm silica nanoparticle in solution at pH 6 was found to swell by 2.1 nm and 39 nm at IS = 100 mM and IS = 1 mM correspondingly. The gel layer was generally thicker at pH 8: 2.9 nm at IS = 250 mM and 58 nm at IS = 1 mM.

Again, two limiting regimes of the kinetic aggregation were identified in (74), (75), (76) and (77), with the value of sticking probability being a controlling parameter. The fast, or diffusion controlled, aggregation takes place when the particle repulsion is weak and sticking probability is close to unity. The opposite case with highly stable colloids is known as reaction controlled, or slow, aggregation. These two regimes are characterised by different kinetics, evolution of PSD and structure of the formed aggregates. The specific "crossover" (74) and "retarded" (78) regimes of aggregation were also identified. The former occurs in the system of colloids of transitional stability and the latter is characteristic for the colloids with time (size) dependent stability.

Within the classical Smoluchowski-Fuchs framework the aggregation in a stagnant colloidal suspension J_{slow}, or else total steady-state mass flux of colloidal particles towards each other, is governed by the Brownian, perikinetic, motion and electrostatic interparticle potential effects (65), (66):

$$J_{slow} = J_{Brwn} + J_{DLVO} = 8\pi D_p m_p r^2 \frac{dn}{dr} + m_p \frac{n}{B}\frac{dV_t}{dr} \tag{21}$$

here $\mathrm{D_p} = \mathrm{k_b T}/6\pi\eta\mathrm{R}$ is the particle diffusion coefficient, m_p average particle mass, η is fluid viscosity, R is particle radius and $\mathrm{n_o}$ and n are bulk and local particle number concentration respectively, $\mathrm{B} = \mathrm{k_b T}/2\mathrm{D_p}$ is the friction factor and V_t is total interaction potential, that equals the sum of the attractive and repulsive potentials given by standard DLVO theory (68), (69), (70):

$$V_t = V_{LW} + V_{EDL} \tag{22a}$$

$$V_{LW} = \frac{-AR}{12H}; H \ll R_p \tag{22b}$$

$$V_{EDL} = \pi\varepsilon\varepsilon_0\left(\frac{R_p}{2}\right)(\zeta_1^2 + \zeta_2^2)\left[\frac{2\zeta_1\zeta_2}{\zeta_1^2+\zeta_2^2}\ln\left(\frac{1+e^{-\kappa H}}{1-e^{-\kappa H}}\right) + \ln(1-e^{-\kappa H})\right] \tag{22c}$$

where $A = 1.5 \cdot 10^{-20} J$ is the Hamaker constant for interactions of the silica particles suspended in water, $H = r - 2R$ is the separation distance between the particles, R is the particle radius, r is a centre-to-centre distance, ζ_1 and ζ_2 are the electrical potential (i.e., the zeta potential at shear plane, reported in Section 3.3.2) of the particle and wall, ε is the relative permittivity or dielectric constant of the medium and ε_0 is the permittivity under vacuum, κ is the Debye-Huckel reciprocal length, defined as

$$\kappa = \sqrt{\frac{2e^2 n_\infty z^2}{\varepsilon k T}} \tag{23}$$

where e is the electron charge, z is the valence, and $n_{\infty}^{i} = 1000 N_A C_s$ is the bulk number density of ions (ion number concentration), N_A is Avogadro's number, and C_s is the electrolyte molar concentration (ionic strength of the solution in Molar units).

The zeta potential of colloidal silica depends on the ionic content and type of electrolyte, pH and temperature (79). The values of zeta potentials for the silica particles implemented in this study were measured a Zetatrac NPA152 particle size and zeta potential analyser (Microtrac Inc.) (Section 3.3.2) and used to calculate interaction potentials in Chapter 6.

Fast and slow coagulation rates (number of coagulations per unit time) can be found by solving the diffusion equation (Eq.21) for the following boundary conditions (53):

$$n = 0 \; for \; r = 2R \tag{24a}$$

$$n = n_0 \,, \; V_t = 0 \; for \; r = \infty \tag{24a}$$

The solutions can be shown to be (67), (53):

$$N_{Brwn} = 8\pi D_p R_p n_0^2, \tag{25a}$$

$$N_{slow} = \frac{8\pi D_p R_p n_0^2}{\int_{-2}^{\infty} e^{\frac{V_t}{k_b T}} \frac{dH}{H^2}} \tag{25b}$$

The ratio of the rapid aggregation rate (Eq.23a), determined by free Brownian diffusion and the slow aggregation rate (Eq.23b) yields the stability value (Eq. 24):

$$W = \frac{Number \; of \; the \; colisions}{Number \; of \; the \; collisions \; resulting \; in \; coagulation} = \frac{N_{Brwn}}{N_{slow}} = 2 \int_{-2R}^{\infty} e^{\frac{V_t}{k_b T}} \frac{dH}{H^2} \tag{26}$$

here $H = r - 2R$ is a separation distance between particles (or particle and wall), r is centre-to-centre (or centre-to-wall) distance. The inverse of this parameter is also known as attachment, or sticking, probability $K = 1/W$. It is commonly used to quantify particle deposition rate.

The pace of the aggregation process is conventionally quantified by the time needed for the number of particles in a solution to decrease by halve. The fast aggregation half-time equals (65), (67):

$$\tau_a^f = \frac{2}{J_{Brwn} C_0} = \frac{3\eta}{4 k_b T C_0} \tag{27}$$

The synthetic sols used in this research are assumed to have had constant concentration of colloidal silica once they were at equilibrium. It can be determined as a difference between

the total silica concentration (Section 3.3: 1.75 g/l) and silica solubility calculated with Eq.2. Thus, at T = 20 °C and pH 7.5 used sols contained 1.63 g of colloidal silica per 1 L. The particle number concentration is then a simple function of the particle size, and, for example, for Ø10 nm average particle size, it equals $n_o = \frac{C_{tot.colloidal\ Si}}{M_{avg.particle}} = 2 \cdot 10^{21}$ m^{-3}. The corresponding fast aggregation half-time τ_a^f in this case is $7.2 \cdot 10^{-5}$ s.

Using the definition of the stability (Eq.26) the slow aggregation half-time can be found as

$$\tau_a^s = \tau_a^f \cdot W \tag{28}$$

The average aggregate size R_a(m) during the fast, diffusion limited aggregation was shown to follow a power law relationship (74)

$$R_a \sim t^{1/d_f} \tag{29}$$

here d_f is a fractal dimension of the formed aggregate. It relates mass of the aggregate cluster to its size (77)

$$\frac{M_a}{M_0} = S = \left(\frac{R_a}{R_0}\right)^{d_f} \tag{30}$$

here M is a mass and S is a number of primary particles in the aggregate, subscripts *a* and *0* denote the aggregate and primary particle values correspondingly. With Eq.30 the aggregate size doubling time τ_a^R can be defined through the aggregation half-time τ_a:

$$\tau_a^R = \tau_a \left[\left(\frac{2R_0}{R_0}\right)^{d_f} - 1\right] \tag{31}$$

The concept of the aggregation half-time gives a convenient method for the experimental estimation of the aggregative stability (from Eq.28). It can be found as a ratio of the slow (experimental, Section 7.1) and rapid (theoretical, Eq.31, 27) particle size doubling times:

$$W_{act} = \frac{\tau_a^{R,s}}{\tau_a^{R,f}} \tag{32}$$

The fractal dimension of the aggregates formed in diffusion limited regime was shown to be lower ($d_f \approx 1.4 \div 1.8$) than of those formed in reaction limited regime ($d_f \approx 2.1$) (76). This reflects a more compact structure of the clusters formed in a reaction limited aggregation.

The process of slow aggregation, observed in stable colloidal systems, has exponential time dependence (74)

$$R_a = R_0 e^{Ct} \tag{33}$$

here parameter C is proportional to the sticking probability: $C \sim 1/W$.

The specific "retarded" reaction limited aggregation, takes place when aggregative stability W increases in the course of the aggregation. It was shown to have universal logarithmic scaling (78):

$$R_a \sim (\log t)^{0.7}. \tag{34}$$

The aggregation process discussed above has included only Brownian motion as a collision driving mechanism of particle transport. This type of aggregation is also called perikinetic.

In general, the rate of particle collisions can be higher due to the fluid motion. This type of collisions is called orthokinetic. Thus, Levich gives the following expressions for the additional rates of particle-particle collisions due to the velocity gradients and turbulent pulsations (67):

$$\text{Gradient encounters:} \quad N_{Grad.} = \frac{16}{3} G d_p^3 n_0^2 \tag{35}$$

$$\text{Turbulent encounters:} \quad N_{Turb.} = \frac{1}{2} \nu \frac{Re^{3/2}}{L^2} d_p^3 n_0^2 \tag{36}$$

where d_p is the particle diameter, n_0 the number of particles per unit volume, G the velocity gradient, Re the Reynolds number, ν the kinematic viscosity and L the characteristic length.

Usually, for sake of simplicity, the contributions of the two aggregation mechanism to the overall aggregation rate are considered to be additive. In this case, the effective aggregation half-time in a flowing colloidal solution can be found by modifying Eq.27:

$$\tau_a^f = \frac{2}{(J_{Brwn} + J_{Grad} + J_{Turb}) C_0}. \tag{37}$$

Although, the assumption about additivity of the aggregation mechanisms can be used in some circumstances, generally it is not true. Thus, recent Brownian dynamics simulations (80) have shown that redistribution of the particles by isotropic Brownian motion in the different directions of the fluid motion distorts the additivity and results in higher or lower effective aggregation rate depending on the problem Peclet number: $Pe = \frac{advective\ transport\ rate}{diffusive\ transport\ rate}$.

1.4 Particle transport in turbulent flow

Silica scaling involves processes of its polymerization, transport and attachment to a wall. Since the regularities of colloidal silica formation, growth and stability were clarified in the

preceding sections we can now move on to the issue of its transport. This section gives brief overview of the particle transport mechanisms, properties of turbulent flow over rough surfaces and recent analytical and numerical calculations of the particle transport rates. The aim of this section is to answer how rate of particle transport depends on the hydrodynamics of suspending flow, surface roughness and size of the depositing particles.

Two flow scenarios are of interest in regard to the scaling at the geothermal power plants. Highly turbulent pipe flow with a well defined near-wall velocity structure is present in the reinjection lines ($Re_{pipeline} = \frac{VD}{\nu} \cong 10^6$). Whereas, underground, inside irregular rock fissures and pores flow is more complex with no stable developed characteristics. In this case flow Reynolds number tends to decrease with the distance from the reinjection point.

Two conceptually different mass transfer mechanisms are relevant for the mineral scaling – diffusion (molecular, Brownian and turbulent) and convection (or else inertial transport in case of particle transport) (67). The relative importance of these mechanisms is determined by the value of the dimensionless Schmidt number

$$Sc = \frac{\nu}{D}, \tag{38}$$

where ν is fluid viscosity, D is a diffusion coefficient. High Sc indicates prevalence of the momentum transport over molecular diffusion.

The molecular diffusion coefficient for silicic acid in water at 25°C was quoted above to be $D_m^{Si} = 1 \cdot 10^{-9} m^2 s^{-1}$. The Brownian diffusion coefficient for a colloidal particle with diameter $d_p = 125\ mm$ in water at 25°C, according to the Stokes-Einstein equation (81), is equal to $D_{Br}^{Si} = \frac{kT}{3\pi\nu\rho d_p} = 4.3 \cdot 10^{-12} m^2 s^{-1}$.

These values together with relatively high viscosity of water ($\nu = 10^{-6} m^2 s^{-1}$) indicate that transport of silica in abovementioned conditions is characterised by high Schmidt numbers: $Sc_{Si\ monomer} \approx 10^3$ and $Sc_{Si\ colloid} \approx 10^6$ for monomeric and colloidal silica respectively.

Therefore, momentum transport, as well as advective transport of silica entrained by fluid motion, prevails over diffusion even at very low flow velocities. Only very close to the wall boundary, where flow velocity tends to zero, does molecular (or Brownian) diffusion become important. This region is called the diffusion boundary layer and it represents the main resistance to mass transfer (Fig.7).

The thickness of diffusion boundary layer δ, besides the Schmidt number, also depends on the structure of the hydrodynamic boundary layer. In case of laminar parallel plate flow it is related to the thickness of hydrodynamic boundary layer d_l as (67):

$$\delta \approx 0.6 \left(\frac{1}{Sc}\right)^{1/3} d_l \tag{39}$$

or $\delta \approx 0.06\, d_l$ and $0.006\, d_l$ for silica monomers and 100 nm colloids correspondingly.

In fully turbulent flow intense velocity pulsations provide effective mixing and accelerate transfer of momentum and mass by orders of magnitude $\left(\frac{\nu}{\nu_{turb}} \approx \frac{1}{Re}\right)$. The so called turbulent diffusion coefficient D_{turb} is of the same order of magnitude as turbulent viscosity which is much greater than molecular viscosity everywhere in a turbulent flow except for a thin layer (δ_0) at the wall (Fig.7), called viscous sublayer (67):

$$D_{turb} \approx \nu_{turb} \sim \nu \left(\frac{y}{\delta_0}\right)^4, \tag{40}$$

here *y* is a wall normal distance.

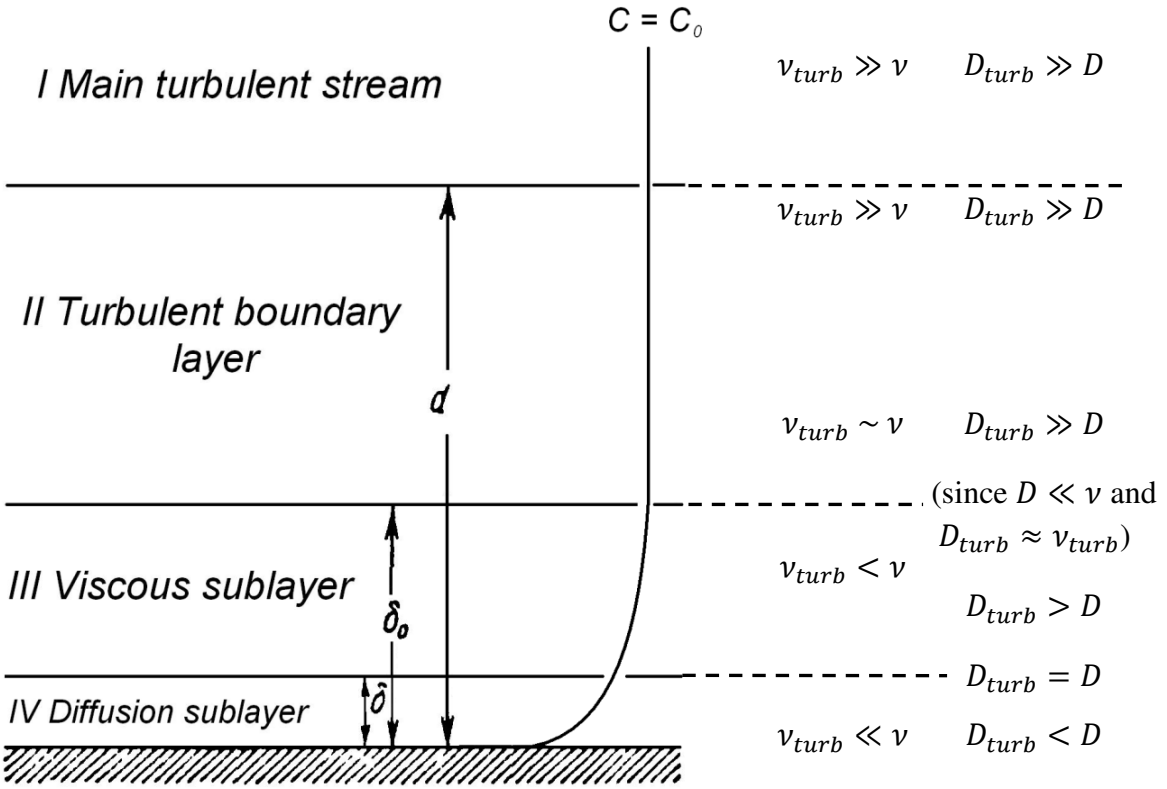

Figure 7: Mass transfer in the turbulent boundary layer (67)

It was shown (67) that with the assumption of gradual damping of turbulent pulsations within viscous sublayer turbulent diffusion remains greater than molecular through the most part of this sublayer. Only at certain distance from the wall δ turbulent diffusion decreases enough to become equal to molecular diffusion (67):

$$D_{turb}^{y=\delta} = 10\,\nu\left(\frac{\delta}{\delta_0}\right)^4 = D \tag{41}$$

Due to the similarity of the mass and momentum transfer processes, the concentration distribution near the solid surface has a layered structure similar to the flow velocity distribution.

In case of turbulent flow over infinite plate there are four regions with different mass diffusion patterns (Fig. 7). Far from the surface there is a zone of developed turbulence (region I) where both average velocity and concentration have constant values ($C_I = C_0$, for $y > d$). Closer to the surface, in the turbulent boundary layer (region II), the average velocity, and so the concentration, decrease slowly.

Under the assumption of gradual decay of turbulence within the viscous sublayer (67), mass transport by residual turbulent pulsations is still stronger than mass transport by molecular/Brownian diffusion within the region III ($\delta_0 > y > \delta$).

Only in the innermost part of the viscous sublayer (region IV), at $y < \delta$, does the molecular (Brownian) diffusion mechanism prevail over the turbulent. Thickness of the corresponding diffusion sublayer in turbulent flow can be determined from Eq.41 and 38:

$$\delta = \frac{\delta_0}{Sc^{1/4}\sqrt[4]{10}} \tag{42}$$

So, it equals about 0.1 and 0.017 of the viscous sublayer thickness for monomeric and colloidal silica respectively.

Overall the rate of the diffusion mass transfer increases with the corresponding diffusion coefficient and local concentration gradient, which is inversely proportional to the thickness of the local viscous boundary sublayer (which in turn is inversely proportional to flow rate; see next subsection for details) (67):

$$j_{Diff} = \frac{DC_0}{\delta} \tag{43}$$

Even though colloidal particles have much lower diffusivity than silicic acid molecules, it was shown (42), (43) that they are responsible for higher scaling rates, especially at low oversaturation of the solution. There could be three explanations to this: first deposition of both, monomeric and colloidal silica is controlled by corresponding surface reaction rate (absorption/attachment) and it is higher for colloidal silica. Second, transport of particles through the boundary layer can be facilitated by some additional mechanisms. Third, some combination of the first two can be in place.

The second, and thus the third, hypothesis can be assessed only after discussing the inertial mechanism of particle transport in the next subsection.

First hypothesis can be tested by considering diffusion kinetics of the scaling process. As with any heterogenic reaction, the apparent rate of the silica scaling is determined by the chemical kinetics of silica absorption at a surface and rate of its transport to this surface. This problem can be solved exactly by finding analytical or numerical solutions of the general advection-diffusion equation (67):

$$\frac{\partial C}{\partial t} + Ugrad\ C = D\ \Delta C \tag{44}$$

It simplifies for steady state processes ($\frac{\partial C}{\partial t} = 0$), but still requires knowledge of the flow field, represented by vector $U = \left(u_x; u_y; u_z\right)$, and boundary conditions that reflect kinetics of the surface reactions:

$$D\ grad\ C = k\ C^m \tag{45}$$

here, as stated in preceding section, the order of reaction is *m=1* for monomers absorption on AS particle surface and *m=3* for their condensation into solid silica.

A number of the exact and approximate solutions of this problem are available for different flow/reaction scenarios (67), (82). The relevant to the silica scaling examples are discussed in the Chapter 2.

1.4.1 Particle transport mechanisms

There are two theoretical approaches to calculating the rate of particle deposition from flowing suspensions – Lagrangian and Eulerian. Within the Lagrangian approach particle motion is described by a set of particle trajectories that are governed by Newton's second law. The random thermal (Brownian) forces can be modelled by Langevin-type equation of motion (83), the solution of which yields stochastic trajectories.

The Eulerian method describes the concentration distribution of particles in space and time. These distributions are governed by a set of coupled Fokker-Plank equations (65). In case of dilute suspensions of spherical, non-interacting particles they reduce to usual continuity equation. The continuity equation that governs particle transport and deposition in fluids is termed the particle transport or convective diffusion equation. It can be written for the concentration of particles, as above in Eq.44, or for particle flux j:

$$\frac{\partial C}{\partial t} + \nabla \bar{J} = 0 \tag{46}$$

General results obtained with Eulerian approach for transport and deposition of non-interacting particles within turbulent parallel flow onto flat, rough surface are considered in this section.

The results of deposition experiments and simulations are usually convenient to present as dependence of nondimensional deposition velocity from nondimensional particle relaxation time. The non-dimensional deposition velocity V_{dep}^{+} is the wall particle flux normalized by bulk concentration of particles C_0 and fluid friction velocity u_*:

$$V_{dep}^{+} = \frac{j}{C_0 \cdot u_*}, \tag{47}$$

with $u_* = \sqrt{\tau/\rho_l}$ determined by wall shear stress τ and fluid density ρ_l.

The dimensionless particle relaxation time is a measure of the particle's ability to deviate from fluid motion. It is calculated as ratio of so called Stokes stopping distance s_p and particle initial velocity u_0:

$$\tau_p = \frac{s_p}{u_0} = \frac{\rho_p d_p^2}{18\mu},$$

and it is commonly nondimensionalized as

$$\tau_p^{+} = \frac{\rho_p d_p^2}{18\rho_l} \cdot \left(\frac{u_*}{\nu}\right)^2, \tag{48}$$

where ρ_p and ρ_l are particle and fluid densities correspondingly and ν the fluid viscosity.

Smaller particles (with short relaxation times) follow the fluid motion more closely than bigger particles, thus as they get closer to the wall they lose the y component of their convective velocity much faster than bigger particles.

The ratio of the dimensionless particle relaxation time and flow characteristic time determines the probability of a particle to deposit onto an obstacle that disturbs the flow. It is also known as Stokes number:

$$Stk = \frac{\tau_p U_0}{L_0}$$

where U_0 is the fluid velocity far away from the obstacle and L_0 is the characteristic dimension of the obstacle. All particles with $Stk \gg 1$ that travel toward frontal area of the obstacle will come into contact with its surface, while all particles with $Stk \ll 1$ (except for those that travel along the streamlines closest to a surface and get intercepted due to their finite size) will follow with the fluid around the obstacle.

The ratio of particles travelling toward the frontal area of the obstacle that actually collide with it is called the collection efficiency. Its exact value for the Stokes numbers in-between above two limiting cases ($Stk \sim 1$) was determined both experimentally (84) and numerically (85). It was found to be virtually independent of bulk flow Re.

Fig. 8 illustrates these results obtained for the particles depositing onto spherical collectors.

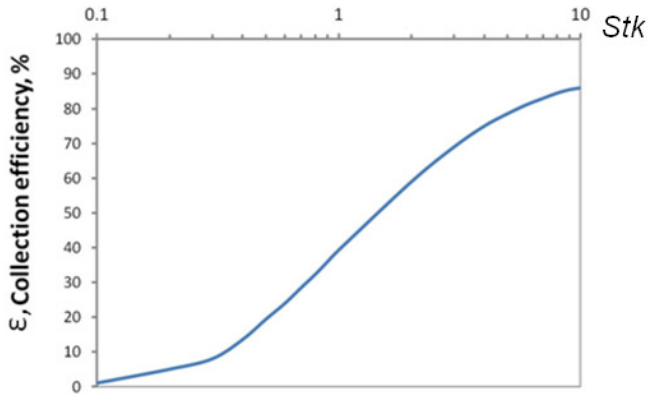

Figure 8: Collection efficiency as a function of Stk number (85)

The generalized equation for particle flux in the direction y normal to the wall in fully developed flow can be expressed as (86):

$$j = -(D_B + D_T)\frac{\partial C}{\partial y} + C\,\bar{U}^c_{py} \tag{49}$$

here the first term on the right-hand side is the diffusion due to the gradient in the particle concentration and the second term represents convective transport emerging from particle inertia. It includes transport of particles by their deviation from flow streamlines; turbophoresis (87) and Saffman lift (88). The particle convective velocity in the y direction $\bar{U}^c_{py}$ is determined from the Reynolds-averaged particle momentum equations (86)

y-momentum: $$\bar{U}^c_{py}\frac{\partial\,\bar{U}^c_{py}}{\partial y} + \frac{U^c_{py}}{\tau_I} = -\frac{\partial\overline{U'^2_{py}}}{\partial y} + F_{S_y} \tag{50a}$$

x-momentum: $$\overline{U}_{py}^{c}\frac{\partial \overline{U}_{px}}{\partial y}=\frac{1}{\tau_I}\left(\overline{U}_{fx}-\overline{U}_{px}\right) \quad (50b)$$

in these equations $\overline{U}_{py}^{c}\frac{\partial\,\overline{U}_{py}^{c}}{\partial y}$ is particle acceleration; $\frac{\overline{U}_{py}^{c}}{\tau_I}$ is the steady-state hydrodynamic drag in normal to wall direction (fluid velocity in this direction is assumed to be $\overline{U}_{fy}=0$), $\tau_I=\tau_p\frac{24}{ReC_D}$ is an inertial relaxation time, with slip Reynolds number equal $Re=\frac{\mathrm{d_p}(U_f-U_p)}{\nu}$ and an empirical particle drag coefficient (89) : $C_D=(24/Re)(1+0.15Re^{0.687})$; $-\frac{\partial\overline{U_{py}'^2}}{\partial y}$ is the turbophoresis and F_{S_y} is the shear induced lift force. Eq. 50 b represents hydrodynamic drag in x direction parallel to a wall.

The expression for a lift force acting on small particles in shear flow was first obtained by Saffman (88):

$$F_{S_y}=3\frac{\rho_l}{\rho_p}\nu\frac{1}{d_p}\sqrt{\frac{1}{\nu}\left|\frac{d\overline{U}_{fx}}{dy}\right|}\left(\overline{U}_{fx}-\overline{U}_{px}\right) \quad (51)$$

here $\overline{U}_{fx}$ is the fluid velocity at the location of particle mass centre, $\overline{U}_{px}$ is the particle velocity, $\frac{\mathrm{d}\overline{U}_{\mathrm{fx}}}{\mathrm{dy}}$ is the shear rate. This force is perpendicular to the direction of flow and is positive in y-direction if $\overline{U}_{fx}>\overline{U}_{px}$ (see Fig.9).

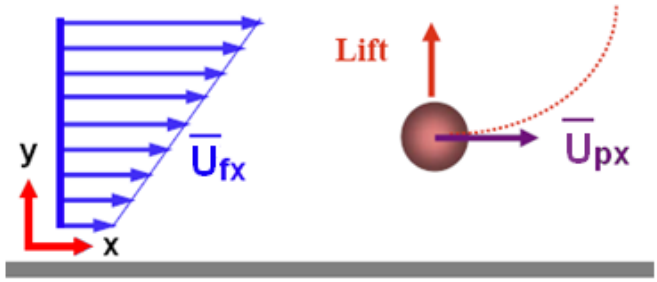

Figure 9: Shear induced lift force

Therefore, if a particle from higher velocity fluid layer (i.e. further from a wall) is moved to a slower layer it can have higher speed than surrounding fluid and as such the lift force will push it further to slower layers (or to a wall). In an opposite case of a particle displaced from slower to faster flowing layers this force is also acts in a direction of particle displacement (away from a wall). In deposition processes when more particles move from bulk flow towards a wall than in opposite direction the cumulative effect of the lift force was shown to enhance the deposition (86), (90).

Eq. 51 shows that magnitude of the lift force is directly proportional to particle slip velocity $\left(\overline{\mathrm{U}}_{\mathrm{fx}} - \overline{\mathrm{U}}_{\mathrm{px}}\right)$ and is inversely proportional to its size (d). Since slip velocity decreases faster for smaller particles (Eq. 50 b) there must exist a critical value of particle size (or its relaxation time) for which the effect of this force on particle trajectory is largest. Therefore, the effect of shear lift force can be significant for intermediate size particles: its magnitude is small for a larger particle (term 1/d in Eq. 51) and the effective time it acts on a particle decreases as they get smaller.

Another mechanism of particle transport towards a wall that caused by the gradient of turbulent velocity fluctuations is called turbophoresis. It represents the combined effect of drag force on a particle and inertia and is expressed as the tendency for particles to migrate in the direction of decreasing turbulence level.

From Eq.50 b particle turbophoretic velocity can be expressed as

$$U_{p.t} = \tau_{\mathrm{I}}\left(-\frac{\partial \overline{\mathrm{U}_{\mathrm{py}}'^2}}{\partial \mathrm{y}}\right). \tag{52}$$

It depends on the particle root-mean-square (RMS) velocity, which for large particles can be different from fluid RMS velocity $\overline{U_{fy}'^2}$. The later can be determined from empirical curve given in (91) for the region $0 < y^+ < 200$:

$$\sqrt{\overline{\left(U_{fy}'^2\right)^2}} = 0.005y^{+2}/(1 + 0.002923y^{+2.128}) \tag{53}$$

here $y^+ = \frac{yu_*}{\nu}$ is dimensionless wall distance.

The particle mean square velocity is related to the fluid RMS velocity as (86):

$$\overline{\left(U_{py}'^2\right)^2} = \mathrm{M}\,\overline{\left(U_{fy}'^2\right)^2} \tag{54}$$

here coefficient of proportionality M is a function of particle inertial relaxation time τ_I and Lagrangian time scale of fluid turbulence T_L and it can be found, for example as (86):

$$\mathrm{M} = \frac{1}{1+0.7(\tau_I/T_L)} \tag{55}$$

For very small particles $\tau_I \to 0$ and thus the two velocities are almost equal and the particles effectively follow the fluids eddies. In this limit Eq.52 gives $U_{p.t} \to 0$. This means that turbophoresis is negligible for small particles.

Guha (86) has used the advection-diffusion model represented by Eq.49 - 55 to find a relationship between non-dimensional deposition velocity V_{dep}^{+} and dimensionless particle relaxation time τ_p^+. Fig. 10 illustrates his results for a total deposition velocity as well as relative importance of individual transport mechanisms.

Molecular and turbulent diffusion, represented by first term on the right-hand side of Eq.49 (solid yellow line in Fig.10), dominate transport of particles with $\tau_p^+ < 0.1$. Corresponding deposition velocity decreases monotonically with increasing relaxation time. As also was discussed in the previous section, particles in this size range are transported by turbulent diffusion through the bulk flow to the viscous sublayer and by Brownian diffusion further down towards a wall. Although, the deposition velocity by diffusion mechanism increases with particle size if the effect of particle interception by a wall is accounted for (broken blue line in Fig.10). Larger particles need to be transported over shorter distance in the viscous boundary layer to reach the surface. With the interception included the lower boundary for the diffusion equation shifts up from the surface by distance equal to the particle radius which leads to a decrease of the effective mass transfer resistance. As evident from the Fig.10 this effect offsets the effect of the lower particle diffusivity for large relaxation times.

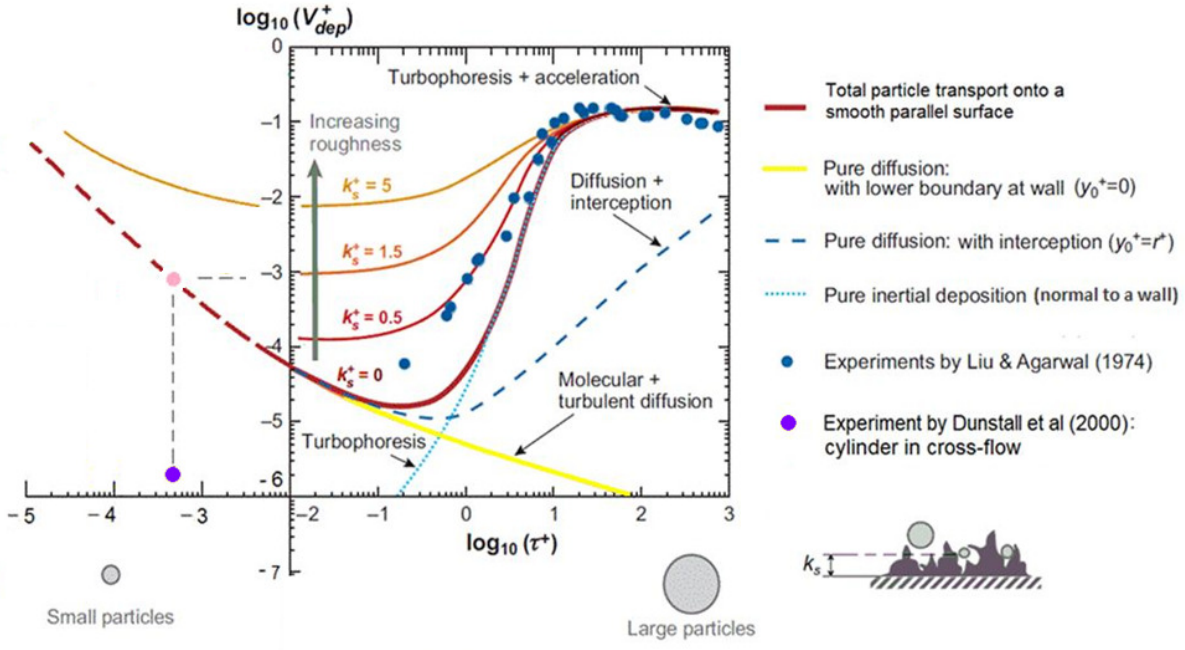

Figure 10: Classification of the particle transport mechanisms (86)

The inertial deposition, represented by convective term on a right-hand-side of Eq.49, tends to zero for very small particles (blue dotted line on Fig.10). Its contribution to total deposition velocity is comparable with that of diffusion for particles with $\tau_p^+ \sim 0.2$. As dimensionless

particle relaxation time increases higher convective velocity can be imparted to particles by turbophoresis. Large particles can gain convective velocity sufficient to enable them to coast all the way through the viscous boundary layer.

Finally, particles with $\tau_p^+ > 10$ are too large to follow fluid velocity fluctuations: $\tau_I \to \infty$ leads to $M \to 0$. Therefore they cannot attain any additional convective velocity through turbophoresis. This region of particle relaxation times is termed impaction dominated.

In his review paper (92) on deposition from parallel suspending flows, Epstein presented a similar semi-empirical classification of the dominant transport mechanisms for increasing non-dimensional particle relaxation time. He also concludes that transport of particles is dominated by diffusion for $\tau_p^+ < 0.1$, inertia - at $0.1 < \tau_p^+ < 10$ and impaction for even bigger particles. Epstein stated the significance of the Saffman lift, but, like Guha, did not include it in the above classification.

Sinclair (93) calculated the non-dimensional relaxation time for the conditions of scaling experiments (43) and determined it to be in the range 10^{-6}-10^{-3}. Approximately the same range applies to the colloidal particles used in the experiments in the present work. Based on Epstein's classification, Sinclair argued for diffusion as the dominating mechanism of the colloid transport.

Interestingly, the dimensionless scaling velocity calculated for the conditions of the experiment (43) is equal to (1.2±0.5)×10^{-6} or about 4 orders of magnitude smaller than V_{dep}^+ predicted by particle transport theory for the same value of τ_p^+ (purple vs. pink circles in Fig.10). This most likely is the outcome of the stabilizing effect of electrostatic particle–wall interactions (discussed above in section 1.3.4) on colloidal silica deposition not being included in the above particle deposition theory.

Guha has also shown that particle deposition velocity is significantly enhanced by the roughness of the surface to which particles are transported (Fig. 10).

Real walls, having roughness elements protruding from their surface, experience higher mass transfer than ideal, perfectly smooth walls. Three mechanisms that contribute to this effect can be envisioned. First, particles need to be transported through the diffusion sublayer over a distance equal to the sublayer thickness less the effective height of these roughness elements k_s. This increases transport of smaller particles for which this diffusion sublayer exists. This mechanism of particle deposition enhancement by surface roughness was included in Guha's

(86) calculations and is reflected in Fig.10. The dimensionless transport rate can increase by as much as 3 orders of magnitude when the effective height of roughness elements $k_s^+ = k_s u_*/\nu$ increased from 0 to 5.

Second, surface roughness can affect velocity and turbulence distribution in near wall region (67), (92). Roughness elements can disturb the flow and generate additional fluctuations both within and outside viscous boundary layer. This can lead to an increase of the momentum and mass transfer rates in near wall region. Progressive accumulation of deposited particle on a surface can in turn change its roughness leading to positive (or negative) feedback between mass and momentum transfer. This mechanism was not included in Guha's calculations. The hydrodynamic side of this mechanism, namely the how constant roughness affects flow parameters, is briefly discussed in the next subsection.

Finally, besides the normal-to-the-wall convection of particles considered in all current models of particle deposition, parallel-to–the-wall convective deposition onto the elements protruding from a surface can take place at certain conditions. This mechanism of particle deposition can be particularly significant in silica scaling. The periodic, spanwise ridges of silica deposits with variable height observed in geothermal scaling experiments (43) can create such conditions. Detailed discussion of this type of convective particle transport and evaluation of its rate will b given in Section 6.2.

The role of roughness in silica scaling process can be estimated by determining values of k_s^+ for the conditions of the experiments (43) (value of υ_* calculated for the measured average surface shear $\tau = 20\text{Pa}$) and relating them to the deposition velocity data in Fig.10. Thus, for new steel surfaces with $k_s = 0.05\,\text{mm}$ the dimensionless effective roughness height is $k_s^+ = 16$. Whereas for the average height of the silica ridges $k_s \approx 0.12\,\text{mm}$ this value is $k_s^+ = 38$.

The comparison of these values with the trends in Fig. 10 shows that the effect of surface roughness in silica deposition onto circular cylinder is significant for both of these cases.

In the case of developed turbulent pipe flow with the wall shear stress of 1-5 Pa, the k_s^+ value for a new steel surface is about 6. This suggests the influence of roughness on silica deposition in pipes is also significant.

Young and Leeming (90) performed another theoretical investigation of particle deposition within the Eulerian approach. They arrived at the same conclusions regarding the extent of the diffusion and inertia dominated regions as Guha. However, they performed more detailed

analysis of the relationship between the Saffman lift force, turbophoresis and viscous drag. Their particle deposition model was used to calculate deposition from fully developed turbulent pipe flow. Thus, they showed that specific radial variation of turbulent fluctuations in pipe flow is such that for $y^+ = \frac{yu_*}{\nu} < 40$ the effect of turbophoresis is to push particles toward a wall, while for $y^+ > 40$, particles are projected towards the pipe centreline.

Shams at al. (94) employed Direct Numerical simulations to study in detail the role of the boundary layer structure in the particle deposition process. As a result the value of the lower boundary of the inertia dominating region was adjusted to $\tau_p^+ \approx 10^{-2}$ and shown to depend on the shear velocity value. Particle transport rate in the diffusion region was found to increase with decrease in shear velocity. Interestingly, the deposition velocity they calculated had V-shape variations in the streamwise direction. This may be one of the manifestations of the hydrodynamic mechanism responsible for the onset and growth of scale "ripples/fences" experimentally observed on the silica scale surfaces.

1.4.2 Turbulent flow over rough walls

The similarity and close relation between momentum and mass transfer on one hand simplify their theoretical analysis – the same methods, e.g. the boundary layer approximation, can be used for the analysis of both phenomena. On the other hand, the interrelations between them give rise to the complex feedback mechanisms, i.e. the effect of scaled surface roughness on the near-wall properties of the flow and vice versa, that may (and most probably do) affect the rate of the scaling process.

The mass transfer rate in flowing fluid can be evaluated only if flow characteristics are known. Thus, the near-wall flow structure, or thickness of the viscous boundary layer in particular, must be known to calculate the rate of advection-diffusion of inertialess entities with the simplified analytical methods (e.g. with Eq.43).

The calculations of the mass transfer of inert particles can be performed by solving the general advection-diffusion equation (Eq.44). This requires the knowledge of the flow velocity distribution in the near-wall region.

The following review outlines hydrodynamics of the fully developed turbulent wall-bounded flow. This type of flow is common in geothermal applications.

Historically pipe flow was the first extensively studied wall-bounded shear flow due to its wide practical use. In this case flow is turbulent if the corresponding Reynolds number is

$Re = \frac{\bar{u}d}{\nu} > 4000$ and fully developed – mean flow does not change in the streamwise direction - at distance $l = 1.36\ d\ Re^{1/4}$ from the pipe inlet (95), here d is the pipe diameter, ν is the fluid kinematic viscosity and $\bar{u} = 4Q/\pi d^2$ is the flow speed average over pipe cross-section at a flow rate Q.

Early investigations were concerned with the pressure losses in water conduits (96), (97). As a result a number of correlations between the pressure drop and flow rate in a pipe were established. Such correlations are usually presented in a dimensionless form through the dimensionless friction factor f defined as (95):

$$\frac{\Delta p}{L} = \frac{f}{2d}\rho\bar{u}^2 \tag{56}$$

where Δp is the pressure drop along the pipe observed over distance L, ρ the fluid density.

The pressure drop is also related to the shear stress τ in the flow and at the pipe surface this relationship can be expressed as:

$$\tau = \frac{\Delta p}{L}\frac{d}{4} \tag{57}$$

Comparison of Eq.56 and 57 gives the relationship between τ and f

$$\tau = \frac{f}{8}\rho\bar{u}^2. \tag{58}$$

The first empirical expression for the friction coefficient in smooth pipes was obtained by Blasius in 1911 (98):

$$f = 0.3164\left(\frac{\bar{u}d}{\nu}\right)^{-1/4}. \tag{59}$$

It is applicable for the Reynolds numbers $Re \leq 10^5$.

Later in 1932 Nikuradse (99) performed thorough measurements of the friction and velocity distributions in smooth pipes for a wide range of Reynolds numbers $4 \cdot 10^4 \leq \mathrm{Re} \leq 3.2 \cdot 10^6$. The profiles of the mean flow velocity (u) he obtained were described by the expression:

$$\frac{u}{U} = \left(\frac{y}{R}\right)^{1/n} \tag{60}$$

where U is the maximum velocity over the pipe cross-section, *y/R* is the dimensionless wall distance, R is the pipe radius and power $1/n$ varies weakly with Re:

$$n = 6 \; for \; Re = 40 \cdot 10^3$$

$$n = 7 \; for \; Re = 110 \cdot 10^3 \tag{61}$$

$$n = 10 \; for \; Re = 3240 \cdot 10^3$$

A deep fundamental relationship between the friction law (Eq.59) and velocity distribution (Eq.60) was first identified by Prandtl (100). Thus, by substituting f from Eq.59 into Eq.58, rearranging and introducing the shear velocity defined as

$$u_* = \sqrt{\tau/\rho} \tag{62}$$

the following expression for the velocity distribution can be derived:

$$\frac{u}{u_*} = 8.74 \left(\frac{y u_*}{\nu}\right)^{1/7} \tag{63}$$

Therefore, the Blasius friction law leads to the law of 1/7 for the velocity distribution.

Since the Blasius friction law is applicable for Reynolds numbers below 10^5, the same is true for the law of 1/7 for the velocity distribution. In order for the Blasius friction law to better represent experimental data at higher Re the power in Eq.59 must be changed from 1/4 to 1/5 or 1/6. Then, the corresponding power in the expression for the velocity distribution would change (decrease) as well.

The decrease of the power in Eq.63 with the increase of Re suggested the existence of the asymptotic law for the velocity distribution at very large Re, which includes a logarithm as a limit of a very small power. Physically this asymptotic law reflects the fact that in a flow with very large Re turbulent friction is much higher than laminar molecular friction. The asymptotic logarithmic law was derived based on the Prandtl's hypothesis of the mixing length (95). This universal law of the velocity distribution in smooth pipes at very large Re is expressed as:

$$\frac{u}{u_*} = \kappa^{-1} \ln\left(\frac{y u_*}{\nu}\right) + A \tag{64}$$

Eq.64 was found to be in a very good agreement with the experimental data not only at the wall but also far from it, all the way down to the pipe/channel centreline.

Since Eq.64 was derived with the assumption that the laminar shear stress is much smaller than the turbulent, it is also applicable only in the regions where this is true. Near the wall, where the turbulent shear stress tends to zero and the molecular viscosity is important, the velocity distribution deviates from Eq.63. Here relevant flow scaling parameters are the friction velocity $u_* = \sqrt{\tau/\rho}$ and the kinematic viscosity ν. From them the viscous length scale ν/u_* is constructed and the dimensionless wall distance $y^+ = yu_*/\nu$ is used as a flow stratification parameter in the wall region.

In the viscous sublayer, defined by the wall distance $y^+ < 5$ the turbulent friction is negligible in comparison with the laminar and linear velocity distribution takes place (Fig.11 (a):

$$\frac{u}{u_*} = \frac{yu_*}{\nu} \tag{65}$$

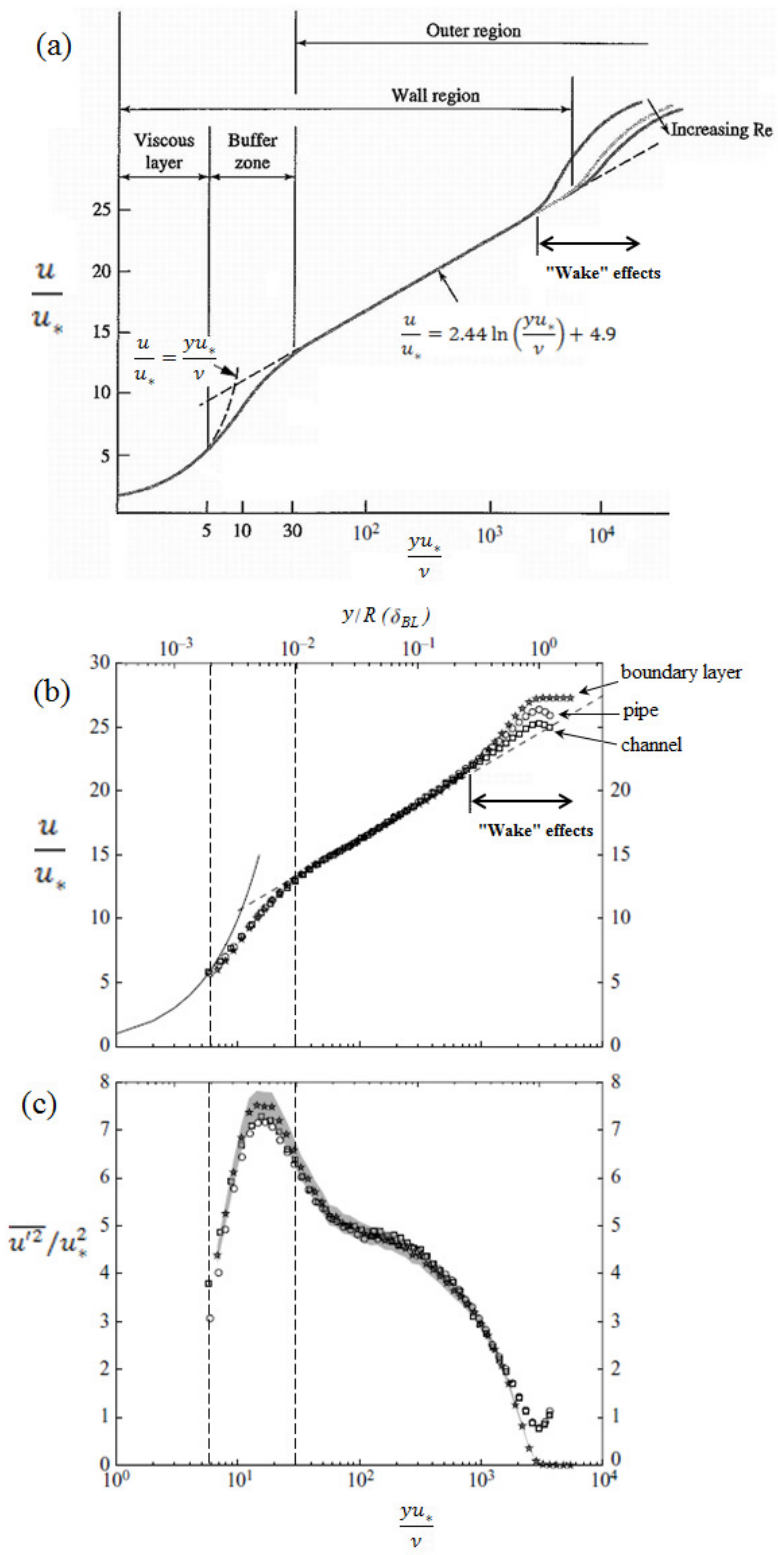

Figure 11: (a) Mean velocity profiles in the fully developed turbulent pipe flow (10), (b) its comparison with channel and zero-gradient boundary layer flows (at matched Re) and (c) corresponding profiles of turbulence intensity (101)

The thickness of the viscous sublayer on a smooth wall, required for the analytical particle flux calculations, equals

$$\delta_0 \approx 5\frac{\nu}{u_*} \tag{66}$$

For wall distances $10 \leq y^+ \leq 100$ the turbulent friction is of the same order of magnitude as laminar. Here the flow velocities were measured by Reichardt (102). He revealed smooth transition from the laminar (viscous) sublayer to the turbulent boundary layer.

This transition region is also known as the buffer zone is the most active part of the flow. A nonlinear self-sustaining cycle (103), (104) acting here is responsible for generating most of the turbulent energy in moderate Reynolds number flows. It comprises of long longitudinal streaks of high and low streamwise velocity, and shorter quasi-streamwise vortices (105).

At distances from the wall of the order of the pipe radius, the size of the structures is limited by R, which becomes the relevant length scale. The Reynolds number $Re_R = Ru_*/\nu$ defines the scale separation between the outer and wall regions. If Re_R is large enough, there is an overlap layer between the outer region and the buffer layer in which y^+ is too large for the viscosity to be relevant and y/R is too small for R to be important. The only available length scale here is the wall distance, which leads to a logarithmic distribution of the mean streamwise velocity (Eq.64) in the overlap layer.

In Eq.64 the Karman constant, $\kappa \approx 0.4$, depends only on the properties of the overlap layer and is agreed to be universal. The no-slip boundary condition at the wall determines the additive constant A but, since Eq.64 is valid for $y^+ \gg 1$, its value depends on the details of the buffer and viscous layers. For smooth walls it was found experimentally to be $A \approx 4.9$.

A composite velocity profile valid for $y^+ \geq 50$ can be expressed as

$$\frac{u}{u_*} = \kappa^{-1} \ln\left(\frac{yu_*}{\nu}\right) + A + \Pi\kappa^{-1}W(y/R) \tag{67}$$

here W is the "wake" component which represents the effect of the outer-layer dynamics. It depends on the external mechanism which is driving the flow. It is typically negligible in the logarithmic layer which has an upper limit at $y/R \approx 0.15$.

If the wake function is normalized to W(1) =2, then $2\Pi\kappa^{-1}$ measures the contribution of the outer-layer structures to the mean velocity profile. This is similar to the way the parameter A represents the influence of the viscous and buffer layers. Parameter Π is less than or equal to unity for zero-pressure- boundary layers, and for pipes and channels. Therefore, between 70

% and 80 % of the total velocity gradient across the boundary layer and at least half of the total production of turbulent energy occur in the logarithmic layer.

As reflected in Fig.11 (b) the logarithmic velocity distribution in Eq. 64 is valid in the wall region of the zero gradient boundary layer and channel flows. This reflects the similarity of the wall-bounded flows in the near-wall region (101).

All studies in this field agree on the similarity of the pipe and channel flows, which is due to the fact that 'the curvature of the [pipe] wall is nearly zero if seen from points close enough to the surface...' (106). They emphasised that while this similarity holds for large-scale eddies in internal (pipe/channel) and external (boundary layer) flows there are also important differences between them near the wall.

The nature of these differences was clarified by Monty et al. (101) through the measurements of the streamwise velocity in these three flows with carefully matched Reynolds numbers and measurement resolution. An excellent collapse of the data up to the edge of the logarithmic region $y/R \approx 0.15$ was observed (Fig.11 (b). The scaled variance of streamwise velocity fluctuations in all three flows is shown in Fig.11 c. It is evident that they all agreed up to $y \approx 0.5$ R which is well beyond the collapse of the mean velocity.

Moreover, the comparison of the pipe and channel data revealed close similarity right across the flows, even in the core region, where effects owing to the different geometries would be expected.

Klebanoff (107) and Schubauer (108) suggested that the outer region of the boundary layer ($y > 0.4\,R$) contains regions of turbulent flow and potential flow. Schubauer illustrated that turbulent kinetic energy in the boundary layer coincides with that of the internal flow right to the edge of the layer if the turbulent kinetic energy is divided by the intermittency factor. From this he concluded that the only difference between the outer-flow structures for internal and external flows is the existence of the intermittent irrotational flow in the boundary layer.

Monty et al. (101) also performed the Fourier analyses of their data and identified important modal differences between internal (pipe, channel) and boundary layer flows. The largest energetic scales were shown to be much longer in pipes/channels not only in the outer/core region, but right down to the wall.

Although the large-scale motion is qualitatively similar, its energy continuously transfers to longer wavelengths with increase of distance from the wall in internal flows. The opposite

occurs in boundary layers, where outer-flow structures shorten very rapidly beyond the logarithmic region. Two explanations of this difference were suggested – first, the effect of the opposite wall in internal flows, and second the intermittency of the outer region in boundary layers.

The above-stated logarithmic velocity distribution (Eq.64) can be used to derive universal friction law for large Reynolds numbers (95). The corresponding equation is referred as to as the Prandtl universal friction factor equation for turbulent flow in smooth pipes

$$\frac{1}{\sqrt{f}} = 2.0\ log\left(\frac{\bar{u}d}{\nu}\sqrt{f}\right) - 0.8 \tag{68}$$

However, in most practical applications, especially at high Re, pipes cannot be considered as smooth. The roughness of walls generates friction additional to that determined by Eq.68. It changes the mean velocity profile near the wall, which leads to the modification of the friction coefficient.

If the height of the roughness elements (k) is comparable with the thickness of the viscous boundary layer (δ_0), the roughness modifies the hydrodynamic picture outlined in Fig.11(a) by interfering with the operation of the buffer-layer viscous cycle, and by completely destroying it when $k^+ \geq 50 - 100$.

The best known early experiments in this field were performed by Nikuradse (1933). He systematically studied flow in pipes roughened with carefully graded, closely packed sand. He found that the logarithmic velocity distribution for the mean velocity profile could be used in the wall layer. He expressed the velocity profile through the same value of the Karman constant as over smooth walls (Eq.67) and modified the additive constant A as

$$\frac{u}{u_*} = 2.44\ln(y/k_s) + 8.5 + \Pi\kappa^{-1}W(y/R) \tag{69}$$

This equation also defines the "equivalent" or "effective" sand roughness k_s, which can be assigned to surfaces with arbitrary roughness elements of height k, but which affect the flow in the same way as sand roughness with height k_s (95).

Two roughness types are distinguished based on the relationship between its height k and effective roughness k^+ (109). The surfaces for which k_s is proportional to the dimensions of the roughness elements in the fully rough limit ($k^+ \gg 1$), when viscosity is irrelevant, are called k-rough. For them the ratio k_s/k depends on the geometry of the roughness, and particularly on its surface density, for the quantification of which (95) introduced a parameter

called solidity λ. It was defined as the total projected frontal roughness area per unit wall-parallel projected area. Schlichting performed a set of experiments to test its effect, and identified two regimes: the sparse one with $\lambda < 0.15$, for which the effect of the roughness increases with the solidity, and the dense one for which it decreases because the roughness elements start to shelter each other. In the sparse region the extra roughness drag is proportional to the frontal surface of the roughness elements, and so $k_s/k \sim \lambda$.

The surface roughness for which effective roughness k_s is not proportional to the roughness height, but to the outer layer scale are called d-rough (110). Thus, in several boundary layers over plates that had been roughened with narrow spanwise square grooves the effective roughness was found to be

$$k_s \approx 0.02\delta_{BL}. \quad (70)$$

The d-roughness was suggested as a prospective way of constructing boundary layers with a single length scale (109). Since, as was shown above the complication of wall-bounded flows arises from the interplay between two independent length scales, the proportionality in Eq. 70 implies that d-type layers are determined only by outer scales and may be considered as pure core flows.

The grooves of d-roughened walls are roughly square, with a solidity $\lambda \approx 0.5$, which is the limit of complete mutual sheltering (Fig. 12). They are believed to sustain recirculation vortices that isolate the outer flow from the roughness. If grooves are wider than about 3 or 4 k the recirculation eddy reattaches ahead of the next rib exposing it to the outer flow. In this case wall behaves like k-type surfaces.

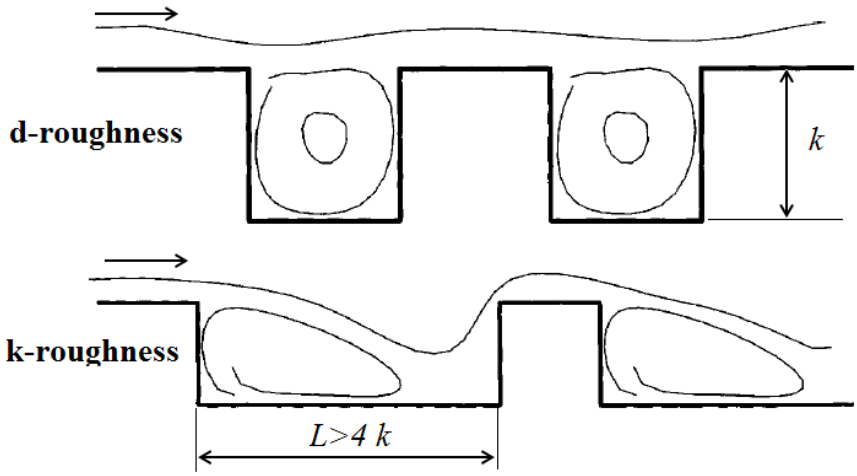

Figure 12: Geometry of k- and d-type slotted walls (109)

Fig.13 illustrates values of friction factors obtained by Nikuradse for sand-roughened pipes. It shows that in laminar flow friction is the same in smooth and rough pipes (line 1). In addition, it reflects three regimes of roughness manifestation in turbulent flows:

1) Hydrodynamically smooth regime: $0 \leq \mathrm{k}_s^+ \leq 5$ – all roughness elements reside within the viscous sublayer and friction factor depends only on the Reynolds number: $f = f(Re)$ (line 2, Eq.68). It was shown that the skin friction of the rough wall can be less than that of the smooth one for $\mathrm{k}_s^+ \leq 4$ (109). Even though, roughness elements are intuitively expected to generate more skin friction than smooth walls, some moderately rough surfaces can reduce drag (111), (112), (113). One of the examples is the flow over narrow grooves aligned with the mean flow. They can decrease drag by up to 10% (114). However, in most cases $\mathrm{k}_s^+ \approx 4$ is a lower limit below which the drag is the same as over a smooth wall.

2) Transitionally rough regime: $5 \leq \mathrm{k}_s^+ \leq 70$ – some of the roughness elements protrude from the viscous sublayer into the turbulent boundary layer and create additional skin friction owing to their form drag. In addition, they weaken the viscous generation cycle, which decreases skin friction. Friction factor is a function the roughness size and Re here: $f = f(k_s/R; Re)$.

3) Fully rough regime: $\mathrm{k}_s^+ \geq 70$ - all roughness elements protrude from the viscous sublayer. Most of the surface friction is due to their form drag and friction factor is determined only by the roughness size: $f = f(k_s/R)$. Therefore, the pressure loss in pipes becomes independent of viscosity in the fully rough limit. This independence was the first indication that something was wrong with the laminar theory and stimulated the development of the turbulence theory. Flows over smooth walls never become fully turbulent, and their theory is correspondingly harder.

Since in the fully rough regime most of the surface friction is due to the form drag of the roughness elements the friction factor follows a square law. Such a law was derived by von Karman based on his hypothesis of the similarity of the turbulent motion and logarithmic velocity distribution for a rough surface (Eq.69):

$$\frac{1}{f} = \left(2\log\frac{R}{k_s} + 1.74\right)^2 \tag{71}$$

here the additive constant on the right side was selected so as to give good agreement with Nikuradse's experimental data (in Fig.12).

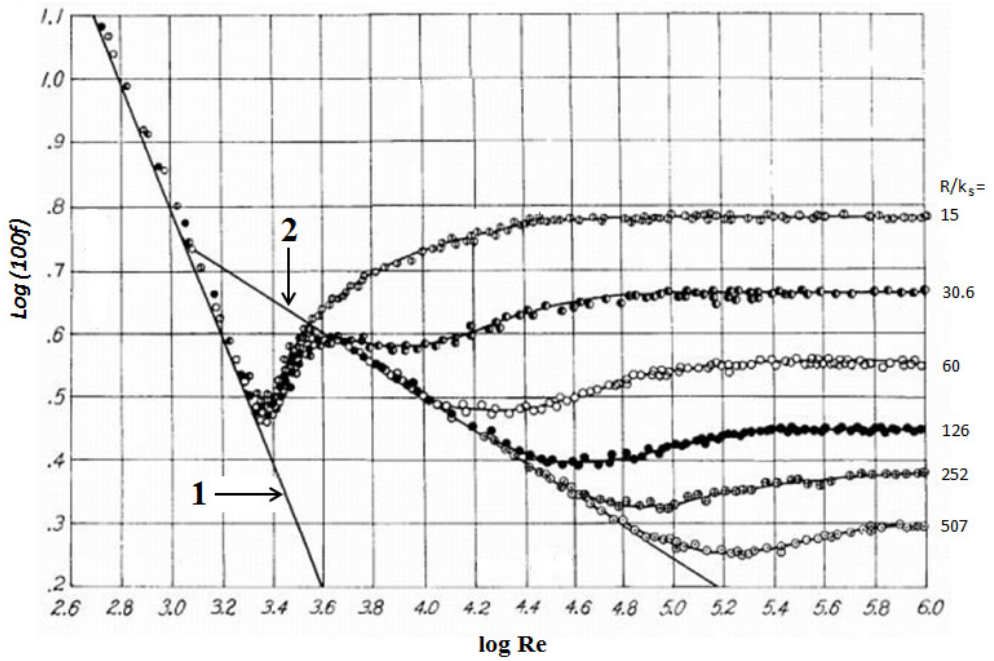

Figure 13: Friction factors for rough pipes measured by Nikuradse (95): 1- laminar flow, 2 – turbulent flow in smooth pipe (Eq.68)

The velocity profile over a rough surface in Eq.69 can alternatively be re-written as

$$\frac{u}{u_*} = \kappa^{-1}\ln(y^+) + A + \Pi\kappa^{-1}W\left(\frac{y}{R}\right) - \Delta\left(\frac{u}{u_*}\right) \tag{72}$$

where the first three terms represent flow over a smooth wall (Eq.67) and the offset term $\Delta\left(\frac{u}{u_*}\right)$, referred as the roughness function, accounts for the effect of roughness.

Fig.14 illustrates roughness function values for several surfaces in transitional regime as functions of the Reynolds numbers defined based on the equivalent sand roughness $k_{s\infty}^+ = k_{s\infty}u_*/\nu$ that corresponds to the surfaces skin friction in the fully rough regime at high Reynolds numbers (109).

Evidently, Nikuradse's (99) finding that the roughness function vanishes at $k_{s\infty}^+ \approx 4$ holds only for graded sand, whereas for industrial surfaces Colebrook (115) observed more a gradual transition.

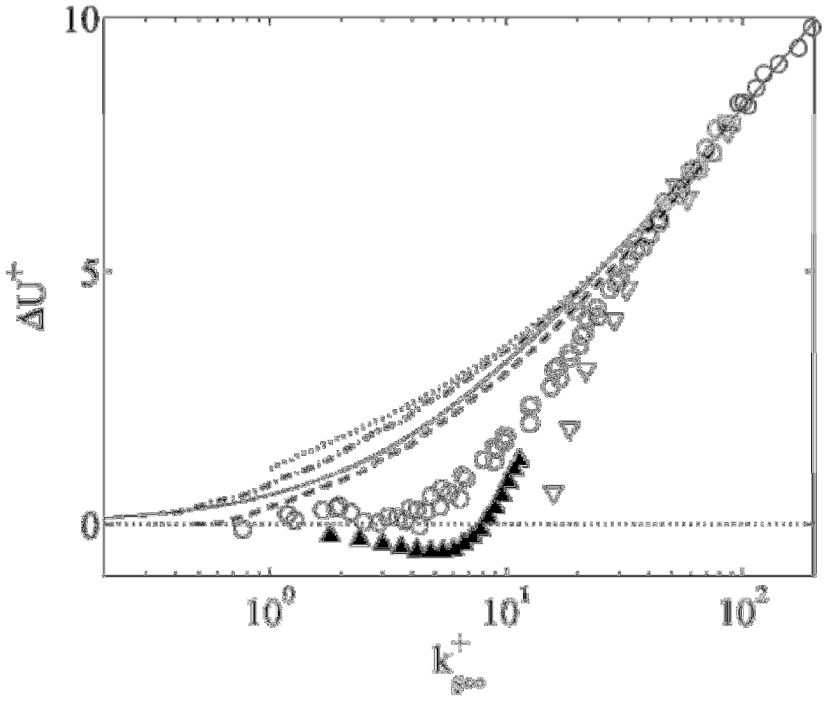

Figure 14: Roughness function in transitionally rough regime for (109): ○, uniform sand (99); , uniform packed spheres (116); ▲ triangular riblets (117); · · · · · ·, galvanized iron; – – – –, tar-coated cast iron; — · —, wrought-iron (115); ——, Eq. 73.

Colebrook obtained slightly varied results for different surfaces, but to simplify their practical use, he proposed an empirical interpolation formula:

$$\Delta\left(\frac{u}{u_*}\right) = \Delta u^+ = \kappa^{-1}\ln(1 + 0.26k_{s\infty}^+). \tag{73}$$

Moody (118) later used this equation to compute his skin-friction diagram for pipes.

Colebrook (115) explained the gradual build-up of the roughness effects in industrial pipes by irregularity in their roughness elements sizes – individual elements start to affect the flow when they reach some critical Reynolds number determined by their individual size. The gradual evolution of the roughness effect observed in Fig.14 for industrial surfaces is the sum of these individual transitions.

An implicit friction factor equation that combines correlations for smooth and rough walls was developed by Colebrook using the mathematical method suggested by White (115). For full-flowing conduits at $\mathrm{Re} > 4000$ it is defined as (95):

$$\frac{1}{\sqrt{f}} = 1.74 - 2\log\left(\frac{k_s}{R} + \frac{18.7}{Re\sqrt{f}}\right) \tag{74}$$

This equation is also applicable for the pipes with non-circular cross-section if radius R is replaced with the corresponding hydraulic radius

$$R_h = 2\,[cross - section\ area]\ /\ [wetted\ perimeter].$$

Eq.74 has a very good agreement with experimental data through entire transition region. When $k_s \to 0$ it gives Eq. 68 for a smooth pipe and for $Re \to \infty$ it yields Eq.71 for a fully rough pipe.

Due to its implicit nature Colebrook's equation (Eq.74) is usually solved numerically using the iterative method. A number of its approximate solutions were suggested (119). Thus, Serghides derived the following iterative procedure for finding friction factor in a full-flowing circular pipe (120):

$$f = \left(A - \frac{(B-A)^2}{C - 2B + A}\right)^{-2} \tag{75}$$

$$\text{where } A = -2\log\left(\frac{k_s}{14.8R} + \frac{12}{Re}\right);\ B = -2\log\left(\frac{k_s}{14.8R} + \frac{2.51A}{Re}\right);$$

$$C = -2\log\left(\frac{k_s}{14.8R} + \frac{2.51B}{Re}\right)$$

Eq.75 was found to match the Colebrook–White equation (Eq.74) within 0.0023% for a test set of ten relative roughness values (in the range from 0.00004 to 0.05) and seven Reynolds numbers (from 2500 to 10^8).

An interesting drag-reducing effect of streamwise riblets is reflected in Fig. 14 (solid symbols) (111). As it follows from the graph this is a transitional roughness effect. When riblets exceed $k^+ \approx 10$ they start to generate additional surface friction, and when $k^+ \gg 1$ they behave like regular k-surfaces.

Luchini, Manzo and Pozzi (121) showed that this particular drag-reducing mechanism is owing to the different effect of riblets on the spanwise and streamwise velocity fluctuations. In the limit $k^+ \ll 1$ the riblets offset the no-slip boundary condition for the spanwise velocity fluctuations further into the flow than for the streamwise ones. They concluded that this must move the quasi-streamwise vortices away from the wall, thicken the viscous sublayer and lower the drag. They also noted that drag of spanwise-mounted riblets should increase linearly with k^+.

Drag reduction by streamwise riblets is effectively a favourable combination of two effects of transitional regime: first, low form drag of flow aligned riblets and second weakening of the viscous generation cycle. This is eventually completely destroyed at higher k^+, and the savings from this effect saturate, and the form drag gradually builds-up.

For surfaces with sparsely distributed roughness elements the form drag contribution becomes significant before the viscous cycle is modified over most of the wall, and so the drag reduction is never realized. Therefore, surfaces with uniform roughness can be expected to provide the best opportunity for drag-reduction in this case.

Since most of the turbulent energy is generated within the logarithmic layer, roughness may also modify the whole flow if k is not negligible with respect to the outer layer scale (radius R for pipe flow or δ_{BL} thickness of the boundary layer). The direct effect of the roughness elements may extend to 2–3 k and so it was suggested that for the roughness not to affect directly more than half of the logarithmic layer its size must satisfy the relationship $R/k > 40$ (109). The effect of roughness extends across the entire wall region when $R/k < 50$ and such flows are better described as flows over obstacles.

Besides the effects of roughness discussed above other subtle mechanisms of its interaction with the near-wall flow were suggested. Thus, it was suggested that some rough walls may affect the whole boundary layer by modifying the form of the "hairpin" eddies generated near the wall, which in turn contribute to the growth of the outer-layer structures (122).

Outline of the present study

The detailed review of the fields relevant to the mineral scaling phenomenon presented in this chapter laid the foundation for further study of this problem. The first sections stated the importance of geothermal heat as a renewable energy source globally and in New Zealand. Some of the technological constraints on the effective development and utilization of geothermal resources were mentioned.

Mineral scaling, as one of these constraints and the subject of the present dissertation, was discussed in more detail. Particularly, the chemical and thermodynamic conditions which contribute to the onset and progression of silica scaling were discussed. The unfavourable effects it creates for the geothermal industry were also emphasised.

The preliminary mechanism of silica scaling, suggested based on the available experimental and theoretical data was outlined. The gaps in the present knowledge were identified. The

need for deeper understanding of a complex combination of the phenomena this process incorporates was argued as prerequisite for the development and continuing improvement of anti-scaling practices.

Specifically, while the chemical kinetics of silica polymerization and colloid formation are relatively well understood, transport of these colloids and their stability, which ultimately control their aggregation and attachment rates, on the other hand, remain unclear. Stability of geothermal colloidal silica and its dependence on the brine chemistry (pH, ionic content) and particle size are particularly vague.

In addition, it is unclear whether the theory of particle transport in turbulent flows discussed above gives a fair representation of silica transport during scaling process. Thus, Fig.10 above shows that the experimental scaling rate is three orders of magnitude lower than the one predicted theoretically. However, this difference may be due to high particle stability and, thus low attachment probability. The unknown particle stability has to be determined to answer this.

In addition, the theory predicts a decrease of the particle transport rate with an increase of the particle size whereas opposite is observed in the experiments.

Therefore it is hard to give the complete diffusion kinetic description of the scaling process – to answer whether it is controlled by transport or attachment of silica to a surface, whether transport is dominated by particle diffusion or inertia. Apparently, the answers to these questions depend on the set of conditions intrinsic to each individual set of chemical and hydrodynamic conditions.

The basic equations of the DLVO theory of particle stability, the kinetics of silica polymerisation and aggregation, the theory of mass and momentum transfer in turbulent flow presented in this chapter are used in the following sections to resolve these questions.

Moreover, the specific regularities of the interactions between the turbulent flow and a rough surface discussed above create the background for a pending explanation of the “rippled” surface structure of the silica scale.

Table 4 below shows how the information presented in this chapter was used throughout the dissertation.

Table 4: Use of Chapter 1 content throughout the dissertation

Data	Used in Chapters #	Purpose
Chemistry of geothermal waters (silica concentration, ionic strength and pH)	2	find monomeric and colloidal silica transport rates, DLVO stability of colloids
Silica polymerisation kinetics	2	calculate rate of the direct deposition
	3	analysis and development of the method for synthesis of colloidal silica solutions
Kinetics of Ostwald Ripening and aggregation	6	analyse observed evolution of particle size in synthesized colloidal solutions and evaluate experimental stability of these colloids
Mass transfer equations	2	find direct and colloidal silica transport rates
Relationships for near-wall velocity distribution and friction factor	2	calculate "normal to wall" mass transport rates
	6	evaluate rate of "tangential to wall" convection of particles onto a rough wall

2 THEORETICAL INVESTIGATION OF SILICA TRANSPORT AND DEPOSITION

This chapter presents results of analytical and computational fluid dynamics (CFD) calculations of colloidal silica deposition. Analytical solution of the convection-diffusion equation (67) was adopted to find the particle transport rate onto a smooth surface of the plate parallel to the flow, cylinder in a cross-flow and internal surface of circular pipe. No inertial effects or particle-particle/particle-wall interactions (i.e. no electrostatic repulsion) were considered in the first section.

Next, the energy of particle–particle and particle–wall interactions was evaluated with standard DLVO theory and combined with the analytical mass transfer calculations. As a result rates of the particle coagulation and deposition were obtained.

Finally, to evaluate the role of inertial particle transport the CFD simulations of particle transport onto a cylindrical collector was reported. As before, the repulsive particle-wall interaction forces were neglected. The analytical and CFD calculations of particle deposition were conducted for the same conditions as the available experimental data (43).

2.1 Silica transport rate calculation with boundary layer approximation

The steady diffusion mass transfer onto an infinite flat plate from turbulent flow can be determined by integrating the reduced Eq.44 for appropriate boundary conditions (Fig.7): silica concentration $C = 0$ at the surface and $C = C_0$ far from the surface. In this case the general expression for the particle flux (Eq.49) takes the form:

$$j = \left(D_{m;B} + D_T\right)\frac{\partial C}{\partial y} = const \tag{76}$$

here $D_{m;B}$ and D_T are molecular (or Brownian) and turbulent coefficients of diffusion for silicic acid or colloidal silica respectively.

The distribution of silica concentration in region II (Fig.7) can be determined by integrating Eq. 76 over this region of the turbulent boundary layer. Since the turbulent diffusion rate, which is much higher here than molecular or Brownian diffusion, can be determined from Prandtl's mixing length hypothesis Eq. 76 changes to

$$j = D_{turb}\frac{\partial C}{\partial y} = \beta_0 y^2 \frac{\partial U}{\partial y}\frac{\partial C}{\partial y} \tag{77}$$

here β_0 is a constant numerical coefficient. With known velocity distribution (Eq.64: $U = \alpha u_* \ln\frac{u_* y}{\gamma\nu}$) and boundary conditions for C integration of Eq. 77 for $\delta_0 < y < d$ gives silica concentration distribution in this range of wall distances (region II):

$$C_{II} = \frac{j}{\beta u_*}\ln\frac{y}{d} + C_0 \tag{78}$$

here $\beta = \alpha\gamma\beta_0$, a constant. The concentration decreases according to a logarithmic law in region II.

The molecular (or Brownian) diffusion is much faster than the turbulent in the innermost part of the viscous sublayer (region IV, in Fig.7), at $y < \delta$, so here expression for particle flux and its integral are:

$$\mathrm{j} = D_{m;B}\frac{\partial C}{\partial y} \text{ and } \mathrm{C_{IV}} = \frac{\mathrm{j}}{D_{m;B}}(y - R) \tag{78}$$

where R is an average particle radius in case of colloidal silica transport and $R=0$ for monomeric silica.

Due to gradual decay of turbulence within the viscous sublayer, mass transport by residual turbulent pulsations through the region III ($\delta < y < \delta_0$) is still stronger than mass transport by molecular/Brownian diffusion. It can be shown (67) that distribution of solute in region III can be found by integrating Eq.76 with the condition of concentration continuity ($\mathrm{C_{IV}} = \mathrm{C_{III}}$) at $y = \delta$:

$$\mathrm{C_{III}} = \frac{\mathrm{j}(\delta - \mathrm{R})}{D_{m;B}} + \frac{\mathrm{j}\delta_0^3}{3\gamma \mathrm{u}_*}\left(\frac{1}{\delta^3} - \frac{1}{\mathrm{y}^3}\right) \tag{80}$$

here γ is a certain numerical coefficient.

Now, continuity of concentration at $y = \delta_0$ i.e. $\mathrm{C_{II}} = \mathrm{C_{III}}$ gives expression for the flux (Eq. 81):

$$j = \frac{D_{m;B}C_0}{-\frac{D_{m;B}}{\beta u_*}ln\frac{\delta_0}{d} + \frac{\delta_0^3 D_{m;B}}{3\gamma u_*}\left(\frac{1}{\delta^3} - \frac{1}{\delta_0^3}\right) + (\delta - R)} \tag{81}$$

The unknown numerical constants β and γ were found experimentally to be of order of unity. The height of the diffusion boundary layer was determined above in Eq. 42:

$$\delta = \frac{\delta_0}{Sc^{1/4}\sqrt[4]{10}} \sim \frac{10^{3/4}\nu}{Sc^{1/4}\sqrt[4]{10}u_*} \tag{82}$$

For high values of the Schmidt number (e.g. Sc>10^3) equation for mass flux (Eq.81) simplifies to (Eq. 83):

$$j \approx \frac{D_{m;B}C_0}{\delta\left[\frac{4}{3}-\frac{1}{(10Sc)^{3/4}\beta}ln\frac{\delta_0}{d}\right]-R} \tag{83}$$

since $\delta \sim 0.1\delta_0$ and the second term in the denominator can be shown to be substantially smaller than the first, and can be neglected to further simplify Eq.83 to Eq.84:

$$j \approx \frac{\mathrm{D_{m;B}C_0}}{\frac{4}{3}\delta - \mathrm{R}} = \frac{C_0 u_*}{\alpha\, Sc^{3/4} - \frac{Ru_*}{\mathrm{D_B}}}, \tag{84}$$

where $\alpha = \frac{4}{3}\, 10^{3/4}$.

The maximum possible, e.g. not limited by the surface reaction rate, diffusion flux toward any surface can be found by integrating Eq. 84 for known bulk silica concentration, diffusivity (molecular for the dissolved and Brownian for the colloidal silica) and thickness of the boundary layer over this area.

In the case of diffusion to a circular cylinder with diameter Ø=A in a cross flow, when the boundary layer is laminar on the upstream part of its circumference and transitions to turbulent downstream from the separation line, the total diffusion flux to the cylinder surface was determined (67) as (Eq. 85):

$$j \approx \frac{196}{360}\frac{\pi A^2}{4}\frac{D_{m;B}C_0}{Sc^{3/4}}\left(\frac{U_0}{\nu A}\right)^{1/2} + \frac{164}{360}\frac{\pi A^2}{4}\frac{\sqrt{K_f}U_0C_0}{Sc^{3/4}} \tag{85}$$

where $\mathrm{U_0}$ is the velocity of undisturbed flow far away from the cylinder and $\mathrm{K_f} \approx \frac{0.27}{\mathrm{Re}^{0.1}}$ the cylinder drag coefficient.

Table 5 below presents the rates of monomeric and colloidal silica diffusion transport calculated with Eq. 85 for the conditions of the experiment (43): $\mathrm{U_0} = 1.96\ \mathrm{m/s}$ (average surface shear stress $\tau = 20$ Pa), A = 0.025 m, $\mathrm{C_{colloidal\ Si}} \approx \mathrm{C_{monomeric\ Si}} = 250$ ppm, average particle size $\mathrm{d_p} = 125$ mm and temperature T = 66 °C.

The monomeric (or direct) silica deposition was found experimentally to be very slow (43) and not responsible for the scale build-up. So, the calculated transport rate of the monomeric silica $\left(V_{dep}^{+} = 5 \cdot 10^{-5}, \text{see Table 5}\right)$ being about forty times higher than experimental deposition rate $\left(\text{see Experiment 2 in Table 5: } V_{dep}^{+} = 1.2 \cdot 10^{-6}\right)$ suggests that silica monomer deposition on the walls must be limited by the surface reaction of its absorption.

Table 5: Comparison of the experimental, analytical and simulation results

Method	Effects resolved	Dimensionless Dep. Velocity		Flow scenario
		Momomeric Si	Colloidal Si	
Field experiment 1 (25)	All		$\sim 2\times10^{-5}$	Reinjection pipeline (Wairakei, NZ)
Advection-diffusion simulations by Guha (Fig.10)	Diffusion& Inertia	-	10^{-3} 10^{-2}	smooth parallel wall rough parallel wall (d_p*=125 nm)
Analytical calculations with boundary layer approx. (Eq.84 and 93)	Diffusion & particle interactions	-	Transport: 9×10^{-5} Deposition: 3×10^{-11}	smooth parallel wall; (d_p=125 nm; K*=10^{-6})
Method of equally accessible surface (Eq.108 and 114)	Diffusion & particle interactions	10^{-10}	6×10^{-11}	Reinjection pipeline (d_p= 125 nm; K=10^{-6})
Field experiment 2 (43)	All	-	$1.2\pm0.5\times10^{-6}$	Cylinder in cross flow; (d_p= 125 nm)
Analytical calculation with boundary layer approx. (Eq.85)	Diffusion	5×10^{-5}	10^{-6}	Cylinder in cross flow; (d_p= 125 nm)
CFD simulation	Diffusion& Inertia	-	3×10^{-1}	Cylinder in cross flow; (d_p= 125 nm)

*** d_p - particle diameter, K – attachment probability**

Indeed, calculations of deposition rate that account for the surface reaction rate (rate of monomeric silica absorption on amorphous silica surface discussed in section 1.3.2) which are performed below in Section 2.3 show that it is much lower (10^{-10}) than calculated here transport rate.

The distribution of dissolved silicic acid in the flow thus must be near uniform (e.g. same at the wall surface and in the bulk flow) unless there is some non-transport reason for the concentration to vary with location (e.g. a thermal gradient).

The analytical rate of colloidal silica transport is within the uncertainty of the mean experimental value. Interestingly, Eq. 85 predicts transport rate to the downstream part of the

cylinder to be higher than to the upstream part. This correlates with the assumption made about the boundary layer state, but contradicts the experimental observation of thicker scale formed on the upstream side of the cylinder.

It is possible that inertial transport, not included in this analytical model, is responsible for this contradiction. CFD simulation of particle transport was performed to investigate the role of inertial mechanisms of particles transport. Its results are presented in the Section 2.3 after investigating effect of electrostatic interactions between particles and a wall on deposition rate.

2.2 Electrostatic and hydrodynamic aspects of particle stability and deposition

Being in continuous Brownian motion in addition to the motion induced by the suspending fluid, colloidal particles experience numerous mutual collisions and collisions with stationary walls. In the absence of any limiting factors each of these collisions would results in close contact between particles followed by chemical bonding and agglomeration or attachment to the wall surface. This process is called fast, or rapid, aggregation (deposition) as it results in all colloidal particles being separated from the solution in a matter of minutes.

However, depending on the solution pH, silica colloids can carry uncompensated surface charge due to ionization of the surface silanol groups. The presence of charge of the same sign on all particles, and on wall surfaces covered with amorphous silica, results in an electrostatic potential barrier (Fig.15) which particles need to overcome to form the bond. Due to this so called electrostatic stabilization, not all collisions of the particles lead to aggregation or particle attachment to the surface. Thus a process of slow aggregation, or deposition, takes place. Under the right conditions charge stabilized colloidal systems can be stable for very long periods of time (years).

The potential barrier between charged particles is usually so high (in terms of potential energy) and wide (in terms of distance of approach) that individual particles are unable to pass it in one attempt – they lose all kinetic energy obtained in separate Brownian projections due to friction with surrounding liquid (viscous interaction) well before they clear the potential barrier. Instead the particles overcome the barrier in a sequence of Brownian collisions.

Therefore, the effect of particle interactions can be represented as an additional diffusion process (53). This was effectively done in Eq. 21 by introducing an expression for particle flux induced by particle interactions:

$$j_{DLVO} = \frac{C}{B}\frac{dV_t}{dy}, \tag{86}$$

where C is local particle concentration, B is the friction factor and V_t is total interaction potential, which equals sum of the attractive and repulsive potentials. Fig. 15 illustrates values of the potential V_t for particles of different diameters interacting with a flat plate. They were calculated with Eq.22, which represents standard DLVO theory (68), (69). Since Eq.22 b and c represent interaction of two spherical particles their RHS must be multiplied by 2 in order to correspond to the sphere-flat plate interaction case. Thus, based on the standard DLVO theory, the magnitude of interaction potential in particle-flat wall collisions is expected to be twice as high as in particle-particle collisions. The surfaces of the particle and plate were assumed to have the same values of zeta potential $\zeta = -30$ mV, and a solution ionic strength of IS = 40 mM which are typical for some geothermal brines (25).

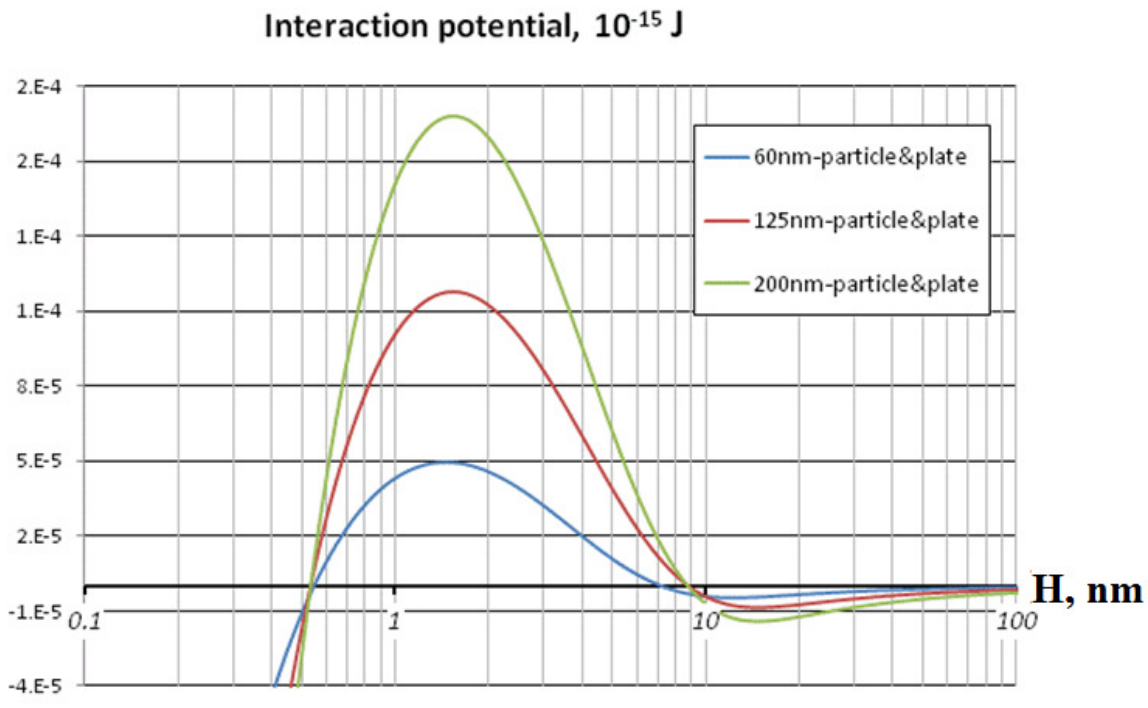

Figure 15: DLVO interaction potential V_t as function of particle-flat plate separation distance H, nm

The aggregative stability in the simplest case of a stagnant suspension, when the rate of particle-particle collisions is determined only by Brownian motion and electrostatic potential was determined above in Eq.26:

$$W_{p-p}^{stg.} = 2 \int_{-2R}^{\infty} e^{\frac{V_t}{k_b T}} \frac{dH}{H^2}$$

The stability of a flowing colloidal solution is of great interest for many applications, including the problem of mineral scaling. The rate of flow-induced, or orthokinetic, particle collisions can be much higher than in a stagnant solution due to the presence of velocity gradients and turbulent pulsations. The number of particle-particle collisions per second per unit volume can be calculated with Eq.25a, 35 and 36 given above:

Brownian encounters: $N_{Brwn} = 16\pi D_p d_p n_0^2$

Gradient encounters: $N_{Grad.} = \frac{16}{3} G d_p^3 n_0^2$

Turbulent encounters: $N_{Turb.} = \frac{1}{2} \nu \frac{Re^{3/2}}{L^2} d_p^3 n_0^2$

Here, as before, D_p is the particle diffusivity, d_p its diameter, n_0 the number of particles per unit volume, G is the velocity gradient, Re the Reynolds number, ν the kinematic viscosity and L the characteristic length of the flow.

These numbers were calculated for the conditions of the experiment (43) and presented in Fig. 16 as functions of particle size. The total suspended mass of colloidal silica was assumed constant in these calculations. This means that particle number concentration n_0 decreases with increasing particle size.

The value of velocity gradient is normally the highest in boundary layers. Here it can be estimated as (67):

$$G \sim \frac{u_*}{\delta_0} = \frac{u_*^2}{\nu} = \frac{\tau}{\mu} \qquad (87)$$

where τ is the surface shear stress and μ is the dynamic viscosity of the solution.

In Fig.16 the broken blue line was obtained for the velocity gradient $G = \frac{50\ \text{Pa}}{4.4 \cdot 10^{-4}\ \text{Pa·s}} = 1 \cdot 10^5\ \text{s}^{-1}$. This corresponds to the maximum surface shear stress of 50 Pa observed in turbulent flow around a cylinder in experiment (43). The number of turbulent collisions (dotted red line in Fig.16) was calculated for $\text{Re} = 1.09 \cdot 10^6$.

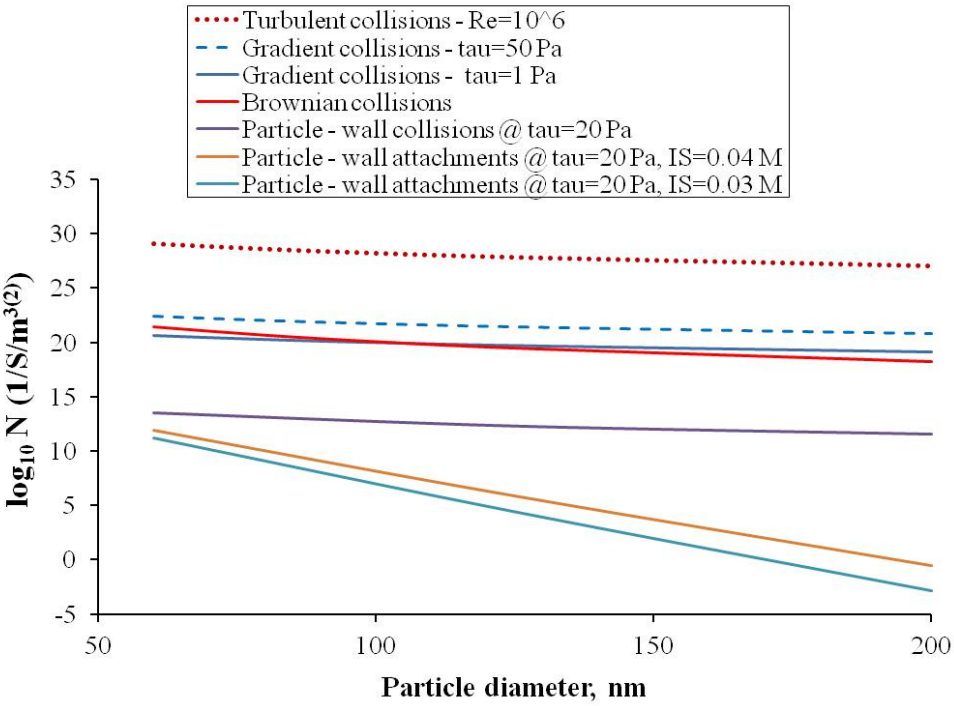

Figure 16: Rates of idealized collision processes

Trends in Fig.16 show that the number of turbulent and gradient encounters can be several orders of magnitude higher than those due to Brownian motion. The difference in slopes of the curves in Fig. 16 indicates a slower decay of the rate of gradient and turbulence induced collision with increasing particle size than for the Brownian collisions.

The inclusion of the gradient and turbulent collisions into the calculation of the aggregative stability of colloidal system poses significant theoretical difficulties. The steady-state convection-diffusion equation (Eq.22):

$$j_{slow} = j_{Brwn} + j_{DLVO} + j_{adv} = 8\pi D_p r^2 \frac{dC}{dr} + 4\pi r^2 \frac{C}{B}\frac{dV_t}{dr} + C\,\bar{U}_{pr}^{c} \qquad (88)$$

with electrostatic particle interaction and advective particle transport (second term on the RHS of Eq.49) terms having to be resolved on the particle size length scale to find the total number of particles reaching the surface of the selected centre particle.

In this case the basic equation cannot be simplified by using the boundary layer approach (as was done to find mass flux to a flat wall, Eq. 84). The thickness of the diffusion boundary layer on the particle is comparable with its size. Thus, inertial effects of the particle's relative motion due to the velocity gradients in mean flow and turbulent pulsations may significantly affect the mass transfer rate.

However, this problem can be reduced down to the problem of stability in Brownian collisions if electrostatic interactions can be assumed not to affect the rates of particle advection significantly. In this case the advective flux of particles is the same irrespective of the electrostatic interactions, and as such it can be replaced with some equivalent diffusive transport. This equivalent diffusive particle transport must take place not within entire region of space (with C = 0 at r = R) but only down to a certain distance from particle surface at which interaction potential cannot be neglected any more. Effectively this additional diffusion can be accounted as a higher bulk concentration of particles in Eq.25 a and b. Since the bulk concentration of particles does not affect stability (Eq.26) the same must be true for the orthokinetic collisions – the fact of their occurrence should not change stability of the colloids. Therefore, the aggregative stability can be expected to be the same in peri- and orthokinetic particle collisions.

The additional particle flux due to the electrostatic interaction (Eq.86) can be included into the problem of particle transport towards a smooth wall. Doing this will allow calculation of the deposition stability of the colloidal solution.

First, the stability of the particle-plate collisions in a flowing solution is determined. In order to simplify the analysis the region of significant inter-particle interaction was assumed to lie entirely within the diffusion boundary layer. This is true for the conditions of the experiment (43). The thickness of diffusion boundary layer was 300-2000 nm in that case, whereas as can be seen from Fig.15, interaction potential can be neglected at separation distances above 50 nm. This assumption is violated only in very fast flows – at shear velocity of about 0.5 – 1 m/s which corresponds to flow rate of 150-300 l/min in NB15 pipe or 16-32 $\cdot 10^3$ t/hr in a 24" pipeline. In addition, the target surface was assumed to carry uniform charge of the same sign and magnitude as silica colloids suspended in the solution. Physically this corresponds to deposition onto an ideally smooth amorphous silica surface.

In line with these assumptions the additional particle flux due to DLVO interactions (Eq.86) can be combined with the diffusion particle flux (Eq.79) to give a total steady-state particle flux through the diffusion boundary layer on a flat plate (region IV in Fig. 7):

$$j_{slow} = D_B \frac{\partial C}{\partial y} + \frac{C}{B}\frac{dV_t}{dy}, \tag{89}$$

Eq.89 can be integrated using same procedure as was used to derive Eq.25. This for the following boundary condition

$$C = 0 \ for \ y = R \tag{90a}$$

$$C = C_\delta , V_t = 0 \ for \ y = \delta \tag{90b}$$

the rate of particle deposition from turbulent flow onto a flat, ideally smooth amorphous silica surface is:

$$j_{slow} = \frac{D_B C_\delta}{\int_\delta^R e^{\bar{V}_t} dy}, \tag{91}$$

In obtaining this flux the particle concentration at the outer edge of the diffusion boundary layer ($y = \delta$) was assumed constant and equal to C_δ. Therefore, Eq.80 for particle concentration distribution in region III in this case takes form

$$C_{III} = \frac{j_{slow}}{D_B} \int_\delta^R e^{\bar{V}_t} dy + \frac{j_{slow} \delta_0^3}{3\gamma u_*} \left(\frac{1}{\delta^3} - \frac{1}{y^3} \right) \tag{92}$$

The particle flux j_{slow} can now be found by using the condition of concentration continuity at the upper edge of the viscous boundary layer ($y = \delta_0$: $C_{III}(\text{Eq. } 92) = C_{II}(\text{Eq. } 79)$). Therefore, after simplifying the result in the same way as with Eq. 84, the flux of interacting particles onto a flat plate from flowing suspension can be shown to be (Eq. 93):

$$j_{slow} = \frac{D_B C_0}{\int_\delta^R e^{\bar{V}_t} dy + {}^{\delta}/_{3}} \tag{93}$$

where δ is the diffusion boundary layer thickness (Eq. 82), R is particle radius, $\bar{V}_t = \frac{V_t}{kT}$ is the ratio of electrostatic interaction potential and molecular thermal energy.

The ratio of j_{fast} (Eq. 84) and j_{slow} (Eq. 93) determines the stability, and thus attachment probability, of the colloids in deposition onto smooth surface from flowing suspension (Eq. 94):

$$W_{p-w}^{fl} = \frac{3 \int_\delta^R e^{\bar{V}_t} dy + \delta}{4(\delta - R)} \tag{94}$$

The numbers of particle collisions and attachments with 1 m^2 of flat plate per 1 s for the variable particle size, shear stress $\tau = 20$ Pa, colloidal silica concentration $C_{\text{colloidal Si}} \approx 250$ ppm and T=66 °C are also plotted in Fig.16. They were calculated by dividing mass fluxes (Eq.84 and Eq.93) by corresponding average particle mass m_p. The graphs show that the rate of particle collisions with a wall is at least seven orders of magnitude smaller than the

rate of particle-particle collisions in bulk for the same conditions and rate of their deposition even lower.

Next, the stability of the particle-plate collisions in a stagnant suspension has to be found for comparison with the result for flowing suspension (Eq.94) and will presumably help understand the hydrodynamic effects on colloid stability reflected in Eq.93.

In this case, the rate of slow deposition can be found by following the same procedure as in derivation of Eq. 25 and 91. Since there are no hydrodynamic mechanisms that provide constancy of particle concentration at a certain distance from the plate the transport of particles within the entire region of interest is due to Brownian diffusion and electrostatic interactions. Thus, Eq.89 must be integrated for the different boundary conditions:

$$C = 0 \; for \; y = R \tag{95a}$$

$$C = C_0 \, , V_t = 0 \; for \; y \to \infty \tag{95b}$$

The integration can be shown to give a steady-state particle flux towards a plate in presence of the particle-wall interactions ($\bar{V}_t$) (similar to Eq.91):

$$j_{slow} = \frac{D_B C_0}{\int_{\infty}^{R} e^{\bar{V}_t} dy}, \tag{96}$$

Analytical determination of the diffusion flux of non-interacting particles from a semi-infinite space onto a flat surface is more complex than the previously considered cases. In this case there is also no particle interaction potential which allow the problem to converge at the infinity and so the transport is determined solely by Brownian diffusion. This problem does not have steady-state solutions since the process of diffusion in semi-infinite space is transient by nature. Therefore, instead of the reduced particle flux equation ($\nabla \bar{j} = 0$) the full diffusion equation (Eq.44) must be integrated for boundary conditions (Eq.95):

$$\frac{\partial C}{\partial t} = D \, \Delta C \tag{97}$$

Solutions can be obtained with methods of Fourier or Laplace transform. The corresponding transient concentration distribution and flux can be shown to be (123):

$$C = C_0 erf\left(\frac{y}{\sqrt{\pi D t}}\right) \tag{98}$$

$$j_{Brwn.} = -D_B \frac{\partial C}{\partial y} = \frac{D_B C_0}{\sqrt{\pi D_B t}} \tag{99}$$

This time-dependent solution is not very practical in present analysis – it cannot be compared with the previous steady-state solutions.

However, the stability of particles that deposit from a stagnant solution onto a flat plate can be found as a ratio of the time-dependent fluxes towards a plate with and without presence of the particle-wall interactions (Eq.99). In order to find the time-dependent flux of interacting particles onto an infinite plate Eq.100 with an additional DLVO term (Eq.86) must be solved for the appropriate boundary conditions mentioned above in Eq.95:

$$\frac{\partial C}{\partial t} = D_B \frac{\partial}{\partial y}\left(\frac{\partial C}{\partial y} + \frac{\mathrm{n}}{\mathrm{kT}}\frac{\partial \mathrm{V_t}}{\partial \mathrm{y}}\right) \tag{100}$$

Stability curves obtained with equations 26 and 19 for 60 nm, 125 nm and 200 nm diameter particles are illustrated in Fig. 17. The solution ionic strength was varied from IS = 10^{-3} M to IS = 10^{-1} M and surface shear stress values from effectively zero (in stagnant flow) to 20 Pa were tested. All integrals of natural exponential functions in these equations (and in Eq. 93 and 96 for particle fluxes) were evaluated numerically since the exponential power, interaction potential V_t, is also a complex function of coordinate y.

The colloid stability *W* in every collision scenario decreases with increasing ionic strength of the solution and with decreasing particle size *d*. Only 1 in 10^{10} collisions result in particle coagulation/deposition in silica sols with sufficiently low ionic content.

It is evident from a comparison of the solid and dashed lines in Fig.17a that particle-particle collisions are less stable (more likely to result in bonding) than collisions of the particles of the same size with a flat plate. Therefore, the idealized particle-wall collisions modelled here are less likely to result in binding than particle-particle collisions. This is due to the electrostatic potential for particle-flat plate interactions being twice as high as that for particle-particle interactions.

In addition, as reflected in Fig.16 the rate of particle-particle collisions even in stagnant sol is at least 5 orders of magnitude higher than rate of particle-flat wall collisions in flowing sol. Thus, based on the theoretical prediction of higher frequency of particle-particle collisions and their lower stability the particle aggregation in solution is expected to be much faster than their deposition onto a smooth surface.

Fig. 17 b illustrates effect of the surface shear stress on stability values calculated with the Eq. 93 for three particle sizes and two solution ionic strengths. The observed slow decrease of stability at lower values of shear stress (thicker boundary layer, slower flow) for the most part

is caused by faster decrease of the "fast" surface particle flux (Eq. 83) at higher diffusion boundary layer thickness if compared to its "slow" counterpart (Eq. 92).

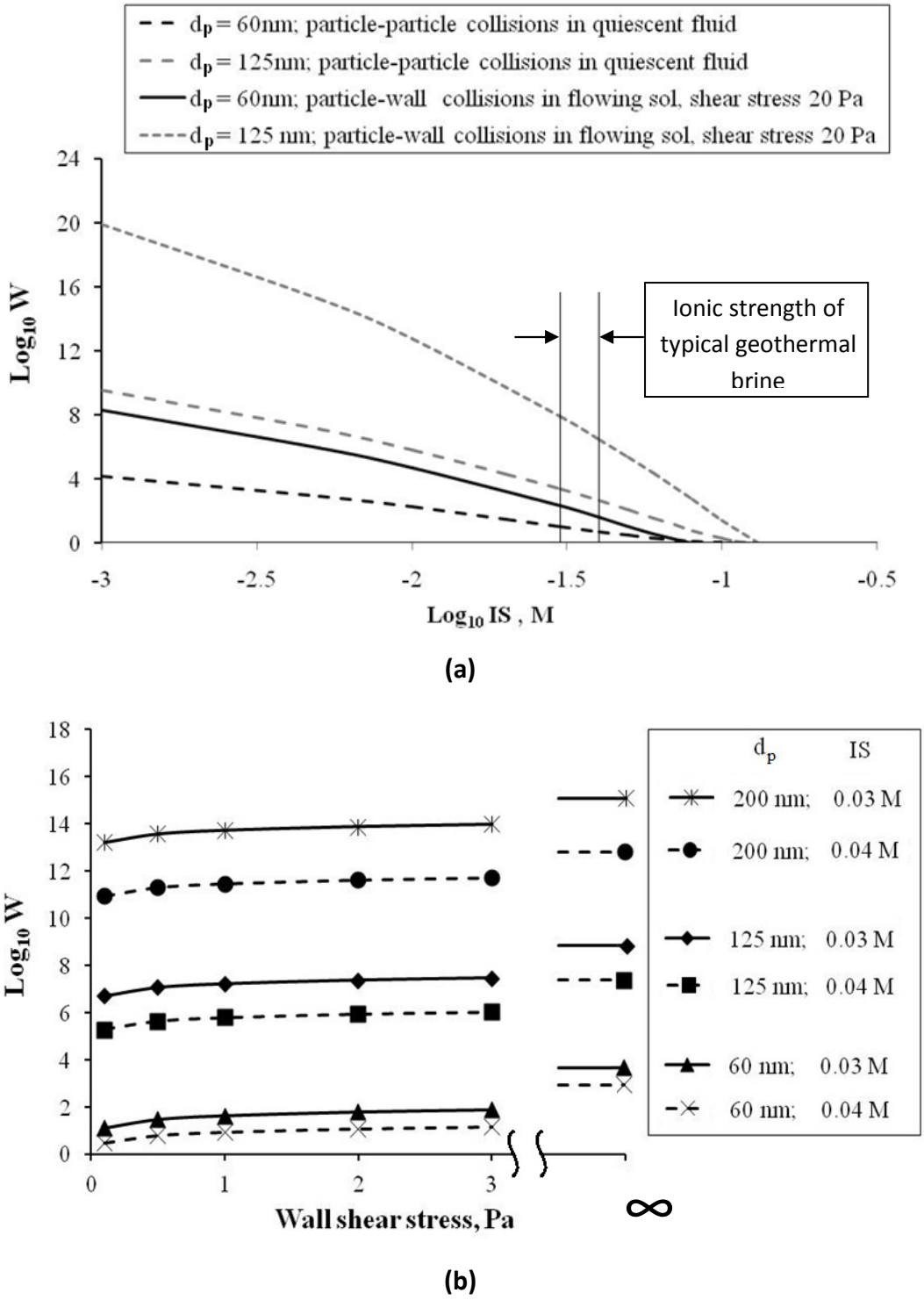

Figure 17: DLVO stability of colloidal silica as function of (a) chemical and (b) hydrodynamic conditions

An asymptotic analysis of the stability in Eq.94 shows that:

$$if\ Wall\ shear\ stress\ \rightarrow 0\ (\delta \rightarrow \infty)\ \ \text{then}\ \ W \rightarrow 1/4 \tag{101}$$

$$if\ Wall\ shear\ stress\ \rightarrow \infty\ (\delta \rightarrow 0)\ \ \text{then}\ \ W \rightarrow \mathrm{f}(\mathrm{d_p}, \mathrm{IS}). \tag{102}$$

The stability being smaller than unity in the limit of quiescent fluid (Eq.29) suggests acceleration of deposition by interaction forces which is unlikely for the type of potentials considered (Fig.15). Moreover, the stability is expected to depend on the properties of the colloidal system and cannot be constant. Thus, Eq.94 is inapplicable for deposition from quiescent fluid and Eq.100 must be solved instead.

It is obvious that particle interactions force extend beyond the diffusion boundary layer in the opposite limiting case of infinite shear stress (Eq.102) and the assumption made at the start of this analysis does not hold. Nevertheless, it is interesting that in this limit Eq.94 yields values for stability that depend on particle size and IS. These asymptotic values, plotted in Fig.17 b, presumably represent the maximum possible values of colloid deposition stability (as a function of hydrodynamic conditions).

However, orthokinetic collisions – due to turbulent pulsations and flow gradients – are expected to contribute significantly to the total rate of particle-wall collisions in limit $\delta \rightarrow 0$. Therefore, same as for particle-particle collisions they can affect deposition stability. Investigation of this effect, as well as the effect of surface roughness on attachment probability, requires a more complex approach than that presented here and presents a possibility for future study.

The rate of "slow" particle deposition (Eq. 93) decreases rapidly with increasing particle size. This is due to increase of the potential barrier observed with particle size increase (Fig.15). For the larger particles and moderate shear stresses typical for geothermal applications ($\tau = 1\ to\ 30\ Pa$) the first term in the denominator of the Eq. 93 is significantly higher than the second. This means that, in these particular conditions, mass transfer to the wall is more severely limited by the inter-particle potential barrier than by the advection-diffusion particle transport.

Transport of particles towards the surface can limit the deposition rate in case of very slow flow speeds and small particles, when convective diffusion rate and particle stability are low. The graph in Fig. 18 represents values of particle diameter (d_p) and surface shear ($\tau = u_*^2/\rho$, in water at 66°C) for which the two terms in the denominator of Eq.93 are equal. Thus, in

region to the right of the line, the first term, which represents deposition resistance due to particle interactions and which is an inverse of attachment efficiency, is larger than second term of the particle transport resistance and the rate of deposition is controlled by attachment. Conversely, to the left of the line the rate of deposition is controlled by the transport. The range of shear stresses encountered in geothermal power plant is indicated.

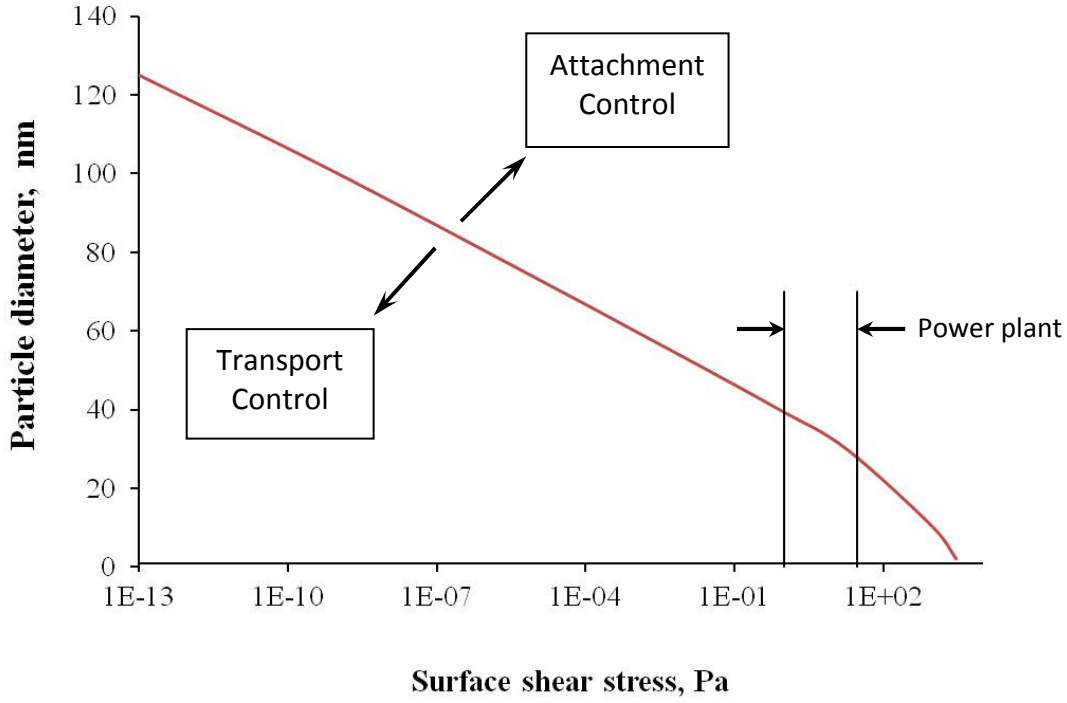

Figure 18: Regions of domination of attachment (standard DLVO based) and transport (using the boundary layer approach) process in deposition of colloids onto a smooth flat plate

The simplified analysis of silica colloid deposition onto flat smooth amorphous silica performed in this section was based on the standard DLVO theory of particle stability and the boundary layer approximation. It suggests that for the hydrodynamic conditions typical for geothermal power plants silica scaling is controlled by mass transfer processes if colloidal particles are less than about 40 nm in diameter. Particles larger than 40 nm in diameter have sufficient stability that no practical change of the flow conditions would affect the deposition significantly: only changes in chemical conditions can control deposition.

The dimensionless velocities (defined in Eq.47) for the fast and slow deposition of colloidal particles onto flat, smooth surface were calculated with the relationships established above (Eq. 84 and 93). They are illustrated in Fig.19 as functions of dimensionless particle relaxation times.

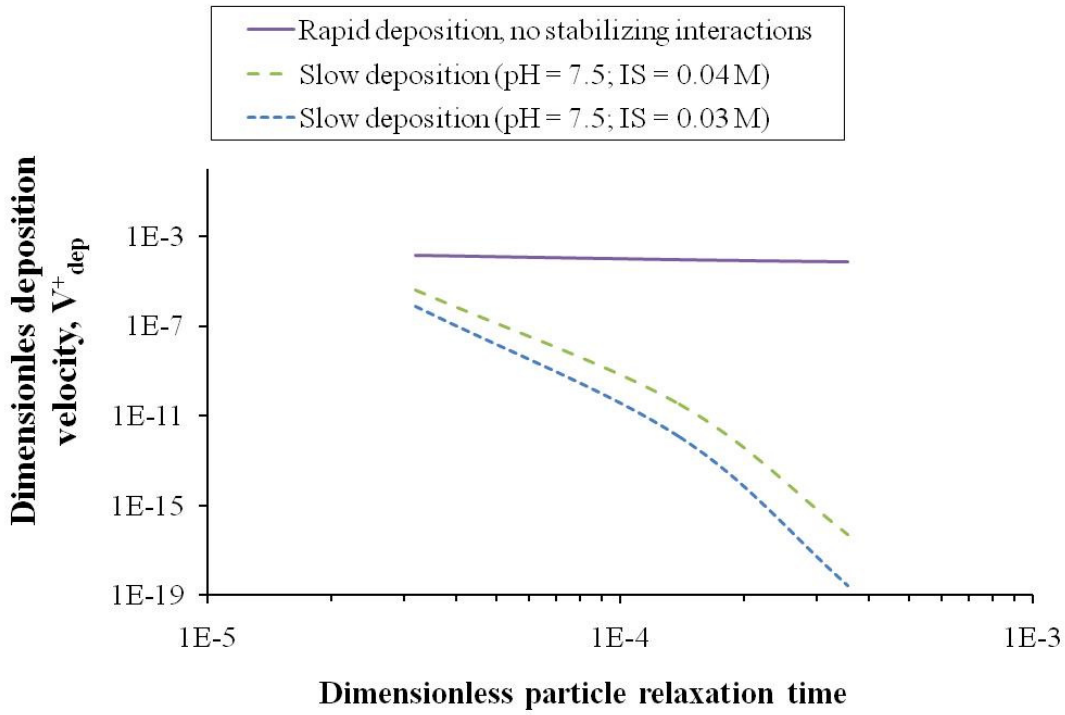

Figure 19: Theoretical dimensionless deposition velocity (Eq.83 and 92) as function of dimensionless particle relaxation time process and solution ionic strength

The magnitude of the rapid deposition shown here is of the same order of magnitude as theoretical result obtained by Guha ((86): $V_{dep}^{+} = 10^{-3}$ for dimensionless particle relaxation time $\tau_p^{+} = 10^{-4}$; Fig.10) and it also slowly decreases with increasing relaxation time. The predicted rate of the slow deposition on the other hand is much smaller than corresponding experimental value obtained by (43) (also in Fig.10): about 10^{-11} derived here against about 10^{-6} measured for the same conditions. Part of this discrepancy can be contributed to the increase of particle transport rate onto real surfaces by their roughness. As mentioned above transport of particles onto a rough wall can be up to 3 orders of magnitude higher than onto a smooth one.

Moreover, increase of the theoretical stability with increase of particle size and corresponding rapid decrease of deposition rate predicted here contradict experimental observation of increase of the scaling rate with particle size.

Therefore, comparison of the present and previous theoretical and experimental results suggests that implemented theoretical approach either underestimates particle transport rate or overestimates particle stability. Both possibilities are explored in this dissertation.

2.3 Analysis of diffusion and kinetics of silica scaling using the method of equally accessible surface

The role of diffusion and chemical kinetics in silica scaling can be accessed with a simplified method developed by Frank-Kameneckii (82). It is known as method of equally accessible surface. It assumes independence of diffusion from the surface reaction kinetics. Particularly every part of the reaction surface is assumed to be equally accessible to diffusion. The solutions of the steady-state diffusion equation for simplified boundary conditions (i.e. C=0) and empirical data can be used with this method to describe deposition process.

With these assumptions balance of the silica reacting (bonding) on the surface and silica transported to the surface can be expressed as:

$$j_{Adv+Diff} = \beta(C_0 - C_s) = kC_s \tag{103}$$

here $\beta = \frac{Sh\ D}{L}$ is a mass transfer coefficient, C_s is silica surface concentration and dimensionless Sherwood number, for instance, for a turbulent pipe flow can be found with Sieder-Tate correlation (124):

$$Sh = 0.26\ Re^{0.8}Sc^{1/3} \tag{104}$$

Eq. 103 gives expression for surface concentration C_s

$$C_s = \frac{\beta C}{k+\beta} \tag{105}$$

mass flux can be expressed through the bulk concentration C_0 and effective rate of reaction k^*

$$j_{Adv+Diff} = \frac{\beta k}{k+\beta} C_0 = k^* C_0 \tag{106}$$

Frank-Kameneckii (82) noted that Eq.106 simplifies if one of the parameters, β or k, is much greater than the other one. Thus, for $k \gg \beta$ effective rate of reaction is completely determined by mass transfer $k^* \cong \beta$ and concentration of reactant (silica in our case) on a surface is much lower than in the bulk: $C_s = \frac{\beta}{k} C_0 \ll C_0$. In the opposite limiting case of $k \ll \beta$ total reaction rate is fully governed by the true chemical kinetics of the surface reaction and concentration on surface is the same as in bulk: $k^* \cong k$, $C_s \cong C_0$.

Now let us consider deposition of monomeric silica in 24" pipeline at Re = $4.5 \cdot 10^6$. The surface reaction rate can be assumed equal to the rate of monomeric silica absorption on

amorphous silica surface ($k_{\text{Si monomer}} = 5.6 \cdot 10^{-10}$ m s^{-1} at pH 7.3) and the mass transfer coefficient can be found with the stated above relationships (Eq.104):

$$\beta = \frac{Sh\ D}{L} = \frac{0.26\ Re^{0.8} Sc^{1/3} D}{24"} \Longrightarrow \beta_{\text{Si monomer}} = 5.4 \cdot 10^{-4}\ (ms^{-1}) \tag{107}$$

Therefore, deposition of monomeric silica for the stated conditions is controlled by the chemical kinetics of surface reaction and deposition rate can be calculated as:

$$j_{\text{Adv+Diff}}^{\text{Si monom.}} = k_{\text{Si monomer}} \cdot C_0 \tag{108}$$

and for a monomer concentration of C_0 = 250 ppm (~0.25 kg/m3) this yields

$$j_{\text{Adv+Diff}}^{\text{Si monom.}} = 1.4 \cdot 10^{-10} (\text{kg m}^{-2}\text{s}^{-1}) \tag{109}$$

Since the rate of the silica absorption is highly dependent on solution pH the rate of monomer deposition can change with pH. In acidified brine at pH 5-6 the rate of surface reaction of silica monomer absorption, and thus the total deposition rate, can be several orders of magnitude lower than the values above. In addition, once absorption of silica monomers starts to be limited by amorphous silica surface rearrangement the overall rate of silica scaling by monomer deposition becomes even slower.

Next, analysis of diffusion and kinetics of colloidal silica deposition is performed in a similar way. For the same hydrodynamic conditions as above mass transfer coefficient for colloidal silica with average particle diameter of 125 nm can be calculated with Eq.107:

$$\beta_{\text{Si colloid}} = 4.3 \cdot 10^{-5} (ms^{-1}) \tag{110}$$

The corresponding Brownian diffusion coefficient ($D_{Br}^{Si} = 2.3 \cdot 10^{-11} m^2 s^{-1}$) was used instead of the molecular diffusion coefficient to find this value.

Even though attachment of colloidal particles to a surface has different physical mechanism from absorption of individual silicic acid molecules the balance of transport and attachment of colloids to a wall can be written in form similar to Eq.103:

$$j_{\text{Adv+Diff}}^{\text{Si colloid}} = \beta_{\text{Si colloid}} (C_0 - C_s) = k_{\text{Si colloid}} C_s \tag{111}$$

In this case right hand side of this equation represents the total mass of particles that collide with and attach to a unit surface area per unit time. It can be estimated by finding the number of particles contained within a distance short enough to be covered in their Brownian motion over time t = 1s. This distance is taken equal root mean square particle displacement (81):

$$x_{rms} = \sqrt{2D_{Br}^{Si}t} \tag{112}$$

Only half of the particles within this distance from the wall travel in a direction towards it and amongst them only small part, determined by attachment probability derived earlier ($K = 1/W$, Eq.26), actually attach to it. Therefore, the effective "surface reaction" rate for colloidal silica in Eq.111 can be expressed as

$$\mathrm{k_{Si\ colloid}} = \frac{1}{\mathrm{W}}\frac{x_{rms}}{2\mathrm{t}} = \frac{1}{\mathrm{W}}\sqrt{\frac{D_{Br}^{Si}}{2\mathrm{t}}}\ (\mathrm{ms^{-1}}) \tag{113}$$

or, once evaluated for the known diffusivity (D_{Br}^{Si}) and stability value of W=10^6 (Fig.17):

$$\mathrm{k_{Si\ colloid}} = 3.4 \cdot 10^{-11}\ (\mathrm{ms^{-1}}). \tag{114}$$

which is much lower than the corresponding mass transfer coefficient (Eq.110).

Therefore, total deposition rate of 125 nm diameter colloidal silica with concentration $C_0 = 0.25\ kg/m^3$ in a geothermal reinjection pipeline is controlled by its attachment to the walls:

$$\mathrm{j_{Adv+Diff}^{Si\ colloid}} = \mathrm{k_{Si\ colloid}} \cdot C_0 = 8.4 \cdot 10^{-12}(kg\ m^{-2}s^{-1}). \tag{115}$$

The approximate analysis of the diffusion and kinetics of silica scaling process conducted herein suggests that for the selected conditions (pH=7.3, Re=10^6 and 125 nm particles) the deposition rate for monomeric silica is two orders of magnitude higher than that for colloidal silica. The lower reaction rates at lower pH typical for the treated geothermal brine can decrease the rate of deposition of silica monomers. However, this still cannot explain experimental observation of much higher scaling rates from silica colloids. In addition, the total deposition rate, from monomers and colloids (Eq.109 plus Eq.115), predicted with this simplified method is at least three orders of magnitude smaller than experimentally observed scaling rate (Table 2).

The simplifying assumptions regarding particle transport and attachment employed in this analysis must be responsible for the disagreements. Indeed, the effects of particle inertia and surface roughness, neglected here, can significantly accelerate particle transport to a wall. The value of the attachment probability used here was derived with standard DLVO theory of particle interactions. It may be correct for some certain condition, but is known to deviate from the real situation significantly as solution pH, ionic strength and particle size change (see Section 6.1).

2.4 CFD simulations of particle deposition onto a cylindrical collector

ANSYS Fluent software was used to model transport of the colloidal particles onto a cylinder in a turbulent crossflow. The Eulerian RANS method with k-ω turbulence model for the continuous phase, and Lagrangian particle tracking, allowed simultaneous calculation of Brownian and turbulent diffusion, turbophoresis and Saffman lift of the particles.

The physical conditions were selected such as to represent conditions of experiment by Dunstall et al. (43). The 2D computational domain developed for this is outlined in Fig.20. It comprised of 180,000 mesh nodes representing a rectangular region of flow (250x125 mm) with a circular cutout (25mm in diameter) in the middle. The circle represented the surface of the cylinder, so the no-slip condition for flow and an ideal sink for the particles were imposed on its boundary.

Water flow was set up to enter the domain through the velocity inlet boundary condition with average velocity of 1.9 m/s at 66 ^{o}C (Re=1.08·10^{5}). Particle injections (of a surface type) were specified at the same boundary. Total colloidal silica mass flow rate was set to 0.098 kg/s, which corresponded to 250 ppm of colloidal silica suspended in the flow.

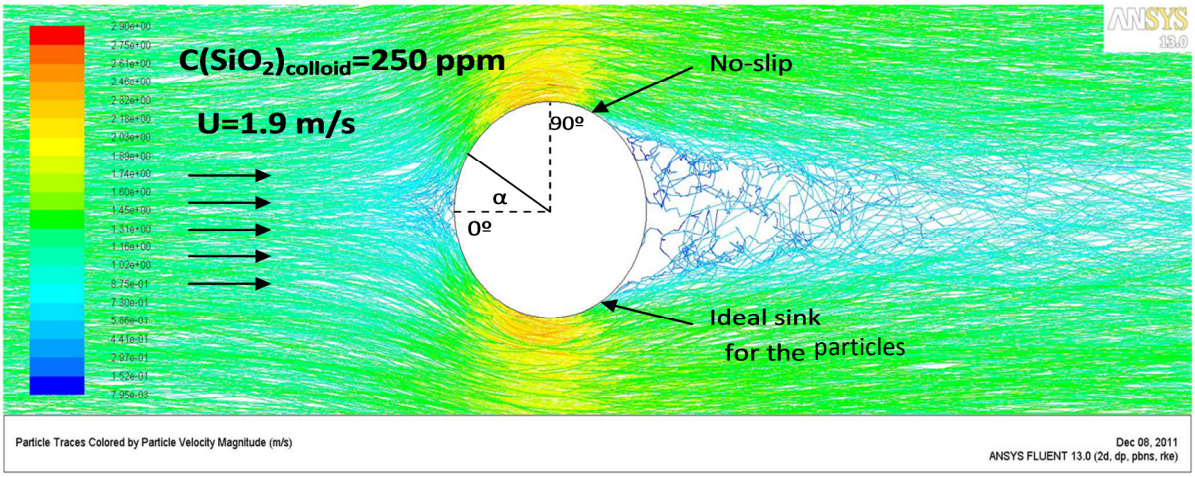

Figure 20: Outline of the computational domain

The problem was solved in two steps. First, a converged steady state solution for the flow equations was obtained. A convergence criterion of 10^{-6} for the scaled residual of the continuity equation was used. The numerically obtained distribution of the pressure coefficient along the cylinder circumference solution was verified against experimental result (43) (Fig.21). Good agreement of the two was found everywhere except for the stagnation point and wake zone. The discrepancy observed in the wake zone can be due to the pressure here depending on the turbulence, which is in turn model dependent. The pressure coefficient

being larger than 1.5 at the stagnation point is unphysical, but it could be an interpolation error if there is no node exactly at the stagnation point.

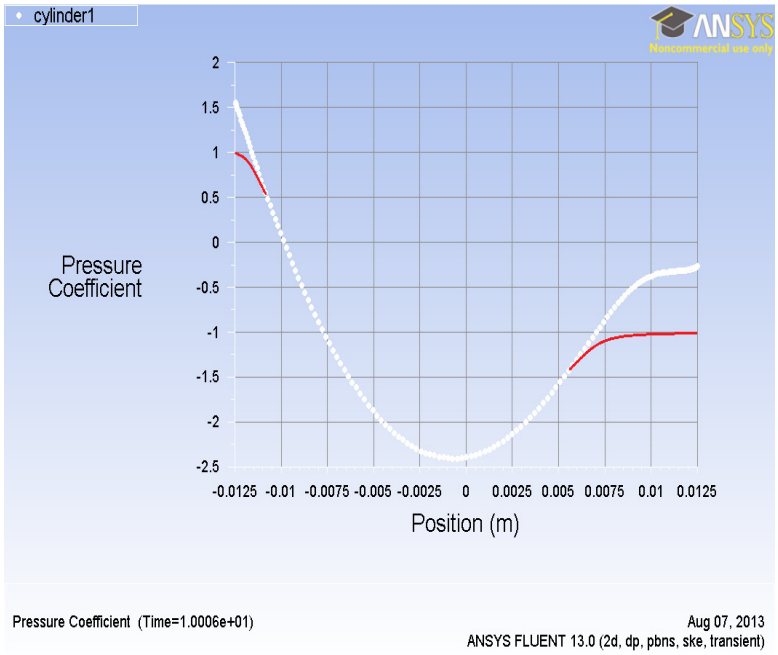

Figure 21: Calculated and experimental values (43) of the pressure coefficient

In the second step, transient calculations of the coupled particle-flow dynamics were performed. For this a discrete phase model, which is based on Lagrangian approach and incorporates all particle transport mechanisms described in Section 1.4.1 was enabled. About 10 seconds of the flow time were resolved in order to allow the flow to travel at least 3 times the length of the computational domain and steady-state mass transfer to establish. Average particle flux on the cylinder surface was determined over this time with the help of the accretion model (125). The corresponding rate of particle transport is reported in Table 5 above, while its distribution over the cylinder circumference is illustrated in Fig. 22.

The rate of transport of colloidal silica in the present CFD simulations was about five orders of magnitude higher than the experimentally measured deposition rate. This discrepancy is expected since as was stated before the scale accumulation is limited by colloidal silica attachment to a surface (chemical bonding).

The present CFD simulation predicts higher rate of particle transport than the analytical results obtained in the previous section and numerical results reported in Section 1.4. There can be several explanations to this discrepancy.

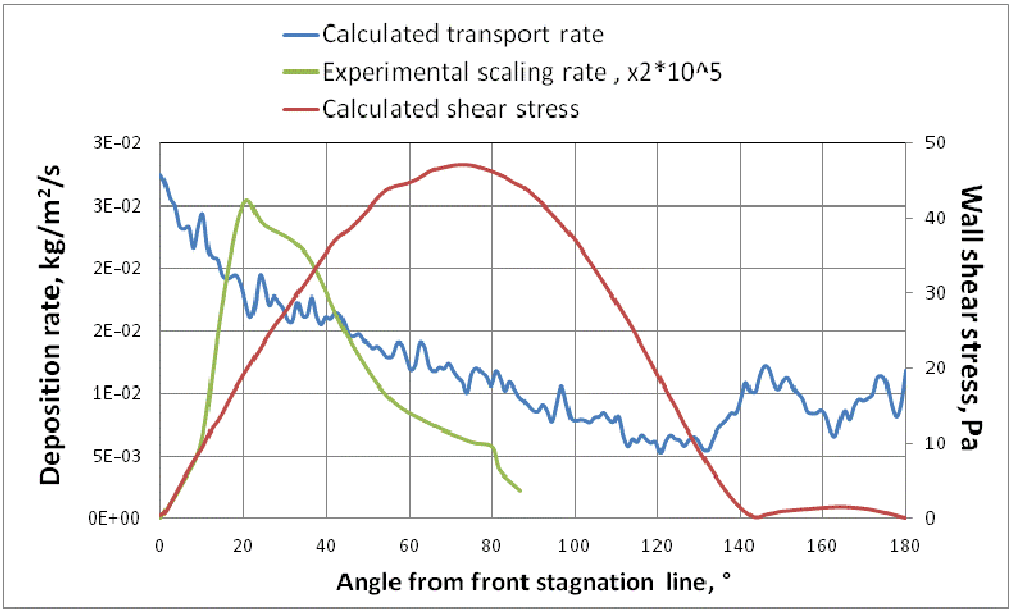

Figure 22: Comparison of CFD and experimental results

First, the CFD simulations generally is able to give better representation of the flow field around the cylinder than analytical approach used for derivation of Eq. 84 and this affects mass transport. Second, the inertial transport of particles, which is not accounted by the analytical model; effects of curvature of the cylinder surface and Saffman lift forces, not reflected in the results in Fig. 10 but resolved in this CFD simulations enhance transport of colloidal silica to the surface.

Third, the present CFD simulation can also overestimate mass transfer due to the flaws of the numerical approach. Thus insufficient resolution of the turbulent pulsations and particle-fluid interactions in the boundary layer can lead to higher rate of particle transport here. In addition, discrepancies in real and modeled flow fields reflected in Fig. 21 could have also affected mass transport.

The distribution of deposition rate over cylinder circumference is also different in the simulation and experiment. The simulated colloid transport rate was highest at the stagnation line on the front of the cylinder, but in the experiment the highest scaling rate was observed at 21°. This can be explained by a combined effect of the surface roughness and shear stress on a cylinder surface.

Real cylinder surfaces used in experiment always have some initial roughness which, apparently, develops further as a result of scale accumulation. This may be the reason for the scale having the observed “rippled” surface structure (see Fig.1).

As it follows from Fig. 22 the highest experimental scaling rate (or height of the scale ridges) was observed at the location where the slope of the calculated surface shear stress curve is the highest. It is possible that some additional convective mechanism of particle transport arising from their acceleration along the surface and subsequent collisions with roughness elements/scale ridges contribute to higher scaling rate observed here. This mechanism will be discussed in detail in Section 6.2 below.

Summary of Chapter 2

Mineral scaling remains one of the main impediments to increase of effectiveness of geothermal resources utilization. Development and continuing improvement of anti-scaling measures requires deeper knowledge about complex combination of the phenomena this process incorporates. Such components as chemical kinetics of minerals polymerization and colloid formation are relatively well understood while transport of these colloids and their stability, which control their aggregation and attachment rates, not as good.

The results of theoretical calculations of the transport and reaction/attachment rates presented in this chapter are summarizes in Table 5 below. Their comparison with the available experimental scaling rates reveals significant disagreement.

The current theory (86) suggested that transport of the particles of relevant size (<1000nm) is limited by their Brownian diffusion through the boundary layer, not by inertial transport (turbophoresis). The theoretical diffusion transport rate, evaluated based on Guha's numerical results, is about three orders of magnitude higher than the experimentally observed deposition rate. In addition, in contrast to the experiments predicted transport rate also decreases for larger particles.

The disagreements were attempted to be reconciled using the notion of particle stability - due to particle-wall interactions only a small fraction of the particles arriving at the surface actually bind to it.

The analytical solutions of the steady-state diffusion equations in combination with the interaction potentials from standard DLVO theory were used to find corresponding stability of particle-particle and particle-wall interactions. The values obtained for the conditions of the experiment (43) suggested that only 1 in a million particles approaching to the surface bond to it – attachment probability $K=10^{-6}$. The DLVO theory also predicts decrease of this attachment probability with increasing particle size.

Consequently, the theoretical deposition rate, found as a product of transport rate and attachment probability, is about three orders of magnitude lower than corresponding experimental rate and decreases as particle size increases.

The CFD simulations of particle deposition onto the cylindrical collector yielded a transport rate which is about five orders of magnitude higher than corresponding experimental scaling rate. With the attachment probability accounted for this gap decreases to only one order of magnitude. The capture of the inertial effects by this CFD simulation of particle deposition onto a curved surface represents a significant enhancement over the analytical approach described above. At the same time, the disagreement between predicted by the CFD simulations and observed in the experiments effect of particle size remains.

The comparison of the detailed hydrodynamic data obtained from the CFD simulations and experimental scaling data lead to the idea of an additional (not accounted in the current theory) mechanism of particle transport. Thus, observed correlation of the distributions of the experimental scaling rate and calculated surface shear stress along the circumference of the cylindrical collector suggested that particle acceleration in the boundary layer on the front side of the cylinder and their subsequent collisions with roughness elements/scale ridges can contribute to overall scaling rate. This mechanism of convective particle transport onto a rough surface will be discussed in detail in Section 6.2 below.

Moreover, as mentioned above in Chapter 1 the DLVO theory does not always predict stability of the colloidal particles correctly, in particular for colloidal silica, and so considerable effort was made to measure actual aggregative stability (Section 6.1) of the colloidal silica produced and used in the silica scaling experiments reported in the following chapters.

3 HYDRODYNAMIC AND CHEMICAL CONDITIONS OF SILICA SCALING EXPERIMENTS

The variability inherent to field scaling experiments can be avoided in laboratory experiments which allow repeatable observations of scaling under controllable chemical and hydrodynamic conditions. Such an experimental procedure was developed by L. Sinclair (93). It involves the use of a flow rig and synthetic colloidal silica with relevant parameters close to those of the geothermal silica colloids: low concentration (250 ppm of colloidal silica), submicron particles (3-100 nm), and relatively high ionic strength (*IS*=30mM) and close to neutral pH. This chapter reports details of the initial flow rig design, experimental procedure and methods of colloidal silica solutions production as well as their continuing modifications necessitated by the early experimental results. In addition, methods used for characterisation of the produced colloidal particles are described.

3.1 Flow rig design and experimental procedure

To study colloidal deposition under controlled hydrodynamic and chemical conditions a flow rig was designed and constructed (93). It allowed circulation of previously produced synthetic silica solution through a closed loop with a centrifugal pump controlling flow rate and flow conditioner providing uniform velocity profile at the inlet to positioned horizontally mild steel pipe section (Fig.23).

The scale accumulated on a pipe internal surface over the duration of the experiment (1-3 weeks) was analysed by scanning electron microscopy (SEM) and energy-dispersive X-ray spectroscopy (EDS), optical microscopy and weighing. To localise scaling to the mild steel (MS) pipe test section all other parts of the rig were made of stainless steel.

In its initial design the rig provided the following range of operational conditions:

- Flow rate 0.6-32 L/min;
- Temperature 25−100 °C
- Pressure 1 atm

A Coriolis flow meter, pressure transducers and thermocouples were set up to control experimental parameters. The rig was designed with the ability to regulate Reynolds (Re)

number both by changing flow rate and test section inner diameter (NB) thus making possible to achieve different developed velocity profile structure in the test section for the same Re. However, only one pipe size was tested so far – NB15. The first 14 scaling experiments were conducted with 150 mm long MS pipe sections. For the later 10 scaling experiments the flow rig was modified to fit 1 m MS pipe sections, long enough for the flow to become fully (hydrodynamically) developed.

Therefore, with the NB15 pipe the rig is capable of sustaining the following hydrodynamic conditions (at 30°C):

- Reynolds numbers from 1000 to 60000,
- Friction velocity (for NB15 pipe at 30°C): 0.03-0.18 m/s.

For each deposition experiment about 20 litres of the synthetic colloidal silica solution were prepared from sodium metasilicate and distilled water (12 MΩ) either by the acid-neutralisation or the ion-exchange method. The corresponding production procedures are reported below in sections 3.3.2 and 3.3.3. At the preliminary stage of the scaling experiments (Chapter 4) a single colloidal solution was used for the entire length of at least one experiment, occasionally, the solutions were used in more than one experiment (up to three consecutive experiments were run with the same solution). Meanwhile, at a later, revised stage of the experimentation a procedure for colloidal solution replacement (fresh sol – same test section) was introduced in order to improve the control over the chemical conditions in some of the experiments (see Chapter 5).

The early scaling experiments with short test sections revealed significant corrosion of the MS test sections. The oxygen exclusion procedure was introduced in order to mitigate this. It involved addition of oxygen scavenger (0.2 g/l sodium sulphite, anhydrous) to the colloidal solutions at the start of each experiment and sustaining a slightly pressurised nitrogen atmosphere inside the mixing tank. For this the nitrogen from a dedicated bottle (oxygen free grade) was flowing continuously into mixing tank and bled outside through a water trap. The content of dissolved oxygen in the colloidal solution was controlled during the experiment with a corresponding probe (HACH LDO101). When needed small amounts of the oxygen scavenger were added to the rig to keep the dissolved oxygen (D.O.) level below 0.1 mg/L.

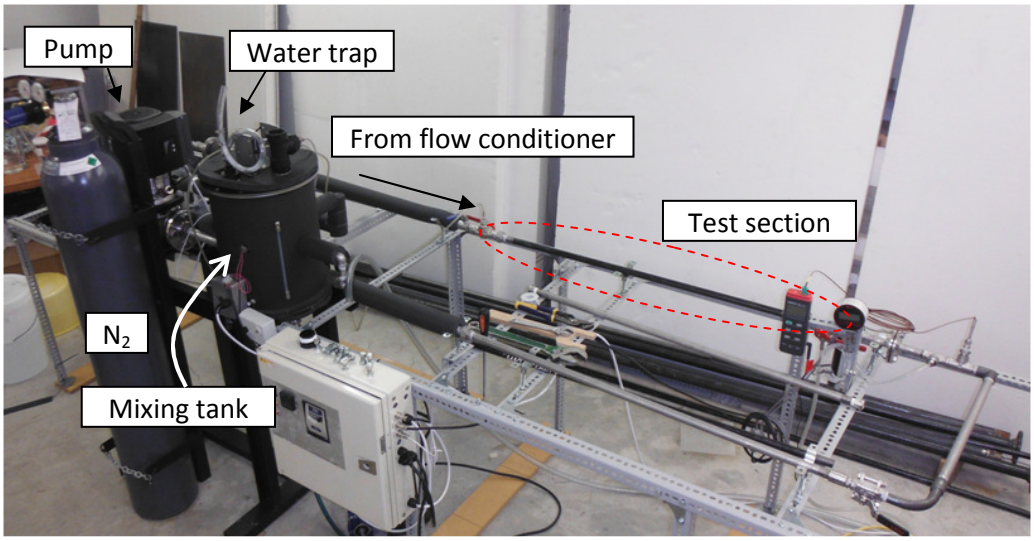

(a)

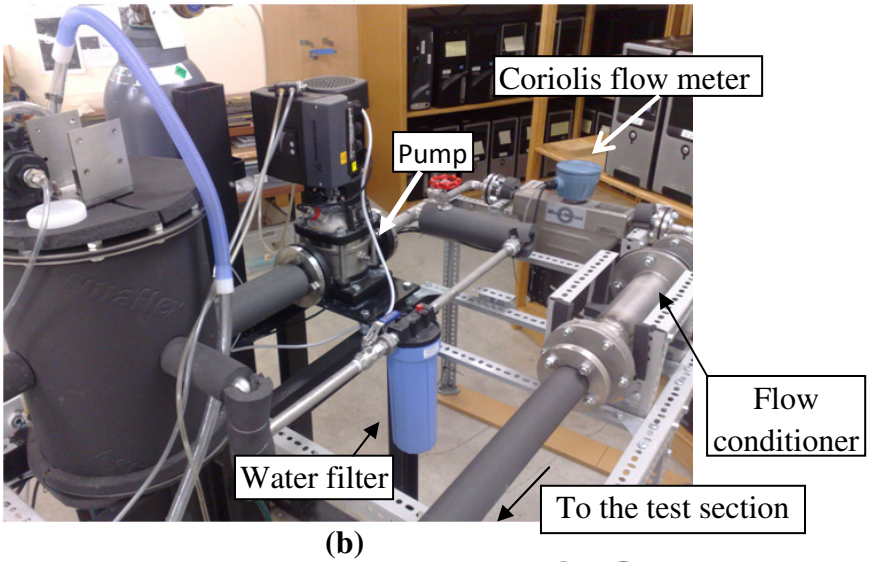

(b)

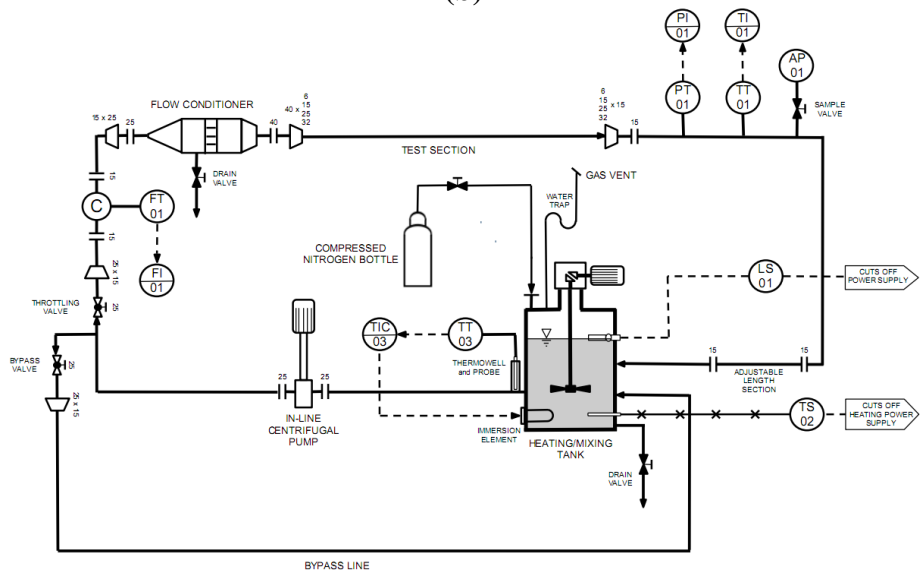

(c)

Figure 23: The scaling flow rig with the modifications: a) front view; b) back view; c) initial test rig piping and instrumentation diagram: source (93)

As a result a significant decrease the corrosion rate was observed. The oxygen removal procedure was further improved in later experiments with long pipe test sections to remove small amounts of oxygen remaining in the rig at the start of the experiment and causing subtle corrosion of MS pipe section internal surface. First of all, colloidal solutions were allowed to circulate in the rig for half an hour to assure complete removal of the dissolved oxygen before installing the MS pipe test section instead of the replacement stainless steel section. Second, the MS test section was flushed with nitrogen to replace air oxygen from it before allowing contact with silica aquasols. For this, two 3-way valves were added to the rig. They allowed shut off of the test section at the start and end of the experiment for flushing it with nitrogen.

The first two scaling experiments with long test sections revealed additional flaws in the experimental procedures and equipment. Particularly, it was difficult to distinguish effects of the scaling on the test surface from those caused by various sources of contamination – either initial contamination of test surfaces (with some kind of grease, which apparently was in contact with MS pipe at some stage of its production or delivery) and with a lacquer used to coat pipe external surface) or that occurring during the experiment (corrosion products, debris from the piping, pump, heating element and threading tape used for test section coupling to the rest of the rig). Therefore, a more thorough cleaning method for the pipe internal surface was implemented in the next experiments. In addition, the mixing motor initially sitting on the top of the mixing tank and intended for additional mixing of the solution was removed in order to avoid contamination of the rig by oil from its gearbox.

The zinc coating on the heating element (1 kW) initially installed in the mixing tank for control of the solution temperature gradually degraded, presumably due to exposure to high pH during the scaling experiments or low pH during cleaning of the rig. That heating element thus was replaced with the more corrosion resistant Incoloy alternative.

Since some of the experimental results and tentative theoretical exercises suggested occurrence of the colloidal silica aggregation in due course of the scaling experiments an additional effort was made to minimize its effect on particle size distribution of the employed colloidal suspensions. The bypass line was complimented with a water filter (washable Pleated 10” Standard Filter – 1 micron) through which the colloidal solution was passed periodically (1- 4 times per 2 days depending on experimental conditions) for 2-3 minutes to remove any aggregates from it. An increase of the filter mass measured at the end of each experiment also provided some reference data for the determination of the aggregation rate.

In the final series of pipe scaling experiments with long pipe test sections all previously gained experience was put to use. Such problematic aspects as initial contamination and corrosion of the tested mild steel pipe and coagulation of the colloidal solution were controlled to the highest degree. As a result the coagulation rate was measured together with the scaling rate.

3.2 Parallel plate flow assembly development

In order to overcome some of the experimental difficulties mentioned above and to obtain more detailed data on the effect of silica scale formation and growth on hydrodynamic properties of the flow, a different experimental approach was envisioned and developed. Instead of scaling of the pipe internal surface, the deposition onto a flat plate in a parallel flow was suggested to be examined. For this a new test section assembly was designed (Fig.24) and built by rapid prototyping (Fig.25), but has not being experimented with by the time this dissertation was written.

It was designed to be connected to the flow rig through the flanges 1 and 2 and to replace the current flow conditioner for circular pipe test sections. In the new flow conditioner the incoming flow first expands and undergoes smooth transition from a round to a rectangular cross-section, further downstream the flow passes through a stainless steel “honeycomb” flow straightener located inside a settling chamber. Next, the contraction section accelerates the flow and provides uniform velocity profile at the test section inlet.

The test section was designed as a rectangular channel fitted with flat plate test piece (2mm thick carbon steel flat plate) located parallel to the largest dimension in the middle of the TS (Fig.26a). Its internal dimensions were selected as:

$$L_{TS} = 120 \text{ mm},$$

$$a = 40 \text{ mm}$$

and of two suggested aspect ratios $a/b = 0.44$ and 0.86 the latter was chosen based on the results of the CFD analysis as one provided optimal minimisation of the corner effects and pressure drop.

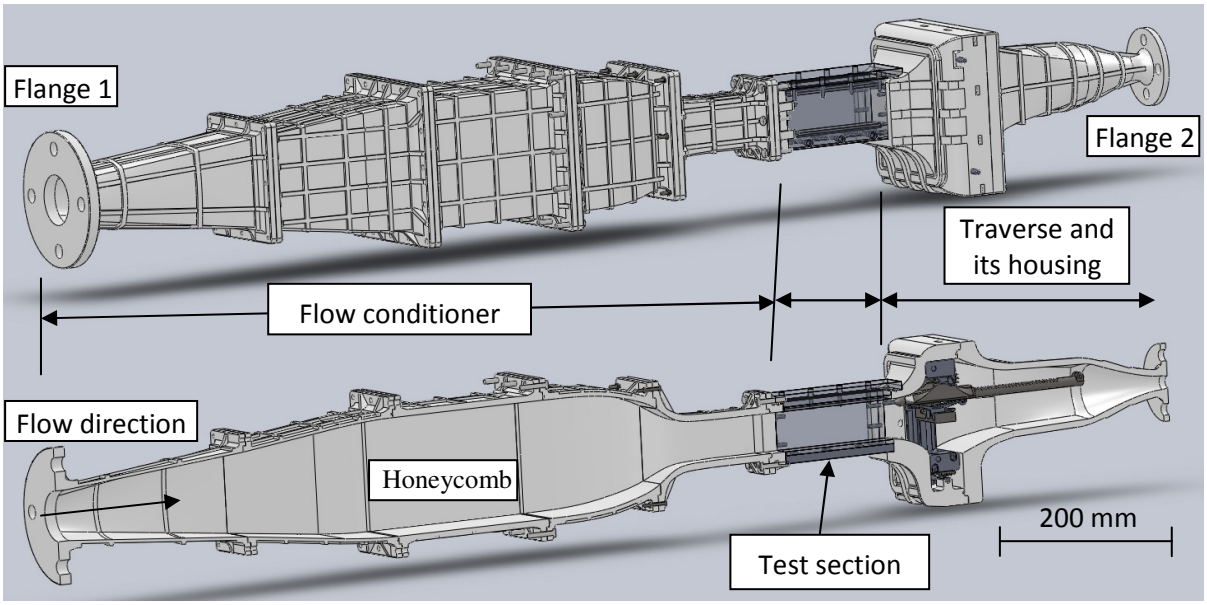

a)

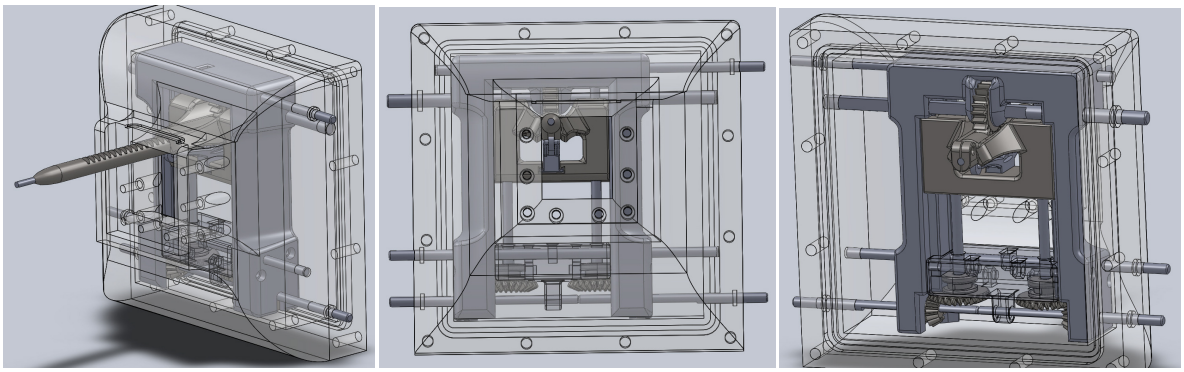

b) c) d)

Figure 24: (a) Test assembly for parallel plate scaling experiments with (b) traversing system for a hot-film anemometer: (c) front and (d) back view

a) b)

Figure 25: (a) 3-D printed parts of the flow conditioner (internal cross-section of the honeycomb/settling section is 200x200 mm) and (b) Perspex test section and traverse

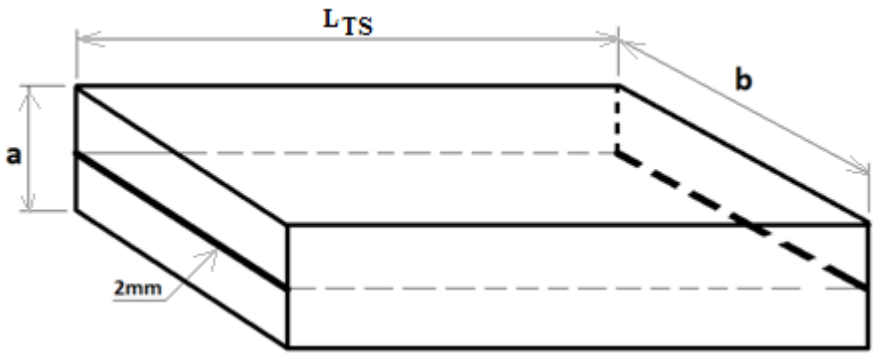

a)

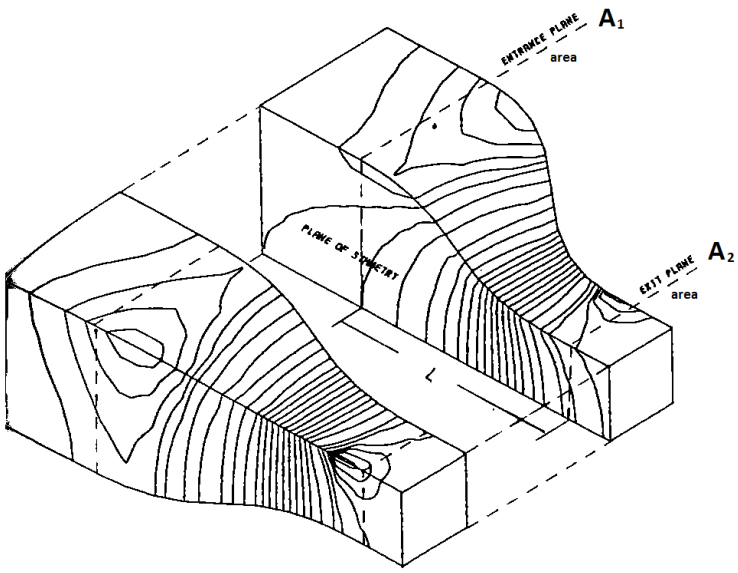

b)

Figure 26: Internal geometry of (a) test section and (b) contraction section (126)

An initial design of the flow conditioner was developed by intern student Antoine Thizy. The design parameters of the contraction and settling sections were chosen based on the work by Su (126). The aim was to provide high uniformity of the flow at the entrance to the test section (exit plane on Fig.26 b). Thus, the highest feasible contraction ratio was chosen as $\mathrm{CR} = \frac{A_1}{A_2} = 10$. For the same reasons a high relative length of the contraction was chosen - $L/\sqrt{A_1} = 2$. The cubic and 7^{th} power profiles for fore part and aft part correspondingly (126) were used to define the contraction internal surface.

The settling section of the flow conditioner was designed to have a square cross section with a side equal $W = \sqrt{A_1} = 147$ mm. This size, as well as the overall dimensions of all other parts, was assured to be within the limitations of the 3-D printer used for their manufacture.

Since available the 3-D printer produced a slightly porous ABS plastic all parts were made watertight by applying several coats of epoxy resin.

As seen in Fig. 24 and 25 the flow from test section goes back to the mixing tank through the traverse housing, Flange 2 and pipe line (shown in Fig.23). A 3-axis traversing system provides fine positioning of a hot-film anemometer (DANTEC Dynamics boundary layer type probe 55R15) inside the test section and, thus, measurement of the local mean and rms velocities.

A flow device (Fig.27) for calibration of the hot-film anemometer was designed and built using specifications suggested in (127).

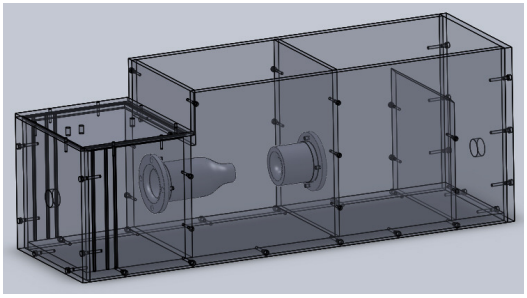

Figure 27: Calibrator for a hot-film anemometer

Once assembled and incorporated into the existing flow rig the new test section assembly described above will allow observation of silica scaling in parallel plate flow with the following parameters:

- solution temperature: $25 - 60$ °C
- mean flow velocity: $0.0097 - 0.26$ m/s
- $\mathrm{Re}_{\mathrm{D_h}} = 354 - 9444$
- boundary layer thickness 70 mm from the test plate leading edge is $\delta = 11.7 - 3.5$ mm.

Ultimately, the new parallel plate test section assembly will provide following improvements to the mineral scaling experiments:

- obtain more accurate measurements of the scale growth rate – use of the flat test surface with higher surface-to-volume ratio will make the measurements of scaling rate simpler and more accurate;
- control surface properties much more easily and effectively, as it is easier to prepare and modify flat surfaces;

- obtain visual data on the chronological and spatial features of the scale onset and development;
- collect detailed, time-dependent, data for the intermediate step of the computer model validation - mean and instantaneous velocities in the near wall region;
- analyse correlations between the scale morphology and changes in near-wall structure of the flow, if there is any;
- allow detailed characterisation of the boundary layer structure (both time averaged and turbulence properties) above various scaled surfaces.

3.3 Synthetic brine production and characterisation

There is a plethora of existing methods of colloidal silica synthesis, allowing choice of a method optimal for particular application. A detailed summary of the methods of colloidal silica synthesis was given by Iler (71) and a review of more recent developments was given in Bergna (128).

The most commonly used methods include acid neutralization of aqueous silicates (129), ion exchange (130), (131), hydrolysis of alkoxysilanes (132) and direct oxidation of elemental silicon (133).

The last two methods yield the most monodisperse sols with the least impurity, but they also have highest production cost. They require a more expensive precursor, solvent and may involve solution filtering or centrifugation steps. The first two methods have advantages of ease of the particle size control and simpler procedures. The acid neutralisation is the cheapest and simplest of all. It utilises the same inexpensive raw material as the ion exchange method (sodium silicate), but lacks the step of sodium ion removal. This predetermines a high level of particle impurity and high ionic strength of the sol. However, this is not a disadvantage for the present purpose, to simulate geothermal colloidal solutions, in which ionic strength is typically high and other dissolved minerals are always present.

The acid neutralisation method of colloidal silica production suggested in (93) was further developed (section 3.3.2) and used to synthesise most of the sols used in the deposition experiments. An ion-exchange process suggested in (128) was also realised and used to produce several colloidal silica solutions (section 3.3.3)

3.3.1 Particle characterisation: particle size and charge measurements

Particle size and electrophoretic mobility measurements were performed with a Zetatrac NPA152 particle size and zeta potential analyser (Microtrac Inc.). This instrument employs two solid-state diode lasers of 780 nm wavelength and nominal optical power 3 mW and a set of two gold-coated optical probes with oppositely positioned electrodes for simultaneous measurements of particle size, by dynamic light scattering (DLS), and particle electrophoretic mobility. Its optical scheme implements a heterodyne detection of the light backscattered from the sample particles. This reduces multiple scattering effects and broadens the concentration and particle size range of the instrument.

The Microtrac Flex 10.5.4 software was used for data processing. It accounts for variable particle scattering efficiency by implementing Mie or modified Mie theory. It can produce particle size distributions in number, volume and intensity-weighted forms. The distribution generated by the software represents a relative weight of the particles from a range of narrow size intervals (channels) in the total number of the particles, volume of the particles or signal intensity detected by the instrument correspondingly. The number distribution is commonly used to represent particle population, whereas the intensity-weighted distribution can be useful for detecting particle aggregates in the solution. However, due to the complex dependence of the scattering efficiency from the particle size (Fig.28) caution must be exercised when interpreting the intensity-weighted data.

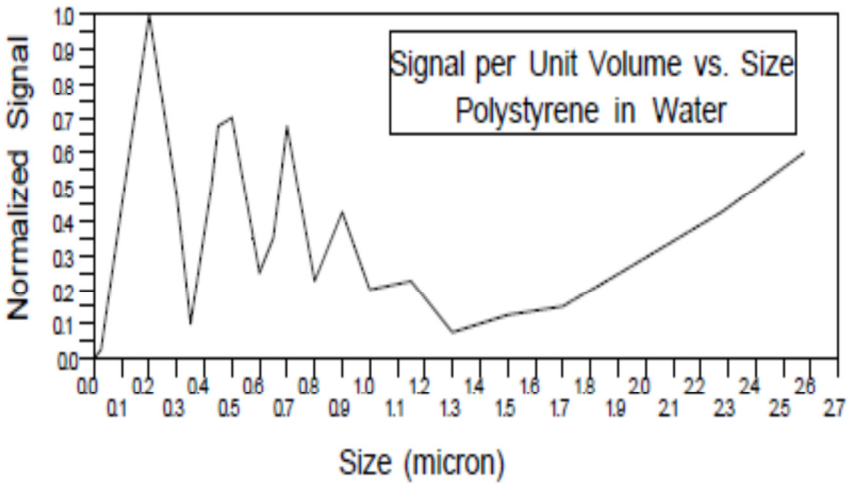

Figure 28: Scattering efficiency as a function of particle size (134)

These features of the instrument are particularly beneficial for the analysis of the colloidal systems with broad particle size distributions. Unless specified otherwise all particle size

distributions (PSD) reported below are in the number form and all particle sizes are the mean diameters in these number distributions.

The software also incorporates a number of algorithms for the analysis of the PSD. The polydispersity index (PI) and inclusive graphic skewness (Ski) are the two used here. The PI is a squared ratio of the standard deviation of the PSD to its mean particle size. The skewness is the measure of the distribution curve asymmetry and its deviation from a normal, bell-shaped curve. A symmetrical distribution has Ski of 0. The values of Ski from +/-1 to +/-0.3 indicate that coarse/fine particles distort the symmetry of the distribution.

The NPA152 particle size analyzer also reports a parameter called 'Loading Index' for each measurement. The Loading Index (LI) measures the total AC signal obtained from the light scattered by the particles moving in the sample. Therefore, keeping in mind the particle scattering efficiency from Fig.28, the LI can be used as a measure of particle concentration – e.g. higher LI for a sol with the same particle size reflects its higher particle number concentration.

The mobility data was converted into zeta potentials using the accepted Smoluchowski relationship. The calibration of the Zetatrac analyser was performed with the Microtrac reference materials. The 100 nm polystyrene and Alumina 165-4 suspensions were used as the particle size and mobility standards correspondingly. Each particle size reported below represents an average of at least 3 consecutive one minute measurement runs.

The DLS particle size measurements were validated by Scanning Electron Microscopy (SEM). Selected sols were analysed on a JEOL JSM 7000F field emission SEM. Sample preparation involved dilution of the silica aquasols to 0.3 g of total solids per litre. Sodium ions present in the sample were removed by ion exchange. A small drop of the obtained solution was placed on a carbon tab, freeze dried overnight and coated with gold prior to the SEM analysis.

The SEM micrographs were manually processed by counting and sizing the particles. At least 50 particles were evaluated in the selected micrographs to produce a particle number distribution over a set of discrete particle size intervals – or channels. The width of the channels was selected to be equal to that of the PCS data channels.

3.3.2 Modified acid neutralisation method of colloidal silica production

The hydrolysis of the sodium metasilicate (SMS) $Na_2SiO{\cdot}5H_2O_3$ was used to synthesise monodisperse silica colloids up to 10 nm in diameter. A two stage production scheme was developed to give up to 20 litres of the colloidal solution. In the first stage, a total of 62 g of SMS were gradually added (0.7 g/min) to two vessels with 5 L of Millipore water (1 Mohm·cm) previously acidified (to 0.02 M H_2SO_4) and heated to 75 °C. After all SMS was dissolved and both solutions pH stabilised at 8.2, by adding 5-10 ml of NaOH (2.5 M) or 1-2 ml H_2SO_4 (18 M), they were held at 75°C for another hour and then cooled down to a room temperature in a water bath, mixed together and acidified to pH 7.5. The obtained solution is referred as Batch 1 hereafter (Fig.29).

In the second stage, 24 hours after preparation of the first two, another two 5 L sols were made in the same way but with less acid used for initial acidification (0.015 M H_2SO_4). These two fresh sols, referred as Batch 2, after being cooled down, were mixed with the Batch 1 sol. The final sol contained 1750 ppm of silica and 1800 ppm of sodium in total. This solution was again adjusted to pH 7.5, kept at room temperature and the particles size monitored periodically. After the desired particle size (in the range of 10 to 50 nm) was reached the pH was increased to 9.5 by addition of NaOH.

The pH, temperature and total silica concentration were controlled during the production of 35 colloidal silica solutions. Fig. 29 illustrates the trends of these parameters typical for all of the solutions while disregarding the minor differences between them. These include temperature and ionic strength variations shown in Table 6 for 11 selected sols. The variations of the sols conductivity (and IS) reflect differences in amounts of the acid/base used in their production.

HACH pHC281 and CDC401 probes were used to measure pH and conductivity of the prepared solutions correspondingly.

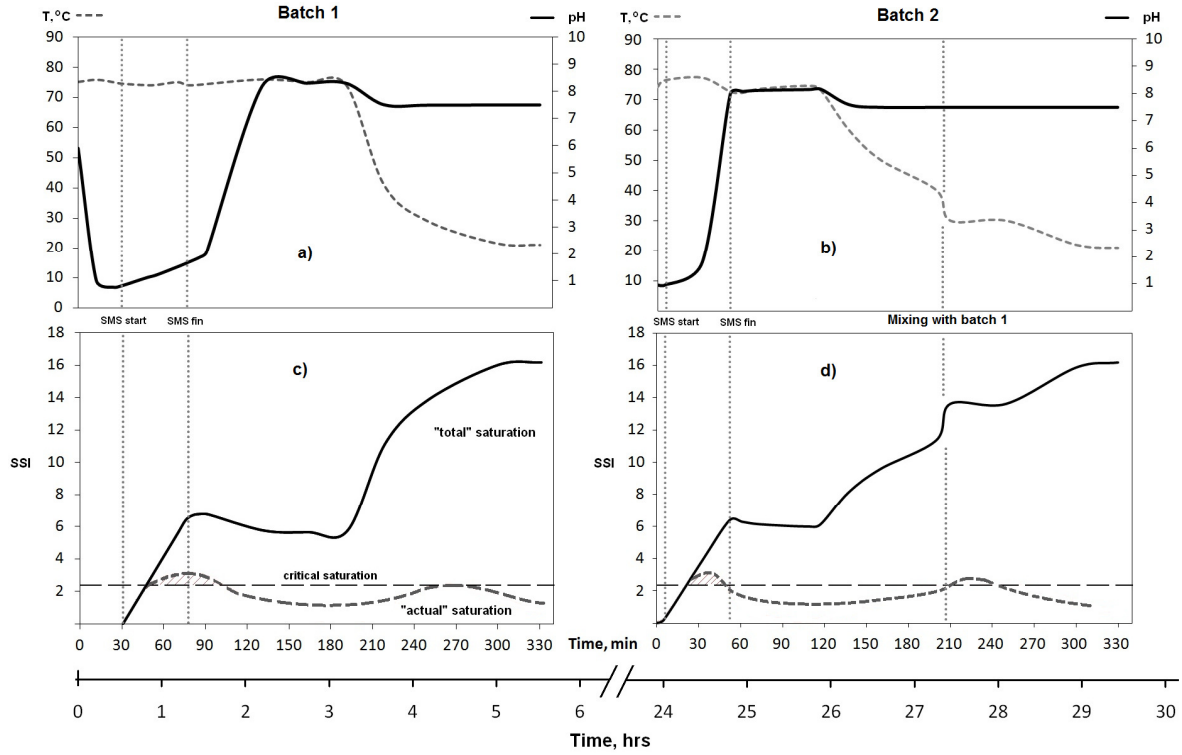

Figure 29: The production conditions (pH, temperature) and silica supersaturation index during two stage particle synthesis

The zeta potential of the particles and solution ionic strength (*IS*) were also determined. The zeta potentials measured with the Zetatrac were -2.5±1 mV for the "growing" sols (pH=7.5) and -30±3 mV for the "stabilised" sols (pH=9.5).

The average IS over all solutions was calculated (Eq. 4) using the known quantities of the chemicals used in their production. This gave an average IS of 67 mM.

This value of IS was derived assuming that all sodium ions initially present in the precursor end up in the solution. However, it was shown (128) that some of the sodium ions are absorbed from the solution into the colloids and that the concentration of the sodium in the particles is 2-3 times of that in solution. Nevertheless, the low particle volume fraction, which will be showed later to be about $1 \cdot 10^{-3} m^3 m^{-3}$, typical for the sols prepared with the acid-neutralisation method means that the fraction of the sodium absorbed in the colloids constitutes only 0.3 % of its total content.

At high IS there is no simple relationship to calculate IS from measured conductivity. It is known though (135) that in this case solution conductivity σ is proportional to the square root of ion concentration. From this square root relationship between the measured conductivity of

the solutions σ (Table 6) and average IS the following relationship between the variations in the corresponding parameters can be derived

$$f(IS) = (1 - f(\sigma))^2 - 1, \quad (116)$$

here f(x) denotes the relative deviation of the parameter x from its average value.

Table 6: Parameters of the selected colloidal solutions

	Sol number	Mixing temp., °C	pH after prod.	Growth, days	pH of a "stabilized" sol	Conductivity μS/m	IS dev, %
Group 1	58+59	30	7.5	10	9.25	7.6	+17
	60+61	30	7.5	17	9.25	7.4	+11
	54+55	30	7.6	21	9.2	7.3	+8
	40+41	30	7.7	19	8.7	-	-
	66+67	30	7.5	27	9.25	-	-
Group 2	42+43	30	7.5	32	8.9	-	-
	68+69	20	7.5	26	9.25	6.7	-9
	62+63	30	7.8	32	9.3	6.6	-13
	56+57	30	7.4	25	9.2	6.4	-17
Group 3	44+45	50	7.6	2	8.7	-	-
	70+71	50	7.4	3	9.3	6.7	-9

The deviations of the selected sols IS from the average value were derived based on Eq.116 and available solution conductivity measurements (Table 6). The range of the tested IS was found to be from 55.6 to 78.4 mM. Therefore, the sols were divided in 3 groups: Group 1 includes the sols with the *IS* above average, in Group 2 the IS is below average and Group 3 sols were mixed together at a higher temperature then Group 1 and 2 sols.

From known temperature, pH and chemical composition the total silica saturation $TSS = \frac{\text{Total silica concentration } C}{\text{Amorphous silica solubility } C_e}$, was calculated (with Eq.2) and plotted over time (solid line in Fig.29 c, d). It has two regions of increase separated by a region of decline and/or stability. The first rise is caused by the addition of the SMS to the solution and the second by its cooling at the end of production. The minor decrease in TSS observed for the first batch (Fig.28 c) is a result of the base addition and pH related increase of the silica solubility.

The actual silica supersaturation, shown as broken line in Fig.29 c, d, was estimated based on the TSS curve and expected silica consumption by particle nucleation and growth. It reaches a maximum (SSI~2.5) when approximately half of SMS has been dissolved and then drops

rapidly due to nucleation and particle growth. Because of the lower pH the nucleation in Batch 1 is expected to proceed more slowly than in Batch 2. Noting that precursor addition rate was virtually the same in both batches, the nucleation period in Batch 1 should be longer than in Batch 2 (shaded area in Fig.29 c and d). This must lead to formation of a less monodisperse assembly, of on average larger particles in the first batch.

Once the supersaturation index has decreased below the critical SSI≈2.5 the remaining oversaturated silica is consumed in the growth of the formed nuclei. The growth continues over a holding stage – 1 hour after end of SMS addition – at a constant silica concentration, pH and temperature, until the actual silica oversaturation reaches zero (SSI=1).

The solution cooling to room temperature (especially rapid upon mixing fresh batch with the one prepared day before) and pH decrease to 7.5 leads to another rise in silica saturation after the holding stage is completed. Since monomeric silica concentration was not measured at this stage it is unclear whether this caused the actual silica saturation index to reach the critical value again and trigger an additional nucleation process. It is however clear that this new oversaturated silica precipitates on existing particles promoting their further growth.

The modification of the acid-neutralisation method of colloidal silica production reported here was found to yield moderately monodisperse sols with polydispersity index PI between 0.05 and 0.2 and a mean particle size from 10 to 100 nm. A more thorough analysis of the particle growth data is conducted in section 6.1.1.

3.3.3 Ion exchange method of colloidal silica production

The ion-exchange (IE) method of colloid silica production was implemented in order to improve characteristics of the sols used in the scaling experiments. With this method sodium ions initially introduced into the solutions with the precursor - $Na_2SiO_3 \cdot 5(H_20)$ - are replaced by hydrogen on active sites of strong acid ion-exchange resin (Amberlite-1000H). This resulted in a decrease of the solutions ionic strength and increase of aggregative stability of obtained silica colloids. Moreover having silica in its active form (H_4SiO_4) allowed controllable build-up of bigger particles (up to 250 nm) over much shorter ageing periods (a few days) than with hydrolysis method (a few weeks).

A two stage production scheme was adopted from (128), (136). First, silica sols with high number density of small particles were prepared (see Fig.30 a). Next, they were used as a “heel” for a bigger particles build-up (see Fig.30 b). Thus this production method included following steps:

1. Obtaining active silicic acid: water (12MΩ) solution of sodium metasilicate (SMS) with 2-5.6 wt% SiO_2 is passed thru a column packed with regenerated ion-exchange resin (Fig.30 a);
2. Synthesis of "heel" particles: the active silicic acid (ASA) obtained in the previous step is titrated to heated (70-80°C) KOH solution (0.5-1.5 wt%) – the particles formed at this stage may have wide size distribution – from 10 to 150 nm (Fig.30 a);
3. Particles "build-up": the seeds are grown further by titrating additional ASA at a lower than above rate in alkaline environment (Fig.30 b).

The first two steps have been trialled using a 100 ml IE column and 300 ml batch process. An optimal recipe for production of the seed sol with highest particle number concentration (thus smaller particle size) was established. Two different Si concentrations (2.2 and 5.6 wt% SiO_2) in the initial solution and two ASA titration rates (10 and 20 ml/min) were tested. The process is illustrated schematically in Fig.30 a and the production conditions for each sol are listed in Table 7. The sols obtained with this method have pH between 9 and 11 and thus are expected to be charge stabilised.

The particle size distributions in the first 16 "heel" solutions produced with the small scale set-up were analysed in order to find the optimal recipe. It is evident from Fig.31 that a higher titration rate benefited production of solutions with more numerous smaller particles. Comparison of the PSD in Fig.32 also showed that two sols (##13 & 14) produced with smaller total amount of more concentrated ASA (5.6 wt% SiO_2) had more monodisperse PSD.

Therefore, the corresponding recipes with higher titration rate of concentrated ASA were adopted for the large scale production of the seed solution preparation. This must lead to higher particle number concentration and monodispersity of the final sol.

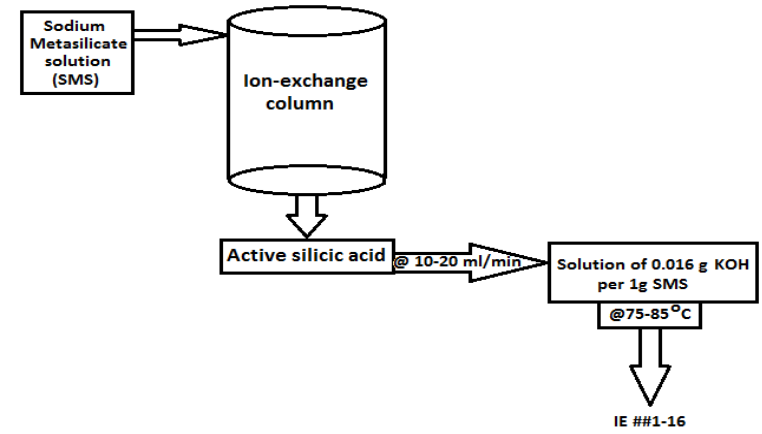

a)

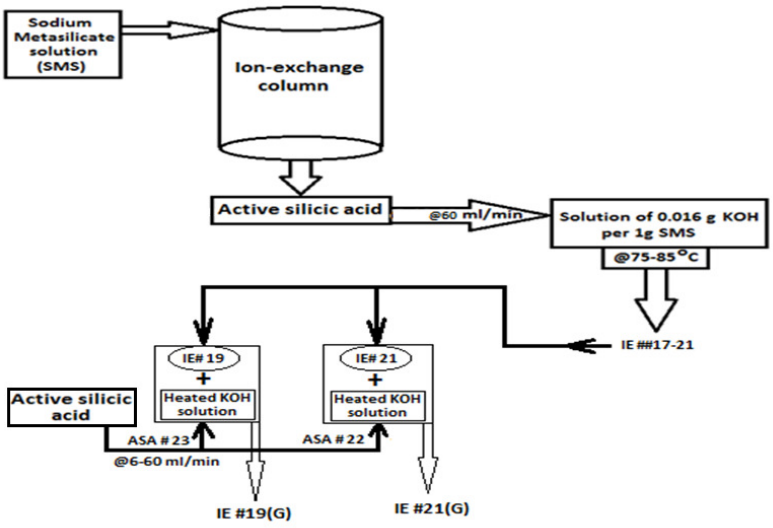

b)

Figure 30: (a) Production of "heel" particles with ion-exchange; (b) Particle build-up from seed sol

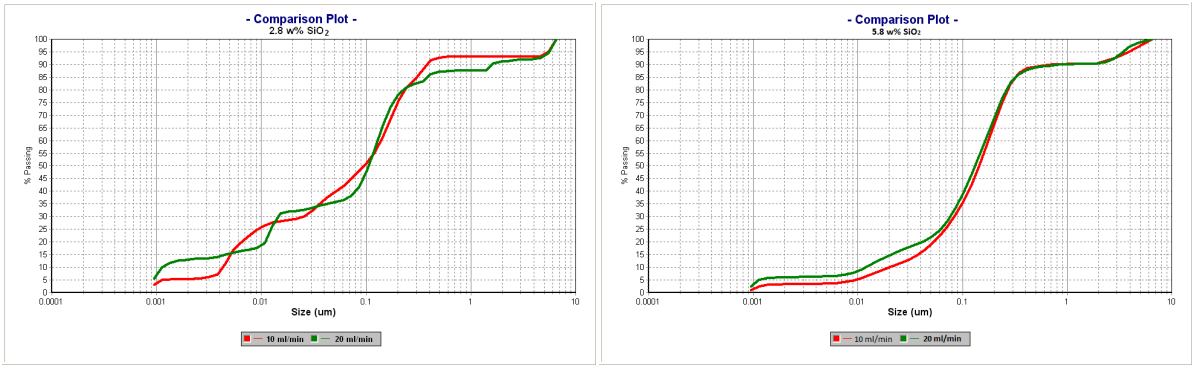

a) b)

Figure 31: Particle size population for two ASA titration rates for (a) 2.2 and (b) 5.6 wt% SiO_2 concentrations

Table 7: Silica sols produced with ion-exchange

Sol #	Initial SMS solution			Active silicic acid		Heated KOH soln.		Titration rate	pH		Final volume,	Notes
	SMS, g	H_2O,ml	SiO_2, wt%	pH	Volume, ml	KOH, g	H_2O,ml	ml/min	final	adjusted	ml	
3	5	80	1.7	-	160	1	50	10	11.55	11	210	
4	5.4	80	1.9	-	160	0.5	50	10	11	-	210	
5	3	30	2.8	-	60	0.2	26	10	11	9.8	86	
6	6	30	5.6	-	60	0.2	25	10	11	9.7	85	
7	6	30	5.6	5	60	0.1	27	10	10.5	-	87	
8	6	30	5.6	-	60	0.1	25	20	11.5	-	85	
9	6	30	5.6	-	60	0.1	25	20	9.9	-	85	
10	6	30	5.6		68	0.1	25	20	10	-	92	
11	6	30	5.6	-	74	0.1	26	20	10.8	-	100	incomplete IE
12	6	30	5.6	10	60	0.1	26	10	11.48	-	86	incomplete IE
13	6	30	5.6	3-4	50	0.1	25	10	10	-	75	
14	6	30	5.6	3-4	50	0.1	25	20	10	-	75	
15	2.5	25	2.8	2.63	38	0.043	25	10	9.3	-	63	
16	2.5	25	2.8	2.63	38	0.043	25	20	9.3	-	63	
17	360	3000	3.4	3 11	@1650 @2200	6	1500	-	-	-	-	Insufficient column exchange capacity
18	360	3000	3.4	3.4	3400	6	1500	62	9.48	-	4900	obtained ASA and sol are yellowish
19	360	3000	3.4	3	3300	6	1500	56	9.4	10.5	4500	signs of aggregation in the column; heat-up
20	360	1800	5.65	3	1800	-	-	-	-	-	1800	ASA gelled prior titration; column heat-up
21	360	5000	2	3.9	5300	8	1500	60	9.2	10.3	6800	
22	360	5000	2	3 - 5	4500	-	-	-	-	-	-	for #21 growth
23	360	5000	2	3	5000	-	-	-	-	-	-	for #19 growth
19(G)*	-	-	1.94	3	5000	30	1000	6-12	10.5	-	10500	
21(G)*	-	-	1.5	3 - 5	4500	23	1800	60	10.8	10.5	13100	

*(G) denotes sols grown in the process (b) in Fig.30

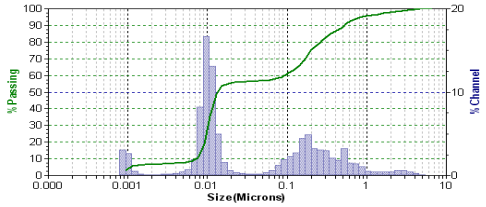

IE#5, $D50^{(1)}$=10nm, $D50^{(2)}$=176nm, 3days old

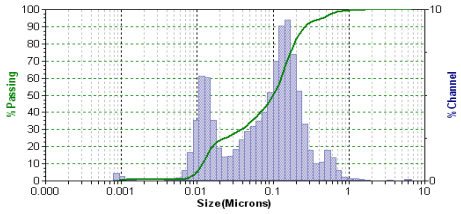

IE#6, $D50^{(1)}$=12nm, $D50^{(2)}$=128nm, 0 days

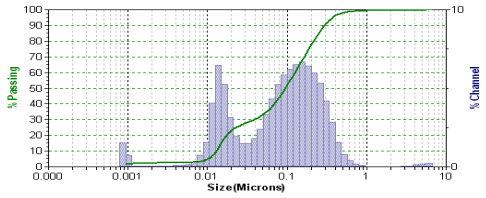

IE#7, $D50^{(1)}$=15nm, $D50^{(2)}$=140nm, 3days

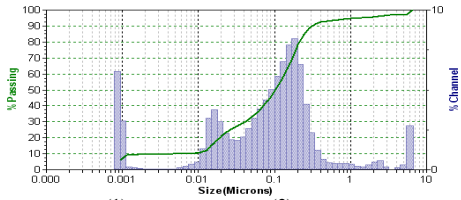

IE#8, $D50^{(1)}$=16nm, $D50^{(2)}$=136nm, 2 days

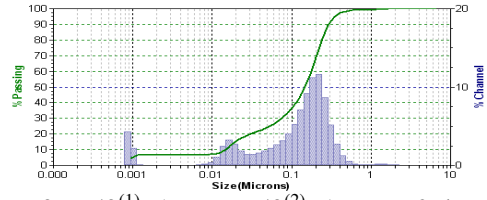

IE#9, $D50^{(1)}$=17nm, $D50^{(2)}$=177nm, 2 days

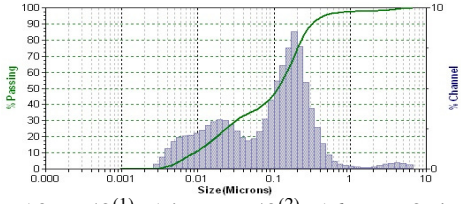

IE#10, $D50^{(1)}$=14nm, $D50^{(2)}$=167nm, 0 days

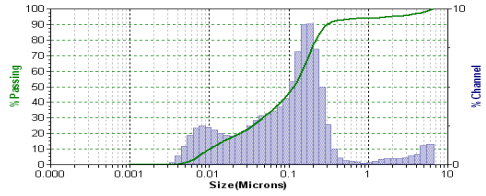

IE#11, $D50^{(1)}$=8nm, $D50^{(2)}$=130nm, 0days

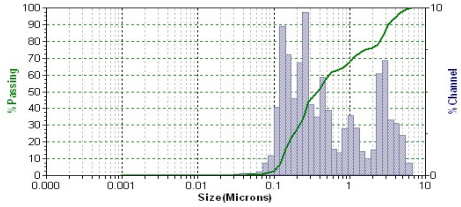

IE#12, D50=137 nm,..., 0 days

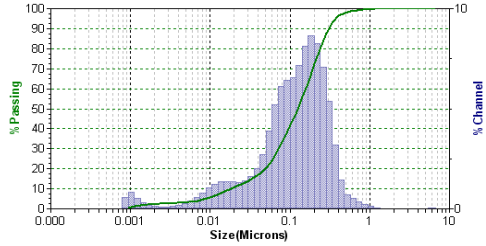

IE#13, D50=137 nm, 1 day

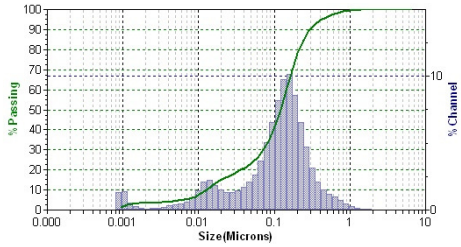

IE#14, D50=123 nm, 1 day

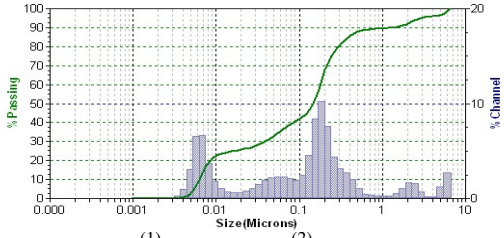

IE#15, $D50^{(1)}$=6nm, $D50^{(2)}$=193nm, 5 days

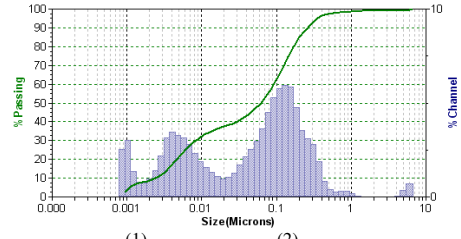

IE#16, $D50^{(1)}$=5nm, $D50^{(2)}$=118nm, 1 day

Figure 32: Particle size distributions in seed silica sols prepared with the ion-exchange method. The superscripts (1) and (2) indicate first and second modes in the sols PSD correspondingly.

The chemical set-up used for the production of 20 L of batches of silica aquasols with the ion-exchange method is shown in Fig.33. A 6 L glass column was used for the ion-exchange step of ASA preparation. The column is a glass cylinder (1.5 m long, 150 mm ID) tightly connected to a funnel drain at the bottom. A perforated plate is located between the tube and funnel, which supports filtration paper and, thus, keeps the ion-exchange resin in the tube while allowing slow drainage of the permeate.

Use of larger column significantly increased the overall time required for the sol preparation. At first, due to inability to conduct resin wash and regeneration in backflow mode inside the column the "bucket" method was used instead. Later the design of the column was modified to make possible its operation in backflow. Particularly, a second drainage outlet for removal of the backflow was added at the top of column and stronger clamps were used to hold column tube and funnel parts together.

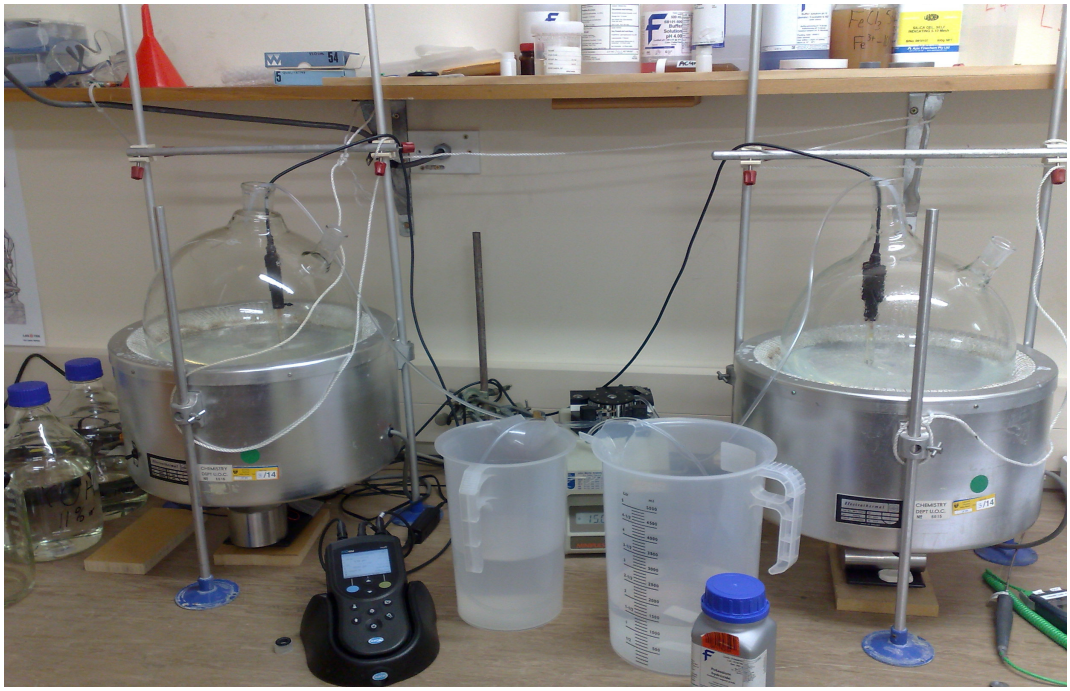

Figure 33: A set-up for silica sol production with ion-exchange method

The scaled-up production of the seed solution was effectively the same as in Fig. 30 a except for the higher titration rate and generally more diluted SMS solutions being used (Table 7: sols# 17-21).

This last parameter was found to be critical in active silicic acid preparation with large scale set-up. Significant heat-up of the column, owing to release of the exothermic heat, was observed when SMS solutions with SiO_2 concentration higher than 2% were passed through the column. This was observed to result in the aggregation of the active silica in the exchange region due to the low pH

conditions present here. Some of this aggregated silica can be expected to remain in the exchange resin pores thus indefinitely decreasing its capacity and SiO_2 content in the final ASA solution.

Moreover, the obtained ASA is in unstable form and can gel before it is used in the next step, particularly if it is concentrated. This is what happened with ASA #20 (Table 7) which contained 5.6 %w SiO_2. Therefore maximum SiO_2 concentration of 2 % in SMS solution was maintained henceforward.

The ASA obtained on ion-exchange step was titrated into two 10 L spherical vessels (Fig.33) containing a certain volume of the water solution of KOH kept at constant temperature (Table 7).

The two most successful seed sols - IE#19 and IE#21 - obtained with this large scale set-up were selected for the next step of particle build-up (Fig.30 b). The PSD measured at different stages for these sols are illustrated in Fig.34.

It is evident from comparison of Fig.34 a and b that polydispersity of the sol IE#19 has increased as a result of the "build-up" process. The ASA added to the "heel" sol seem to deposit onto both large and small particles giving a sol with bimodal particle size distribution (Fig.34 b) and resulting in a very small increase in particle sizes. The higher rate of ASA titration to the seed solution realised during growth of the sol IE#21 (Table 7) resulted in its higher final monodispersity (Fig. 34 b vs. e). However, only minor growth of smaller particles and, apparently, a decrease of the number of larger particles was observed in case of IE#21 (Fig.34 d vs. e).

This, together with ASA concentration limitations discussed above means that to grow large particles with this method one would need to titrate a larger volume of ASA to the seed solution over an even longer period of time.

However, just as with the hydrolysis method, particle growth can be promoted by lowering pH of these sols. To test this about 100 ml of sol IE#19(G) were separated and acidified to pH=7.5. It is evident from comparison of Fig.34 b and c this caused disappearance of the smaller particles and an increase of number of medium size particles. A single peak developed at average particle size of 65 nm immediately after acidification which grown to about 250 nm in just 3 days (Fig.35). Afterwards the sol was alkalinized back to pH 10.5 and further particle growth was effectively stopped (Fig.35). The scattering and peaks in data represented in Fig.35 (as well as later in Fig.52-56) reflect the uncertainty of pH and particle size measurement and reaction of the colloidal solutions to change of pH respectively.

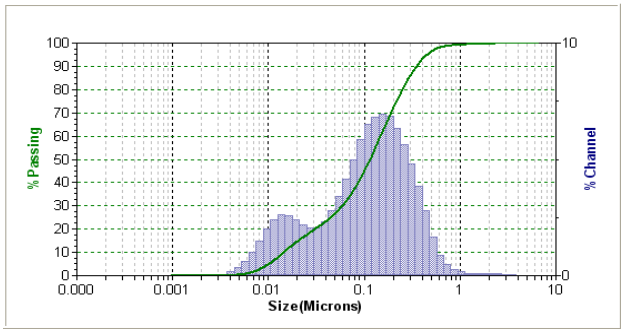

a) IE#19$_{(S)}$: D50$^{(1)}$ = 13nm, D50$^{(2)}$= 144nm, 3 days old

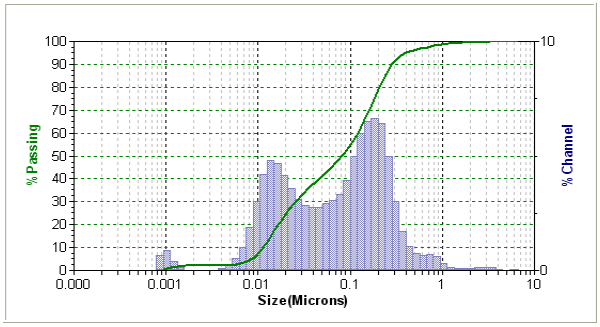

d) IE#21$_{(S)}$: D50$^{(1)}$= 15nm, D50$^{(2)}$= 150nm, 0 days old

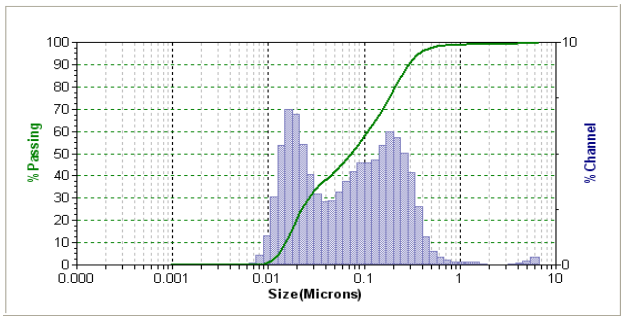

b) IE#19$_{(G)}$: D50$^{(1)}$ = 19nm, D50$^{(2)}$= 154nm, 11 days old

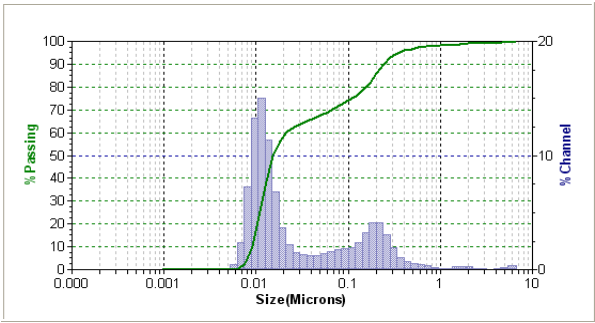

e) IE#21$_{(G)}$: D50$^{(1)}$ = 12nm, D50$^{(2)}$ = 170nm, 8 days old

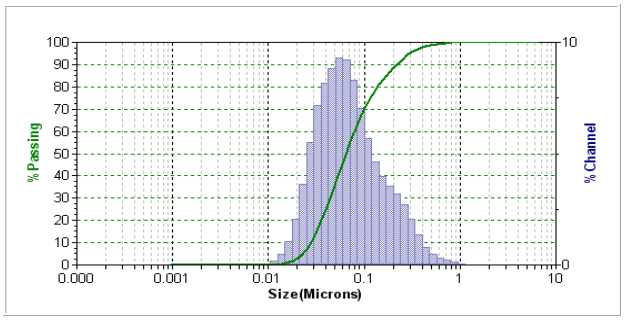

c) IE#19$_{(G)pH\ modif.}$, D50$^{(1)}$ = 65nm, 16 days old

Figure 34: PSD of the selected silica aquasols produced with the large scale ion-exchange (IE) set-up. The subscripts (S) and (G) stand for the "seed" and "grown" (measured after step 3 of particle build-up) sols correspondingly. The superscripts (1) and (2) indicate first and second modes in the sols PSD correspondingly.

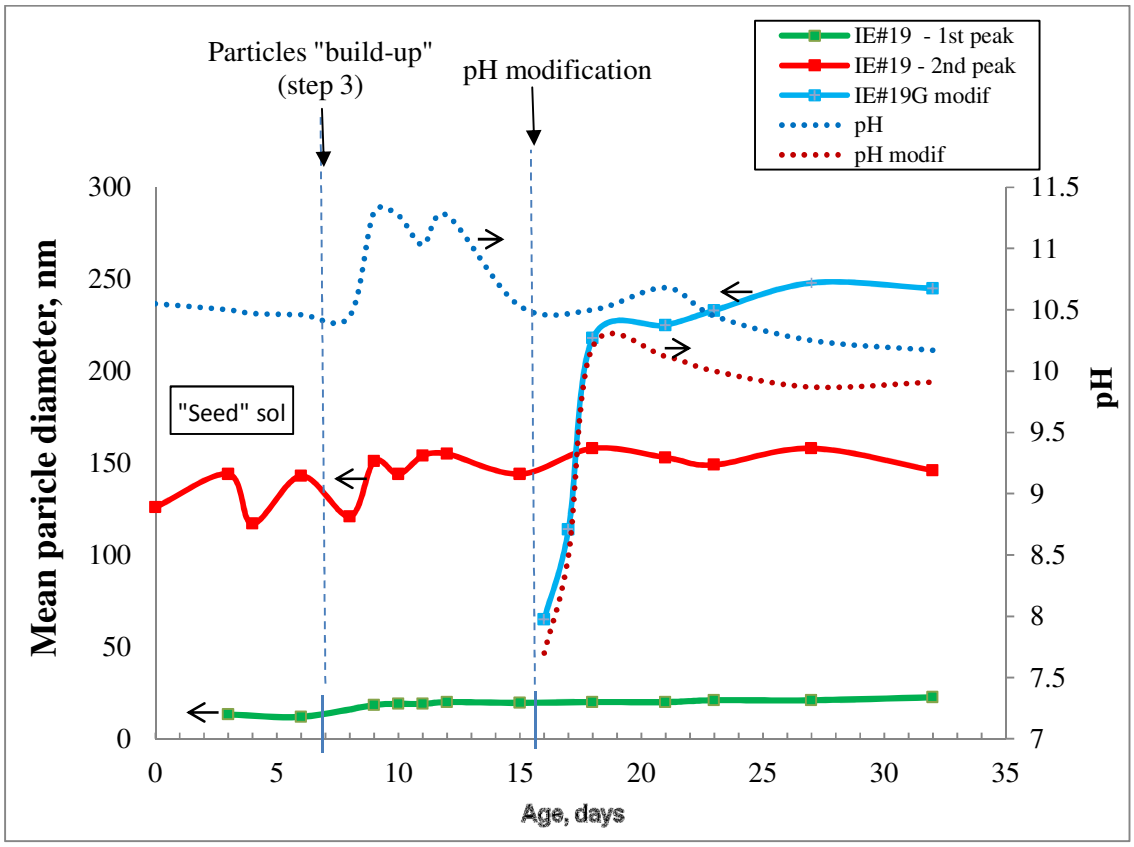

Figure 35: pH and mean particle diameter of the sol IE#19

Based on these results, two methods for production of 100-200 nm silica colloids with ion-exchange removal of sodium can be suggested. The first one is the two step approach described above – production and re-growth of the seed particles using ASA and their further growth facilitated by sol acidification.

Alternatively, only the first step, of "seed" particle production (Fig. 30a), can be used at lower ASA titration rate. It is evident from the small batch trials (Fig.32 IE ##13, 14) that this should result in synthesis of large particles. However, due to the limited size of the heating vessels it can be hard to achieve 1% SiO_2 concentration in the final solution. Two 5 L batches of ASA would need to be produced and titrated simultaneously at an identical rate and temperature to the water solutions with same KOH concentration. This must yield two ~6 L batches of 2 % silica sol with very close particle size distributions. Next they can be mixed together and diluted to 1% colloid SiO_2 to give enough sol for use in the deposition experiments. If there is significant difference in particle sizes between these two batches their mixture can also be acidified to promote particle growth and quickly smooth out any particle size discrepancies (as was observed for sol IE#19 in Fig.34 b vs. c).

The ionic strength, saturation with silica and total silica colloid concentration in the sols prepared with the ion exchange and acid-neutralisation methods were calculated (with the relationships given in Chapter 1) for the known amounts of the chemicals used for their production (Table 8). Assuming colloidal silica density to be 1500 kg/m^3 (71), (128), approximate particle number concentration was calculated as a function of mean particle size (Table 8). These values were used in Chapter 6 for calculation the coagulation and deposition rates to be expected in test rig experiments.

Table 8: Characteristics of colloidal silica solutions

Obtained from	SiO_2^{tot}, %w	$SiO_2^{colloid}$, ppm	Na_2O, wt%	IS, mol/L	Particle size, nm			
					15	70	100	150
					Particle number concentration, ppL			
Ion-exchange	1.02	9900	~0	0.03	3.74E+12	1.15E+11	3.96E+10	1.17E+10
Acid neutralisation	0.169	1600	0.175	0.1	5.95E+11	1.84E+10	6.30E+09	1.87E+09
Typical geothermal brine (25)	0.05-0.09	250-1000	-	0.03-0.05				

The advantages and disadvantages of the ion exchange and acid-neutralisation production methods are summarised below in Table 9.

Table 9: Comparison of colloidal silica production methods

Method	Pros	Cons
Ion-exchange	High SiO_2 conc. → High transport rate	Complex, time demanding
		Low IS→ Low attachment rate
		Uncertain SiO_2 concentration
Hydrolysis	Simple	Low SiO_2 conc.→ Low transport rate
	Na → High IS→ High attachment rate	

The sols produced with the IE method have the clear advantage of the silica colloids concentration being one order of magnitude higher than in those from acid-neutralisation method. Therefore, they are expected to provide higher rate of silica colloid transport in deposition experiments. On the other hand, according the DLVO theory the lower IS of these sols must also provide higher stability of their colloids. This may negate their higher transport rate and result in a same deposition rate as for the sols produced with acid-neutralisation method.

Since, the ion-exchange method is also much more time and resource demanding than acid-neutralisation only one of the sols prepared with it (IE#19) was used in the deposition experiments (Chapter 5).

Summary of Chapter 3: Outline of the methods used to control hydrodynamic and chemical conditions in the silica scaling experiments

The equipment, techniques and procedures used for the experimental study of the silica scaling process were described in this chapter. The implemented experimental approach consisted of the two parts: first, production of the colloidal silica solutions and second, their use in the deposition experiments with the flow rig.

The recirculation flow rig was designed and built by previous postgraduate (93) student to run synthetic colloidal solutions through a carbon steel pipe sections at controllable flow rate, temperature, pH and D.O. concentration.

The following range of operational conditions can be provided by the experimental setup:

- Reynolds number from 1000 to 60000
- Friction velocity (for NB15 pipe at 30°C): 0.03-0.18 m/s
- Temperature: 25−100 °C
- Pressure 1 atm
- Dissolved Oxygen concentration as low as 0.1 mg/L

Each deposition experiment lasted from 1 to 3 weeks allowing a detectable amount of scale to accumulate on the internal surfaces of carbon steel pipe sections. The test sections were then cut open and scale composition, morphology and mass were analysed.
Several modifications to the flow rig and experimental procedure were made in order to extend its capabilities and resolve some of the flaws revealed in the early experiments. In particular this included following changes:

- the rig was modified to fit longer pipe test sections (upto 1 m) and perform their flushing with N2 at the start and finish of each experiment with aim to minimise corrosion effect on a final result;
- the experiment commencing procedure was changed to assure complete removal of the dissolved oxygen from a colloidal solution before allowing its contact with the test section;

- an in-line sol filtration procedure was introduced to periodically remove silica aggregates from the flow rig during the deposition experiments.

Moreover, a different experimental set-up that would allow study of silica scaling in a parallel plate flow scenario was suggested. A corresponding new channel flow assembly was designed and built. It is expected to facilitate future silica scaling experiments by improving control over the initial contamination of the test surface, by making possible in-situ observations of the scale development and constant temperature anemometry (CTA) probing of the near-wall region, which is expected to be affected by the scale build.

Next, two methods of colloidal silica synthesis were described. First, a straightforward, inexpensive and scalable method for production of silica aquasols through a two-step hydrolysis of sodium metasilicate was reported. The production conditions leading to synthesis of silica sols with mean particle sizes ranging from 10 to 60 nm and low polydispersity (PI between 0.05 and 0.2) were identified. Although, this method yields relatively dilute sols, their colloidal silica concentration of about 1600 ppm is still more than three times that of the total silica concentration in geothermal brine. Therefore, these sols are suitable for laboratory scaling experiments, where measurable amount of the scale need to be deposited over a reasonably short period of time.

Second, a more complex method which involves use of ion-exchange step for the production of active silicic acid and it consecutive polymerisation into silica colloids was also reported. Again, a series of production trials was performed and optimal conditions for synthesis of more concentrated and monodispersed colloidal solutions with large particles (up to 250 nm) were identified. While this method is capable of producing concentrated sols with larger particles than the hydrolysis of sodium metasilicate its complexity has eventually limited its use in this research to a single deposition experiment.

Therefore, adopted for this research methods of colloidal silica production can provide following range of chemical conditions:

- Average colloidal silica diameter from 10 to 200 nm
- Colloidal silica concentration up to 10000 ppm
- Solution ionic strength 0.03-0.1 M

4 PRELIMINARY DEPOSITION EXPERIMENTS WITH SHORT MILD STEEL PIPE SECTIONS

4.1 Experimental conditions

A series of thirteen initial scaling experiments was conducted with the purpose to test the experimental setup, establish the range of its operational parameters which can maximize the rate of data accumulation and, finally, to gain preliminary knowledge about the scaling process. Therefore, in most cases the conditions were at the extreme of the hydrodynamic and chemical parameter space explored (Table 10).

In all these experiments 150 mm long 15 mm ID mild steel pipe sections and colloidal silica solutions obtained with the simple production method (see section 3.3.2) were used in order to reduce operational costs and facilitate data output.

Table 10: Conditions of preliminary scaling experiments

	Exp. #	Average Flow rate, L/min	T,°C	Duration, days	Sol #	Mean particle size, nm	Average Loading Index	Average pH
Preliminary testing – 150mm NB15 MS pipe	1	6.6	25	14	29+30	18	-	-
	2	6.6	25	14	31+32	12±2	0.005	8.7
	3	6.6	27	21	36+37	14±3	0.009	8.5
	4	31.2	30	28	38+39	19±3	0.006	8.65
	5	31.2	34	14	33+34	21	0.007	8.1
	6	6.6	44	16		20±0.5	0.007	8.3
	7	31.2	45	15		21±1	0.008	8.3
	8	6.6	45	17	Saturated Si Solution			8.4
	9A	6.6	25	21	40+41	45±2	0.019	8.7
	9B	6.6	25	21		47±2	0.02	8.7
	10	31.8	34	10		40±3	0.02	8.6
	11	31.8	34	16	42+43	35±2	0.018	8.8
	12	31.8	36	14	44+45	35±3	0.027	8.7
	13	31.8	36	14		40±5	0.037	8.7

Q, l/min	6.6	32
V, m/s	0.48	2.3
$Re_{@30°C}$, 10^3	9.1	53.2

Table 11: Effects tested in deposition experiments ## 2-10

Experiment number	Tested Effect
2, 3 vs. 6	Temperature and Particle size effects
3 vs. 4 6 vs. 7 10 vs. 9 A,B	Flow rate effect
4 vs. 5 9A,B vs. 3 10 vs. 5, 4	Particle size effect
5 vs. 7	Temperature effect
6 vs. 8	Colloidal vs. Monomeric deposition
9A vs. 9B	Pipe surface state (cleaning technique)

The experimental conditions and tested effects are described in Table 10 and 11 correspondingly and also discussed below:

Thermal and Hydrodynamic:

- Flow rate: experiments with the minimum and maximum flow rates realizable on the rig – 6.6 and 32 L/min ($Re = 9\text{-}50 \cdot 10^3$) were conducted;
- Temperature: working sols were additionally heated up to 45^{o}C in the experiments # 6-8 and left at equilibrium temperature (determined by the pump thermal output: 25 ^{o}C at the low and 34 ^{o}C at high flow rate) in all other experiments;
- Local flow disturbances: in the experiments # 1-8 the longitudinal weld seam and minor extruded lips (local bore contractions caused by pipe cutting with roller blade) at the pipe section inlet and outlet were introduced by the pipe production and test section preparation processes respectively. The seamless pipe sections with the extruded lips cut off was used in experiments # 9-13;

Chemical:

- Dissolved Oxygen content in the sol: was not controlled (and, so can be assumed to be at saturation value) in the experiments #1, 2 and was kept below 30 % of saturation in the experiments # 3-13;
- Colloidal vs. direct deposition: on average, 1550 ppm of colloidal and 140 ppm of monomeric Si were present in the solutions during all deposition experiments except for the experiment # 8 in which water solution with 185 ppm of monomeric silica was used;

- Particle size: was 10 – 20 nm in experiments # 1 through 7 and 35 – 50 nm in experiments # 9 - 13;
- Degree of sol aggregation: experiments # 1-10 were conducted with nearly monodisperse sols, while in the experiments # 11-13 about 30 % of the particulate volume was represented by micron sized silica (which presumably occurred due to the hydrodynamically induced aggregation).

Surface properties:

- Thermal treatment of the pipe surface in the near weld region may have affected scale distribution in the experiments # 1-8;
- Chemical pre-treatment: different degrees of test surface initial contamination were encountered (rust, lubricant from the threading machine) and thus different cleaning methods were attempted: soaking in and spraying with ethanol or acetone, wiping with a cloth and/or paper towel (the spraying with acetone and wiping with a paper towel worked the best).

The duration of the experiments was from 10 to 28 days. At the end of the experiments each test section was dried and cut open in longitudinal direction giving two parts – top and bottom. This was not enough to observe significant scaling and complete coverage of the surface was never seen. Even though colloidal silica concentration in our deposition experiments is three times higher than in previous scaling experiments conducted using natural geothermal brine (43), it was deemed impracticable to determine the rate of silica scale growth. However, information about the location of first deposition and the morphology of the first stages of scale growth was obtained.

4.2 Scale distribution, morphology and composition

Fig. A1-A85 in the Appendix A illustrate the optical, scanning electron and energy dispersive (SEM/EDS) observations of the scale obtained in the preliminary scaling experiments. They allowed characterisation of the scale in terms of its terminal distribution across the test section length and circumference, morphology and composition presented below in Table 12:

Table 12: The examination of the deposits formed in the preliminary scaling experiment

Exp. #: *Flow rate; P. size*	Observations	
	Visual/Optical	SEM/EDS
1a:	Most of the test surface was covered with	n.a

6 L/min; 18 nm; 25°C	orange-red layer of bumpy deposits. The vicinity of weld seam and few patches at the inlet and outlet were clear. Optical close-up suggested that first thick layer of corroded iron formed and then some silica was deposited on top of it.	
1b: *6 L/min; 18 nm; 25°C*	If compared to the experiment #1a much less corrosion was seen downstream from test piece centre. Again, no deposition near the weld seam was observed.	n.a.
2: *6 L/min; 12 nm; 25°C*	The discontinuous layers of brown deposit at the wall and white deposit on top of it were seen. They covered more of the surface close to the pipe section inlet and outlet, less – at its centre section. No deposition was near the weld seam.	The brown deposit was found to be a ferric oxide and the white deposits seen on top of the brown ones were recognized as dense silica plates and agglomerations of silica globules on their surfaces.
3: *6 L/min; 14 nm; 27°C*	Barely visible deposits were present, with more deposits found at the bottom part the (horizontally positioned) pipe section close to its outlet.	The congestions of the silica globules (0.1-2 µm in diameter), concentrated at the edges of the native mill scale plates were observed.
4: *31 L/min; 19 nm; 30°C*	A distinctive stripe of relatively thick deposit broadening towards the pipe outlet was observed at its bottom part next to the weld seam. The remaining surface was speckled with yellowish stains.	The densely packed silica globules constituted the stripe. The stains were observed to be "islands" (0.3-0.6 mm in diameter) of flocculent silica fringed by the denser silica border.
5: *31 L/min; 21 nm; 34°C*	Greenish scale continuously covered entire test surface. Vicinity of the weld seam was dark grey in colour along its whole length. Closer look on the greenish scale showed that it is speckled	White substratum of the strange lines of deposit was determined to be a nickel deposit arranged in a net of honeycomb shaped cells. It was covered with a structureless silica film.

	with smoothed, pale red bumps and greenish cover in between them. Two distinctive green lines of deposit stretched from the inlet to the centre of the top half of the test piece. Optical magnification revealed layered structure of the lines of deposit. Brilliant white substratum under the yellowish-green film was seen.	The rest of test surface was covered with same silica film and irregularly shaped bumps with high content of silica and oxygen.
6: *6 L/min;* *20 nm;* *44°C*	No prominent deposits, interlaced yellow-black stains over the most of the surface, bigger yellow stains closer to the weld seam, dark contaminant immediately next to it were observed	No globules; smooth, flocculent silica; high content of carbon, oxygen, silica and less sulphur in the yellow stains were detected. More carbon and sulphur and less silica were found in the dark region next to the weld seam
7: *31 L/min;* *21 nm;* *45°C*	0.05-0.1 mm green-red bumps were spread all over the tested surface, their number concentration was higher closer to the pipe inlet, where yellowish stains were also observed.	The bumps were accumulations of elongated oval shaped silica globules 50-100 μm in size. Interspaces between the bumps were covered with silica plates and a number of similar elongated globules.
8: *6 L/min;* *-;* *45°C*	The test surface appeared clean from a prominent deposition. There was slight discolouration of the test surface. A pattern of small dark patches was observed all over the test surface. This was not characteristic for a clean pipe. Higher magnification (Fig.A40) revealed darker plates with lighter interspaces on pipe surface.	A thin, smooth, structureless layer of silica (similar to that seen in experiment #5) was observed in between the native mill scale plates. The deposit was not particulate in any way.
9A: *6 L/min:*	Starting from the inlet ¼ of test surface length was black with no visible scale or	The structure and composition of the "islands" were identical to those

45 nm; 25°C	signs of corrosion. Further downstream the surface was smooth and gold-yellow with light-yellow dots spread across it. More of these dots, arranged in the lines parallel to the flow, were found closer to the pipe outlet. Optical close-up showed that the dots were white, spherical bumps 0.01-0.05mm in diameter. They were most common inside closed areas of dark-yellow deposits similar to the "islands" seen in the experiment #4.	observed in the experiment #4. The bumps were seen to be agglomerations of densely cluttered silica globules (0.1-2 μm in diameter). The bump surface morphology and shape seemed to be affected by the flow – they were densely packed and blunt at the windward side and crumbly and elongated at the leeward side. A number of smaller bumps was also formed downstream from the bigger bumps (in their wake zones).
9B: *6 L/min; 47 nm; 25°C*	The entire test surface was pale grey in colour with darker rough deposits concentrated at the inlet and central part of the test piece. The sparse white bumps and yellow stains were seen in-between the dark rough elements.	The dark roughnesses were observed to be the build-ups of smooth, unstructured silica on top of rust. A few bumps similar to those seen in experiment #9A and stains of small scales of silica with high content of carbon and oxygen were detected.
10: *32 L/min; 40 nm; 34°C*	The test surface was entirely covered with yellow streamwise lines, lighter spanwise ridges and darker bumps. More lines were seen closer to the outlet, while more ridges were noticed at the centre and more bumps - at the inlet sections of the test piece. The ridges were arranged in 0.5 mm spaced rows perpendicular to the flow direction. Optical magnification showed that the bumps were dark red in colour and had irregular shape (in range from a hemisphere to a plate, being 0.01-0.15 mm in size correspondingly).	The bumps consisted of number of the hemispherical silica globules, 1-10 μm in biggest dimension; stacked together to form structures protruding above the surface for about 0.1 mm. The shape and surface morphology of the globules were affected by the flow even more than in experiment #9A. The globules which were located closer to the pipe surface were smoother and more symmetrical. While the globules on the flow facing sides of the bumps were smoothed on the windward side and covered with

	White ridge-like deposits seem to be formed by colloidal deposition onto the bumps windward side. Their length and width were 0.075-0.2 mm and 0.04-0.13 mm correspondingly. The lines had a width of 0.1 mm and seemed like the spatters of yellow deposit located between the groups of the bumps.	friable, stretched in flow direction agglomerations of smaller (0.1-0.5 μm) silica globules on their elongated downstream part. In between the bumps tested surface was covered with a smooth, continuous film of silica deposit. Some pattern of cracks was noticeable on its surface. Closer examination suggested that the film was formed by the small, up to 1 μm, silica globules cemented in by even smaller silica elements. The lines of spattered deposits consisted of the rows of silica structures following one another (see Fig.A58-5) sitting atop the film. Their in-plane size was 1-10 μm and they did not appear to protrude much from the surface. They had irregular shapes, usually elongated in the flow direction. The flow facing side sometimes had a horseshoe shape, with the edges shifted upstream.
11: *32 L/min;* *35 nm;* *34°C*	The entire bottom half of the test section except for a small patch at the outlet was covered with numerous small (0.1-0.5 mm), closely positioned yellowish bumps of deposits. The bumps seemed to be seating on top of the thin, continuous film of greenish deposit. At some locations this film separated and formed circular stains of exposed pipe surface. Fewer of these protruding bumps were	The bumps composed of silica; the smaller ones had irregular shape, the larger ones were irregular at the base with flat, wall-like top facing the flow. The sides of the bumps were covered with agglomerations of cluttered silica arranged in a branched system of lines (about 10 μm long and 1-2 μm wide). The globular silica agglomerations sometimes were present on the leeward

	found on top half of the test section, especially in its middle section. Most of its middle part had a smooth, brown coating with the bumps preferably located on the patches of more dark coating. The outlet section at the top part was also almost clean of deposits and had dark mirror-like surface.	sides of the bumps. The test surface which was free of the bumps had thin coating composed of silica, copper, iron and oxygen.
12: *32 L/min;* *35 nm;* *36°C*	Virtually no protruding deposits were observed. A thin film of dark brown, in some places greenish deposit was present on the top and bottom parts. Optical close-up showed that it consists of multiple, small (0.1 mm), dark-reddish bumps. It was thinnest, almost absent, in the middle of the bottom part of the test section. There were multiple round stains of the exposed wall surface, same as seen in experiment #11.	The bumps composed of silica and iron oxide; they had smooth, as if melted, surface morphology and seemed to be built of several discrete layers of material which was often arranged in circular patterns. The flat test surface composition was mainly iron oxide with traces of silica and copper.
13: *32 L/min;* *40 nm;* *36°C*	The scale was represented by several types of structures: large (1-2 mm), dark red lumps; light-yellowish spanwise ridges (located 2-3 mm apart in flow direction); dark-green coating in-between them. Fewer of these deposits were found at the middle of the test section.	The dark coating was identical to the bumpy deposit seen in experiment # 12. The ridges appear to be assemblies of wall-like bumps seen in experiment #11. The lumps were described as bulky structures of densely packed silica. Noticeable cracks (probably occurred due to the thermal creep during test piece drying) were seen on their surface. The lumps had smooth leeward sites and windward sites covered with globular silica.

4.3 The effects of the hydrodynamic and chemical conditions on the silica scaling process

The effect of flow rate on the scaling process was tested in three pairs of experiments (## 3 vs. 4, 6 vs. 7 and 9 vs. 10). An overall increase of the deposition rate with the flow rate increase was observed. The comparison of the experiments #3 and #4 suggested that scaling proceeds faster at the locations with thicker boundary layer and/or local hydrodynamic disturbances.

The fastest scaling was observed in experiment #10, at high flow rate and with large particles. Comparison of the distribution and structure of the scale formed in the experiments #10 and #9, which differed from #10 only in lower flow rate, suggested that particle deposition proceeded in three steps. First, by particle attachment to the flat regions of the test surface and formation of thin, eventually, continuous film covering entire test surface.

Second, by the deposition onto the roughness elements initially present on the surface or onto the spontaneously formed bumps of deposits. These bumps grow into hemispherical agglomerations of presumably initial colloidal particles at low flow rate. At high flow rate they grow bigger and appeared to be built up of several hemispherical agglomerations, similar to those mentioned above, stuck together. It is possible that after the bumps become large enough another more rapid process of colloidal deposition on their windward sides commences, which results in their widening and formation of the characteristic spanwise ridges of scale.

The third deposition process is responsible for the formation of long, thin, parallel to the flow lines of deposit consisting of small equally spaced lumps of silica. Their positioning between the bumps and on top of the film suggests that the corresponding deposition mechanism responsible for their formation starts later than the first two.

The rates of all these deposition processes were found to increase gradually downstream from the test section inlet.

Two experiments (#6 and #7) were conducted at elevated temperature to test thermal effects on the scaling process. The scaling rate was found to be lower at higher operation temperature as was expected due to the increased silica solubility and thus partial dissolution of the colloids (see section 1.3). The unusual oval shaped silica scale structures were formed in the experiment #7 under nonisothermal conditions (temperature of the bulk flow was 45°C and ambient temperature was 20°C). Their elongated shape can be explained by the correlation between the particle attachment

probability and temperature dependence from the normal-to-wall distance. A relatively low thermal conductivity of amorphous silica (~1.5 W/m·K) determines a high temperature gradient across the bump height – its top must be at temperature much closer to the bulk flow temperature than its base. The regions with lower local temperature, which were closer to the pipe wall in case of the experiment #7, had higher local silica oversaturation degree and thus higher density of the ionized sites on the amorphous silica surface with which the new depositing particles can bond. In addition, more of the oversaturated monomeric silica is present in solution at these locations to cement the particles in.

The experiment #8 confirmed that direct (monomeric) silica deposition occurs at a much lower rate than colloidal. It also showed that silica monomers deposited more uniformly than colloids and formed a thin amorphous film covering flat regions on the mild steel surface with slightly higher thickness around the base of the mill scale plates (see Fig. A41).

The comparison of the scale formed in experiments #4 vs. 5 and 3 vs. 9 showed that colloidal deposition rate increased as the particle size increased. The deposits with more complex structure were formed by the larger particles.

Significant differences in the outcomes of the otherwise identical deposition experiments were contributed to the differences in test surface state. For example the more rigorous prior cleaning of the test surface that was used in the experiment #9B and resulted in less scaling than in the experiment #9A. The test piece was cleaned by first soaking it in ethanol (for couple of hours) and then gently wiping with paper towel prior to the experiment #9A. The #9B test piece was sprayed with ethanol and thoroughly cleaned with the same paper.

The SEM/EDS examination of the native pipe surface pre-soaked in ethanol revealed traces of the rust and other contaminants (e.g. phosphorus, sulphur) present on its surface. It is possible that, in addition to the corrosion, part of the lacquer coating, present on the outer surface of the pipe, was dissolved in ethanol and contaminated the internal surface. The dirtier and partially rusted surface most probably promoted scaling in experiment #9A if compared with the experiment #9B.

Test surface contamination by traces of a lubricant (originated from the process of cutting the threads of the test pieces) was likely responsible for a lower scaling rate observed in the experiment #6. The nickel presumably dissolved from the threading tape and re-deposited on the test surface and formed the specific “cellular” undercoat in the experiment #5.

Early experiments (##1-3) showed the importance of the dissolved oxygen (D.O.) concentration for the scaling process. High D.O. content in the sol caused immediate corrosion of the test surface at the start of the deposition experiments. A thick layer of rust was formed first which promoted later silica deposition on top of it. Since this obviously did not correspond to the pursued process of pure silica deposition, the test rig was upgraded with oxygen exclusion system (section 3.1).

The effect of aggregation on the deposition process was identified in the experiments ## 11, 12 and 13 identified. As will be seen from the Fig.53 and 54 later in section 6.1.2 experiments #11 and 12 were started with fairly monodisperse sols. In due course of these experiment the sols started to aggregate which was detected by particle size measurements as appearance of the secondary peaks in the micron range of the particle size distributions.

The deposition of silica aggregates was presumed to be responsible for the formation of unusually shaped, large, tower-like bumps found in higher number on the bottom part of test section from the experiment # 11. The SEM images showed that the surface of these protrusions was represented by a numerous branched rows of rough silica (Fig. A69). Their structure and spatial configuration suggested that they could have been grown by the advective deposition of 1-2 μm silica flocs preliminary formed in the flowing suspension.

Even though the sol in the experiment #12 experienced higher rate of aggregation the amount of deposited material was less than in the experiment #11. This was suggested to be due to more significant contamination of the surface in the experiment #12.

Apparently an additional source of contamination was present in the experiments #11 and 12. High SEM magnification of the corresponding sample surfaces revealed the presence of a large number of small (<100 nm) conducting particles on flat pipe surfaces. The EDS analysis suggested those to be copper nanoparticles. Since these particles appeared to sit atop (see Fig.A68) a thin film deposit untypical for the native pipe surface (see Fig.A86-89) it is likely that they deposited either during or after the completion of the experiment. The later could have occurred for example while cleaning the test samples with acetone at the end of the experiment. The black stains that appeared close to the edges of the test samples (see Fig.A63 and A65) most probably were formed by the re-deposition of the black lacquer coat dissolved by acetone from the outer wall of the pipe.

However, the possibility of these copper nanoparticles and unusual surface morphology to be present on the native pipe cannot be disregarded completely. The relevant sample surface was not examined prior to the deposition experiment to test this.

Another possible source of copper in the test rig was copper heating element which apparently corroded and lost part of its zinc coating. Therefore, it was later replaced by Incoloy heating element.

The larger number of these copper nanoparticles observed on the test piece surface in experiment #12 might have retarded the scaling if compared with experiment #11.

The experiment # 13 was conducted with the sol left after completion of experiment #12. It was already partially aggregated (see Fig.54 Chapter 6). This can explain the higher rate of deposition than in the experiment #12.

The increase of the scaling rate with the distance from the test section inlet observed in the majority of the reported above experiments suggested that diffusion is unlikely to be the dominant particle transport mechanism.

Since the thickness of the viscous sublayer in the inlet region of the turbulent pipe flow increases with distance from the inlet (95) the corresponding diffusion mass transfer across the boundary layer would be expected to decrease with distance from the pipe inlet.

Once the viscous sublayer reached its constant maximum height, approximately after 40 pipe diameters past the inlet, flow is said to be hydrodynamically developed. Since rate of the mass transfer, governed by the particle Brownian diffusion, is lower than momentum transport rate, governed by the water viscosity, it takes longer for the developed concentration profile to establish. The diffusion mass flux must be highest at the inlet and decrease to a constant value reached after about 100 pipe diameters from the inlet.

However, diffusion still can be the dominant transport mechanism if the following is true. The deposits protruding from the wall surface can disturb the flow immediately downstream and significantly increase the rate of turbulent mass diffusion to the surface. Cascaded downstream, such events would result in an increase of the scaling rate with the distance from the inlet, even though diffusion is still main particle transport mechanism.

This hypothesis of the self-accelerated growth of the scale can be tested with a knowledge of the scale formation chronology. If the scale first forms at the locations of thin boundary layer and then propagates (with accelerating rate) downstream then the hypothesis is true. Otherwise, if the scaling has higher rate and constant in time, where the boundary layer is thicker than alternative explanations must be considered.

The inertial mechanism of particle transport was proposed as one such possibility (Chapter 1). The rates of the inertial transport mechanisms which depend on the local velocity gradients may increase with thickening of the boundary layer downstream from the pipe inlet. For example, the Saffman lift force may transport particles to the wall more effectively due to the wider region of non-uniform velocity distribution.

Preferential deposition onto the areas protruding above the wall surface was noticed in some of the experiments, especially those where larger particles were used. While both diffusion and inertia may be responsible for this (see section 1.4.1), the inertial effects can be expected to be stronger in this case.

In contrast to a flow over flat surface a particle moving in a flow around a protrusion above the flat surface can deviate from the flow path lines and become projected onto the surface. This particle ability is characterized by the Stokes number – if it's higher than unity the particle can deviate from the flow direction. It can be shown that under the conditions of the present experiment, the Stokes number for a particle moving around a roughness element or protrusion can be higher than (see section 6.2). In this case higher deposition rate would be expected at the windward side of the protrusion.

As mentioned above, protrusions generate additional turbulent mixing downstream and thus increase diffusion flux to the surface. In this case a higher deposition rate would be expected on the leeward side of the protrusion. Thus, the scale elements being inclined towards the flow direction (i.e. preferential growth on the windward side) suggests prevalence of the inertial mechanism of their growth.

Summary of Chapter 4

This chapter presents overview of the initial scaling experiments which were conducted with the purpose to test the experimental setup, establish the range of its operational parameters and to gain preliminary knowledge about the scaling process.

The total amount and distribution of the scale and type of the test surface did not allow accurately quantification of the rate of the scale growth in these experiments. Its mass was too small to be measured either by weighing scraped-off scale or by measuring the difference in the test piece mass before and after the experiment. The latter method was inaccurate due to the small ratio of the surface area exposed to scaling and pipe test section volume. A test surface with higher surface-to-volume ratio (e.g. a thin plate) might suit better for such measurements. Moreover, in most

experiments the obtained scale was too thin and non-uniformly distributed for accurate profile height measurements. Only in experiment # 10 was the scale was thick enough and evenly distributed at the outlet part of the test section to make these measurements possible.

In general, use of the sols with larger particles was found to cause higher scaling rate and thus to be more promising for growing measurable silica scale covering the entire test surface. However, as experiments ##9-13 showed these sols were also prone to aggregation (especially when subjected to the high flow rates). This means that they cannot be used in the deposition experiments for longer than 1-2 weeks without obscuring the results by the deposition of the aggregates.

The high irregularity of the scale observed in the experiments ##11-13 may be due to the presence of up to 30 % (volumetric fraction) of micron size silica aggregates. Such large particles must exhibit deposition behaviour different from 10-50 nm particles, making the experimental results inconclusive.

There are two possible solutions to the aggregation problem. The first is to prevent or slow down the aggregation of the primary particles during the deposition experiments. This can be achieved chemically – by increasing stability of the sols by using the ion-exchange process to remove sodium ions from them. This, as was discussed in Section 3.1, would decrease the ionic strength of these sols, allow increased silica concentration and duration of their continuous use in the deposition experiments. However, together with the aggregation the deposition rate would also decrease as a result of increasing particle stability

Therefore, the second possible solution - to remove the formed aggregates from the solution before they can deposit – can be more promising and easier to implement. It was done in the scaling experiments with long pipe test sections reported in the next chapter.

In addition, the preliminary scaling experiments revealed following experimental difficulties:

- Control of the test surface properties prior to the experiment – as the pipe sections did not allow access to the test surface prior the experiment, it was very hard to provide known, repeatable surface conditions;
- Control of the sol parameters during the experiment – after implementation of the nitrogen blanket sol sampling was performed through the tap at the bottom of mixing tank. This way was proved to be unsuitable both for the D.O. (due to the sample contact with atmospheric oxygen upon drainage) and particle size measurements (since aggregates and contaminants tend to accumulate at the bottom of the mixing tank). In the following experiments the D.O.

and pH readings and sol samples were taken directly from the mixing tank through the open plastic lid on top of it.

- Observation of the scale growth – an ambiguity in the origin of exotic silica structures observed in some of the deposition experiments (silica "islands" in experiments ## 4, 9A) was established. An ability to observe the deposition process in situ would help to determine what scale structures formed during the experiment and what were the result of the test surface treatment at the end of the experiment.

The increase of the scaling rate with the distance from the test section inlet observed in reported above experiments suggested that diffusion is unlikely to be the dominant mechanism of particle transport onto a flat surface. However, acceleration of the diffusion particle transport downstream from the scale elements protruding from the surface may take place. An alternative experimental test section was suggested and developed (section 3.2) in order to provide relevant scaling data and test this hypothesis.

Preferential deposition onto the areas protruding above the wall surface was noticed in some of the experiments, especially when large particles were used. While both diffusion and inertia may be responsible for this the inertial effects are expected to be stronger in this case.

The increase of scaling rate with the increasing flow rate and particle size suggests that inertial transport plays a prevailing role. However, this increase in scaling rate may also be an outcome of the lower stability, and thus higher attachment probability of the larger particles. The issues of particle stability and particle inertial deposition onto wall protrusions will be discussed in detail in Chapter 6.

5 SILICA SCALING AND AGGREGATION IN DEVELOPED TURBULENT PIPE FLOW

5.1 Scope and peculiarities of the experiments

The effects of the flow rate, particle size and concentration on the rate of silica scaling were studied in the second series of deposition experiments with stricter control over the hydrodynamic and chemical conditions. Thus, the usage of 1 m long NB15 MS pipe test sections assured realisation of the fully hydrodynamically developed flow. The control over the particle size and concentration was improved by the introduction of periodic filtration (see section 3.1) and replacement of the solution over the course of these experiments.

The variation of scaling rate along the test section length, and thus its correlation with the hydrodynamic and diffusion boundary layer thicknesses represented an additional research interest.

Ten scaling experiments were performed (Table 13). Their duration was between 11 and 21 days. Two values of the flow rate - 16 and 32 L/min were tested in three pairs of experiments (see Table 14). The particle size effect was studied by comparing the results of three deposition experiments (with 20, 46 and 54 nm particles correspondingly, with all other conditions held constant). Finally, two particle concentrations - $C_{Si\ colloid} \approx 1600$ and 10000 ppm - were experimented with.

The different particle concentrations were achieved by employing colloidal silica solutions prepared with different methods – acid neutralization (section 3.3.2) and ion-exchange method (section 3.3.3) for experiments with low ($C_{Si\ colloid} \approx 1600$ ppm; sols ##52-69) and high ($C_{Si\ colloid} \approx 10000$ ppm; sol IE#19) particle concentration respectively.

The Loading Index (LI), which was measured during dynamic light scattering (DLS) particle size analysis and which measures total light scattered by particles (section 3.3.1), was presented in Table 13 as a measure of particle concentration. The larger value of LI reflects higher particle concentration if the particle size is constant (and vice versa).

The variable heat output of the pump at different flow rates resulted in a slight difference of the solution temperature in these experiments ($25-37$ °C). The Reynolds numbers and friction

velocities evaluated at 30 °C for the two flow rates stated above are 28000 and 56000 and 0.09 and 0.18 m/s respectively.

The ionic strength (IS) of the colloidal solutions was not initially intended as a research parameter, but introduction of the conductivity measurements in this series of experiments and, as a result, the variability revealed in the solutions IS (owing to differences in production conditions) allowed observation of its effect on the scaling process as well. However, a rather narrow range of the IS values was tested: 0.06-0.08 M.

In addition, it should be kept in mind that IS was different in the two experiments aimed to test particle concentration effect (#23 vs. #24). The sol prepared with the ion-exchange method and used in experiment #24 had lower IS: 0.03 M.

Table 13: Conditions of scaling experiments with developed pipe flow

Exp. #	Average Flow rate, L/min	T,°C	Duration, days	Sol	Mean particle size, nm	Average Loading Index	Average pH	Average Conductivity, μS/cm
18 a	16	25	21	52+53	46±4	0.088	9	7
18 b	16	25	21		51±3	0.11	8.6	7.13
19	30	36	14	54+55	53±4	0.15	9.3	7.3
				56+57	45±2	0.11	9.1	6.8
20	30	37	12	60+61	45±4	0.09	9.2	6.76
				58+59	50±8	0.1	9.4	7.6
21	16	32	11	62+63	46±3	0.07	9.2	6.6
				64+65	46±1	0.06	9.3	6.7
22	16	32	16	66+67	54±4	0.065	9.3	6.25
23a	16	32	21	68+69	20±1	0.03	9.1	6.3
23b	31	36	21		21±1	0.032	9.5	6.2
24a	16	33	21	IE#19	21±1	0.37	8.8	5.5
24b	31	36	21		21±1	0.33	8.8	5.2

Table 14: Effects tested in deposition experiments ## 18-24

19, 20 vs. 22 23a vs. 23b 24a vs. 24b	Flow rate effect
21, 22, 23a	Particle size effect
18a,b vs. 21 19 vs. 20	Solution ionic strength effect
23a,b vs. 24a,b	Particle concentration (and IS) effect

The results of the experiments #16 a and b and #17 are not reported herein since they were impaired by rig contamination with oil, which most probably leaked into the mixing tank from the mixer motor gearbox (Fig.36). Three cleaning runs conducted in-between these experiments (by circulating soapy warm water in the rig over 2-3 days and rinsing it with tap and distilled water) were seen to render the rig free of oil. The mixing motor was since removed to avoid recurrence of the contamination.

a) **b)** **c)**

Figure 36: (a) Mixer shaft (enters the holding tank through its lid) and contaminated fluid in the mixing tank at the end of the experiments (b) #16a and (c) #17

5.2 Observations of the colloidal silica aggregation and deposition

Fig. A90-A285 in Appendix A illustrate the optical, scanning electron and energy dispersive (SEM/EDS) observations of the scale formed in the experiments ## 18-24. They allowed characterisation of the scale in terms of its morphology, composition and distribution across the circumference and length of the test section.

The experiments #18a and b were conducted with 50 nm silica particles and a flow rate of 16 L/min. Except for the reddish gel settling at the bottom of holding tank at the end of experiment #18b (Fig.A91), the sol remained clear over the duration of these experiments. The scale distribution was highly uneven in the experiment 18a with more deposits evident at the bottom of the test pipe than at the top (Fig.A90).

This was suggested to be either due to the settling of colloidal silica aggregates, formed during this experiment, or due to the initial contamination of the top part of the pipe section. The calculation of the settling velocity (neglecting particle lift and convective/turbulent redistribution) for a 5 micron aggregate showed that it can settle down only by about 0.01 mm during its residence in the pipe test

section. On one hand this may be enough to affect particle number distribution over the section diameter, but on the other hand intensive turbulent mixing, which was actually present in the experiment, must had rendered this settling effect negligible. So, most probably non-uniformity of the initial surface properties affected particles attachment and/or the rate of surface corrosion, and lead to a preferable deposition on the bottom part of the test section.

Experiment #18b was performed at the same conditions as experiment #18a. Only the test pipe section was replaced. The same colloidal silica solution was left in the rig and used for the experiment #18b. This time equal scaling rate for the bottom and top halves of the test section (Fig.A90) was observed. This supported the "initial surface state" explanation of the uneven scale distribution observed in the experiment #18a.

The larger amount of scale formed in the experiment #18b can be explained by a higher degree of the aggregation and higher concentration of corrosion products (ferric oxides promote colloid aggregation) characteristic of this experiment.

The scale formed in these two experiments had a soft, loose structure (Fig.A93). This supported the hypothesis that it was formed by the deposition of aggregates. The larger particles are expected to have larger gaps in-between them as they deposit. It is suggested that the sparser and weaker scale structure must be formed by the aggregates.

A closer examination of the scale showed that it consisted of two types of deposit: first, relatively large (up to 0.2x0.2 mm and 0.07 mm high), reddish bumps with a smoother, inclined upstream side and white fringes (Fig.A93). Second, the entire test surface was covered with white globular deposits (except for small patches downstream from the bumps). The globular elements were seen to be slightly elongated in the flow direction (Fig. A94).

The bumps were distributed slightly unevenly over the sample surface: more of them were seen in regions with orange coloured globular deposits (Fig.A93). The SEM examination of the sample surface inside one of these regions (Fig.A99) showed that globular deposits sat on top of a flat film, cracked in some places, which was not typical of a native pipe surface (Fig.A86-89). The surface of this film was also covered with tiny, thin "crystals" (Fig.A99) similar to those observed on the corroded surfaces of carbon steel (137)

The EDS analysis (Fig.A100 and 101) confirmed higher concentration of iron on the orange coloured stains seen in Fig.A93. From now on they will be referred to as rusty islands.

The experiment #19 was conducted at higher flow rate (30 L/min) than experiment #18, but with similar particles (50 nm in diameter). The scale formed in this experiment differed significantly: instead of more or less uniform distribution (observed in #18) the scale was highly localised. Numerous relatively large tower-like protrusions (up to 1 mm tall and 0.7 mm wide) and few yellowish deposits in the areas in-between the "towers" were observed in experiment #19 (Fig.A107-109).

The upstream incline of the "towers" suggested that they were formed by inertial deposition (Fig. A108).

Naturally such large protruding elements scattered over the surface of the pipe test section generated an additional hydraulic head loss. The corresponding drop in static pressure was measured to be 3 kPa. The head loss calculations (conducted with the relationships discussed in section 1.4.2) showed that such pressure drop can be explained by ether presence of uniform sand roughness of 0.25 mm or by the decrease of the pipe nominal bore by 1 mm (which is in a good agreement with the stated above size of the scale protrusions).

A closer examination of the pipe surface showed that seemingly clean surface of the sample is in fact a smooth black coat (Fig. A109). In some places this coat peeled off, assumedly together with some of the tower protrusions that were located there, and exposed a whitish underlayer.

This marks a significant difference to experiment #18 where the test surface in-between the bumps was covered with globular silica structures. This may be explained either by the hydrodynamic or surface chemistry effects.

The higher shear stress typical for the experiment #19 (twice as high as #18) means that a larger tangential force was exerted by the flow on the particles at the wall. This in turn could have resulted in a lower chance for a particle to deposit by diffusion and stay on (bond to) it to form the globular type deposit seen in the experiment #18. Instead the particles may tend to follow the flow up to the next protrusion and deposit on it by the inertial impaction if it was large enough (this in turn explains the growth of the tower-like deposits).

The unusual composition of the black coat revealed by SEM/EDS analysis can provide an alternative explanation. It showed that the coat consisted of numerous, small (<100 nm) copper rich particles (Fig.A114-118). It is possible that their presence (owing to some source of contamination) hindered silica colloid attachment.

The tower-like protrusions were found to be composed mostly of silica and oxygen (Fig.A111).

The SEM and EDS observations showed in Fig.A119-133 suggested that large elements of scale, including the tower-like protrusions, were formed on the test surface regions with higher degree of corrosion – on so called "rusty islands or stains" similar to those found in experiment #18. Thus, Fig.A119 presumably shows some of the emergent tower protrusions located inside those islands. Moreover, the morphology (flake-like: Fig.129, 130) and composition (more iron: Fig.A131 vs. A133) of the undercoat under the broken off protrusions support the hypothesis that the iron oxides promote attachment of the colloidal silica in these regions of the test surface.

The rusty islands might have formed at the beginning of the deposition experiments when the colloidal solution, with not all dissolved oxygen absorbed by scavenger, came in contact with mild steel (MS) test pipe surface. Therefore, the experiment commencing procedure was altered for subsequent experiments: prior to fitting the MS test section into the rig the solution as allowed to circulate (through the stainless pipe section) for about 30 min after introduction of the oxygen scavenger. In addition, the MS pipe test section was flushed with nitrogen after it was fitted into the rig and before the flow of colloidal solution was started to circulate through it.

Significant aggregation of the colloidal silica solution was observed in experiment # 19. Most probably it was caused by the higher flow rate and solution IS distinguishing this experiment from the previous one (#18). In order to decrease the effect of the aggregates on the scaling process and keep average particle size closer to its initial target value the sol was replaced on the fifth day of experiment #19. The initial sol #54+55 was drained and the rig was refilled with the sol # 56+57 which had almost identical (initial) particle size distribution (Fig. 37 a and b).

The evolution of the particle size distribution (PSD) in both of these sols during the experiment was monitored with the Microtrac particle size analyser (PSA) (see section 3.3.1). The histograms in Fig. 37 illustrate these PSD in the intensity-weighted form which tends to shift the size distribution from the actual number distribution towards the larger sizes (due to the increase of corresponding scattering efficiency with particle size, see Fig.28 in section 3.3.1). This explains why in Fig. 37 the initial average particle size is about 100 nm instead of the 50 nm reported above, which is the number distribution average. The examination of the intensity-weighted form of PSD allowed detection of the aggregates which were not present in the number PSD due to their low relative number.

It is interesting that the intensity-weighted PSDs in Fig.37 show two peaks and no particles in between them. If aggregates form with any number of primary particles, particles with the sizes in between those two peaks would be expected to be present in the solution. It is possible that these

a)

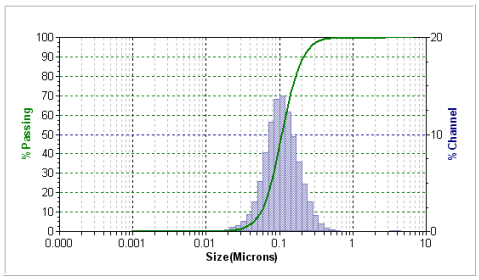

Initial Sol #54+55

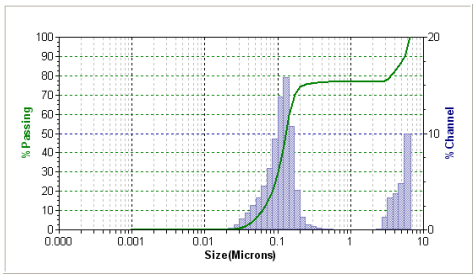

1 Day after start of exp.#19

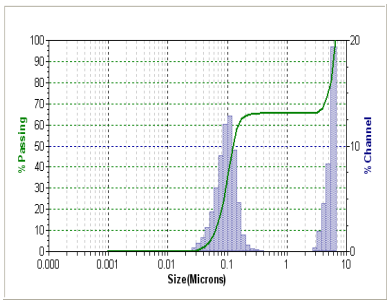

2 Days

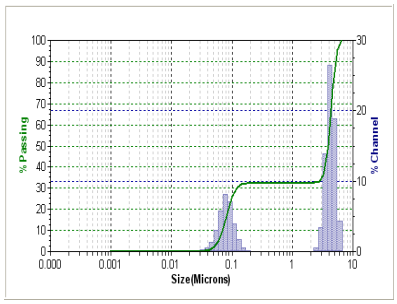

5 Days

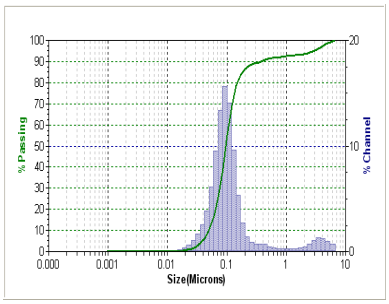

5 Days - filtered

b)

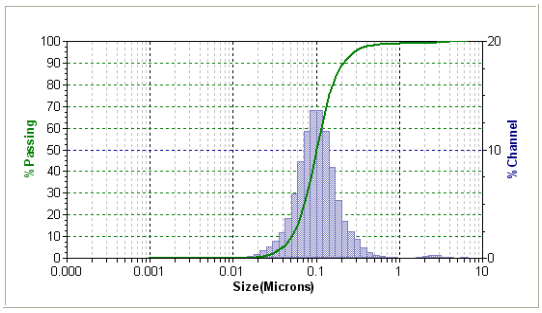

Replacement sol #56+57

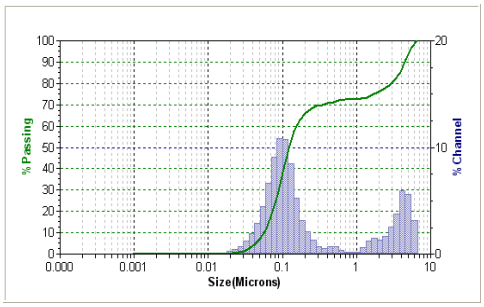

6 Days

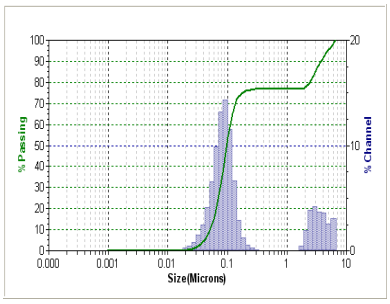

8 Days

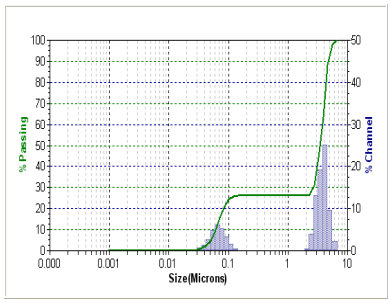

14 Days

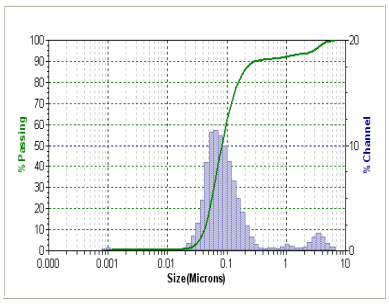

14 Days - filtered

Figure 37: Evolution of particle size distribution of the (a) initial and (b) replacement sol in experiment #19

a) **b)**

Figure 38: Silica sols drained from the rig in the experiment #19:

(a) starting sol # 54+55, (b) replacement sol # 56+57

intermediate size particle aggregates have lower scattering efficiency (Fig.28, section 3.3.1) and thus generate weaker signal than aggregates larger than 1 micron and primary particles represented in Fig.36 by the two peaks.

The PSDs in Fig.37 show that the initially monodisperse sol #54+55 developed a significant secondary peak in its PDS, which reflected the presence of the micron range particles (aggregates) as early as on the next day after the start of the experiment #19. This peak was seen to develop further as the experiment progressed with time.

At the end of the sols usage in the experiment #19 (on 5^{th} and 14^{th} days respectively) a small sample of each was passed through the filtration paper (5 qualitative, 2.5 micron). As a result a significant decrease of the intensity of the secondary peak was observed in the filtrate (compare 5 days and 14 days PSDs in Fig.37). This suggested that the most of the aggregates were retained by the filter. The filter paper's average dry mass gain was measured to be 0.6 g per 1 litre of the sol. This was about 1/3 of the total (monomeric and colloidal) silica content.

The two sols drained from the flow rig (at the end of their use) were visually different (Fig. 38). The sol with which the experiment was started had much more lumps of reddish gel settled on the bottom of a bucket than the replacement sol.

It is possible that minor corrosion of MS pipe test section that occurred at the initial stage of the experiment #19 also promoted aggregation in the initial sol. The iron oxide ions may have entered the solution, reduced the stability of the colloids and at the same time become trapped in the formed gel networks giving characteristic reddish colour to the lumps seen settled on Fig.38a.

Since the mild steel surface of the pipe test section was already covered with a layer of silica scale when the sol was replaced, no further corrosion (or much less significant), and associated aggregation, occurred after the replacement of the sol. An overall lower magnitude of the secondary peak (representing the aggregates) observed in the replacement sol #56+57 than #54+55 supported this hypothesis. The higher opacity of the sol #56+57 observed in Fig.38 was probably due to the aggregates formed on the second leg of experiment #19 remaining suspended in the solution (in contrast to the settling as in the sol #54+55).

The experience gained from the observations of aggregation in the experiment #19 lead to an idea for another modification of the experimental procedure. In-situ filtration of the colloidal solution during the subsequent deposition experiments was implemented. For this a water filter was installed into the bypass line of the rig (Fig.23, section 3.2). If a significant degree of the aggregation was detected in a working colloidal solutions (judged by the magnitude of the secondary peak in its PSD) is was diverted through the filter for 3-5 min (at maximum pump setting and both main and bypass lines fully open). In the experiments with a high rate of aggregation this filtration procedure was performed once in 1 or 2 days.

The periodic removal of the aggregates together with the modifications mentioned above (aimed to minimize the test surface corrosion at the start of the experiment) likely contributed to the decreased scaling rate observed in the experiment #20 (Fig.A134-A136). This experiment was performed at hydrodynamic conditions similar to those of experiment #19: flow rate of 30 L/min and temperature 37 °C. A colloidal solution with slightly lower IS and smaller average particle size (45 nm) was used.

The visual examination of a sample of the scaled surface showed the presence of spanwise silica tower-type protrusions (Fig.A137) similar to those seen in experiment #19. They were smaller (0.5x0.5 mm) and less numerous, but as before, inclined in the upstream direction (Fig.A147).

Also a few small (<0.1 mm) pale yellow spherical deposits and larger (1-2 mm x 0.5-1 mm) reddish bumps were observed. The bumps spanned over larger area of the test surface with their larger dimension being parallel to the flow direction. They protruded from the surface by less than 0.1 mm (Fig.A137, A138).

A curious “cellular” surface morphology of the bumps was observed with the SEM (Fig.A139).

The back, or downstream, side of the “towers” had a net of branched ridges with the largest of them aligned with the mean flow direction (Fig.A146). Each one of them was seemed to be built up of a multiple primary particles or small aggregates.

The “clear and flat” surface of the test sample from Fig.A138 appeared to be a native mill scale with the patches of orange deposits in valleys between the mill scale plates (compare Fig.A140, A141 with A88, A198 and A199) (Fig.A138). EDS confirmed that the orange deposits consisted mostly of iron oxides (Fig.A155 - A157).

The EDS analysis also indicated that the “tower” protrusions consisted of the silica, oxygen and iron.

The scaling experiment #21 was performed at a low flow rate of 16 L/min and with particles of approximately the same size (46 nm in diameter) as experiment #20.

Spanwise, tower-like silica ridges characteristic of the previous experiments were found on the scaled surface. They were shorter (~0.5mm), wider (~1 mm) and whiter than those seen in experiment #19 (Fig.A168-A170) and also the ones located further downstream from the test pipe inlet had hemispherical shape (Fig.A177).

A large number of the reddish, bulky bumps of deposits similar to the bumps found in experiment #19 were seen. Their surface was covered with light, barely visible yellow lines (Fig.A173).

As before, the “flat” surface of the test sample from experiment #21 appeared to be a native mill scale surface (Fig.A169).

The SEM magnification showed that the yellow lines on the reddish bumps were the assemblies of globular silica that form ripples which are periodic, spanwise to the mean flow direction, and located on a smoother surface of a bump (Fig.A174). Some of the agglomerations were also elongated in the direction of the mean flow.

The scaling experiment #22 was performed at the same low flow rate (16 L/min) and with larger particles (54 nm) than in the experiment #21. Visually more scale was formed as a result (Fig.A179, A180, and A190). The same types of the deposits were observed: the spanwise tower-like deposits (up to 1 mm high) and reddish bumps (but in larger number and size (2-5 mm x 1-2 mm) than in the experiment #21).

The SEM investigation of the scale showed that surface of the bumps was covered with the silica agglomerations arranged in a spanwise periodic ridges similar to those described above in experiment #21 (Fig.A182).

As before the “flat” surface as identified as a native mill scale surface (Fig.A181b), with the traces of silica and copper identified by EDS analysis (Fig.A195)

The “tower” tops were composed of numerous silica (Fig.A196) blocks smaller than 1 micron stuck together (Fig.A187).

The towers were found to reside on the up-wind sides of the reddish bumps (Fig.A189a). Therefore, either the towers were formed first and then promoted the deposition downstream from their location which resulted in a build-up of the bumps or the bumps were formed first and once they grew large enough the accelerated deposition on their front side lead to formation of the towers.

The bumps also had a peculiar, “cellular” surface morphology immediately behind the towers (Fig.A189b). The recirculation of the flow in the wake zone of the tower may be responsible for the deposition of silica arranged in such a way.

In the next two deposition experiments (#23a and b) the effect of the flow rate was tested while using single colloidal solution with small particles (with 20 nm average diameter). First, this solution circulated in the rig at the rate of 16 L/min over 3 weeks (experiment #23a). Next, the MS test section was replaced and the experiment (#23b) was continued for another 3 weeks at doubled flow rate (32 L/min) with the same sol.

The aggregation observed during experiment #23a was insignificant presumably owing to the low flow rate and small particle size. Therefore there was no need to perform solution filtration and the sol can be assumed to have same parameters at the start of the both experiments #23a and b. In contrast, a noticeable aggregation of the solution occurred in the experiment #23b (due to its higher flow rate) and so, periodic filtration was performed as described above (once in 1-2 days).

Not much deposit was observed visually on the test section from experiment #23a (Fig.A204). A few small dark patches were seen on the surface of the middle sections of the test pipe while the inlet and outlet sections were virtually clean (except for a dark flat deposit immediately downstream from the inlet to the test pipe).

The optical close-up of the sample surface from the middle sections showed that the dark small patches were represented by sparse, red bumps (<0.2 mm high) and smaller yellow and brown

deposits scattered unevenly and without apparent order on top of the native mill scale surface (Fig.A205).

The SEM examination indicated that red bumps had smooth surface close to the base and short, spanwise ripples on the top (Fig.A206). Some of the bumps had cracks on their surface which revealed voids. Therefore, these bumps could be empty silica shells (Fig.A210). The EDS analysis confirmed that they composed mainly of silica and oxygen and traces of sodium, iron and sulphur (Fig.A210).

The remaining, "clear" surface of the test sample was found to be native mill scale structures covered with thin amorphous film and small (<100 nm) bright particles (Fig.A207). The EDS examination indicated the presence of iron, oxygen and smaller amount of copper and silica.

The scale with similar morphology and composition was formed at the higher flow rate in the experiment #23b (Fig.A215-A218). In general more numerous and larger red irregular bumps were formed (Fig.A217)

The same experimental approach as in the experiment #23 was adopted for the final two scaling experiments (# 24 a and b) – a single sol and two flow rates were experimented with. Only in this case the employed colloidal solution originated from a different production method – the ion-exchange method instead of the acid-neutralisation. It had same average particle diameter of 20 nm, but a higher concentration of colloidal silica and lower ionic strength (IS). It experienced less significant aggregation during these two experiments (due to the lower IS) than in all previous - there was no need for filtration in lower flow rate experiment and filtration was conducted only once a week during the high flow rate experiment.

In contrast to the experiment #23a more and larger reddish bumps (however smaller than in #23b) and more yellow deposits were formed in the experiment #24a (Fig. A233, A234).

The optical (Fig.A235), SEM (Fig.A239 and EDS (Fig.A241, A251) examination of the sample surface showed that the red bumps were structurally and compositionally similar to these observed in the earlier experiments.

The yellow deposits, in turn, were unusual – they were numerous agglomerations of bright deposits. The largest of them were arranged into thin, spanwise ripples (0.05 mm wide) predominantly positioned between or downstream from the red bumps (Fig.A235, A237). Their structure was similar to the light yellow globular scale formed in experiment #18b. However in experiment #18b it covered almost entire test surface whereas here it was arranged into regular spanwise rows with

intervals from 0.01 to 0.1 mm between them (larger intervals between the larger ridges). The EDS analysis confirmed their silica/oxygen composition (Fig.A246).

The SEM examination showed that test sample surface clear of the above-mentioned deposits was the native mill scale surface with irregular incrustations of an amorphous film (Fig.A238). The EDS analysis found significant amount of silica and smaller amount of copper besides iron and oxygen to be present here (Fig.A242, A247-A250).

The scale formed in the high flow experiment #24b had uneven properties along the length of the test section (Fig.A252, A253). The 3-5 mm wide stripes of orange coating were seen along the first two inlet sections of the test pipe. They widened and eventually disappeared further downstream. The optical magnification showed that the coat was discontinuous – there were patches of the flat pipe surface. Their number and size gradually increased with the distance from the inlet and thus the coat evolved into a set of separated red stains (about 0.5x0.5 mm). The yellow, fine deposits were arranged in periodic, spanwise rows with in some of the gaps (Fig. A254). The spacing between them was 0.1-0.2 mm.

Fig.A255 shows that some of the red bumps had flat spanwise protrusions (approximately 0.3 mm high) on their front side

The test section surface was entirely covered with those spanwise ripples closer to the outlet (A256, A257). The largest of them were about 0.1 mm thick and less than 0.1 mm high. The longitudinal spacing between them was approximately 0.5 mm. Even thinner ripples were present in the spaces between the larger ones. The spacing between them was about 10 microns (Fig.A258b).

A closer examination showed that larger ridges had layered structure (Fig.A260) – their base had loose structure, apparently formed by the elements smaller than 1 micron stuck together, and smooth, thin shell on top and flow facing sides.

The smaller ripples had structure similar to that of the base of the large ones. They, as well as the large ones, appeared to sit on top of a smooth, amorphous film (Fig.A260). This film was cracked in some places which revealed that it is reasonably thick – it was thick enough to cover the unevenness of the native mill scale surface, but probably thin enough (<10 microns) for the X-rays generated in the deeper layers to indicate the presence of iron and copper (Fig.A266) typical for native mill scale surface.

The EDS analysis also indicated that white, spanwise ridges composed silica, oxygen and potassium (Fig.A268, A276, and A277).

In addition small amounts of potassium and sulphur were detected in the amorphous coat under the ripples (Fig.A267, A282). They were introduced into the colloidal solution IE#19 used in this experiment during their production and could have deposited together with silica when this coat was formed.

The SEM micrographs in Fig.A259 show that the orange coat, mentioned above, had a ragged surface structure. This together with its colour and, as determined by EDS, the presence of large amount of oxygen, silica and iron (Fig.A261-265, A271, A273, A274, A275) suggests its corrosion related origin.

5.3 Deposition rate as a function of hydrodynamic and chemical conditions

The rate of scaling occurred in the experiments #18-24 was measured as a function of the flow rate, solution ionic strength, particle size and concentration and distance from the pipe section inlet. To make this measurement a number of samples were cut from the corresponding pipe test sections. The deposits were scraped off their surface (with a steel knife until no more material came off) and the changes in the sample mass were measured with an analytical balance (d=0.1 mg). To find the scaling rate these values were normalised by the respective samples' surface area A (from which the deposits were removed) and the duration of the corresponding experiment t:

$$V_{dep} = \frac{m}{At}$$

The "scaled" area of each test sample (which was the internal surface of the pipe) was determined from its dimensions as:

$$A = L\big(\pi R - 2(R - h)\big),$$

here L and h are the sample dimensions (see Fig.39) and R = 8.5 mm is the internal radius of the test pipe. The deviation of the sample area from the half-cylinder shell was assumed small when deriving this relationship: $\frac{(R-h)}{R} \ll 1$.

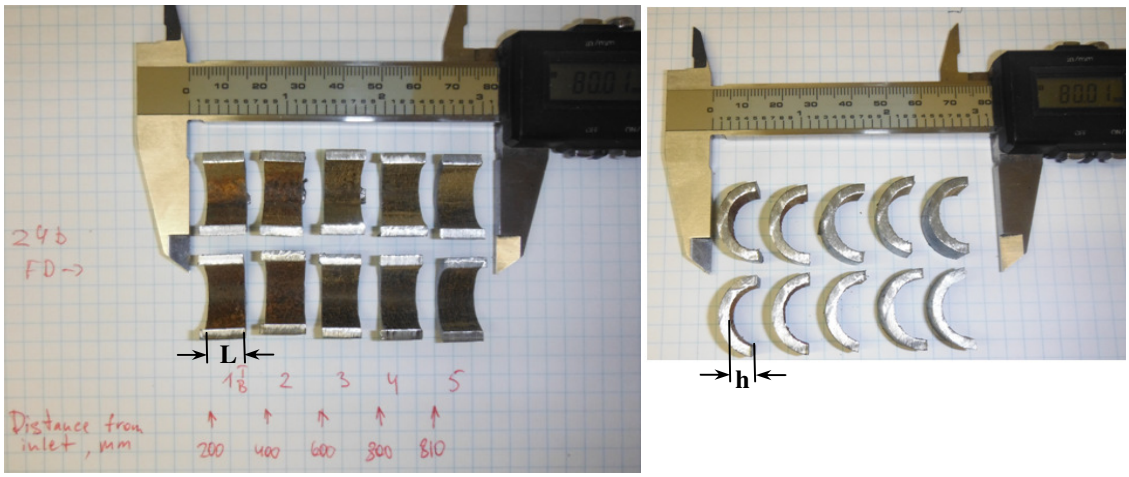

Figure 39: Finding sample surface area

The scaling rates determined through the methods and relationships described above are reported in Fig. 40-43.

The following uncertainties pertinent to the scaling rate determination were accounted for:

- an instrumental uncertainty in finding the deposit mass was taken equal to the balance precision $\Delta m = \pm 0.1$ mg;
- an uncertainty in measuring the sample dimensions was $\Delta x = \pm 0.5$ mm;
- the total time usually required to start up and close down the deposition experiment was taken as the corresponding uncertainty in its duration $\Delta t = \pm 6$ hours.

Since all variables involved in finding the scaling rate can be assumed independent, the propagation of the corresponding uncertainties can be performed using the variance formula which in this particular case can be written as:

$$\frac{\Delta V_{dep}}{V_{dep}} = \sqrt{\left(\frac{\Delta m}{m}\right)^2 + \left(\frac{\Delta A}{A}\right)^2 + \left(\frac{\Delta t}{t}\right)^2}.$$

Using this equation the average relative uncertainty of the experimental value of the scaling rate was found to be: $\left(\frac{\Delta V_{dep}}{V_{dep}}\right)_{max} = 9.5\ \%$. This and the uncertainty in the sample distance from the pipe inlet (which was half the average width of the sample $\Delta X = \pm 0.5L = \pm 5\ mm$) are represented by the error bars (which were of the same size as the data point markers) in Fig. 40-43.

The graphs in Fig.40 indicate that the scaling rate was overall higher at higher flow rates. The only exception was the rate measured for the sample located 0.8 m from the pipe inlet in the experiment #22. The unexpectedly high scaling rate observed here may be due to an unaccounted random error or unknown local

hydrodynamic or surface conditions. Meanwhile, the unusually high scaling rate measured in the experiment #24b closer to the inlet (0.2 and 0.4 m data points in Fig.40c) is due to the higher degree of surface corrosion observed here.

Therefore disregarding these irregularities, doubling of the flow rate caused an increase of the average scaling rate by approximately a factor of 1.4, 3.5 and 2 in the experiments with large particles (Fig.40a), small particles (Fig.40b) and small particles with higher concentration and lower IS (Fig.40c) respectively.

Fig.41 shows that the average scaling rate increased by a factor of 4.4 and 10 when the average particle size increased by a factor of 2.3 and 2.7 (in range from 20nm to 54 nm) respectively.

The increase of the scaling rate with the solution ionic strength is depicted in Fig.42. The IS effect was particularly substantial in a combination with the flow rate effect (Fig.42b). Thus, the high flow rate and IS realized in experiment #19 were found to result in the highest scaling rate among all of the experiments. Approximately 20% higher IS (and probably higher concentration of the iron oxides in the sol) in experiment #19, if compared to experiment #20, promoted aggregation of the silica colloids. In turn, faster, presumably inertial, deposition of these aggregates contributed to the observed high scaling rate in the experiment #19.

The effect of the particle concentration on the scaling rate is illustrated in Fig.43. However, besides the different particle concentration the IS of the corresponding solutions was also different in the experiments compared here. The flow rate and particle sizes were the same.

The sols used in experiments #24a and b had approximately five times higher particle concentration and half the IS of those used in the experiments #23 a and b. Therefore the expected proportional increase of the scaling rate with particle concentration was probably offset by higher particle stability due to lower IS. Thus, the almost fivefold increase of the particle concentration was found to increase the scaling rate only by a factor of 2 and 1.2 (the 0.2 and 0.4 m data points from experiment #24b were disregarded to find this value) in the experiments at the low and high flow rate respectively. Moreover, other effects, like corrosion (e.g. in experiment #24b, Fig.43b) and inconsistencies in the test surface properties could have affected these results.

a) IS = 65 mM; Particle diameter d_p = 50 nm; C= 1600 ppm

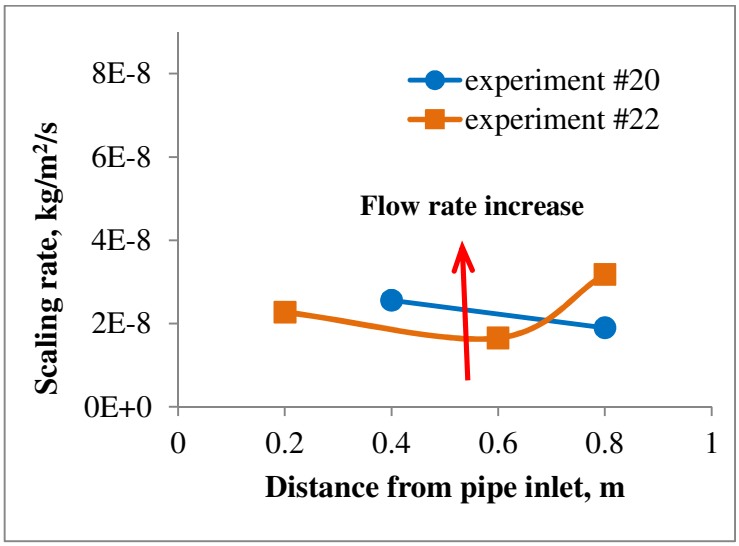

b) IS = 65 mM; d_p = 20 nm; C = 1600 ppm

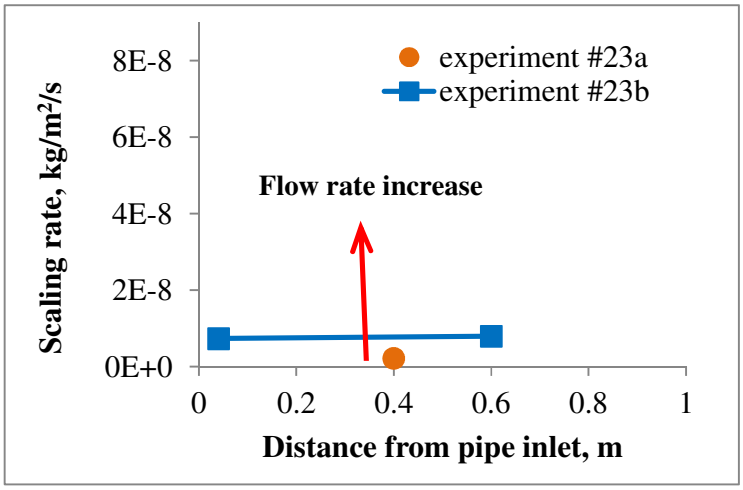

c) IS=50 mM; d_p=20 nm; C = 10000 ppm

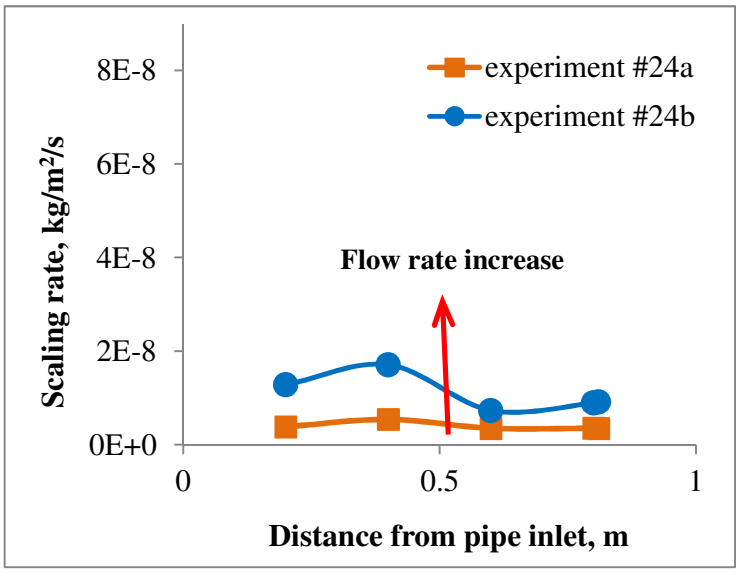

Figure 40: Effect of the flow rate on the scaling rate

Q=16 L/min;

IS=65 mM

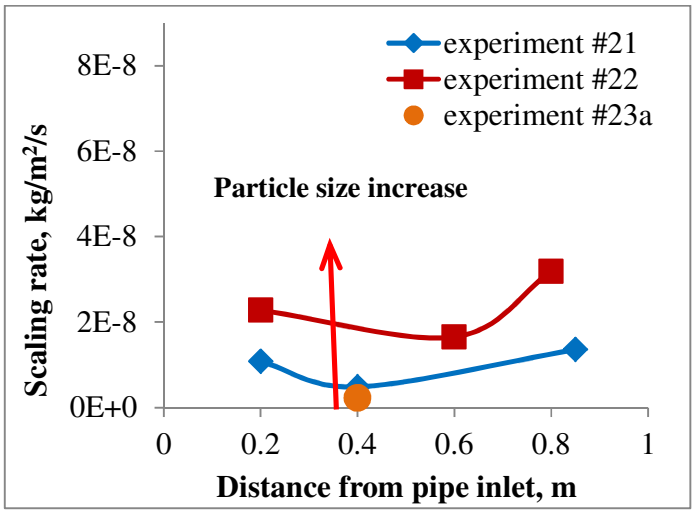

Figure 41: Effect of the particle size on the scaling rate

a) Q=16 L/min;

d_p = 50 nm

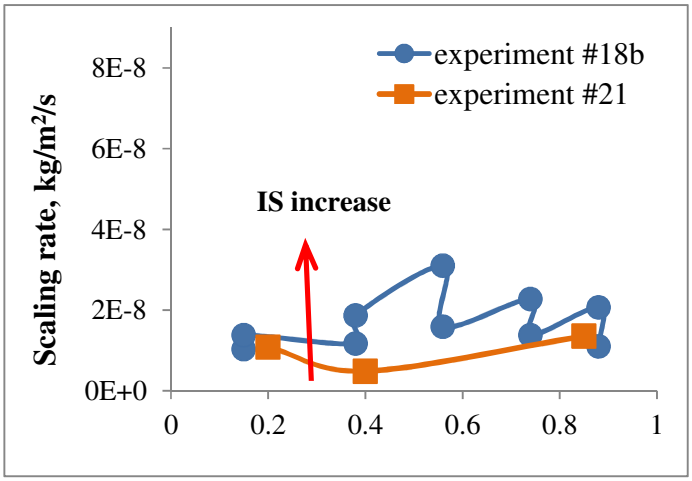

b) Q=30 L/min;

d_p = 50 nm

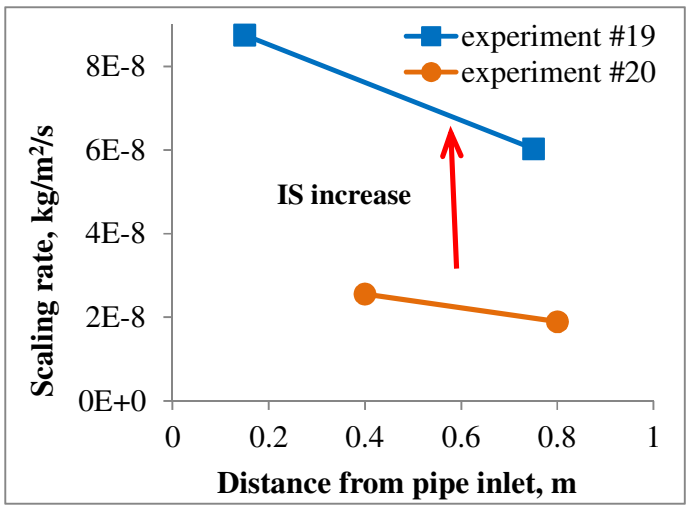

Figure 42: Effect of the solution ionic strength on the scaling rate

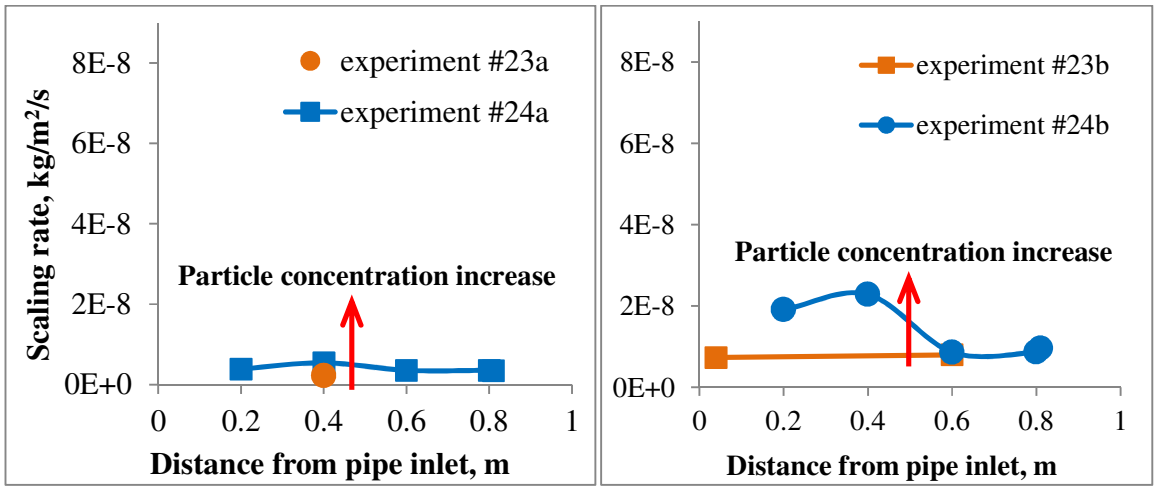

a) low flow rate **b) high flow rate**

Figure 43: Effect of the particle concentration on the scaling rate

The scaling rate observed in Fig.40-43 did not show clear correlation to the distance from the test pipe inlet. It decreased with the downstream distance in the experiment with the high average scaling rate (##19, 20) and remained constant or even increased in the experiments with the lower average scaling rate. Since no experimental information on the actual local structure of the boundary layer was available it was not possible to study the correlations between this local hydrodynamic parameter and the scaling rate.

Finally, a non-dimensional deposition velocity was calculated as a ratio of the experimental scaling rate to the particle concentration and shear velocity (see section 1.4.1, Eq.47). The values presented in Fig.44 were obtained for the experiments #21, 22 and 23 – results of which were less affected by such processes as corrosion and aggregation. Therefore, the increase of the deposition velocity with dimensionless particle relaxation time illustrated in Fig.44 reflects the nature of relatively untainted scaling process.

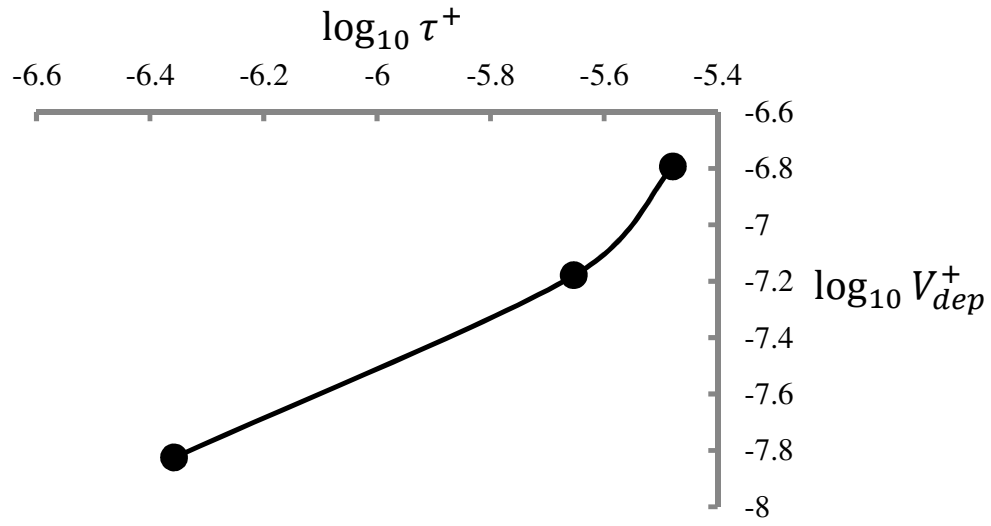

Figure 44: Dimensionless scaling velocity

Summary of Chapter 5

An experimental study of the effects of hydrodynamic and chemical conditions on the process of silica scaling was reported. It involved ten deposition experiments conducted on the flow rig with fully developed turbulent flow and a synthetic colloidal solution. A better control over such conditions as the solution ionic strength and dissolved oxygen concentration, particle size and concentration than in the experiments reported in Chapter 4 was realised. In particular, the introduction of the in-situ filtration and replacement of the colloidal solutions during the deposition experiments allowed control of their aggregation and particle concentration respectively.

The examination of the deposit morphology and composition was conducted by means of the optical and scanning electron microscopy and energy-dispersive X-ray spectroscopy (EDS).

It was found that three types of the scale elements were formed in these experiments: bulky, red, bumps with hemispherical, elongated or irregular shape; red/dark brown, perpendicular to the flow "towers" that protruded significantly from test surface and inclined upstream; and visually superficial, light-yellow ridges forming periodic spanwise ripples. The dimensions of these types of scale elements are summarised in Table 15. The dependence of these dimensions on the experimental conditions can also be observed here.

The composition and morphology analysis of the red bumps suggested that they were formed by precipitation of silica on the iron–oxygen rich sides present on the test surface due to its subtle corrosion occurred at the beginning of some of the reported experiments. In these experiments the irregular stains of the red/orange discoloured test surface were observed together with the bumps (and the "towers"). They were suspected to form at the beginning of an experiment when oxygen

scavenger has not yet absorbed all of the dissolved oxygen present in the solution which led to spotted corrosion of the test surface.

Table 15: Experimentally observed dimensions of the scale elements

Exp. #	Average Flow rate, L/min	Duration, days	Mean particle size, nm	"Reddish bumps" L×W×H*, mm	"Spanwise towers" W×H*, mm	"Ripples" axial width × axial spacing
18 b	16	21	51±3	0.2×0.2×0.07	-	-
19	30	14	53±4 45±2	-	0.7×1	-
20	30	12	45±4 50±8	(1-2) × (0.5-1) ×0.1	0.5×0.5	-
21	16	11	46±3 46±1	-	1×0.5	~1 × 10 μm
22	16	16	54±4	(2-5) × (1-2) ×0.1	0.7×1	~1 × 10 μm
23a	16	21	20±1	0.2 × 0.2 × 0.2	-	~1 × 10 μm
23b	31	21	21±1	-	-	~1 × 10 μm
24a	16	21	21±1	-	-	0.05 × (0.01-0.1) mm
24b	31	21	21±1	(<1)×0.5×0.1**	0.5 × 0.3**	0.1 × 0.5 mm ~1 × 10 μm

*Dimensions: L - axial (parallel to the flow), W- spanwise (normal to the flow) and H - normal to the pipe wall; axial width of the "spanwise towers" was approximately 20 μm;
**Observed close to the pipe section inlet only.

The aggregation of the colloidal solution during the experiments was another undesirable process. The effect of the aggregates was found to depend on the flow rate (see Table 15): at a low flow rate they deposited as a loose scale relatively uniformly distributed over the test surface and also settled in the mixing tank (experiment #18b), whereas at a high flow rate highly localised, tower-like protrusions were formed (experiment #19). This and the upstream inclination of the "towers" suggest that they were formed by the inertial (advective) deposition of the aggregates.

It is evident form Table 15 that the tower-like protrusions formed in the experiments with large particles at both testes flow rates.

The experiments that involved in-situ filtration of the colloidal solutions (#20-22) showed that similar, but smaller and less numerous tower-like protrusions form by deposition of the primary colloidal particles.

Finally, the deposition of the primary colloidal silica particles was also believed to be responsible for the formation of the superficial, spanwise ripples. Interestingly, these periodic structures were observed both on micro- and macroscale: 1 micron thick ridges were found on the surfaces of some of the red bumps described above and larger, about 50-100 micron thick, ridges were found covering large areas of the "flat" test sample surface. Actually, these larger silica ridges were found to sit on

top of a smooth, amorphous silica film. Therefore, these silica ripples can be concluded to form only on the preliminary deposited silica by deposition of smaller (~ 20 nm avg. diameter) colloidal particles.

The axial (parallel to mean flow direction) distance between the ridges and their thickness (axial width) were found to increase with the flow rate on the macroscale and not to change with flow rate on the microscale (see experiment #24, Table 15).

The morphology of the rippled scale obtained in the experiments #24 a and b was very similar to that observed for the geothermal scales (93). Therefore, the ion-exchange method, used for the production of the corresponding colloidal solution, can be more beneficial for future scaling studies.

The average scaling rate was found to increase with the flow rate, particle size, concentration and solution ionic strength. The dimensionless deposition velocity was determined to be $(1.6 \pm 0.2) \cdot 10^{-7}$ at dimensionless particle relaxation time of $3.3 \cdot 10^{-6}$.

The higher sensitivity of the scaling rate to the flow rate observed in the experiments with smaller particles can be explained by considering an inertial mechanism of their transport – its insignificance for smaller particles at low flow rate and increasing role at higher flow rate and complete manifestation for larger particles at both tested flow rates can determine the observed trends. Such inertial mechanism of particle transport is suggested and assessed in Chapter 6.

A stronger effect of a slight decrease (by about 10%) of the solution ionic strength (thus increase of colloid stability and decrease of their attachment probability) on the scaling rate than 10 fold increase of the particle concentration indicates an attachment limited nature of the scaling process.

No discernible regularity in the scale distribution along the pipe length was established. All three kinds of behaviour were observed: increase, decrease and steadiness of the scaling rate over the length of the test pipe section. It is possible that some complex flow-scale interactions are responsible for this. It is expected that growth of the scale can affect the boundary layer structure, which in turn determines the rate of the mass transfer process. Since no experimental information on actual local structure of the boundary layer was available in the reported experiment it was not possible to study the correlation between the local hydrodynamics and scaling rate. This missing experimental information can be obtained with the alternative experimental set-up which was developed and reported in section 3.2. This would be a task for the future study of the silica scaling process.

6 COLLOIDAL SILICA GROWTH, TRANSPORT AND ATTACHMENT TO A STATIONARY ROUGH SURFACE

6.1 Theoretical and experimental observations of the colloidal silica during its production, ageing and use in deposition experiments

6.1.1 Synthesis conditions and particle growth by monomer polymerisation

The measurements of mean DLS particle sizes for the selected sols are presented in Fig.45. The measurements were started on the day after the two batches were mixed, and were repeated at 2-5 day intervals. The data presented in Fig.45 were acquired both before and after the solutions were alkalinized to stop the growth. The duration of the growth period for each sol was shown in Table 6 (Chapter 3).

The particle size data obtained within the growth period was analysed to identify the mechanism of this growth. All sols, except two, had the same initial particle size (~10 nm) and appear to follow the same growth trend for the first 5-10 days of observation. Further on, most sols from Group 1 (see Table 6, empty symbols in Fig.45) exhibit faster growth than the sols from Group 2 (solid symbols in Fig.45). Initially this behaviour was suggested to be due to the domination of different particle growth mechanisms in these two groups.

The lines in Fig.45 represent the two possible growth mechanisms: the solid grey line is the rate of particle growth by the reaction controlled Ostwald ripening (OR) (Chapter 1, Eq. 20: $d = 1.04 \cdot t^{0.5}$), and the broken black line is the rate of particle growth by slow aggregation (Chapter 1, Eq. 33 fitted to Group 1 data as $d = 11.1 \cdot e^{0.065t}$). It is clear from Fig.45 that growth rate in all three groups is higher than the rate that can be expected in the OR suggesting that particle aggregation is the dominant growth mechanism.

A correlation between the rate of particles growth and the conductivity (or IS) of the colloidal solutions (Table 6) was observed. It was especially clear in Group 1 – the particles grew faster in the sols with higher conductivity (see Sol#58+59 in Fig.45).

The experimental particle size doubling time was estimated from the Fig.45. Initially it was similar in all the sols – 10 days on average. As the sols aged the time needed for mean particle size to double stayed the same in Group 1 and increased to about 25 days in Group 2 sols (for example Sol#42+43).

Two colloidal solutions that stand out (#44+45 and 70+71) had a first measured particle size at least twice that of the others. This can be explained by different temperature regime during their preparation. Namely, their batch 2 was mixed with the first one while being at a temperature higher (~50°C) then for other sols (~30°C).

Fig.45 also illustrates behaviour of the mean particle size after sol stabilization by alkalization and before their use in the deposition experiments. In Group 1 (see Sol #54+55, dotted line) an increase of pH leads to the initial minor drop in particle size followed by its stabilization. Alkalized colloidal solutions from Group 2 exhibit less prominent decrease of the particle size (sol #56+57, dotted line) and its later stabilization.

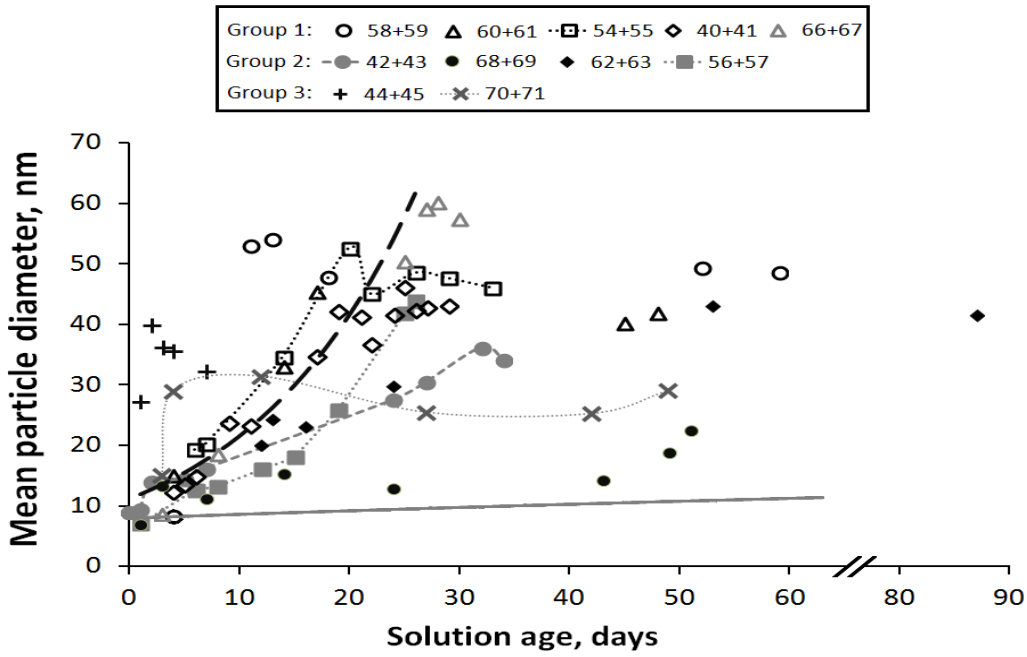

Figure 45: Particle size evolution of the selected sol measured by DLS during their ageing: -- aggregation, - OR

The particle size was observed to remain relatively constant for up to 90 days (or until the start of the deposition experiment) in all "stabilised" sols. Generally, the sols had grown further (not shown

in Fig.45) after exposure to the hydrodynamic effects in the deposition experiments. This is discussed below in section 6.1.2.

The changes in particle size distribution (PSD) observed over time for the selected sols are illustrated in Fig.46-48. The lines in Fig.46 a, b and c represent the particle populations obtained for the selected sols at different ages. They are the outlines of the bar graphs of the relative number of particles (% Channel) in a range of narrow particle size intervals, with a width of 17 % of the average particle size in each interval.

The particle growth in Group 1 and 2 sols is reflected in Fig.46 a, b as a monotonic shift of the entire PSD to the right. The polydispersity increased and PSD skewness decreased during this initial particle growth period (see Fig.47 a, b and 48 b). After the increase of pH no further growth of mean particle size in Group 1 and 2 sols was observed (Fig.76 a, b). After the alkalinisation the PSD first shifted to the left, to smaller sizes and later to the right, back to larger sizes (compare lines for 20^{th}, 22^{nd} and 26^{th} days in Fig.46 a). At the same time, the polydispersity has decreased in Group 1 and 2 sols as a result of the increase of pH (Fig.48 b).

The number of small particles in PSD increased (Fig.46 a: 20^{th} vs. 22^{nd} day lines) after the alkalization. Meanwhile, the number of medium size particles decreased and the number of the biggest particles remained approximately the same. This is reflected in Fig. 37 as an increase of PSD skewness observed for some sols after the alkalization.

The sols in Group 2 had narrower initial PSDs than Group 1 sols, although they broadened in the same manner as they aged (Fig. 48 b). Their skewness decreased during the “growth” period but was not as significant as in Group 1 sols (Fig. 47 b). The IS of the solution was suspected to cause these differences.

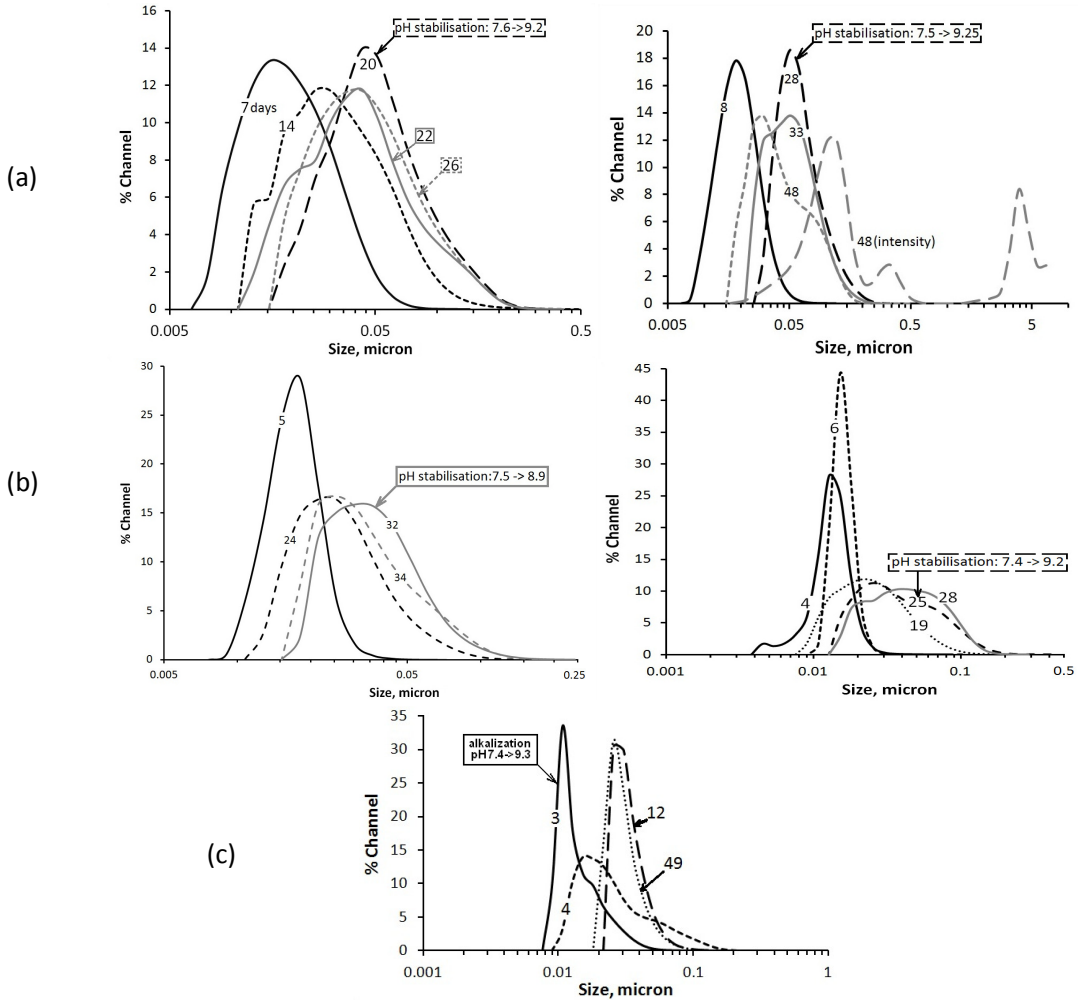

Figure 46: Evolution of the particle number distribution in (a) Group 1 (#54+55, #66+67); (b) Group 2 (#42+43, #56+57) and (c) Group 3 (#70+71) sols

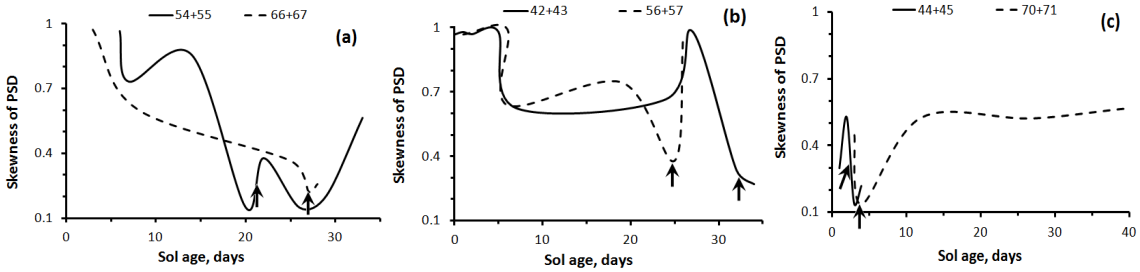

Figure 47: Skewness of the particle size distributions in (a) Group 1 (## 54+55, 66+67); (b) Group 2 (## 42+43, 56+57) and (c) Group 3 (## 44+45, 70+71) sols. (↑ indicate the alkalization of a sol)

Reliable PSDs could not be obtained in the first days of the sol's growth due to the limitations of the PCS particle size analyser. Thus, PSDs observed in Fig.48a reflect the effect of the aggregation during these first couple of days as well as that of the production conditions. Nevertheless, the

graphs in Fig.48a and b clearly show the effects of the solution IS, mixing temperature and pH on the polydispersity of the sols. The sols with higher *IS* (Group 1 vs. 2) in general had higher polydispersity. Higher mixing temperature (Group 3 vs. 1, 2) during production yielded sols with higher initial polydispersity (Fig.48 b) and lower skewness of their PSD (Fig.47 c). However, after the "stabilisation" by alkalization their polydispersity eventually decreased below that of the Group 1 and 2 sols (Fig.48 b).

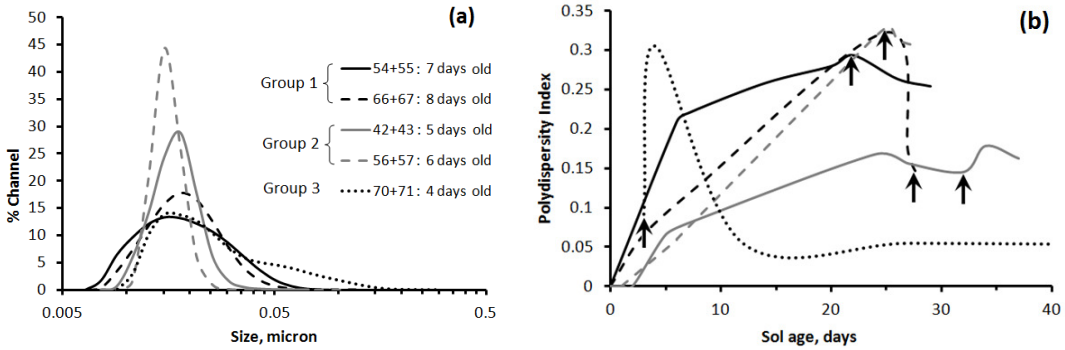

Figure 48: Comparison of the (a) early stage PSDs, (b) time development of the Polydispersity Index for three groups of sols (↑ indicate the alkalization of a sol)

The immediate effect of the alkalization on the Group 3 sols was different. In this case, instead of the minor decrease of mean particle size observed in Group 1 and 2 sols, the sol was observed to continue the growth for a while after the pH increase. Fig.46 c illustrates how PSD in sol # 70+71, first, shifted to the right after the alkalization (compare lines of 3rd and 4th day in Fig.46 c) and then stabilized (lines for 12th and 49th day).

The polydispersity of the Group 3 sol was observed to increase significantly immediately after the alkalization and then to decrease as rapidly (Fig.48 b) resulting in a relatively monodisperse sol.

The effects of the production conditions, IS and pH on the initial particle size are analysed next. The fresh colloids in Groups 1 and 2 (Table 6) had similar initial mean diameters – about 6-10 nm. This suggests that the rates of the nucleation and initial particle growth change insignificantly within the tested narrow range of the solution *IS*. The recorded initial particle size is in good agreement with the 5-8 nm colloidal silica reported in (138).

Group 3 colloids had an initial size of 15-20 nm. Apparently, mixing two batches of the sol at a higher temperature facilitated initial growth of the particles, although this also invoked higher initial polydispersity (see Fig.48). This can be explained by the higher concentration of the dissolved silica [SiO_{2aq}] in the second batch (due to its higher temperature) when it was mixed with the first one (see

Fig.29). This dissolved silica precipitated on the particles as the solution cooled down. Therefore, the mixing at higher temperature, effectively supplied additional oversaturated silica for the growth of older (thus bigger) particles from the first batch. This additional growth of the Batch 1 particles took place at the expense of further growth of the particles in the Batch 2, which would have occurred if it was allowed to cool down before mixing with the Batch 1.

Moreover, the abrupt decrease of the solution temperature upon mixing (see Fig.29 b) caused an equally sharp rise of the SSI thus accelerating the absorption controlled particle growth by polymerisation of monomeric silica. Careful control of the magnitude of this temperature drop is required in order to avoid the additional nucleation that would result in a further increase of the sols polydispersity.

The rate of the absorption controlled particle growth was shown in (55) to accelerate rapidly with increasing particle size until a certain "critical" size is reached. Afterwards, a slow decrease of the growth rate follows. This leads to the broadening of PSD on an early stage of the growth with the "focusing" possible on the later stage. According to the generalised diffusion model of particle growth (55), the "critical" radius separating these two stages for the colloidal silica, characterised by a small ratio of the monomer diffusion to surface reaction rate - D/k=0.08 nm, is about 30 nm (55). All the particles studied here were smaller than this critical value during their growth by monomer precipitation. Thus, the growth is expected to be faster for particles of greater initial size, and therefore should result in a colloidal solution with a broad PSD.

Consequently, to produce a monodisperse sol its oversaturation with silica needs to be maintained for a sufficiently long time so that particles can grow beyond 60 nm in diameter. This is not practical for the acid neutralisation production method – the supply of silica by addition of the SMS precursor would also result in the increase of the solution IS and rapid aggregation of the sol after critical coagulation concentration (c.c.c) is reached. However, the "focusing" of PSD (i.e. reduction in polydispersity) can be achieved with the ion exchange method where additional silica for particle growth is supplied in its active form with no sodium present in it.

The particle size dependence of the growth rate contributed to a higher initial polydispersity of the Group 3 sols (Fig.48 b). Older and thus larger particles from Batch 1 had grown faster in the mixed solution than those from Batch 2.

The increase of the sols polydispersity with IS (Fig.48: Group 1) could be due to a faster aggregation at higher IS. Fig.48 b demonstrates the correlation between the polydispersity of the

sols and their IS and pH. The changes of the sols PSD observed after synthesis are the outcome of the combined effects of aggregation and pH determined solubility of silica.

Scanning electron micrographs, shown below (Fig.49, 50) allowed the shape of the synthesised particles to be seen, and their size to be measured independently, so that the PCS particle size data could be validated. The particle size distributions obtained by sizing at least 50 particles in the following micrographs were given in a graphical form (broken lines) for convenient comparison with PCS data.

Fig.49 (a) and (b) compare the PCS and SEM particle size distributions for the sols #68+69 and #70+71 at the age of 3 days. Even though the particles were clumped together in the SEM micrographs their individual sizes still could be recognised. For both sols the PCS distribution in number form gave better representation of the particles observed with SEM than the corresponding intensity distribution.

Fig.50 illustrates the DLS and SEM particle size data for the sol #66+67 after it was exposed to the deposition experiment. This was done in order to observe the structure of the aggregates. The micron range size of the formed aggregates made it possible to resolve some features of their surface structure (Fig. 40 c).

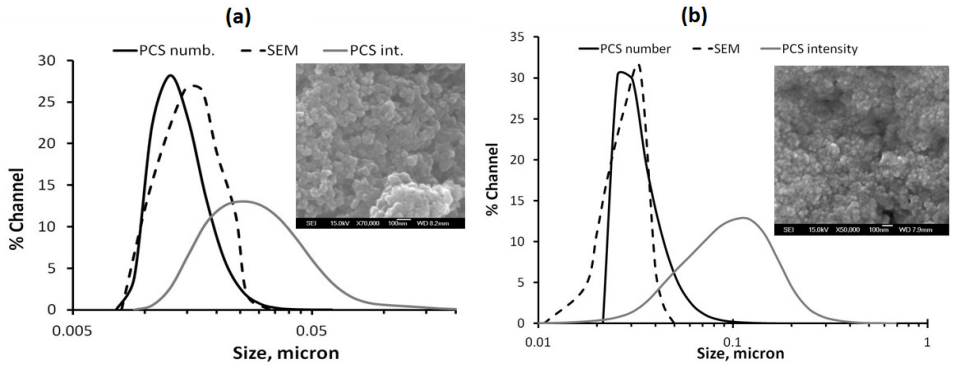

Figure 49: Comparison of the PSD measured with PCS and derived from SEM micrograph for the sols (a) #68+69 and (b) #70+71

The SEM particle size distribution in this case agreed better with the PCS distribution in the intensity form (Fig.50 a). The majority of the particles were about 100 nm in size with a smaller number of 1 micron particles, whereas the PSC mean particle size was about 40 nm. The low contrast of the SEM micrograph and wide range of the particle sizes were suspected to contribute to this disagreement. The smaller particles could have also formed a continuous layer underneath the big ones, thus also complicating their visual identification on the micrograph.

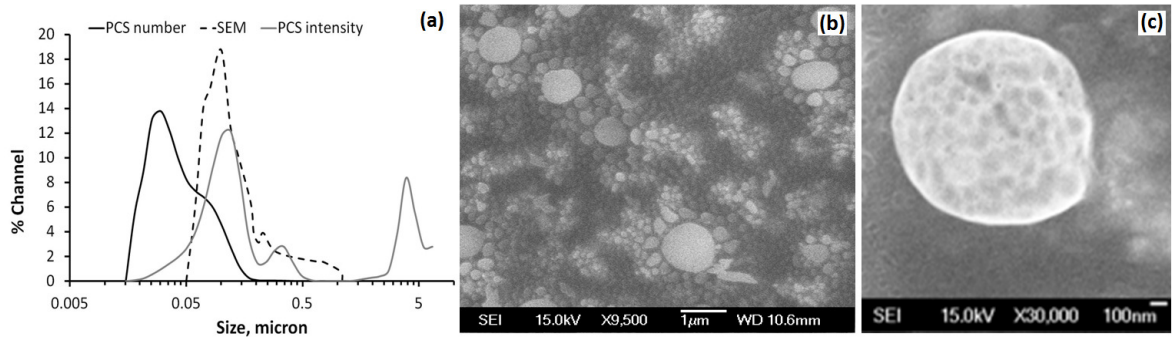

Figure 50: (a) Sol #66+67 PSD measured with PCS and derived from (b) SEM micrograph and c) close-up of one of the aggregates

Fig.50 (a) also illustrates the difference between the particle distribution presented in number and intensity forms. While number distribution gives a representation of colloidal system population the intensity distribution allows detection of fewer, bigger particles.

An example of the aggregate, presumably formed during the deposition experiment, is shown in Fig.50 c. This aggregate is about 1 micron in diameter and it contains hundreds of primary (100 nm) particles. Its compact structure suggests its high fractal dimension ($d_f \approx 2.1$, as discussed in the introduction section 1.3.3).

6.1.2 Behaviour of the colloidal silica in deposition experiments

The graphs in Fig.52-55 illustrate the evolution of the mean particle size, its volumetric weight (vol%) in the distribution (both obtained with Microtrac PCS) and pH of the selected sols during their ageing and use in the deposition experiments.

The volumetric weight of mean particle size is the ratio between the total volume of particles with this particular mean diameter and total volume of all detected particles. This parameter was used here to characterize monodispersity of the sols. Higher values of this parameter correspond to the sols with higher monodispersity. For example, Fig.51 illustrates particle size distribution for a sol with two particle types detected: first, the main peak has mean at 58 nm and fraction in the total particulate volume of 77 vol% and second peak (for aggregates) has mean particle size 2.8 μm and volumetric fraction of 23 vol%.

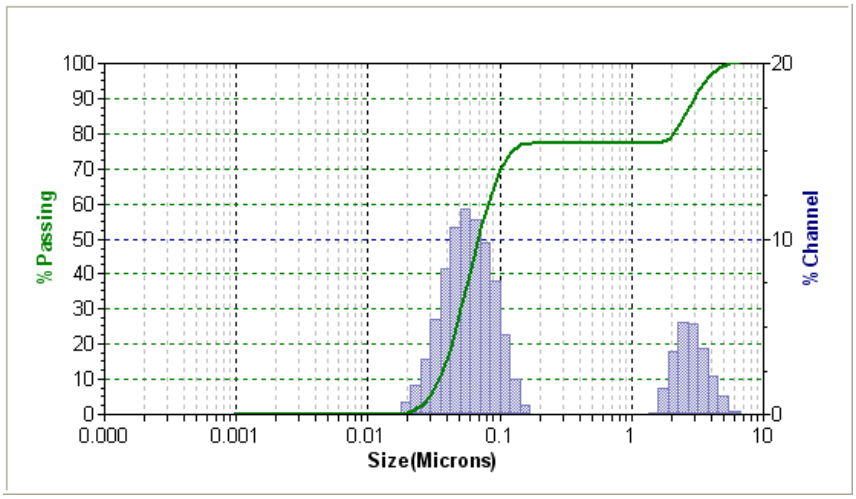

Figure 51: PCS particle size distribution for a partially aggregated sol

The features of the production method lead to a high "natural" pH of the sol #36+37 and thus, presumably to its high aggregative stability. Even though at the beginning of the ageing (Fig.52) the sol had high monodispersity (indicated by 90% volumetric weight of main peak in the distribution) it had decreased (to 50-60 % volumetric weight of main peak) by the start of the experiment #3 and continued to decrease (reaching ~40% by the experiment end).

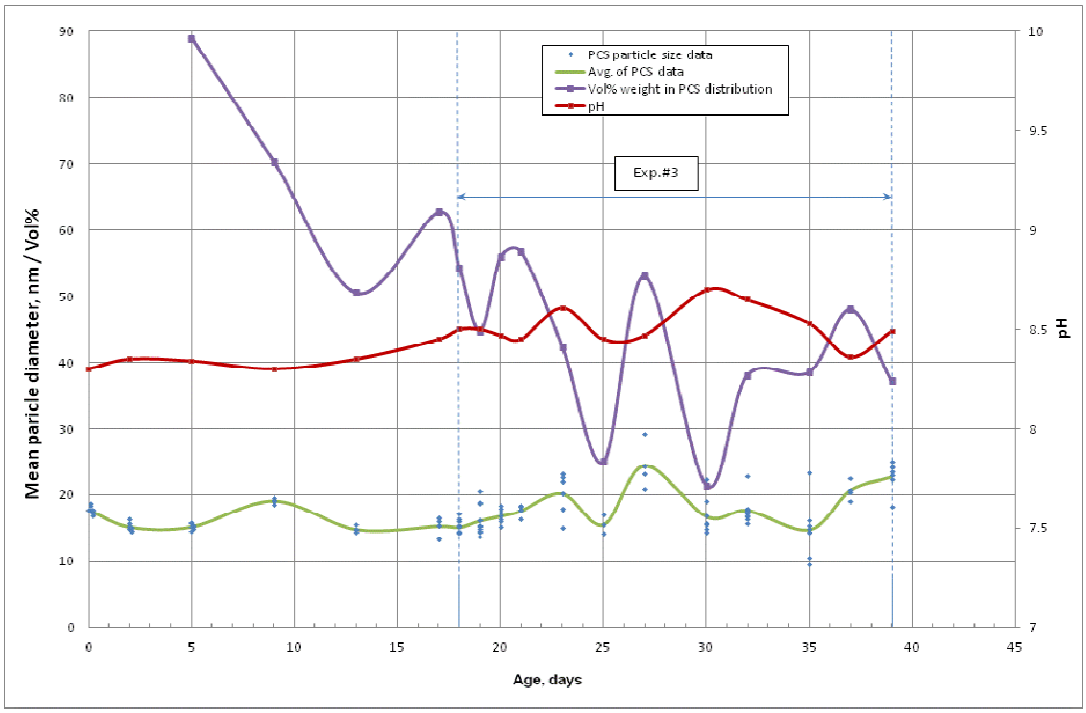

Figure 52: Sol #36+37 development history

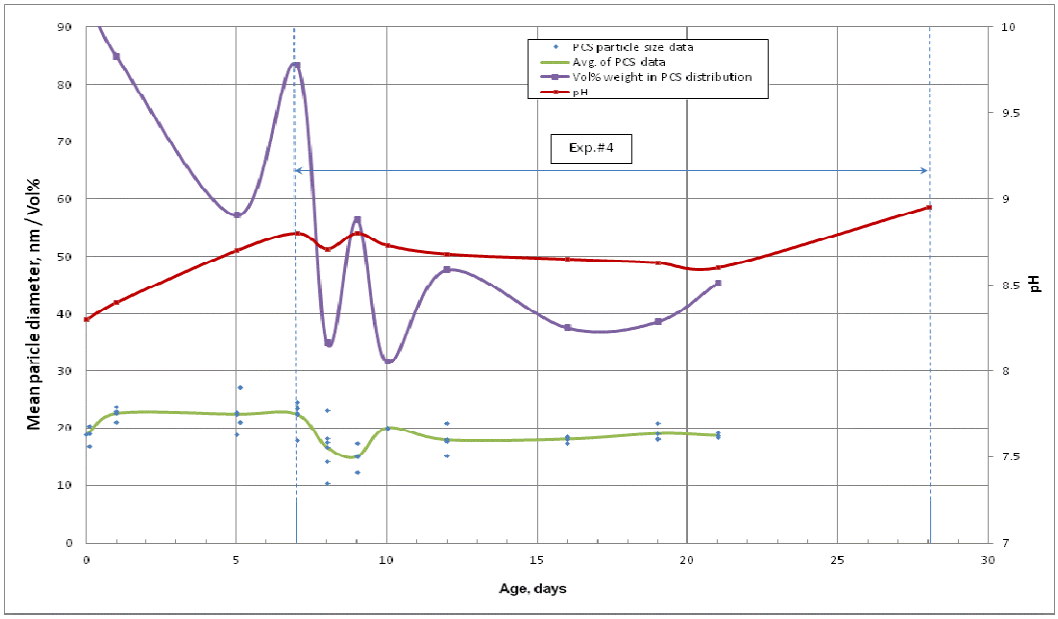

Figure 53: Sol #38+39 development history

The sol #38+39, which was prepared in a same way as #36+37, also showed signs of dispersity instability from very start of the ageing (Fig.53). This suggested that there was a systematic flaw in the production method of the small (10-30 nm) particles. Most probably, the relatively high particle number density and sodium concentration promoted particle aggregation in these sols.

Distinctive fluctuations in the sol parameters after it was introduced into the deposition experiment #4 indicated changes in its chemical and colloidal characteristics. The pH and mean particle size decreased at first and stabilized at values slightly lower than prior to experiment. However, volumetric fraction of the mean particle size in overall distribution decreased dramatically suggesting that more than a half of the particulate volume was contributed by the aggregates.

This was suspected to be caused either by the chemical/mechanical contamination of the sol or by the hydrodynamically promoted aggregation of silica colloids.

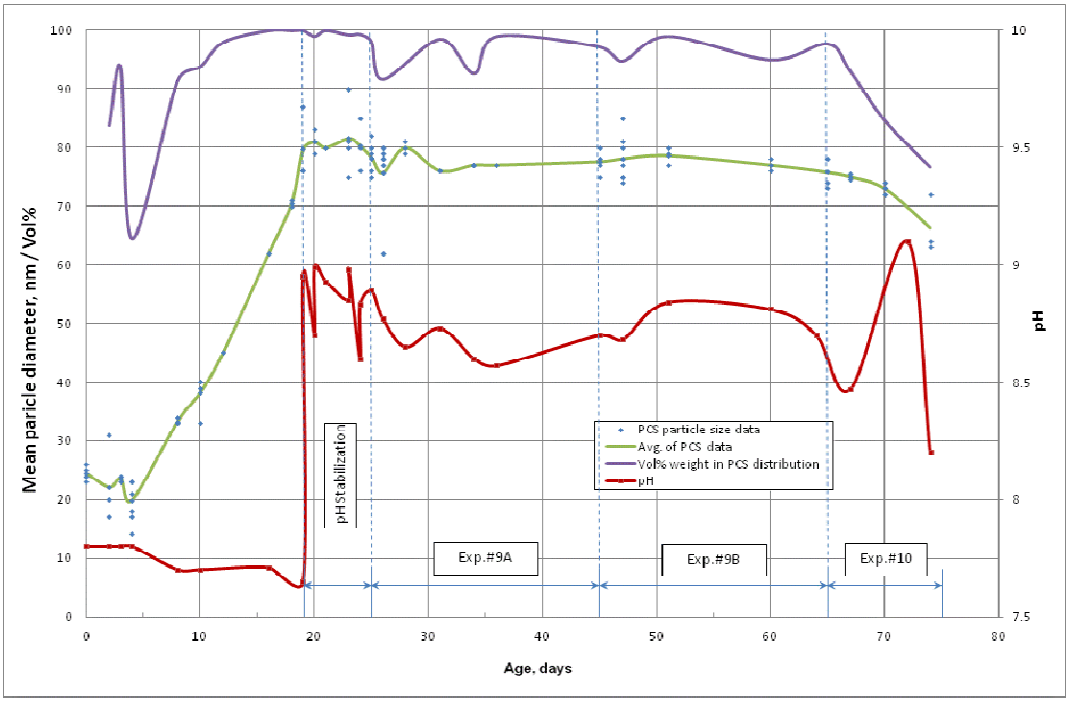

Figure 54: Sol # S40+41development history

A gradual build up of silica oversaturation during the production of the sol #40 resulted in a fewer, but larger particles generated over the SMS dissolution step compared to the sols ## 36-39. The following increase in SSI, associated with the sol cooling, may have initiated more particles to nucleate, but, as discussed above, also contributed the growth of larger particles already present in the solution.

The relatively high initial monodispersity (~80 %) that increased to about 100 % in due course of the ageing supported this and suggested occurrence of the PSD "focusing" in this case (Fig.54).

Before using sol #40+41 in the deposition experiments its pH was increased from 7.5 to 8.5. As a result particle size stabilised at roughly 80 nm and remained constant over first two deposition experiments it had being used in (#9a and 9b). The decrease of the sol monodispersity was observed with the start of the experiment #10, with the aggregates settling down at the bottom of mixing tank on the 10th day of the experiment #10. The only parameter that changed between experiments #9 and #10 was the flow rate, being higher in the latter. Therefore, the observed aggregation of the sol must have being due to the hydrodynamic effects.

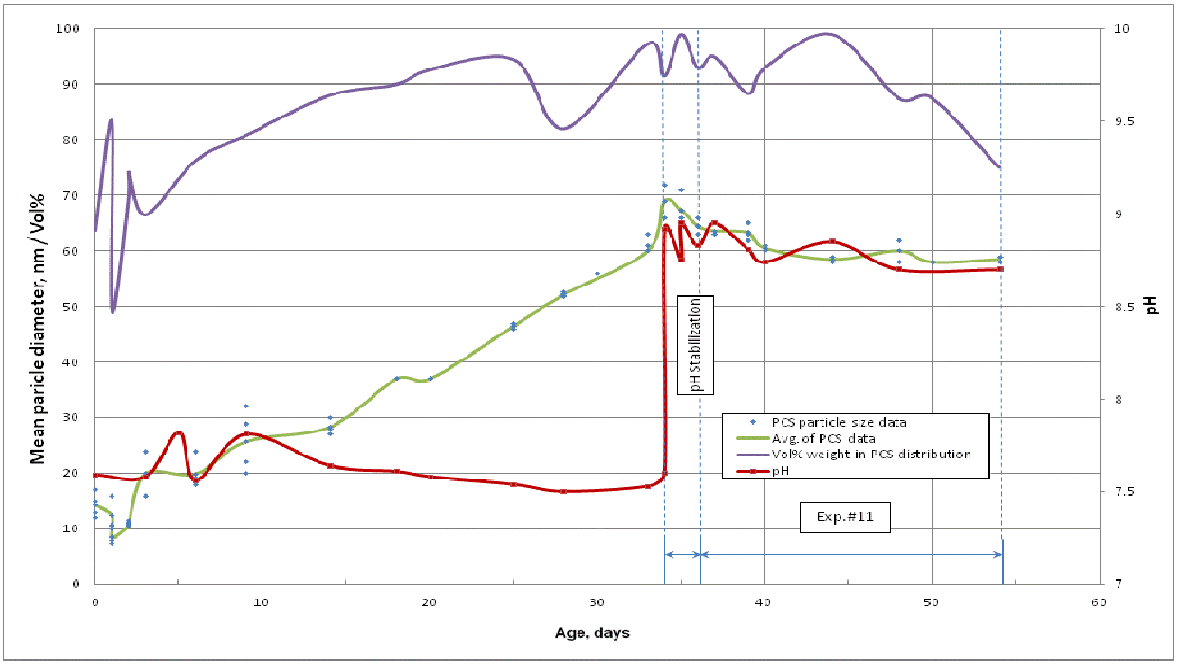

Figure 55: Sol #42+43 development history

The sol #42+43 was produced with lower amount of acid and higher SMS addition rate than sol #40+41. Its particle diameter reached 70 nm in 35 days (Fig.55) – compared to 80 nm in 20 days for #40+41. Its monodispersity had similar trend to sol #40+41. It increased over the period of ageing and went down during the experiment #11 (also conducted at higher flow rate).

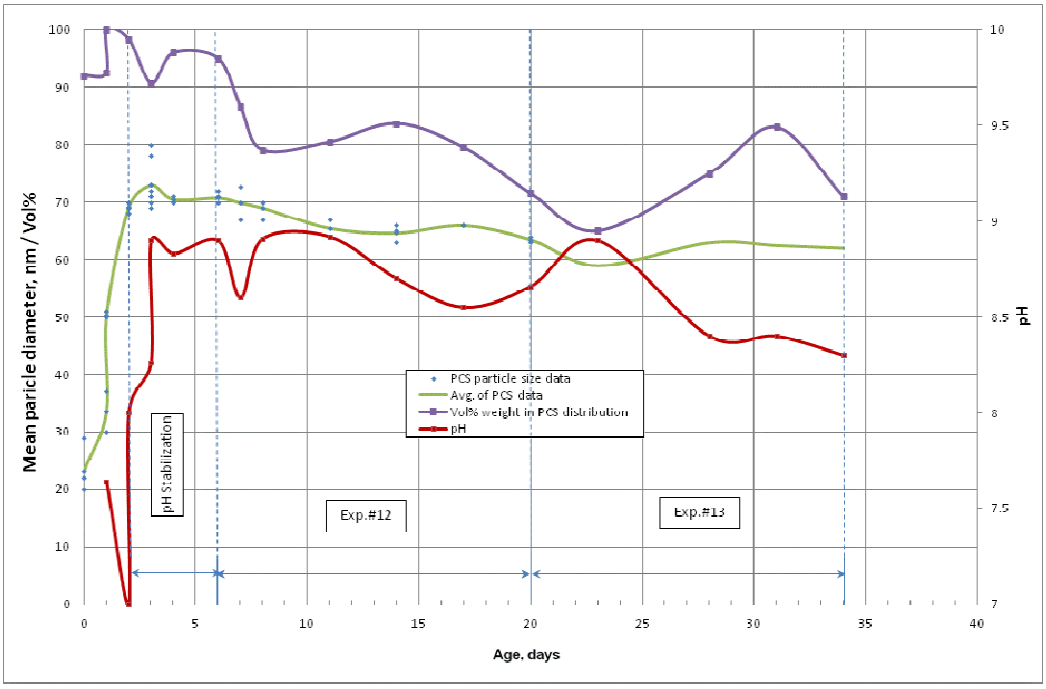

Figure 56: Sol #44+45 development history

The recipe for the sol #44+45 differed from sol #40+41 by the method of mixing two parts (44 and 45) together. The second part, two 5 L batches of the sol #45, was added to the first one (#44) being cooled only to 50 °C (in contrast to 30 °C for sol #40+41).

This difference in initial thermodynamic state of the mixture has resulted in much greater particle growth rate as compared to the sol #40+41. The particle size reached 70 nm in just 3 days of ageing. However, there is a collateral effect - the dispersity of the sol might be impaired as a result. The sol was stabilised by alkalisation and used in the experiment #12.

The opacification of the sol was observed at the bottom of mixing tank over the course of experiments #12 and #13. This again suggested that aggregation and settling of the sol took place, as well as its contamination in the rig.

6.1.3 Colloidal silica growth in a saturated solution (SSI≈1)

As was mentioned above in section 6.1.1, the long term particle size measurements suggested that OR cannot be the main mechanism of particle growth, although it outlines the lowest possible rate for the given conditions.

The process of kinetic aggregation, therefore, must govern the observed evolution of the colloidal system. A simple comparison of the theoretical (section 1.3.3: $2 \cdot 10^{-4}$ s) and experimental (section 3.3: 10 days) particle size doubling times suggests that a slow, reaction limited aggregation process took place and thus the exponential growth law best describes the observed growth (Eq. 33): $d_a = d_0 e^{Ct}$.

Indeed, the particle growth data in Fig.45 fits this equation well – the high values of the corresponding coefficients of determination support this (Table 16). The graphs and fitting parameters for a number of selected sols are presented in Fig.57 and Table 16. The variations in the slopes of the graphs in Fig.57 reflect the effect of the sols IS and mixing temperature on the aggregation rate.

The coefficient C in the exponential factor of Eq. 33, as a measure of the graph slope, is used to represent the effects of the IS and mixing temperature on the aggregation rate (Table 16). As mentioned before, C is proportional to the sticking probability or inversely proportional to the aggregative stability.

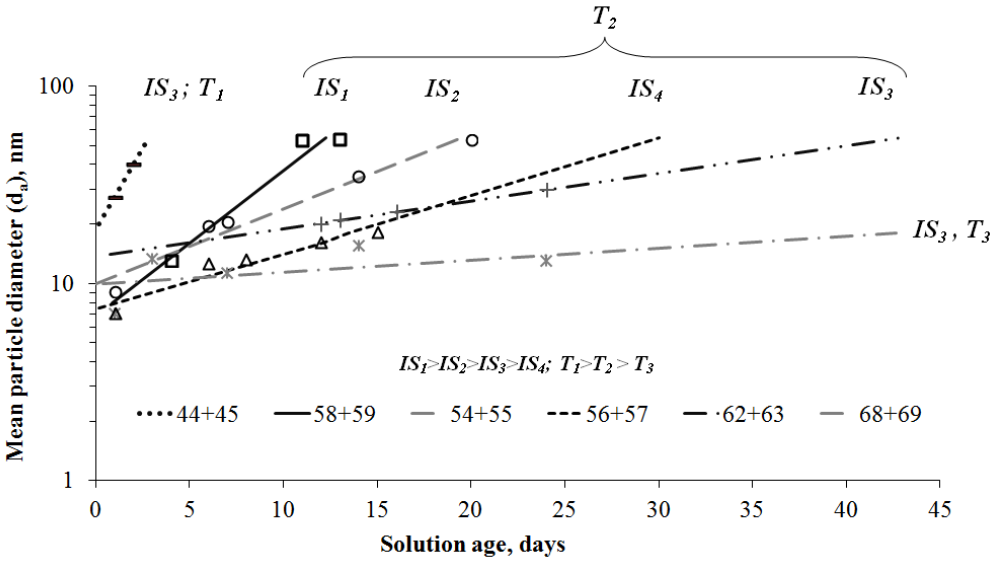

Figure 57: Slow aggregation of colloidal silica at the variable solution ionic strength (IS) and production conditions (T)

The experimentally obtained values of the coefficient C and the slopes of the lines in Fig.57 showed that the colloids stability increases with decreasing IS until some critical value is reached. Further decrease of the IS leads to decrease of the stability. This effect was particularly pronounced at higher particle sizes – as we can see in Fig.45, the sol with the lowest tested IS (#56+57) showed significant increase of the growth rate after an average particle size of 20 nm was reached.

Fig.57 and Table 16 indicate that the aggregation rate was also higher in the sols that were mixed at higher temperature. In fact, the sol for which the two parts were mixed at the lowest temperature (Sol# 68+69) had the lowest growth rate. It was better fitted with the logarithmic law for the "retarded" (78), reaction limited aggregation (Eq.34): $d_a = 0.16(\log t)^{2.5}$ with $R^2 = 0.64$.

For the tested temperature difference of 30°C, the thermal effect can explain only 10 % increase in the particle collision (and thus aggregation) rate. Furthermore, any thermal effects – either kinetic or chemical - must be localised to the first couple of days of the growth before the equilibrium (ambient) temperature is established in the sol.

Moreover, the observed difference in the aggregation rates for the relevant temperature range was much higher (about an order of magnitude) than the expected increase of aggregation rate of 10 % due to the thermal effect. All this suggests, first, that the mixing temperature also affects the stability of the tested colloidal silica. Second, its effect extends well beyond the period of the thermal relaxation – to at least 5 days after production. Possible explanations of this phenomenon are discussed in the next section.

Table 16: The parameters of slow aggregation of colloidal silica

Group	Sol#		*IS*, mM	*T*, °C	d_0	*C*	R^2	W_{exp}, 10^9	
								d=10nm	*d=20nm*
G1	58+59	IS_1	78.4		3.5	0.22	0.96	1.13	0.14
	54+55	IS_2	72.4		9.9	0.088	0.96	2.88	0.36
	66+67		70.2		8.1	0.069	0.97	3.69	0.46
	42+43		63	T_2 = 30	11.5	0.036	0.94	4.47	0.87
	62+63	IS_3	58.3		13.6	0.032	0.99	4.38	0.96
G2	56+57 d = 7.5÷15 nm	IS_4	55.6		7.4	0.064	0.92	4.09	-
	56+57 d = 15÷30 nm				6.2	0.074	0.98	-	0.43
	68+69		60.9	T_3 = 20	9.7	0.018	0.31	14.1	1.76
G3	44+45		60.9	T_1 = 50	18.7	0.38	1*	0.065	0.083
	70+71		-		2.1	0.65	1*	0.39	0.048

*only two data points were available for fitting, so the coefficients of determination are not representative

Even though the Ostwald ripening was found not to be the main mechanism of the observed particle growth it should not be neglected. It still can take place simultaneously with the aggregation. As it effectively reflects the tendency of the colloidal system to minimize its free surface energy it would be expected to proceed especially rapidly in regions with high surface curvature, for example at the contact between two bonded particles.

As was shown in (23) the amorphous silica-water interface has a lower density of ionized silanol groups, and thus higher surface tension, at lower IS. This means that the rate of Ostwald ripening (Eq. 18, 20) is higher at lower IS and thus must result in a faster smoothing out of the high curvature features of the aggregates. The smooth surface of the aggregates observed with SEM (Fig.50 b) supports this and also illustrates the high fractal dimension of the aggregates.

Moreover, the aggregates shown in Fig.50 were formed in an alkalized sol (at pH=9.3). That implies a lower surface tension at the amorphous silica – water interface than at pH=7.5 (23). Therefore, according to Eq.20, the OR must proceed even faster in "growing" sols at pH=7.5 and result in smoother aggregates than those shown in Fig.50.

This suggests that the process of Ostwald ripening, while not being a dominant mechanism of particle growth, has significant impact on the structure of the aggregates and through that also on their stability (next section). The dependence of its rate on the IS is used below to explain the deviation of the sols ##56+57 and 62+63 growth from the theoretically expected behaviour.

6.1.4 Theoretical and experimental aggregative stability of colloidal silica

The colloidal stability for the known zeta potentials and *IS* (Section 3.3.2) can be found with the standard DLVO theory of particle interactions and Smoluchowski approach to collision rate calculations (Eq.22 and 26; Chapter 1). The corresponding stability curves for a range of particle sizes, pH and IS are shown in Fig.58.

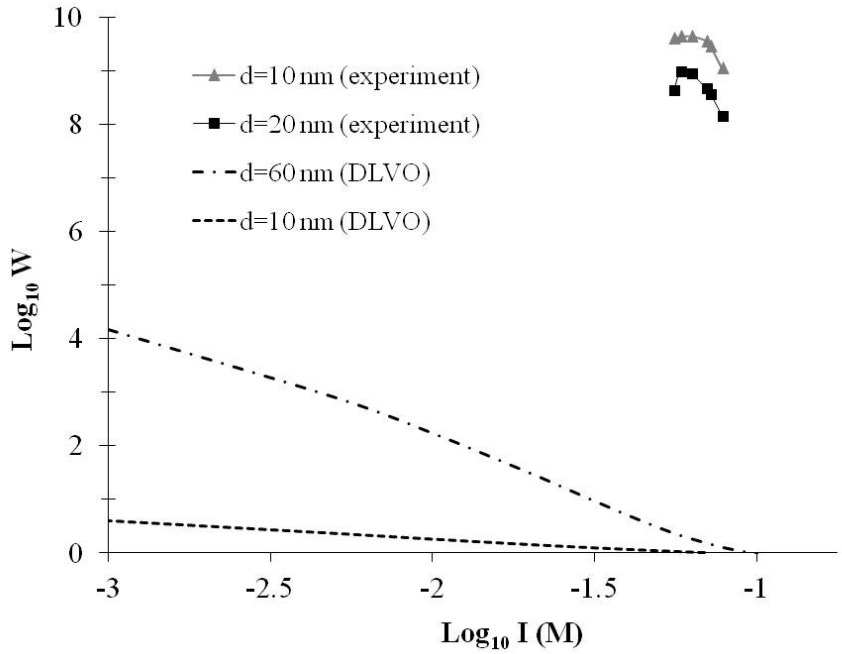

Figure 58: Aggregative stability of the silica aquasols

Fig.58 illustrates prediction of the DLVO theory that aggregative stability is lower for smaller particles and in a sol with higher IS and lower pH. According to the theory, all sols studied here are expected to be unstable (at least at early ages). Stability W_{DLVO} of the 10 nm particles in the 0.07 M solution is predicted to be just above 1 at pH 9.5 and about 0.8 at pH 7.5. Thus, the aggregate size doubling time calculated from Eq.31 equals $7 \cdot 10^{-5} \times (2^{2.1}-1)$ s = $2.4 \cdot 10^{-4}$ s and $2 \cdot 10^{-4}$ s at pH 9.5 and pH 7.5 correspondingly.

The exponential law of the colloids growth established in the previous section was used to find actual aggregative stability as a function of the IS. These values of the experimental stability for the selected sols calculated as a ratio of the actual and rapid aggregation rates (Eq. 32) are presented in Table 16 and Fig.58.

The size doubling time of the rapid coagulation $\tau_a^{R,f}$ was calculated from Eq. 31 and 27 (with d_f =2.1 as discussed above). The actual size doubling times for 10 and 20 nm particles at pH 7.5 and

different IS were evaluated from the exponential growth law (Eq. 33) with experimentally determined coefficients (Table 16).

The fact that actual stability, particularly for small particles, is much greater than predicted by DLVO theory ($W_{DLVO} \approx 1$) suggests the presence of additional repulsive forces not accounted in the standard theory. As was mentioned in section 1.3.3, these forces may arise from the strong short range interaction between "gel" layers present on the surface of the particles.

An empirical relationship between the thickness of the "gel" layer (S) and pH and IS of the solution established in (73) can be implemented here to estimate the extent of the "gel" layer on our colloids. The interpolation of the data presented in (73) showed that on a 150 nm silica colloid the "gel" layer swells by 20 % when IS is decreased within the range tested here and by more than 200 % when pH is increased from 7.5 to 9.5 (Table 17).

Table 17: Thickness of the "gel" layer (s) on a 150 nm silica colloid (73)

	Ionic strength, mM	pH = 7.5		pH = 9.5	
		s, nm	$s/\bar{s}$	s, nm	$s/\bar{s}$
Group 1	74	5.7	0.9	13.1	2.1
$\bar{IS}$	67	6.2	1	14.2	2.3
Group 2	59	6.8	1.1	15.7	2.5

The downside of the data in Table 17 is that it corresponds to a 150 nm particle whereas 10 nm particles are of interest here. However, the observed effects of pH and IS must be true irrespective of the particle size – higher pH and lower IS cause higher ionisation of the silica surface which is related to the extent of the soft gel layer on the particle surface.

The size of the particle has its own effect on the thickness of the surface "gel" layer. It was examined in (139) by performing the hydrogen/deuterium exchange within the surface layers of the colloidal silica. It was revealed that the thickness of the exchange layer is higher for smaller particles: 3.5, 2.9 and 1.8 nm for 7.1, 9.5 and 16.5 nm particle respectively. Since the exchange is expected to occur within the outer rough layer with exposed OH groups it can be suggested that the "gel" layer, discussed here, must have similar dependence on the particle size.

Alternatively, the thickness of the gel layer for the relevant pH, IS and particle size can be determined by matching theoretical and experimental stability. For this we adopted an approximate

analytical potential for electrosteric repulsion between soft shell - solid core particles, developed in (140). While following the same approach as in section 1.3.3 the electrostatic repulsion term was replaced with the electrosteric potential. The surface charge density was taken as being constant and equal to 0.02 C/m2 (from the surface charge measurements reported in section 3.3).

The theoretical stability (Eq.26) was matched to the experimental (Table 16) by setting the "gel" layer thickness to 2.9 nm and 1.4 nm for 10 nm and 20 nm particles correspondingly. These values are in good agreement with the 2.9 nm and 1.8 nm depth of the hydrogen/deuterium exchange measured in (139) for 9.6 nm and 16.5 nm silica particles respectively.

Therefore, the stability of the silica colloids for conditions close to c.c.c. predicted by DLVO must be governed by the effects of the pH, IS and particle size on the thickness of the "gel" layer. Similar to the standard DLVO theory, the gel layer mediated stability increases with increasing pH and decreasing IS.

The decrease of the stability observed with time in all Group 1 sols and some sols from Group 2 (Table 16) can now be explained by the thinning of the gel layer as the particles grow. Moreover, since the DLVO stability increases and experimental stability decreases with particle size they can be expected to converge for a large enough particle size (Fig.58). This also means that stability must have its minimum value at this particular particle size ($\mathrm{R_{cr}}$) and its inverse, which determines aggregation rate constant (K_{ag}), increases as particle size increases until this critical size is reached and decreases afterwards (Fig.59). Therefore, "focusing" of the PSD can also be observed as a result of the kinetic aggregation of the colloidal particles larger then $\mathrm{R_{cr}}$.

The decrease of actual stability for large particles can also be a result of the aggregation in a secondary minimum (73) - as the gel layer shrinks and van der Waals attractions extend beyond it, the secondary minimum in the potential energy-distance curve can become deeper than 2 kT (Fig.60).

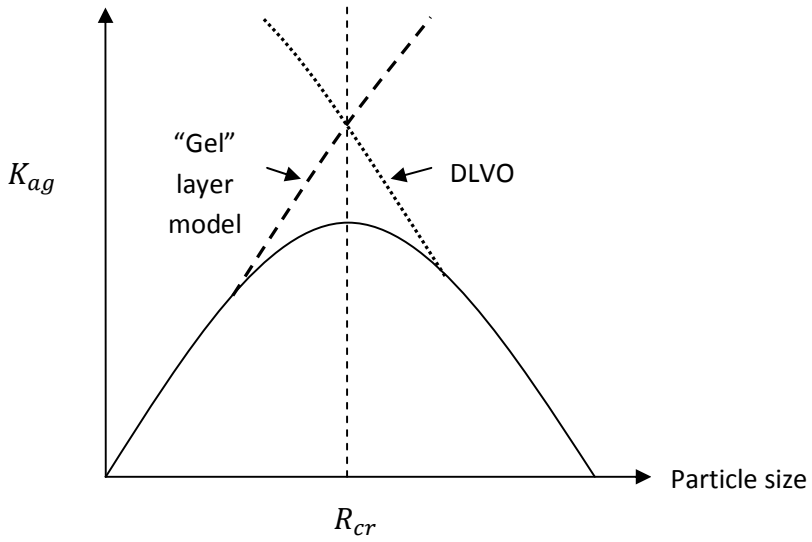

Figure 59: Speculated dependence of the aggregation rate constant on colloidal silica size

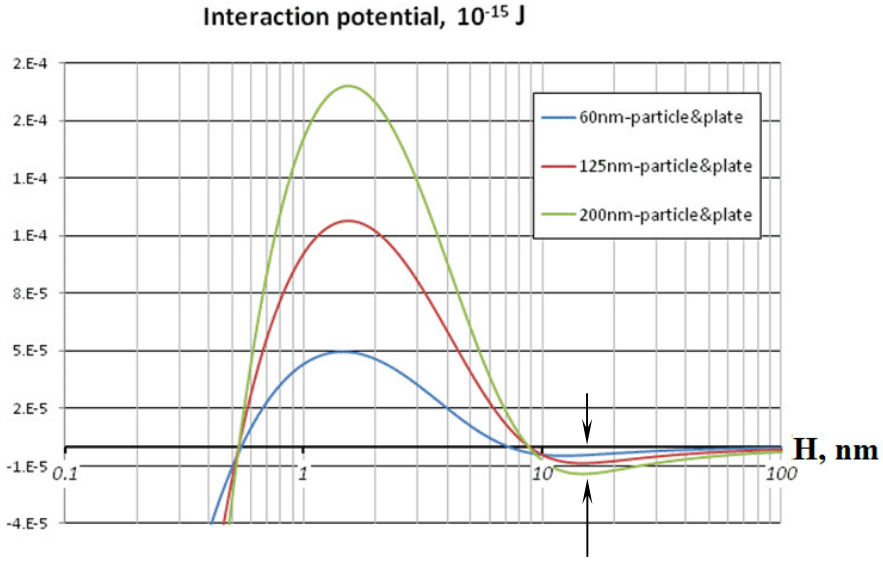

Must be >2kT for a particle to be trapped (73)

Figure 60: Secondary minima in DLVO interaction potential

Thus, the approaching particles are able to form a temporary bond in this secondary minimum and sustain it for a long time. DLVO calculations of the electrosteric potential show that for sufficiently large silica particles (d>60 nm) the average separation distance between these temporarily bonded particles is comparable to the size of the silicic acid ion (0.9 nm). This makes possible the "bridging" of this temporary gap between two gel layers by polymerisation of monomeric silica. However, for the 10 - 40 nm particles considered here the depth of the secondary minimum is less than 2 kT and the drop in their stability with increasing particle size can only be explained by the

"gel" layer shrinking. The aggregation in secondary minima can also change the behaviour illustrated in Fig.59 by increasing aggregation rate to the right from the critical particle size R_{cr} (since it also expected to be $R_{cr} > 60\ nm$).

Unexpectedly, two sols from Group 2 with lowest IS exhibited decrease of the stability (Fig.58) after reaching a certain particle size (d ~ 15nm). According to the theory discussed here they should have a thicker "gel" layer and thus higher stability at any particle size. It is unlikely that the experimental stability values are incorrect – they are supported by direct particle size measurements – although, the range of the tested solution IS needs to be increased to test this anomaly. Most probably, though, the empirical expression developed in (140) for evaluation of the electrosteric interactions between soft shell–solid core particles does not fully reflect the complexity of the collision processes.

First, the "gel" layer was assumed to be stiff with respect to the energy of the particle's Brownian motion, while it is clear that the stiffness of its structural elements – "hairs" of the polysilicic acid – must decrease as their length increases with "gel" layer thickness. As a result the empirical approach from (73) can slightly underestimate the thickness of the gel layer at low IS. Second, the disregarded compressibility of the "gel" layer may allow closer approach for colliding particles, thus raising the possibility of their aggregation in the secondary minimum.

Moreover, the theory does not consider non-central collisions and collisions between non-spherical aggregates. In fact, a newly formed cluster of two particles must have a region of much higher curvature at the contact between the two primary particles. In this region, from here on referred as a fissure, the tendency of the system to minimise surface free energy is expected to cause a collapse of the "gel" layer. This, in turn, can promote attachment of the next colliding particle in this region.

On the other hand, if the fissure is significant in size the particle approaching its vicinity effectively interacts with two primary particles (through their "gel" layers) (Fig.61 (a)). The corresponding attachment probability in this case must be lower than for a central collision of two spherical particles. It must also be lower than for the cluster collisions away from the fissures, that can also be considered as central collisions of two primary particles (141), (142). Therefore, the theoretically expected inverse relationship between the IS of the solution and its stability must hold in this case.

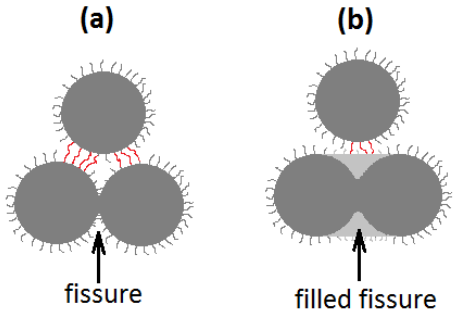

Figure 61: Two types of cluster collisions

Furthermore, the fissures tend to be smoothed out by monomer precipitation in the course of the Ostwald ripening process. The increased rate of the OR at lower IS (23) leads to a faster smoothing out of the fissures. The low curvature regions (Fig.61 b) formed in their place alter the stability of the cluster. While standard DLVO theory predicts stronger repulsion between surfaces with high radii of curvature (or bigger particles), the negligible role of the electrostatic repulsion in stability of the studied colloidal silica, justifies disregarding this effect.

The dominant steric repulsion, on the other hand, is expected to be weaker in this region of low curvature. Here, reduced local thickness of the "gel" layer results in higher likelihood of particle attachment if compared to the rest of the cluster surface. Therefore, the overall stability of the colloidal system in this case (Fig.61 b) must be lower than if only collisions between similar spherical particles (or collisions in Fig.61 a) were occurring.

Finally, the extremum in the stability curve shown in Fig.58 can be explained by the following effects. At first, as the increase of the sol IS causes swelling of the "gel" layer the stability of both the initial particles and product clusters increases. After a certain point the further increase of the IS yields no additional strengthening of the "gel" layer – most likely due to its decreasing stiffness. This is observed in Fig.58 as levelling of the stability curve for primary (10 nm) particles. As for the clusters, the acceleration of the OR with increasing IS leads to increase of the success rate for a portion of collisions. That, together with the presumably "saturated" growth of the "gel" layer determines the observed decrease of the stability.

Interestingly the similar, but less expressed, extremum in the stability curves was observed by Skvarla (73). The fact that they tested bigger particles (50-200 nm) and observed the aggregation over a much shorter time interval (2-100 s) distinguishes our studies. It is safe to assume that the effect of the OR on the colloid stability suggested above is too slow to alter the aggregation rate

over this short time. Furthermore, the time needed for the OR to change the structure of the aggregate, and thus affect its stability, must increase with the size of the primary particles.

Now, by using the regularities in the colloidal silica behaviour discussed above we can return to the effect of mixing temperature during production of the sols on their long term stability. The combination of the following two factors can explain the observed decrease of the stability for sols mixed at higher temperature: first, higher initial polydispersity (Fig.48) and, second, higher concentration of the monomeric silica.

It was shown in (143) that particles of different size aggregate faster than particles of similar size. Thus, at least initially, the aggregation is expected to proceed faster in the sols with higher polydispersity. Later on, if stability of the formed aggregates increases with their size, the "focusing" of the particle size distribution can occur. This is exactly what was observed in Group 3 sols (Fig.48b). Moreover, as these sols progress to a state of thermal equilibrium some of the dissolved monomeric silica becomes oversaturated and it can contribute to the process of cementing of the clusters fissures discussed above.

The effects of increase of the sol's pH from 7.5 to 9.5 at the end of the "growth" stage are discussed next. The shortest "growth" period in our sols was 2 days (Table 6). This is much longer than that measured by Tobler (138) 2-3 hours required for complete depletion of the oversaturated [SiO_{2aq}] by monomers precipitation on the particles.

Therefore, it is safe to say that at the time of the alkalization all our silica sols were at the state of thermodynamic equilibrium – the colloid phase was at equilibrium with the solution. The alkalization thus should have caused a decrease of the SSI below unity and partial dissolution of the silica from the colloids back into solutions.

The soft "gel" shell, as the most exposed and sparse assembly of the polysilicic acid chains, most penetrable by the solution (144) would be expected to dissolve first when the pH is increased. Due to the gel layer impenetrability by the flow (144) its dissolution must be observed as a decrease of DLS hydrodynamic diameter. This was the immediate reaction to pH increase observed in most of our sols (see Fig.45).

On the other hand, removal of the "gel" layer stabilizing effect must cause an increase in the aggregation rate – this effect is particularly prominent for the smaller particles. First, as discussed above, smaller particles have thicker "gel" layer, thus their stability decreases more significantly upon its removal. Second, according to the standard DLVO theory, a pH driven increase of the

particle surface charge compensates, to some extent, this loss of steric stability for bigger particles (see Fig.58) Moreover, if we assume that the rate of the "gel" layer dissolution is controlled by the diffusion of the ions (both to and within the layer) then smaller particles would be expected to lose it faster due to their higher mobility in the solution.

It was reported previously (143), that the aggregation of small particles (d ~ 10 nm) is possible even with substantial repulsive interactions. As a result, an aggregative mechanism for the PSD focusing was suggested (143).

Therefore, owing to the reduced stability and higher collision rate, small particles aggregate faster than big particles leading to the decrease of the polydispersity and increase of the average size. Both of these effects were recorded in all our sols at different times after the alkalization (see Fig.45, 46 and 48b).

Finally, the last effect of the pH increase in colloidal solution is a significant increase of the equilibrium thickness of the gel layer. As follows from Table 17 this thickness is expected to double as the pH is increased from 7.5 to 9.5. Naturally, the process of the silica particle core decomposition into the gel layer is slower than its dissolution. Its rate must be of the same order of magnitude as the rate of condensation of the silica chemisorbed on the surface into solid silica. Consequently, re-growth of the dissolved "gel" layer can start only after the saturation of the solution with the silica is re-established and particle dissolution stopped. The re-growth of the "gel" layer, to a thickness higher than prior to the alkalization, and also increased particle surface charge (and so the electrostatic repulsion) determine the relatively high stability of the final colloidal solutions. This is reflected by the observed high stability of the mean particle size in all our sols after the alkalisation (Fig.45, 52-56).

6.2 Assessment of particles advection onto scale protrusions

The dimensionless scaling velocity measured in the experiments presented above (Chapters 4 and 5) and in previous experiments (43) is 4 to 7 orders of magnitude smaller than V_{dep}^{+} predicted by particle transport theory for the corresponding values of τ_p^{+} (Chapter 1, Fig.10). This difference can partially be explained by moderate stability of the investigated colloidal silica discussed in Chapter 1 and evaluated in the preceding section. However, when calculating the theoretical scaling rate as a ratio of the DLVO colloid stability and transport rate for a 125 nm particle:

$$V_{dep}^{+} = \frac{transport\ rate}{stability} = \frac{10^{-2}}{10^{6}} = 10^{-8}$$

it was noticed that the theoretical transport rate is underestimated (see Chapter 2). It must be higher in order to provide the observed deposition rate $\left(V_{dep}^{+} = 10^{-6}\right)$ for the given particle stability.

Moreover, for the relevant particle size range the theory of particle transport predicts a significant decrease in the transport rate with increasing particle size. The standard DLVO theory, in turn, predicts higher stability for larger particles. When combined together these two trends result in a decrease of the theoretical deposition rate with increasing particle size. This contradicts the experimentally observed increase of the scaling rate for the larger particles.

The actual particle attachment probability, which is also an inverse of the aggregative stability of colloidal silica (Fig.59), increases with particle size until some critical size. This resolves the contradiction for the particles smaller than this critical size. However, the issue of the different theoretical and experimental trends, as well as of the underestimated theoretical deposition rate, remains open for the larger particles.

It can be resolved if the current theory of particle transport is complemented with an additional, particle transport mechanism. Thus we hypothesize that the inertia of particles in the diffusion dominated size range, although it has insignificant effect on convection normal to a wall, still can promote their tangential (parallel to the wall) convection onto roughness elements protruding from the wall.

This hypothesis may also explain the spatial distributions of the scale on the cylinder observed in the experiment (43). As it was mentioned in Chapter 2 higher scaling rate was observed at the locations with higher wall shear stress (Fig.22). First, the thickness of the diffusion boundary layer is smaller here which makes the effect of existing surface roughness more significant. Second, at the locations with higher wall shear stress particles have higher tangential velocity and thus more significant additional convection. The possible contribution of the additional advection mechanism towards a total transport rate is assessed next by first finding the flux of particles colliding with a protrusion as a result of their parallel to a wall motion and then multiplying it by the surface number density of the protrusions.

The tangential component of convective particle transport during silica scaling is evaluated analytically by considering a problem of particle movement with a flow around a single protrusion on a wall (Fig.62). First, to simplify the analysis we neglect the effect of particle redistribution by Brownian motion on the particle transport by the fluid motion. This allows treatment of the total particle transport as a simple superposition of the diffusion and inertial transport.

Second, the role of the turbulent pulsations in particle motion is also neglected. The convection of particles in a direction normal to a wall due to turbophoresis, as well as other inertial mechanisms, is already accounted for in Guha's result (Fig.10, Chapter 1). Meanwhile, the effect of the turbulence pulsations on the tangential convective transport of particles can be safely neglected if the protrusion is smaller than the thickness of the viscous boundary layer δ_v. Otherwise, intense pulsations of the instantaneous tangential velocity in near wall region ought to affect the inertial transport of particles onto the protrusion. This complex effect is a subject for a future study. Only the mean flow parameters are considered here.

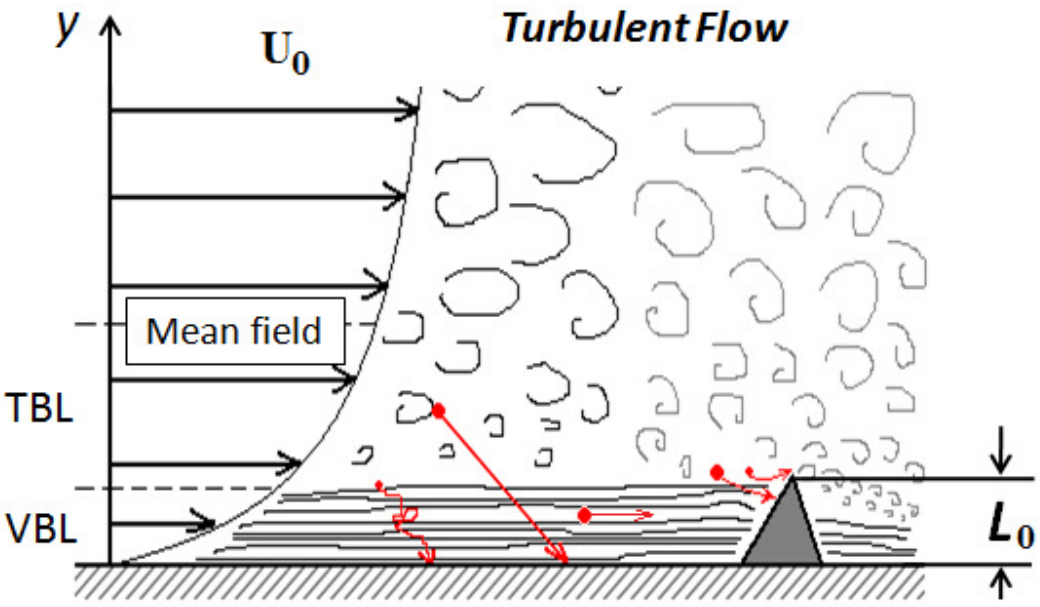

Figure 62: Particle advection onto a scale protrusion: viscous boundary layer VBL≈0.02 mm and protrusion height $L_0 \leq 0.25$ mm for the relevant conditions (Chapters 4, 5 and (43))

The particles are assumed to deviate from fluid streamlines only due to their inertia. The ability of particle to deviate is measured by its relaxation time - the time constant in the exponential decay of the particle velocity due to drag - $\tau_p = \frac{\rho_p d_p^2}{18\mu_l}$ – here ρ_p is the particle density, d_p is the particle diameter and μ_l is the dynamic viscosity of water .

Meanwhile, the probability of a particle to collide with an obstacle is determined by the dimensionless Stokes number: $Stk = \frac{\tau_p U_0(y)}{L_0}$ - here L_0 is the characteristic dimension of the obstacle and $U_0(y)$ is x component of the fluid velocity away from the obstacle as a function of wall distance y.

Based on the height of scale protrusions observed in present (Chapters 4, 5) and previous scaling experiments (43) the characteristic length was taken to be $L_0 = 0.25\,\mathrm{mm}$. The near wall velocity distribution of pipe flow with average velocity of 2.8 m/s was calculated with Eq.65 and 69:

$$\mathrm{U_0(y)} = \begin{cases} \frac{\mathrm{y}u_*}{\nu} & \mathrm{y} < \delta_\mathrm{v} \\ 2.44u_* \ln\left(\frac{\mathrm{y}}{k_s}\right) + 8.5 & \mathrm{y} > \delta_\mathrm{v} \end{cases} \tag{117}$$

where the friction velocity u_* is calculated using Serghide's solution for the friction factor for a full-flowing circular pipe (Eq. 58, 62 and 75). The surface around a protrusion is assumed to have effective sand roughness of size $k_s = 0.05\,\mathrm{mm}$ – typical for a clean carbon steel surface. In practice, silica scale on the surface around the protrusions can increase its roughness. This would result in a steeper flow velocity rise outside the viscous sublayer than used here result of Eq.117, and thus higher local Stk number.

Fig.63 a presents values of the Stokes number calculated for the abovementioned flow conditions and variable particle and obstacle sizes.

These values can be used to find the ratio of particles travelling towards the frontal area of the obstacle that will collide with it. This ratio, introduced in Chapter 1, is called the collection efficiency ϵ. Its dependence on the Stk number for spherical collectors found in previous experimental (84) and numerical (85) studies was used here. Fig.63 b illustrates their results and shows that the ratio of particles that collide with the roughness to the total number of particles travelling towards its frontal area increases with the Stk value.

For the sake of simplicity the relationship between the collection efficiency and Stk number obtained in (85) for various size spherical collectors in uniform flow is transferred onto our case of a hemisphere in a boundary layer. The main difference is that in our case collection efficiency is a function of wall normal distance. (because Stk number which is a function of the flow speed depends on the wall distance in this case).

Taking this into account and recalling the definition of the collection efficiency the rate of particles inertial transport on a single hemispherical protrusion can be shown to be (see Appendix B):

$$\mathrm{j^{in}} = 2\mathrm{c_p}\int_0^{\mathrm{L_0}} \epsilon\left(\mathrm{Stk}\left(\mathrm{U_0(y)}, \mathrm{d_p}\right)\right) \cdot \mathrm{U_0(y)} \cdot \sqrt{\mathrm{L_0}^2 - (\mathrm{y} + \mathrm{dy}/2)^2}\,\mathrm{dy}\,. \tag{118}$$

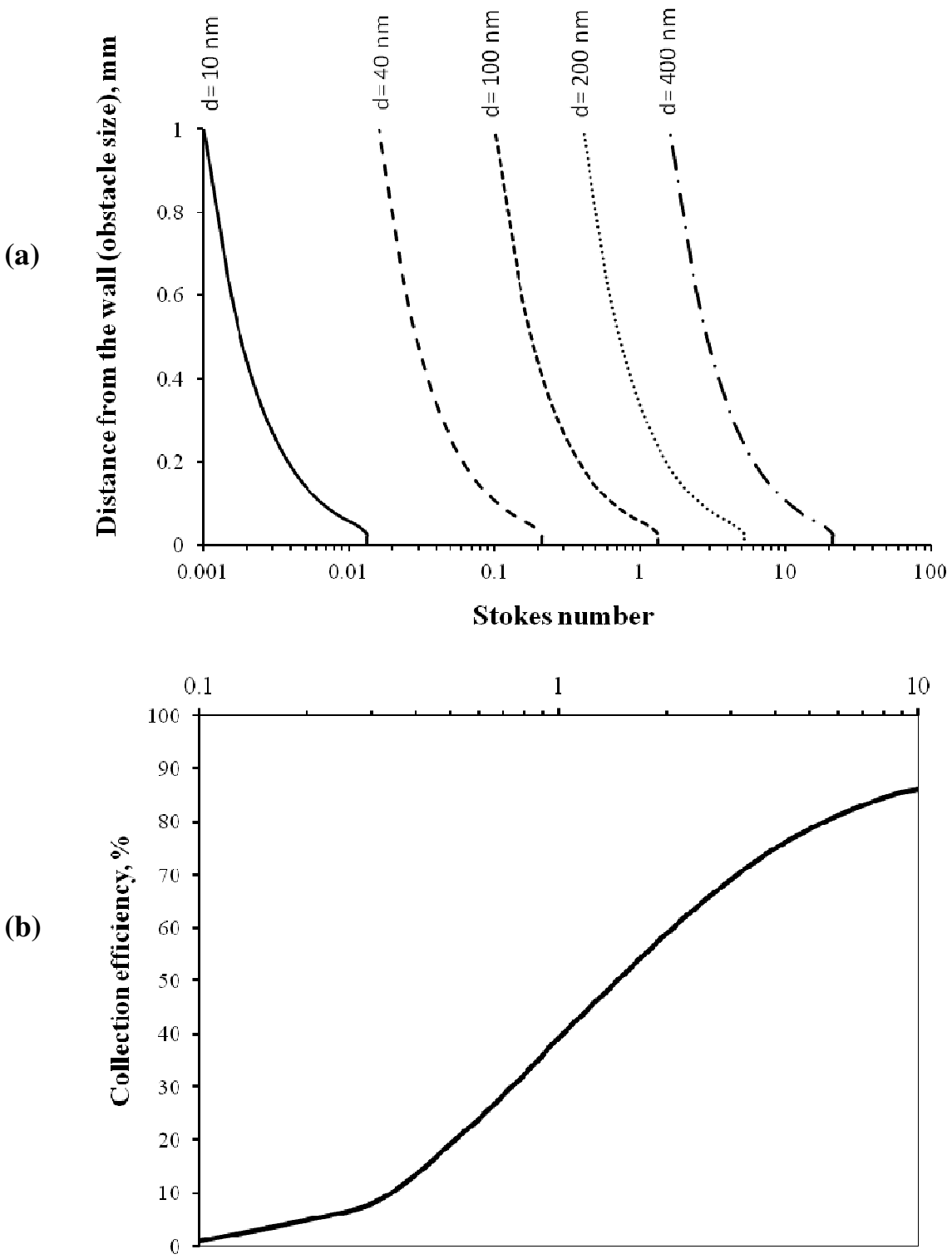

Figure 63: a) St number for the different size particles as a function of scale element size; b) collection efficiency as function of Stk number $\epsilon(y, d_p)$ (85)

This integral was calculated for the known near wall velocity distribution $U_0(y)$ (Eq.118), bulk concentration of the particles ($c_p = 1.6\ kg/m^3$), collection efficiency $\epsilon(y, d_p)$ (Fig.63) and variable

particle size (50-125 nm). Its value gave the rate of inertial particle deposition onto a single hemispherical protrusion. Corresponding particle transport rate per unit area is a product of this integral value and number of the protrusions per unit area. According to the experimental observations reported in Chapter 4 and 5 this number was taken to be 0.2×10^6 protrusions per m^2.

Fig.64 compares rate of the additional inertial particle transport (green data points) with other transport mechanisms and experimental scaling rates (red and purple data points for pipe and a cylinder in crossflow scaling experiments correspondingly). It is evident that the additional advection is faster than diffusion for the particles with $\tau_p^+ > 10^{-4}$, which is still within the diffusion dominated regime according to the current theory of particle transport.

The values of theoretical scaling rate, found as a sum of the transport rates multiplied by the attachment probability, are compared in Table 18 with the corresponding experimental deposition values for two particle sizes.

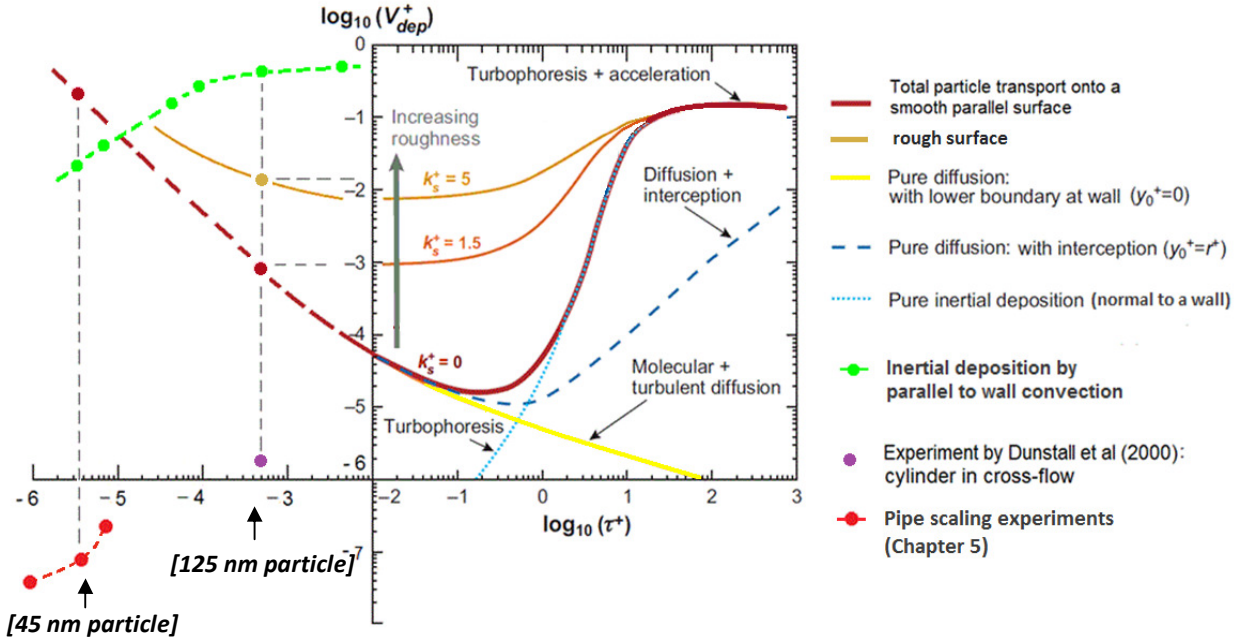

Figure 64: Comparison of the parallel to wall advection onto scale protrusions with other particle transport mechanisms (86) and experimental data (Chapter 5, (43))

Table 18: The experimental and theoretical scaling rates (nondimensionalized with Eq.47; colour coding corresponds to that of the data points in Fig.64)

	1	2	3			
Particle size, nm	Attachment probability, K=1/W	Theoretical transport rate, (86)	Parallel to wall advection onto scale protrusions (Eq.118)	Theoretical scaling rate {1}*({2}+{3})		Experimental scaling rate
45	~10^{-7} (experiment, sec. 6.1.4)	10^{-1}	$1.9 \cdot 10^{-2}$	$\mathbf{1.2 \cdot 10^{-8}}$	≈	$\mathbf{6.6 \cdot 10^{-8}}$ (Ch. 5)
125	10^{-6} (DLVO, Ch. 2)	10^{-2}	$1.7 \cdot 10^{-1}$	$\mathbf{1.8 \cdot 10^{-8}}$	<	$\mathbf{1.2 \cdot 10^{-6}}$ (43)

The value of attachment probability for 45 nm particles used in Table 18 was determined based on the experimental data reported in Section 6.1.4. Since no direct measurement was available for this particle size the corresponding stability value was estimated based on the trend observed in Fig.58. Taking into account the effect of the particle size discussed in the previous section (see Fig.59), the attachment probability for the 125 nm particles was determined with the standard DLVO theory.

First, we notice that for the smaller particles (45 nm diameter) theoretical scaling rate is of the same order of magnitude as the experimental and that tangential advection is less significant than diffusion. The remaining minor difference can either be due to the contribution of the aggregates, present in a small number in the scaling experiment and not accounted for in the calculations or due to the approximate value of the attachment probability being used.

Meanwhile, for the larger particles the experimental scaling rate (43) is still 2 orders of magnitude higher than product of corresponding attachment probability and theoretical total transport rate. However, the contribution of the parallel to wall advection is more significant in this case and without it the difference between the theory and experiment would have been one order of magnitude higher.

It is obvious from Fig.64 that, for the relevant physical conditions, transport rate can't be much higher and thus actual stability of the larger colloids used in the experiment (43) must have been lower than value predicted based on the DLVO theory. This may be due to the presence of many metal ions in real geothermal brine, which tend to be incorporated into silica colloids and affect their surface charge distribution and so, the stabilising repulsive forces.

Finally, the increase of the rate of the parallel-to-wall advection (see Fig.64) with increasing particle size together with the decrease, at least in some particle size range (see previous section, Fig.59), of their stability explains the experimentally observed increase of the scaling rate.

Summary of Chapter 6

Analysis of the experimental and theoretical findings performed in this chapter provided partial resolution to the disagreements between theory and experiment identified in Chapter 2.

First, the peculiarities of the rate of the silica colloids growth observed after their synthesis and before the "stabilization" (e.g. at SSI≈1 and pH 7.5) were discussed in detail in section 6.1. The effects of the sols ionic strength (IS) and particle size on the aggregative stability were quantified based on these observations.

The ageing of the sols was observed over a prolonged period after the production. Based on the recorded particle growth rates the mechanism of the growth and stability of the silica colloids (with diameter ranging from 10 to 60 nm) were determined. The reaction limited cluster aggregation was demonstrated to be the main mechanism of particle growth. The corresponding aggregative stability was measured to be much higher than that predicted by standard DLVO theory. Further discussion of the relationships between the stability and sol parameters was based on the hypothesis of the existence of the "gel" layer on the surface of the particles. All observed relationships supported this model.

In contrast with the standard DLVO theory, the stability was found to decrease with increasing particle size in the tested particle size range. A possibility of the convergence of the DLVO and "gel" models of particle stabilities at some intermediate particle size was proposed. It was based on a simple observation that as particle size increases the thickness of the "gel" layer decreases and at some point electrostatic repulsion overtakes the stabilising role from the steric repulsion due to the "gel" layer and thus, further on, the stability can be expected to increase with particle size according to the DLVO theory.

A more complex, than according to the DLVO theory, dependence of the stability on the solution ionic strength was revealed. On one hand, a decrease of the IS causes swelling of the "gel" layer, and consequently increase of the stability. On the other hand, it also accelerates the processes responsible for the rearrangement of the aggregate's surface structure (topology) that may lead to a decrease of their stability.

The stability of silica colloids was found to be higher at higher solution pH. The pH was increased from an initial 7.5 to 9.5 after the particles have reached a certain size. Virtually no further increase of the mean particle size was observed. The transient processes of the "gel" layer dissolution – re-growth caused by the change of solution pH was identified to be responsible for the "focusing" of the particle size distribution observed in the final stage of the sol preparation before use in the deposition experiment.

The changes of the sols parameters (mean size, particle size distribution) that were occurring during the deposition experiments were also analysed. As a result, the ongoing aggregation of the colloidal silica in due course of the deposition experiments was confirmed. It was shown to proceed faster at higher flow rates.

Ultimately, the study of the colloidal silica behavior at different stages of the undertaken experimentation helped to find an explanation of the disagreements between the theory and experiment. In particular, the measured values of particle stability, being order of magnitude higher than the standard DLVO theory predicts, and increasing with decreasing particle size, explained the low (and increasing with the particle size) silica scaling rates observed in the experiments with small particles (10-60 nm).

However the experimental scaling rate observed with the larger particles (125 nm) was found to be three orders of magnitude higher than would be expected based on the current theory of particle transport in turbulent flow and on the DLVO theory of particle interactions, which is assumed to govern stability of such large particles (see Fig.59).

Moreover, the particle size effects observed in the experiments and predicted by the theory were contradictory. The theory suggested domination of the diffusion transport and increase of particle stability with particle size, and thus lower deposition rate for larger particles, in the relevant particle size range. The experiments, in turn, indicated faster scaling for larger particles.

These persistent discrepancies between the experiment and theory together with some specifics of the silica scale morphology generated a hypothesis of the significant inertial mechanism of particle transport not accounted by current theory.

While the current theory considers only the wall-normal component of the convective particle transport, its tangential component was evaluated in Section 6.2 as such mass transfer mechanism specific to deposition of silica nanoparticles onto a rough, scaled surface.

This was done by first, finding particle flux onto an upstream side of a single scale protrusion. Second, it was multiplied by the experimentally derived surface density of the protrusions to give the estimated transport rate for this mechanism.

This additional convective particle transport was found to be significant in comparison with the transport rate predicted by the current particle transport theory. Its rate was also shown to increase with particle size and its magnitude to be significant enough to decrease disagreement between the experimental and theoretical scaling rates by one order of magnitude. Therefore, the additional inertial mechanism of particle transport suggested here should be included into future numerical silica scaling simulations.

Since particle transport rate conceptually can't be much higher (since at $\log_{10} V_{dep}^{+} > 0$ particle concentration at the wall, found as $V_{dep}^{+} \cdot c_p^0 = j/u_*$, would be higher than in the bulk solution c_p^0) the remaining two orders of magnitude difference between the theory and experiment was explained by a lower than predicted by the DLVO theory actual stability of the larger colloids used in the experiment (43). This, in turn, can be explained by the presence of many metal ions in real geothermal brine, which tend to be incorporated into silica colloids and affect their surface charge distribution and the stabilising repulsive forces.

Clearly, finding the actual stability of the silica colloids for a wider range of the conditions (particle size, IS) than tested herein presents great interest. The approach and methods reported in this dissertation may well equip one for such a task.

7 THE IMPLICATIONS FOR ANTI-SCALING PRACTICES

Taken together, the experimental and theoretical observations strongly suggest that such parameters as surface roughness and average colloid particle size have significant effect on the rate of the scaling process. The following discussion is general and applicable to any fouling mechanism with a predominantly colloidal mechanism of deposition.

Observations of particle transport in situations relevant to power plant (highly turbulent flow and rough wall surfaces) suggest that the roughness of the scale can be used as a maintenance criterion. According to our findings (145), (Chapters 5 and 6) the onset of the inertial deposition of the particles leads to a rapid growth of the roughness elements initially present on a wall surface. A random ensemble of these protrusions gets slightly more material deposited than neighbouring smooth areas, and due to positive feedback – the greater the roughness the faster the deposition – they grow into more prominent protrusions.

These protrusions have been observed to arrange into sequential, equally spaced rows spanwise to the flow, at least under certain conditions, and an as-yet unidentified hydrodynamic cause is suspected to be responsible for this. Once the protrusions grow beyond the viscous boundary layer and penetrate into the turbulent boundary layer they significantly increase rates of momentum, mass and energy transport in the near wall region. Along with the increase of the pressure drop this can result in a temporary increase of the heat transfer in heat exchangers. Over time, the accelerated fouling will surely reduce it.

Therefore, if currently the decision to start heat exchanger maintenance is made based on the observed decrease of its efficiency, this new understanding may help develop more efficient maintenance criteria. Namely, instead of starting heat exchanger cleaning after a continuous layer of contaminant has accumulated on the surface and its efficiency has dropped significantly to observe it through the temperature readings it may be preferable to clean it before the roughness protrusions grow large enough to accelerate the fouling. This may require a shorter time interval between cleaning cycles, but because much less deposit will need to be removed, an overall shorter idle time in heat exchanger operation may be achieved. Variations in the pressure drop across the heat

exchanger, as well as its efficiency, may prove useful in determining the optimal moment for the start of the heat exchanger maintenance.

When only very small particles are present in the brine, the rate of inertial transport is small and deposition is controlled by particles diffusion towards a wall. Similar to the case of large particles discussed above, a positive feedback mechanism due to scale roughness growth exists - the colloidal particles need to be transported over a shorter distance, normal to the wall, to reach the protrusion. In this case the resultant scale ridges are seen to be smaller and more closely spaced (see Chapter 5). The transport to the protrusions and flat surfaces in-between is due to the same diffusion mechanism. These smaller protrusions still cause an increase of the diffusion transport downstream of their location, though not as significant as in the inertial deposition mode.

So, with inertial deposition the steady-state height of the scale protrusions is reached when inertial particle flux onto the protrusions is equal to the diffusion flux to the flat surfaces in between (which is accelerated by these protrusions). While for diffusion controlled transport, the steady-state scale roughness is established when diffusion flux onto protrusions is equal to the diffusion onto a flat surface (also enhanced by the presence of the roughness elements).

The morphology and hardness of the scale formed in the laboratory experiments were observed to depend on the particle size. Larger particles built up as a softer, more rough and less uniform scale. This effect must be caused by the lower stability of the larger particles and reflects the similarity to the process of kinetic aggregation. Similarly, in the case of reaction limited aggregation, the higher stability of the particles means that they experience more collisions before they attach. This allows them to sample more locations on the surface of a wall (or an aggregate) before attaching and forming a denser scale (or an aggregate with a higher fractal dimension). Therefore, while smaller particles are less prone to deposition, due to their higher stability and less significant convective transport, they deposit as a denser, harder to clean and more uniform scale.

Particularly intense scaling could take place in pipe bends and valves (25). The higher shear stress and flow recirculation characteristic of these locations must cause this. The former determines higher transport rates and the latter implies that fluid resides much longer there, which allows the particles to grow larger and, as a result, to have higher likelihood to attach to a wall. For particularly critical cases, fouling at such locations can be mitigated by implementing active flow control. It may be feasible to stimulate ejection of the fluid vortices from the recirculation zones into the main flow.

This can both decrease the residence (growth) time for the particles and reduce the average shear stresses on the equipment walls.

As mentioned earlier the size of the colloids effectively governs the rate of the above ground scaling processes. Moreover, it may be presumed to have a similar effect on the injectivity index decline. Larger colloidal particles, because of their lower mobility and stability, are expected to become trapped in the pores at a higher rate. Smaller particles suspended in brine can travel further away from the reinjection point into the formation. This increases the probability of their dissolution due to the brine reheating before they can affect the permeability of the formation. Therefore, it is expected that a brine with more numerous smaller particles will cause slower fouling and loss of injectivity than a brine with the same total oversaturation ratio but fewer, larger particles.

Up to this point we have considered the situations in which colloids formed in the heat exchangers, reinjection pipelines or wellbores. For certain conditions, formation of colloidal silica particles can also occur once the brine has reached the formation. If the pH of the acid-treated injected brine returned back to neutral (for instance by reaction with calcite) faster than its temperature then nucleation and consequent growth of the particles may start.

It is possible to control the brine parameters to affect the size distribution of the formed particles. For example if the brine is forced to reach its final oversaturation ratio more rapidly the corresponding nucleation process consumes more of the excess silica (or stibnite) and less of the mineral is available on the later particle growth stage. This can be achieved by flashing the brine (146) or by running it through large plate heat exchangers.

Effectively, such brine would have many smaller particles and would cause less fouling in the aboveground and underground pathways. Whereas, in the situations where final oversaturation of the brine is reached gradually, as in the slow recovery of pH in the reinjected brine mentioned above, prolonged nucleation and slower growth may yield larger, more polydisperse particles.

8 CONCLUSIONS AND FUTURE WORK

The process of precipitation of silica from oversaturated water solutions onto solid walls, also known as silica scaling, was studied in this dissertation using theoretical and experimental methods.

The detailed review of the fields relevant to the mineral scaling in hydro-geothermal systems presented Chapter 1 laid the foundation for further study of this problem. The importance of geothermal heat as a renewable energy source globally and in New Zealand was stated. Some of the technological constraints on the effective development and utilization of geothermal resources were mentioned.

Mineral scaling, as one of these constraints, was discussed in more detail. Particularly, the chemical and thermodynamic conditions which contribute to the onset and progression of silica scaling were discussed. The unfavourable effects it creates for the geothermal industry were also emphasised.

The preliminary mechanism of silica scaling, suggested based on the available experimental and theoretical data was outlined. The gaps in the present knowledge were identified. The need for deeper understanding of a complex combination of the phenomena this process incorporates (hydrodynamics, colloid and surface chemistry) was argued as prerequisite for the development and continuing improvement of anti-scaling practices.

Specifically, while the chemical kinetics of silica polymerization and colloid formation are relatively well understood, transport of these colloids and their stability, which ultimately control their aggregation and attachment rates, on the other hand, remain unclear. Stability of geothermal colloidal silica and its dependence on the brine chemistry (pH, ionic content) and particle size are particularly vague.

In addition, it is unclear whether the theory of particle transport in turbulent flows discussed in Section 1.4 gives a fair representation of silica transport during scaling process. The current theory suggested that transport of the particles of relevant size (<1000nm) is limited by their Brownian diffusion through the boundary layer, not by inertial transport (turbophoresis). Thus, the corresponding scaling rate was evaluated to be three orders of magnitude higher than the experimental one. However, this difference may be due to high particle stability and, thus low attachment probability. The unknown particle stability had to be determined to answer this.

In addition, the theory predicted a decrease of the particle transport rate with an increase of the particle size whereas opposite was observed in the experiments.

Therefore it was hard to give the complete diffusion and kinetic description of the scaling process – to answer whether it is controlled by transport or attachment of silica to a surface, whether transport is dominated by particle diffusion or inertia. Apparently, the answers to these questions depend on the set of conditions intrinsic to each individual set of chemical and hydrodynamic conditions.

The basic equations of the DLVO theory of particle stability, the kinetics of silica polymerisation and aggregation, the theory of mass and momentum transfer in turbulent flow presented in Chapter 1 were used later to resolve these questions.

Moreover, the specific regularities of the interactions between the turbulent flow and a rough surface discussed in Section 1.4.2 create the background for a pending explanation of the "rippled" surface structure of the silica scale.

The disagreements between the theory and experiment were attempted to be reconciled by performing additional theoretical study.

The results of corresponding analytical and computational fluid dynamics (CFD) calculations of colloidal silica deposition were presented in Chapter 2. Analytical solutions of the convection-diffusion equation were adopted to find the particle transport rate onto a smooth surface of the plate parallel to the flow, cylinder in a cross-flow and internal surface of circular pipe. No inertial effects or particle-particle/particle-wall interactions (i.e. no electrostatic repulsion) were considered at first.

Next, the energy of particle–particle and particle–wall interactions was evaluated with standard DLVO theory and combined with the analytical mass transfer calculations. As a result rates of the particle coagulation and deposition and corresponding stability of particle-particle and particle-wall interactions were obtained. Only 1 in a million particles approaching to the surface were predicted to bond to it – which corresponds to the attachment probability $K=10^{-6}$. The DLVO theory also predicted decrease of this attachment probability with increasing particle size.

Consequently, the theoretical deposition rate, found as a product of transport rate and attachment probability, was about three orders of magnitude lower than corresponding experimental rate and decreased as particle size increases.

Therefore, comparison of the present and previous theoretical and experimental results suggests that implemented theoretical approach either underestimated particle transport rate or overestimated particle stability. Both possibilities were explored in this dissertation

Finally, to evaluate the role of inertial particle transport the CFD simulations of particle transport onto a cylindrical collector was reported. As before, the repulsive particle-wall interaction forces were not accounted for.

The CFD simulations of particle deposition onto the cylindrical collector yielded a transport rate which was about five orders of magnitude higher than corresponding experimental scaling rate. With the attachment probability accounted for this gap decreases to one order of magnitude. The capture of the inertial effects by this CFD simulation of particle deposition onto a curved surface represents a significant enhancement over the analytical approach described above. At the same time, the disagreement between predicted by the CFD simulations and observed in the experiments effect of particle size remains.

The comparison of the detailed hydrodynamic data obtained from the CFD simulations and experimental scaling data lead to the idea of an additional (not accounted in the current theory) mechanism of particle transport. Thus, observed correlation of the distributions of the experimental scaling rate and calculated surface shear stress along the circumference of the cylindrical collector suggested that particle acceleration in the boundary layer on the front side of the cylinder and their subsequent collisions with roughness elements/scale ridges can contribute to overall scaling rate. This mechanism of convective particle transport onto a rough surface was discussed in detail in Section 6.2.

Moreover, as mentioned in Chapter 1 the DLVO theory does not always predict stability of the colloidal particles correctly, in particular for colloidal silica, and so considerable effort was made to measure actual aggregative stability (Section 6.1) of the colloidal silica produced and used in the silica scaling experiments reported in the Chapters 4 and 5.

The equipment, techniques and procedures used for the experimental study of the silica scaling process were described in Chapter 3. The implemented experimental approach consisted of the two parts: first, production of the colloidal silica solutions and second, their use in the deposition experiments with the flow rig.

The recirculation flow rig was designed and built (by L. Sinclair) to run synthetic colloidal solutions through a carbon steel pipe sections at controllable flow rate, temperature, pH and Dissolved Oxygen (D.O.) concentration.

The following range of operational conditions can be provided by the experimental setup:

- Reynolds number from 1000 to 60000
- Friction velocity (for NB15 pipe at 30°C): 0.03-0.18 m/s
- Temperature: 25−100 °C
- Pressure 1 atm
- D.O. concentration as low as 0.1 mg/L

Each deposition experiment lasted from 1 to 3 weeks allowing a detectable amount of scale to accumulate on the internal surfaces of carbon steel pipe sections. The test sections were then cut open and scale composition, morphology and mass were analysed.

Several modifications to the flow rig and experimental procedure were made in order to extend its capabilities and resolve some of the flaws revealed in the early experiments. In particular this included following changes:

- the rig was modified to fit longer pipe test sections (up to 1 m) and perform their flushing with N2 at the start and finish of each experiment with aim to minimise effect of corrosion on a final result;
- the experiment commencing procedure was changed to assure complete removal of the dissolved oxygen from a colloidal solution before allowing its contact with the test section;
- an in-line sol filtration procedure was introduced to periodically remove silica aggregates from the flow rig during the deposition experiments.

Moreover, a different experimental set-up that would allow study of silica scaling in a parallel plate flow scenario was suggested. A corresponding new channel flow assembly was designed and built. It is expected to facilitate future silica scaling experiments by improving control over the initial contamination of the test surface, by making possible in-situ observations of the scale development and CTA probing of the near-wall region, which is expected to be affected by the scale build.

Next, two methods of colloidal silica synthesis used during this study were described. First, a straightforward, inexpensive and scalable method for production of silica aquasols through a two-step hydrolysis of sodium metasilicate was reported. The production conditions leading to synthesis

of silica sols with mean particle sizes ranging from 10 to 60 nm and low polydispersity (PI between 0.05 and 0.2) were identified in a series of production trials. Although, this method yielded relatively dilute sols, their colloidal silica concentration of about 1600 ppm was still more than three times that of the total silica concentration in geothermal brine. Therefore, these sols were considered suitable for laboratory scaling experiments, where measurable amount of the scale need to be deposited over a reasonably short period of time.

Second, a more complex method which involved use of ion-exchange step for the production of active silicic acid and it consecutive polymerisation into silica colloids was also reported. Again, a series of production trials was performed and optimal conditions for synthesis of more concentrated and monodisperse colloidal solutions with large particles (up to 250 nm) were identified. While this method is capable of producing concentrated sols with larger particles than the hydrolysis of sodium metasilicate its complexity has eventually limited its use in this research to a single deposition experiment.

Employed for this research methods of colloidal silica production provided following range of chemical conditions:

- Average colloidal silica diameter from 10 to 200 nm
- Colloidal silica concentration up to 10000 ppm
- Solution ionic strength 0.03-0.1 M

The overview of the initial scaling experiments was presented in Chapter 4. These experiments were conducted with the purpose to test the experimental setup, establish the range of its operational parameters and to gain preliminary knowledge about the scaling process.

The total amount and distribution of the scale and type of the test surface did not allow accurate quantification of the rate of the scale growth in these experiments. Its mass was too small to be measured either by weighing scraped-off scale or by measuring the difference in the test piece mass before and after the experiment. The latter method was inaccurate due to the small ratio of the surface area exposed to scaling and pipe test section volume. A test surface with higher surface-to-volume ratio (e.g. a thin plate) might suit better for such measurements. Moreover, in most experiments the obtained scale was too thin and non-uniformly distributed for accurate profile height measurements. Only in experiment # 10 the scale was thick enough and evenly distributed at the outlet part of the test section to make these measurements possible.

In general, use of the sols with larger particles was found to cause higher scaling rate and thus to be more promising for growing measurable silica scale covering the entire test surface. However, as experiments ##9-13 showed these sols were also prone to aggregation (especially when subjected to the high flow rates). This meant that they could not be used in the deposition experiments for longer than 1-2 weeks without obscuring the results by the deposition of the aggregates.

The high irregularity of the scale observed in the experiments ##11-13 was probably due to the presence of up to 30 % (volumetric fraction) of micron size silica aggregates. Such large particles must exhibited deposition behaviour different from 10-50 nm particles, which made the respective experimental results inconclusive.

There two possible solutions to the aggregation problem were explored. The first is to prevent or slow down the aggregation of the primary particles during the deposition experiments. This can be achieved chemically – by increasing stability of the sols by using the ion-exchange process to remove sodium ions from them. This, as was discussed in Section 3.1, decreases the ionic strength of these sols and allows increased silica concentration and duration of their continuous use in the deposition experiments. However, together with the aggregation the deposition rate would also decrease as a result of increasing particle stability

Therefore, the second possible solution - to remove the formed aggregates from the solution before they can deposit – can be more promising and easier to implement. It was implemented in the scaling experiments with long pipe test sections reported in Chapter 5.

In addition, the preliminary scaling experiments revealed following experimental difficulties:

- Control of the test surface properties prior to the experiment – as the pipe sections did not allow (full) access to the test surface prior the experiment, it was very hard to provide known, repeatable surface conditions;
- Control of the sol parameters during the experiment – after implementation of the nitrogen blanket sol sampling was performed through the tap at the bottom of mixing tank. This way was proved to be unsuitable both for the D.O. (due to the sample contact with atmospheric oxygen upon drainage) and particle size measurements (since aggregates and contaminants tend to accumulate at the bottom of the mixing tank). In the following experiments the D.O. and pH readings and sol samples were taken directly from the mixing tank through the open plastic lid on top of it.

- Observation of the scale growth – an ambiguity in the origin of exotic silica structures observed in some of the deposition experiments (silica “islands” in experiments ## 4, 9A) was established. An ability to observe the deposition process in situ would help to determine what scale structures formed during the experiment and what were the result of the test surface treatment at the end of the experiment.

The observed increase of the scaling rate with the distance from the test section inlet suggested that diffusion is unlikely to be the dominant mechanism of particle transport onto a flat surface. However, acceleration of the diffusion particle transport downstream from the scale elements protruding from the surface may take place. An alternative experimental test section suggested and developed in Section 3.2 can provide relevant scaling data and test this hypothesis.

Preferential deposition onto the areas protruding above the wall surface was noticed in some of the experiments, especially when large particles were used. While both diffusion and inertia may be responsible for this the inertial effects are expected to be stronger in this case.

The increase of scaling rate with the increasing flow rate and particle size suggests that inertial transport plays a prevailing role. However, this increase in scaling rate may also be an outcome of the lower stability, and thus higher attachment probability of the larger particles. The issues of particle stability and particle inertial deposition onto wall protrusions were discussed in detail in Chapter 6.

An experimental study of the effects of hydrodynamic and chemical conditions on the process of silica scaling was reported in Chapter 5. It involved ten deposition experiments conducted on the flow rig with fully developed turbulent flow and a synthetic colloidal solution. A better control over such conditions as the solution ionic strength and dissolved oxygen concentration, particle size and concentration than in the experiments reported in Chapter 4 was realised. In particular, the introduction of the in-situ filtration and replacement of the colloidal solutions during the deposition experiments allowed control of their aggregation and particle concentration respectively.

The examination of the deposit morphology and composition was conducted by means of the optical and scanning electron microscopy and energy-dispersive X-ray spectroscopy (EDS).

It was found that three types of the scale elements were formed in these experiments: bulky, red, bumps with hemispherical, elongated or irregular shape; red/dark brown, perpendicular to the flow “towers” that protruded significantly from test surface and inclined upstream; and visually

superficial, light-yellow ridges forming periodic spanwise ripples. The dimensions of these types of scale elements were summarised.

The composition and morphology analysis of the red bumps suggested that they were formed by precipitation of silica on the iron–oxygen rich sides present on the test surface due to its subtle corrosion occurred at the beginning of some of the reported experiments. In these experiments the irregular stains of the red/orange discoloured test surface were observed together with the bumps (and the "towers"). They were suspected to form at the beginning of an experiment when oxygen scavenger has not yet absorbed all of the dissolved oxygen present in the solution which led to spotted corrosion of the test surface.

The aggregation of the colloidal solution during the experiments was another undesirable process. The effect of the aggregates was found to depend on the flow rate (see Table 15): at a low flow rate they deposited as a loose scale relatively uniformly distributed over the test surface and also settled in the mixing tank (experiment #18b), whereas at a high flow rate highly localised, tower-like protrusions were formed (experiment #19). This and the upstream inclination of the "towers" suggest that they were formed by the inertial (advective) deposition of the aggregates.

The experiments that involved in-situ filtration of the colloidal solutions (#20-22) showed that similar, but smaller and less numerous tower-like protrusions form by deposition of the primary colloidal particles.

Finally, the deposition of the primary colloidal silica particles was also believed to be responsible for the formation of the superficial, spanwise ripples. Interestingly, these periodic structures were observed both on micro- and macroscale: 1 micron thick ridges were found on the surfaces of some of the red bumps described above and larger, about 50-100 micron thick, ridges were found covering large areas of the "flat" test sample surface. Actually, these larger silica ridges were found to sit on top of a smooth, amorphous silica film. Therefore, these silica ripples can be concluded to form only on the preliminary deposited silica.

The axial (parallel to mean flow direction) distance between the ridges and their thickness (axial width) were found to increase with the flow rate on the macroscale and not to change with flow rate on the microscale.

The morphology of the rippled scale obtained in the experiments #24 a and b was very similar to that observed for the geothermal scales (93). Therefore, the ion-exchange method, used for the production of the corresponding colloidal solution, can be more beneficial for future scaling studies.

The average scaling rate was found to increase with the flow rate, particle size, concentration and solution ionic strength. The dimensionless deposition velocity was determined to be $(1.6 \pm 0.2) \cdot 10^{-7}$ at dimensionless particle relaxation time of $3.3 \cdot 10^{-6}$.

No discernible regularity in the scale distribution along the pipe length was established. All three kinds of behaviour were observed: increase, decrease and steadiness of the scaling rate over the length of the test pipe section. It is possible that some complex flow-scale interactions are responsible for this. It is expected that growth of the scale can affect the boundary layer structure, which in turn determines the rate of the mass transfer process. Since no experimental information on actual local structure of the boundary layer was available in the reported experiment it was not possible to study the correlation between the local hydrodynamics and scaling rate. This missing experimental information can be obtained with the alternative experimental set-up which was developed and reported in section 3.2. This would be a great task for the future study of the silica scaling process.

Analysis of the experimental and theoretical findings performed in Chapter 6 provided partial resolution to the disagreements between theory and experiment identified in Chapter 2.

First, the peculiarities of the rate of the silica colloids growth observed after their synthesis and before the "stabilization" (e.g. at SSI≈1 and pH 7.5) were discussed in detail in Section 6.1. The effects of the sols ionic strength (IS) and particle size on the aggregative stability were quantified based on these observations.

The ageing of the sols was observed over a prolonged period. Based on the recorded particle growth rates the mechanism of the growth and stability of the silica colloids (with diameter ranging from 10 to 60 nm) were determined. The reaction limited cluster aggregation was demonstrated to be the main mechanism of particle growth. The corresponding aggregative stability was measured to be much higher than that predicted by standard DLVO theory. Further discussion of the relationships between the stability and sol parameters was based on the hypothesis of the existence of the "gel" layer on the surface of the particles. All observed relationships supported this model.

In contrast with the standard DLVO theory, the stability was found to decrease with increasing particle size in the tested particle size range. A possibility of the convergence of the DLVO and "gel" models of particle stabilities at some intermediate particle size was proposed. It was based on a simple observation that as particle size increases the thickness of the "gel" layer decreases and at some point electrostatic repulsion overtakes the stabilising role from the steric repulsion due to the

"gel" layer and thus, further on, the stability can be expected to increase with particle size according to the DLVO theory.

A more complex, than according to the DLVO theory, dependence of the stability on the solution ionic strength (IS) was observed. On one hand, a decrease of the IS causes swelling of the "gel" layer, and consequently increase of the stability. On the other hand, it also accelerates the processes (similar to Ostwald ripening by nature) responsible for the rearrangement of the aggregate's surface structure (topology) that may lead to a decrease of their stability.

The stability of silica colloids was found to be higher at higher solution pH. The pH was increased from an initial 7.5 to 9.5 after the particles have reached a certain size. Virtually no further increase of the mean particle size was observed. The transient processes of the "gel" layer dissolution – re-growth caused by the change of solution pH was identified to be responsible for the "focusing" of the particle size distribution observed in the final stage of the sol preparation before use in the deposition experiment.

The changes of the sols parameters (mean size, particle size distribution) that were occurring during the deposition experiments were also analysed. As a result, the ongoing aggregation of the colloidal silica in due course of the deposition experiments was confirmed. It was shown to proceed faster at higher flow rates.

Ultimately, the study of the colloidal silica behavior at different stages of the undertaken experimentation helped to find an explanation of the disagreements between the theory and experiment. In particular, the measured values of particle stability, being order of magnitude higher than the standard DLVO theory predicts (and increasing with decreasing particle size), explained the low (and increasing with the particle size) silica scaling rates observed in the experiments with small particles (10-60 nm in diameter).

However the experimental scaling rate observed with the larger particles (125 nm) was found to be three orders of magnitude higher than would be expected based on the current theory of particle transport in turbulent flow and on the DLVO theory of particle interactions, which is assumed to govern stability of such large particles (see Section 6.1.4).

Moreover, the particle size effects observed in the experiments and predicted by the theory were contradictory. The theory suggested domination of the diffusion transport and increase of particle stability with particle size, and thus lower deposition rate for larger particles, in the relevant particle size range. The experiments, in turn, indicated faster scaling for larger particles.

These persistent discrepancies between the experiment and theory together with some specifics of the silica scale morphology generated a hypothesis of the significant inertial mechanism of particle transport not accounted by current theory.

While the current theory considers only the wall-normal component of the convective particle transport, its tangential component was evaluated in Section 6.2 as such mass transfer mechanism specific to deposition of silica nanoparticles onto a rough, scaled surface.

This was done by first, finding particle flux onto an upstream side of a single scale protrusion. Second, it was multiplied by the experimentally derived surface density of the protrusions to give the estimated transport rate for this mechanism.

This additional convective particle transport was found to be significant in comparison with the transport rate predicted by the current particle transport theory. Its rate was also shown to increase with particle size and its magnitude to be significant enough to decrease remaining disagreement between the experimental and theoretical scaling rates (for large particles) by one order of magnitude (to two orders of magnitude).

Since particle transport rate conceptually can't be much higher (since at $\log_{10} V_{dep}^{+} > 0$ particle concentration at the wall, found as $V_{dep}^{+} \cdot c_p^0 = j/u_*$, would be higher than in the bulk c_p^0) the remaining two orders of magnitude difference between the theory and experiment was explained by a lower than predicted by the DLVO theory actual stability of the larger colloids used in the experiment. This, in turn, can be explained by the presence of many metal ions in real geothermal brine, which tend to be incorporated into silica colloids and affect their surface charge distribution and the stabilising repulsive forces.

Clearly, finding the actual stability of the silica colloids for a wider range of the conditions (particle size, IS) than tested herein presents great interest. The approach and methods reported in this dissertation may well equip one for such a task.

The sum of the reported experimental and theoretical studies clarified the effects of the brine chemistry (pH and ionic strength), size of the colloidal particles present in the brine and flow parameters on the rate of scaling. By analyzing its two governing processes, transport and attachment of the colloidal particles to a surface, the rate of scaling was shown to be higher for: 1) larger particles, higher ionic strength and lower pH of the brine and 2) higher roughness of the surface.

A number of anti-scaling practical implications for the geothermal applications were drawn from this knowledge (Chapter 7). First, the size of the scale roughness observed through the variations in the pressure drop and heat fluxes across the heat exchanger can be used as a key criterion for optimal maintenance cycle design.

Second, the deposition of smaller and more stable particles was found to form harder scale. Therefore, for some cases a compromise between the ease of cleaning and the rate of fouling could be made by controlling the particle size, brine pH and ionic strength.

Third, active or passive flow control can be used to mitigate scaling in the critical locations like pipe bends and valves.

Finally, the reduction of the formation permeability due to scaling brought about by the reinjected brine can be decreased by fine tuning the operating parameters during the colloid formation phase. For instance, if the brine is forced to reach its final mineral oversaturation faster it will form smaller particles that are less likely to cause formation pore occlusion.

Besides these practical recommendations which may ultimately help to increase the efficiency of geothermal power stations, the results of the present study may be of value in the fields of mass transfer and colloid science.

REFERENSES

1. **Fridleifsson, I. B., et al.** *The possible role and contribution of geothermal energy to the mitigation of climate change.* Luebeck, Germany : 2008. IPCC Scoping Meeting on Renewable Energy Sources. pp. 59-80.

2. **Davies, J. H., Davies, D. R.** Earth's surface heat flux. *Solid Earth.* 2010, Vol. 1, 1, pp. 5-24.

3. **Jaupart, C., Mareschal, J. C.** Heat flow and thermal structure of the lithosphere. *Treatise on Geophysics.* 2007, Vol. 6, pp. 217-251.

4. **Schroder, K. P. and Connon, S. R.** Distant Future of the Sun and Earth Revisited. *Monthly Notices of the Royal Astronomical Society.* 2008, Vol. 386, 1, pp. 155-163.

5. **Carter, B. and McCrea, W. H.** The anthropic principle and its implications for biological evolution. *Philosophical Transactions of the Royal Society of London.* 1983, Vol. A310, 1512, pp. 347-363.

6. **Bignami, G. F. and Sommariva, A.** *A Scenario for Interstellar Exploration and Its Financing.* Springer, 2013. ISBN 978-88-470-5337-3.

7. **Matek, B.** *2014 Annual U.S. & Global Geothermal Power Production Report.* Washington, DC : Geothermal Energy Association, 2014.

8. *Statistical Review of World Energy .* BP, 2014.

9. **Tester, J. W., et al.** *The Future of Geothermal Energy:Impact, of Enhanced Geothermal Systems (Egs) on the United States in the 21st Century.* Idaho National Laboratory. Idaho Falls : Massachusetts Institute of Technology, 2006. ISBN 0-615-13438-6.

10. **Strube, O.** Scaling Geothermal for Reliable Baseload Power. [Online] 10 5, 2007. [Cited: 10 8, 2014.]

11. **Cothran, H.** *Energy Alternatives.* Greenhaven Press, 2002. ISBN 0737709049.

12. U.S. Department of Energy. [Online] [Cited: 10 2, 2014.] http://www1.eere.energy.gov/tribalenergy/guide/costs_geothermal_energy.html.

13. *Energy in New Zealand 2014.* Modelling & Sector Trends Infrastructure and Resource Markets. Wellington : Ministry of Business, Innovation & Employment. ISSN 2324-5913.

14. **Zarrouk, S. J. and Hyungsul, M.** *Efficiency of geothermal power plants: a worldwide review.* Auckland, New Zealand : 2012. New Zealand Geothermal Workshop 2012.

15. **Erkan, K., et al.** *Understanding the Chena Hot flopë Springs, Alaska, geothermal system using temperature and pressure data.* 2008, Geothermics, Vol. 37, pp. 565-585.

16. **Kawereau station manager.** personal communication. 2012.

17. *Assessment of Current Costs of Geothermal Power generation in New Zealand (2007 Basis).* Sinclair Knight Merz Pty Ltd., 2007.

18. **Potapov, V.V.** Formation of Solid Deposits of Amorphous Silica in a Flow of Hydrothermal Solution. *Glass Physics and Chemistry.* 2004, Vol. 30, 1, pp. pp. 82–89.

19. **Brown, K. L. and Bacon, L. G.** Pilot plant experiments atWairakei Power Station. *Geothermics.* 2009, Vol. 38, pp. 64-71.

20. **Olafsson, J., Riley, J. P.** Geochemical studies of the thermal brine from Reykjanes (Iceland). *Chemical Geology.* 1978, Vol. 21.

21. **Tarcan, G.** Mineral saturation and scaling tendencies of waters discharged from wells (N150 8C) in geothermal areas of Turkey. *Journal of Volcanology and Geothermal Research .* 2005, Vol. 142.

22. **Gallup, D. L.** Geochemistry of geothermal fluids and well scales. *Ore Geology Reviews.* 1998, Vol. 12.

23. **Weres O., et al.** Kinetics of silica polymerization. *Journal of Colloid and Interface Science.* 1981, Vol. 84, pp. 379-402.

24. **Fleming B.A.** Kinetics of reaction between silicic acid and amorphous silica surfaces in NaCl solutions. *Journal of Colloid and Interface Science.* 1986, Vol. 110, pp. pp. 40-64.

25. **Mroczek, E. K.** *Review of silica deposition rates at Ohaaki, Rotokawa, and Wairakei geothermal fields and comparison of observed rates with predicted deposition rates calculated using three different kinetic deposition models.* s.l. : Institute of Geological and Nuclear Sciences, 1994.

26. **Mroczek, E. K. and McDowell, G.** *Silica Scaling Field Experiments.* 1988. 10th New Zealand Geothermal Workshop.

27. **Brown, K. L. and McDowell, G.** *The effect of aeration on silica scaling.* 1982. 4th New Zealand Geothermal Workshop. pp. pp. 127-130.

28. **Mroczek, E. K. and Reeves, R. R.** *The effect of colloidal silica on silica scaling from geothermal fluid.* 1994. 16th New Zealand Geothermal Workshop.

29. **Rothbaum, H. P. and et al.** Effect of silica polymerisation and pH on geothermal scaling. *Geothermics.* 1979, Vol. 8.

30. **Yanagase, T., et al.** The properties of scales and methods to prevent them. *Geothermics.* 1970, Vol. 2.

31. **Mahon, W. A.J., Klyen, L. E. and McDowell, G. D.** *Silica deposition from waters discharged from geothermal wells.* Chemistry Division Report. GNS, 1975.

32. **Gunnarsson, I. et al.***Reducing silica deposition potential in waste waters from Nesjavellir and Hellisheidi power plants, Iceland.* Bali, Indonesia, 2010. World Geothermal Congress.

33. **Yoshitaka, K., Hiroaki, S. and Kokan, K.** Technology to Counter Silica Scaling in Binary Power-Generating System Using Geothermal Hot Water. *Fuji Electric Review.* 2013, Vol. 59, 2.

34. **Addison, S. J., Stabler, I. M. and Gresham, T. J.** *Design and successful operation of a new pH measurement system for geothermal brine.* Rotorua, New Zealand :2013. 35th New Zealand Geothermal Workshop.

35. **Itoi, R. and al., et.** Experimental study on the silica deposition in a porous medium. *Geothermal Resources Council, Transactions,.* 1984, Vol. 8.

36. **Kiyota, Y., et al.** *Evaluation on geothermal injection treatment by pH modification.* Kyushu-Tohoku, Japan, 2000. World Geothermal Congress. pp. 3077-3082.

37. **Mroczek, E. K., et al.** Deposition of amorphous silica in porous packed beds - predicting the lifetime of reinjection aquifers. *Geothermics.* 2000, Vol. 29, pp. 737-757.

38. **Weres, O. and Tsao, L.** Chemistry of silica in Cerro Prieto brines. *Geothermics.* 1981, Vol. 10, pp. 255-276.

39. **Sugama, T. and Gawlik, K.** Anti-silica fouling coatings in geothermal environments. *Materials Letters.* 2002, Vol. 57, pp. 666-673.

40. **Chan, S. and et al.** Silica Fouling of Heat Transfer Equipment-Experiments and Model. *Journal of Heat Transfer.* 1988, Vol. 110, pp. 841-849.

41. **Garibaldi, F. and Freeston, D. H.** *Effect of hydrodynamic flow conditions on silica deposition.* 1981. 3rd New Zealand Geothermal Workshop. pp. 203-208.

42. **Dunstall, M. and Brown, K. L.** *Silica scaling under controlled hydrodynamic conditions.* Kyushu-Tohoku, Japan , 2000. World Geothermal Congress. pp. 3039-3044.

43. **Dunstall, M., Zipfel, H. and Brown, K. L.** *The onset of silica scaling around circular cylinders.* Kyushu-Tohoku, Japan, 2000. World Geothermal Congress. pp. 3045-3050.

44. **Jamieson, R. E.** *Geothermal Silica Scaling, Masters.* Auckland: University of Auckland, 1984.

45. **Bohlmann, E. and et al.** *Kinetics of silica deposition from simulated geothermal brines.* s.l. : Oak Ridge National Laboratory, 1980.

46. **Pott, J., Dunstall, M. G. and Brown, K. L.** *Numerical simulation of silica scaling.* 18th New Zealand Geothermal Workshop, 1996. 18th New Zealand Geothermal Workshop. pp. 41-46.

47. **Zipfel, H.** *Investigation of Hydrodynamic Influence on Silica Scaling on Circular Cylinders, Certificate of Proficiency.* Auckland : Geothermal Institute, University of Auckland, 1998.

48. **Brown, K.** Thermodynamics and kinetics of silica scaling. *International Workshop on Mineral Scaling.* 2011.

49. **Chan, S.** A review on solubility and polymerization of silica. *Geothermics.* 1989, Vol. 18, pp. 49-59.

50. **Gallup, D.** Aluminium silicate scale formation and inhibition: scale characterization and laboratory experiments. *Geothermics.* 1997, Vol. 26, 4, pp. 483-499.

51. **Cole, D. and al., et.** Development of a classical force field for the oxidized Si surface: Application to hydrophilic wafer bonding. *The journal of chemical physics.* 2007, Vol. 127.

52. **Makrides, A. C. and et al.** *Study of Silica Scaling From Geothermal Brines, Report.* U. S. Dept. of Energy, 1978. COO-2607-5.

53. **Hunter R. J.** *Introduction to modern colloid science.* Oxford : Oxford University Press, 1993.

54. **Sugimoto, T.** Preparation of monodispersed colloidal particles. *Adv. Colloid Interface Sci.* 1987, Vol. 28, pp. 65-108.

55. **Wen, T., et al.** A generalized diffusion model for growth of nanoparticles synthesized by colloidal methods. *Journal of Colloid and Interface Science.* 2014, Vol. 419, pp. 79–85.

56. **Rebreanu, L., Vanderborght, J. P. and Chou, L.** The diffusion coefficient of dissolved silica revisited. *Marine Chemistry.* 2008, Vol. 112, pp. 230–233.

57. **Addison, S.** Personal communication (2013).

58. **Ostwald, W.** Studien über die Bildung und Umwandlung fester Körper (Studies on the formation and transformation of solid bodies). *Zeitschrift für physikalische Chemie.* 1897, Vol. 22, pp. 289-330.

59. **Lifshitz, I. M. and Slyozov, V. V.** The Kinetics of Precipitation from Supersaturated Solid Solutions. *Journal of Physics and Chemistry of Solids.* 1961, Vol. 19, (1–2), pp. 35–50.

60. **Wagner, C.** Theorie der Alterung von Niederschlägen durch Umlösen (Ostwald-Reifung)" [Theory of the aging of precipitates by dissolution-reprecipitation (Ostwald ripening). *Zeitschrift für Elektrochemie.* 1961, Vol. 65, 7, pp. 581–591.

61. **Elder, K. R., et al.** Theory and simulation of Ostwald ripening. *Phys. Rev. B.* 1993, Vol. 47, 14110.

62. **Burlakov, V.M.** *Ostwald Ripening on Nanoscale.* [arXiv] 2007. Standart Number: 0710.5224.

63. **Finsy, R.** On the critical radius in Ostwald ripening. *Langmuir.* 2004, Vol. 20, pp. 2975–2976.

64. **De Smet, Y., Deriemaeker, L. and Finsy, R.** Ostwald Ripening of Alkane Emulsions in the Presence of Surfactant Micelles. *Langmuir.* 1999, Vol. 15, 6745.

65. **Smoluchowski, M.** Uber brownsche molekularbewegung unter einwirkung auserer kruafte und deren zusammenhang mit der verallgemeinerten diffusions- gleichung. *Ann Phys.* 1917, Vol. 48, pp. 1103–1112.

66. **Fuchs, N.** Ueber die stabilitat und aufladung der aerosole. *Z.Phys.* 1934, Vol. 89, pp. 736–743.

67. **Levich, V.** *Physicochemical hydrodynamics.* Prentice-Hall, Inc., 1962.

68. **Derjaguin, B.V., Landau, L.** Theory of the stability of strongly charged lyophobic sols and of the adhesion of strongly charged particles in solutions of electrolytes. *Acta Phys Chim.* 1941, Vol. 14, pp. 633–662.

69. **Verwey, E. J.W. and Overbeek, J. T.G.** *Theory of the stability of lyophobic colloids.* Amsterdam : Elsevier, 1948.

70. **Adamczyk, Z., Weronski, P.** Application of the DLVO theory for particle deposition problems. *Advances in Colloid and Interface Science.* 1999, Vol. 83, pp. 137-226 .

71. **Iler, R. K.** *The Chemistry of Silica.* New York : Wiley, 1979.

72. **Kobayashi, M., et al.,** Aggregation and Charging of Colloidal Silica Particles: Effect of Particle Size. *Langmuir.* 2005, Vol. 21, pp. 5761-5769.

73. **Škvarla, J.** Quantitative Interpretation of Anomalous Coagulation Behavior of Colloidal Silica Using a Swellable Polyelectrolyte Gel Model of Electrical Double Layer. *Langmuir.* 2013, Vol. 29 (28), pp. 8809–8824.

74. **Weitz, D. A., et al.** Limits of the Fractal Dimension for Irreversible Kinetic Aggregation of Gold Colloids. *Phys. Rev. Lett.* 1985, Vol. 54.

75. **Ball, R. C., et al.** Universal kinetics in reaction-limited aggregation. *Phys. Rev. Lett.* 1987, Vol. 58.

76. **Lin, M. Y., Lindsay, H. M., Weitz, D. A., Ball, R. C., Klein, R. and Meakin, P.** Universality in colloid aggregation. *Nature.* June 01, 1989, Vol. 339, pp. 360 - 362.

77. **Carpineti, M., et al.** Salt-induced fast aggregation of polystyrene latex. *Phys. Rev. Lett.* 1990, Vol. 42, 7347.

78. **Lebovka, N.I.** Aggregation of Charged Colloidal Particles. *Adv. Polym. Sci.* 2014, Vol. 255, pp. 57–96.

79. **Evenhuis, C. J., et al.** Variation of zeta-potential with temperature in fused-silica capillaries used for capillary electrophoresis. 2006, 27, 672–676. *Electrophoresis.* 2006, Vol. 27.

80. **Sheng-Hua, X., et al.** Coupling effect of Brownian motion and laminar shear flow on colloid coagulation: a Brownian dynamics simulation study. *Chin. Phys. B.* 2012, Vol. 21, 5.

81. **Einstein, A.** *The Theory of Brownian Movement.* New York : Dover, 1956.

82. **Frank-Kamenetskii, D. A.** *Diffusion and Heat Transfer in Chemical Kinetics (in Russian).* Moscow-Leningrad : USSR Academy of Science Press, 1947.

83. **Gupta, D. and Peters, M. H.** A Brownian dynamics simulation of aerosol deposition onto spherical collectors. *J Colloid and Interface Science.* 1985, Vol. 104, 375.

84. **Hähner, F., Dau, G. and Ebert, F.** Inertial impaction of aerosol particles on single and multiple spherical targets. *Chem. Eng. Technol.* 1994, Vol. 17, pp. 88-94.

85. **Martin, S.** *Particles Deposition on an Array of Spheres using a Hybrid Euler/Lagrange CFD Method. Trainee Report* : Paul Sherrer Institute, 2009.

86. **Guha, A.** Transport and Deposition of Particles in Turbulent and Laminar Flow. *Annu. Rev. Fluid Mech.* 2008, Vol. 40, 311–41.

87. **Caporaloni, M., Tampieri, F. and Trombett, F.** Transfer of particles in nonisotropic air turbulence. *J. Atmos. Sci.* 1975, Vol. 32, pp. 565–568.

88. **Saffman, P. G.** The lift on a small sphere in a slow shear flow. *J. Fluid Mech.* 1965, Vol. 22, pp. 385-400.

89. **Clift, R., Grace, J. R. and Weber, M. E.** *Bubbles, Drops, and Particles.* Academic Press Inc., 1978.

90. **Young, J. and Leeming, A.** A theory of particle deposition in turbulent pipe flow. *Journal of Fluid Mechanics.* 1997, Vol. 340, pp. 129-159.

91. **Kallio, G. A. and Reeks, M. W.** A numerical simulation of particle deposition in turbulent boundary layers. *Int. J. Multiphase Flow.* 1989, Vol. 15.

92. **Epstein, N.** Elements of particle deposition onto nonporous solid surfaces parallel to suspension flows. *Experimental Thermal and Fluid Science.* 1997, Vol. 14, pp. 323-334.

93. **Sinclair, L.** *Development of a Silica Scaling Test Rig, Masters.* Christchurch : University of Canterbury, 2012.

94. **Shams, M., Ahmadi, G. and Rahimzadeh, H.** A sublayer model for deposition of nano- and micro-particles in turbulent flows. *Chemical Engineering Science.* 2000, Vol. 55, pp. 6097-6107.

95. **Schlichting, H. and Gersten, K.** *Boundary Layer Theory.* 8th ed. Springer-Verlag, 2004. ISBN 81-8128-121-7.

96. **Hagen, G.** Uber den Einfluss der Temperatur auf die Bewegung des Wasser in Röhren. *Math.Abh. Akad. Wiss.* 1854, pp. 17-98.

97. **Darcy, H.** *Recherches expérimentales relatives au mouvement de l'eau dans les tuyaux.* Paris : Mallet-Bachelier, 1857.

98. **Blasius, H.** *Das Aehnlichkeitsgesetz bei Reibungsvorgängen in Flüssigkeiten .* Berlin : VDI-Verlag, 1913, Mitteilungen über Forschungsarbeiten auf dem Gebiete des Ingenieurwesens, Vol. vol.131.

99. **Nikuradse, J.** *Laws of flow in rough pipes. Translation of Stromungsgesetze in rauhen Rohren, Nikuradse, Forschung auf dem Gebiete des Ingenieurwesens, 1933.* Washington : NACA Technical Memorandum 1292, 1950.

100. **Prandtl, L.** *Uber den Reibungswiderstand stromenderluft.* Gottingen : Ergeb. Aerodyn. Versuch., 1927, Vol. III series.

101. **Monty, J. P., et al.** A comparison of turbulent pipe, channel and boundary layer flows. *Journal of Fluid Mechanics.* 2009, Vol. 632, pp. 431-442.

102. **Reichardt, H.** Die Warmeubertragung in turbulenten Reibungsschichten, translated as Heat transfer through turbulent friction layers, Nut. Adv. Comm. Aero., Wash., Tech. Mem. no. 1047,1943. *Z. angew. Math. Mech.* 20, pp. 297-328;.

103. **Jimenez, J. and Moin, P.** The minimal flow unit in near wall turbulence. *J. Fluid Mech.* 1991, Vol. 225, pp. 221-240.

104. **Jimenez, J. and Pinelli, A.** The autonomous cycle of near wall turbulence. *J. Fluid Mech.* 1999, Vol. 389, pp. 335-359.

105. **Robinson, S. K.** Coherent motions in the turbulent boundary layer. *Ann. Rev. Fluid Mech.* 1991, Vol. 23, pp. 601-639.

106. **Tennekes, H. and Lumley, J. L.** *A first course in turbulence.* Cambridge, Massachusetts, and London, England : The MIT Press, 1972.

107. **Klebanoff, P.** Characteristics of turbulence in a boundary layer with zero pressure gradient. *Nut. Adv. Comm. Aero., Wash., Tech. Note no. 3178.* 1954.

108. **Schubauer, G.** Turbulent processes as observed in boundary layer and pipe. *J. Appl. Phys.* 1954, Vol. 25, 188-96.

109. **Jimenez, J.** Turbulent flows over rough walls. *Ann. Rev. Fluid Mech.* 2004, pp. 173-196.

110. **Perry, A. E., Schofield, W. H. and Joubert, P.** Rough wall turbulent boundary layers. *J. Fluid Mech.* 1969, Vol. 37, pp. 383–413.

111. **Tani, I.** Drag reduction by riblet viewed as a roughness problem. *Proc. Jpn. Acad. B.* 1988, Vol. 64, pp. 21-24.

112. **Sirovich, L. and Karlsson, S.** Turbulent drag reduction by passive mechanisms. *Nature.* 1997, Vol. 388, 735-55.

113. **Bechert, D. W., Bruse, M. and Hage, W.** Experiments with three-dimensional riblets as an idealized model of shark skin. *Exp. Fluids.* 2000, Vol. 28, 403-12.

114. **Walsh, M. J.** Riblets. [ed.] D. M. Bushnell and J. N. Hefner. *Viscous Drag Reduction in Boundary Layers.* New York : AIAA, 1990.

115. **Colebrook, C. F.** Turbulent flow in pipes, with particular reference to the transition region between smooth and rough pipes. *J. Inst. Civ. Eng.* 1939, Vol. 11, pp. 133-156.

116. **Ligrani, P. M. and Moffat, R. J.** Structure of transitionally rough and fully rough turbulent boundary layers. *J. Fluid Mech.* 1986, Vol. 162, pp. 69-98.

117. **Bechert, D. W., et al.** Experiment on drag-reducing surfaces and their optimization with an adjustable geometry. *J. Fluid Mech. .* 1997, Vol. 338, pp. 59–87.

118. **Moody, L. F.** Friction factors for pipe flow. *Transactions of the ASME.* Vol. 66, pp. 671-684.

119. **More, A. A.** Analytical solutions for the Colebrook and White equation and for pressure drop in ideal gas flow in pipes. *Chemical Engineering Science.* 2006, Vol. 61, 16.

120. **Serghides, T. K.** Estimate friction factor accurately. *Chemical Engineering Journal.* 1984, Vol. 91, 5, pp. 63-64.

121. **Luchini, P., Manzo, F. and Pozzi, A.** Resistance of a grooved surface to parallel flow and cross-flow. *J. Fluid Mech.* 1991, Vol. 228, pp. 87–109.

122. **Bandyopadhyay, P. R. and Watson, R. D.** Structure of rough-wall turbulent boundary layers. *Phys. Fluids.* 1988, Vol. 31, 1877–83.

123. **Luikov, A. V.** *Theory of Thermal Conductivity.* Moscow : Visshaya Shkola, 1967.

124. **Incropera, Frank P. and DeWitt, David P.** *Fundamentals of Heat and Mass Transfer.* 4th ed. New York : Wiley, 2000. p. p. 493. ISBN 0-471-30460-3.

125. *Theory Guide.* [ANSYS Fluent Documentation]: ANSYS, 2013.

126. **Su, Y.** Flow analysis and design of three-dimensional wind tunnel contractions. *AIAA Journal.* 1991, Vol. 29, 11.

127. **Uchiyama, H. and Ide, M.** Development of a hot-film anemometer calibrator for water flow measurement. *Flow Measurement and Instrumentation.* 2009, Vol. 20, pp. 75-80.

128. **Bergna, H. E.** The Colloid Chemistry of Silica. *Advances in Chemistry.* H. E. Bergna, 1994, Vol. Chapter 2, Series 234.

129. **Alexander, G.B and Iler, R.K.** *Patent:Aqueous acidic polyvinyl alcoholsilica solution. 2,601,235,* U.S. Patent, 1952.

130. **Bechford, M.F. and Snyder, O.E.** *U.S. Patent . 2,574,902* 1951.

131. **Bird, P.G.** *U.S. Patent 2,224,325,* 1941.

132. **Stober W., Fink A. and Bohm E.** Controlled growth of monodisperse silica spheres in micron size range. *Journal of Colloid and Interface Science.* 1968, Vol. 26, 1, pp. 62-69.

133. **Guo J. J., Liu X. H., Cheng Y. C., Li Y., Xu G. J. and Cui P.** Size Controllable Synthesis of Monodispersed Colloidal Silica Nanoparticles via Hydrolysis of Elemental Silicon. *Journal of Colloid and Interface Science.* 2008, Vol. 326, 1, pp. pp. 138-142.

134. *Nanotrac particle size analyzer Models NPA150, 151, 250, 251, 252, 253 Operation and maintenance manual, Rev D, Jan 2009.* Microtrac Inc., 2002.

135. **Gupta.** Forum: Convert and Calculate: Specific conductivity (umho/cm) to Ionic strength via Russell factor. *VBulletin online page.* [Online] February 7, 2011. [Cited: August 7, 2014.] http://onlineconversion.vbulletin.net/forum/main-forums/convert-and-calculate/247-specific-conductivity-umho-cm-to-ionic-strength-via-russell-factor?t=458.

136. **Tsai, M., Huang, P. and Yang, C.** Formation mechanisms of colloidal silica via sodium silicate. *Journal of Nanoparticle Research.* 2006.

137. **Antunes, R. A., Costa, I. and Lúci, D.** Characterization of corrosion products formed on steels in the first months of atmospheric exposure, *Mat. Res.* 2003, Vol. 6, 3.

138. **Tobler, D. J., Shaw, S. and Benning, L. G.** Quantification of initial steps of nucleation and growth of silica nanoparticles: An in-situ SAXS and DLS study. *Geochimica et Cosmochimica Acta.* 2009, Vol. 73, pp. 5377-5393.

139. **Suzuki, T., et al.** Analysis of Surface Structure and Hydrogen/Deuterium Exchange of Colloidal Silica Suspension by Contrast-Variation Small-Angle Neutron Scattering. *Langmuir.* 2008, Vol. 24, 9, pp. 4537–4543.

140. **Ohshima, H.** Electrostatic interaction between soft particles. *J. Colloid Interface Sci.* 2008, Vol. 328, pp. 3-9.

141. **Babick, F., et al.** van-der-Waals interaction between two fractal aggregates. *Advanced Powder Technology.* 2011, Vol. 22, pp. 220-225.

142. **Schießl, K., et al.** Calculation of double layer interaction between colloidal aggregates. *Advanced Powder Technology.* 2012, Vol. 23, pp. 139–147.

143. **Bogush, G. H. and Zukoski, C. F.** Uniform Silica Particle Precipitation: An Aggregative Growth Model. *Journal of Colloid and interface Science.* 1991, Vol. 142, 1. pp. 19-34.

144. **Bitter, J. L., et al.** Anomalous Silica Colloid Stability and Gel Layer Mediated Interactions. *Langmuir.* 2013, Vol. 29, p. 8835−8844.

145. **Kokhanenko, P., Jermy, M. C. and Brown, K.** *Hydro- and Electrochemical Aspects of Silica Colloid Deposition from a Turbulent Flow onto a Rough Wall.* 19th Australasian Fluid Mechanics Conference. Melbourne, Australia: 8-11 December 2014.

146. **Mroczek, E. K., et al.** *Silica scaling trial and injection of cold separated geothermal water at Wairakei,* 35th New Zealand Geothermal Workshop. *New Zealand.* Rotorua, 2013.